UNIVERSITY OF WARSAW

Magnetotransport properties of the MBE-grown transition-metal compounds

Author:

Zuzanna Ogorzałek-Sory

Supervisor:

Dr hab. Marta Borysiewicz

Institute of Experimental Physics

Faculty of Physics

University of Warsaw

Warsaw, 2025

Podziękowania

Szczególne słowa wdzięczności kieruję do mojej Promotorki - dr hab. Marty Borysiewicz, która od początku stworzyła mi warunki do swobodnego rozwoju naukowego i osobistego. Dzięki jej otwartości miałam możliwość mierzyć się z ambitnymi, nowatorskimi tematami, które były nie tylko wyzwaniem, ale i źródłem ogromnej satysfakcji. Bardzo doceniam, że mogłam liczyć nie tylko na wskazówki merytoryczne, ale też na rozmowę i wsparcie w sytuacjach wykraczających poza samą pracę badawczą. Ta równowaga między profesjonalizmem a ludzkim podejściem sprawiła, że nasza współpraca była efetywna i jednocześnie przyjemna. Dziękuję za cierpliwość, zaufanie i poświęcony czas - to one w dużej mierze ukształtowały mnie jako badaczkę i jako osobę.

Realizacja badań opisanych w niniejszej rozprawie była możliwa dzięki wsparciu pomiarowemu wielu osób. Podziękowania pragnę skierować również do:

Dr. hab. Janusza Sadowskiego, dr. hab. Wojciecha Pacuskiego oraz dr. Bartłomieja Seredyńskiego, za wzrost próbek metodą epitaksji z wiązek molekularnych, obejmujących różne materiały, w tym m.in. $MoTe_2$, $NiTe_2$ oraz TaAs, które stanowiły kluczowy wsad eksperymentalny do niniejszej pracy.

Dr. hab. Januszowi Sadowskiemu dziękuję również za możliwość uczestnictwa i realizacji grantu 2017/27/B/ST5/02284 "Wzrost metodą epitaksji z wiązek molekularnych i badanie heterostruktur topologicznych półmetali z ferro i antyferromagnetykami."

Dr. Piotra Dziawy oraz dr. hab. Janusza Sadowskiego za wykonanie pomiarów ARPES dla próbki $NiTe_2$. Dr. Piotrowi Dziawię dziękuję również za analizę otrzymanych wyników.

Dr. hab. Sławomira Kreta, mgr Wiktorii Zajkowskiej-Pietrzak oraz dr Anny Kalety za przeprowadzenie analiz transmisyjnej mikroskopii elektronowej oraz wykonanie zdjęć dla licznych próbek wykorzystanych w niniejszej pracy.

Dr. Jarosława Domagały za przeprowadzenie pomiarów wysokorozdzielczej dyfrakcji rentgenowskiej, w tym reflektometrii a także za wsparcie w analizie uzyskanych danych.

Dr. Mateusza Tokarczyka za możliwość uczestniczenia w wielu pomiarach dyfrakcji rentgenowskiej oraz za pomoc w analizie uzyskanych wyników.

Prof. Dariusza Wasika i prof. Michała Baja za ogromne wsparcie merytoryczne i opiekę naukową. Prof. Michałowi Bajowi dziękuję również za wykonanie obliczeń MSA.

Dr. Adama Kwiatkowskiego za wsparcie eksperymentalne w trakcie pierwszych dwóch lat mojej pracy w Laboratorium Magnetotransportu Nanostruktur Półprzewodnikowych, a także za pomoc w prowadzeniu pomiarów i przygotowaniu eksperymentów.

Prof. Krzysztofa Korony za pomoc w napylaniu kontaktów indowych do próbek $MoTe_2$.

Dr. Karola Nogajewskiego za pomoc w trakcie prób eksfoliacji próbek $MoTe_2$ uzyskanych metodą MBE oraz wykonanie bramkowanych próbek h-BN / $MoTe_2$-h-BN z użyciem warstw z bulkowego kryształu 2H-$MoTe_2$.

Dr Magdaleny Grzeszczyk za przekazanie mi wiedzy i umiejętności w zakresie samodzielnego wykonywania pomiarów Ramanowskich.

Mgr. Jakuba Polaczyńskiego za przygotowanie próbek pojedynczych nanodrutów $MoTe_x$ z wykonanymi kontaktami elektrycznymi, niezbędnych do przeprowadzenia pomiarów magnetotransportowych.

Dziękuję Współautorom z zagranicy za wykonanie obliczeń teoretycznych, które umożliwiły lepsze zrozumienie oraz opisanie wyników dotyczących próbek $NiTe_2$ i TaAs. Są to: prof. Christoph Heil (Institute of Theoretical and Computational Physics), prof. Luiz T. F. Eleno (University of Sao Paulo), dr Pedro P. Ferreira (University of Sao Paulo and Institute of Theoretical and Computational Physics), dr Antonio L. R. Manesco (Kavli Institute of Nanoscience) oraz prof. Hsin Lin (Institute of Physics, Academia Sinica, Taiwan), prof. Chi-Cheng Lee (Department of Physics, Tamkang University, Taiwan) i mgr Bao-Huei Huang (Institute of Physics, Academia Sinica, Taiwan).

Dziękuję również Współautorom z Uniwersytetu Łódzkiego za dodatkowe pomiary Ramanowskie, XPS i AFM dla próbek $MoTe_2$ oraz TaAs. Są to: prof. Paweł J. Kowalczyk, dr Iaroslav Lutsyk oraz mgr Wojciech Ryś (Wydział Fizyki i Informatyki Stosowanej, Uniwersytet Łódzki).

Dziekuję również całej grupie Laboratorium Magnetotransportu Nanostruktur Półprzewodnikowych oraz wszystkim pozostałym Współprawcownikom, którzy dołożyli swoje cegiełki do powstania tej pracy.

Dziękuję moim Rodzicom, którzy wspierali mnie od początku mojej kariery zawodowej i zawsze we mnie wierzyli.

Dziękuję również mojemu Mężowi za codzienne wsparcie i motywację.

Pracę dedykuję Rodzicom.

Abstract

The work presents the results of research on thin films of $NiTe_2$, $MoTe_2$ and TaAs grown by the MBE method. The transport and structural properties of those materials were used to provide insight into their physical properties, basic parameters to relate them to the MBE-growth conditions. Those materials are well-known in the bulk form for their diverse electronic properties (from semiconducting to metallic) depending on their crystal phase. It is the metallic phase that is the most interesting, as it shows topological character, with chiral carriers and relativistic dispersion E(k). These inherent properties are linked to the lack of inversion or time reversal symmetry in the crystal structure. Since the growth technology of these thin films was in its nascent state at the beginning of this thesis and the $NiTe_2$ and TaAs were demonstrated by the MBE laboratory of the Faculty of Physics, University of Warsaw, for the first time in the World, a comprehensive characterization of their properties was undertaken as the goal of this work, in order to gain the understanding of these MBE-grown materials. Magnetotransport measurements were a major tool, and a number of complimentary experimental methods (XRD, SEM or Raman scattering, performed by the Author of the thesis and TEM, ARPES, STM, AFM in collaboration) and theoretical calculations (in collaboration) were used to determine the phase and reveal the properties of $NiTe_2$, $MoTe_2$ and TaAs in the thin film form.

The $NiTe_2$ layers showed high crystalline quality, smooth morphology and well-pronounced interfaces. Substantial strain was present in the films, possibly due to inter-layer defects or intercalated atoms, and local substrate-related strain, which was evidenced as well. The electronic properties of the $NiTe_2$ layers were governed by substrate temperature during the growth - at low temperatures metallic $NiTe_2$ was observed, while at high temperatures semiconductor-like phase was revealed due to the observed Te deficiency. In magnetotransport measurements of the most resistive samples with metallic R(T), a 3D weak antilocalization was observed, which evolved into positive magnetoresistance at higher temperatures, suggesting topological origin. This was correlated with the observation of topological states in the APRES data. However, no other transport phenomena, predicted for Dirac semimetal were observed, most probably due to very high carrier concentration.

$MoTe_x$ samples proved much harder to grow with only one sample containing the topological 1T′-$MoTe_2$ phase. Unfortunately, the phase was buried between two conducting materials making meaningful characterization by electronic transport measurements impossible. The characterization of other grown $MoTe_x$ samples was however performed, helping to understand their transport properties. In particular, these were 2H-$MoTe_2$ for low substrate

temperature - and net of 2H-$MoTe_2$ / Mo_6Te_6 nanowires - when the substrate temperature was higher. 2H-$MoTe_2$ showed an increase of resistivity when the growth temperature was decreased, indicating a substantial degree of disorder in the layers. As air-sensitivity was observed for thin layers, AlO_x capping was proposed and tested, showing a way to protect the layer from atmosphere impact.

Finally, the TaAs thin films showed nanocolumnar morphology, correlated with an anisotropy of conductivity, which was up to 5 times higher for current aligned along the nanocolumns than across them. The crystalline structure of individual nanocolumns was dominated by atom arrangement observed in stacking faults in the tetragonal TaAs. This atomic structure was characteristic of an orthorhombic phase, which was confirmed by phase-specific reflections in the XRD patterns. DFT calculations showed that an orthorhombic configuration is energetically favorable for TaAs and that such phase is a Weyl semimetal. Low-temperature magnetotransport showed weak antilocalization as the only fingerprint of topological carriers. Indeed, all the Weyl points lie far from the experimental Fermi level and stay unpopulated. All these points allow to state that a new Weyl semimetal phase - orthorhombic TaAs - was observed.

Streszczenie

Praca przedstawia wyniki badań nad cienkimi warstwami $NiTe_2$, $MoTe_2$ oraz TaAs otrzymanymi metodą MBE. Właściwości transportowe i strukturalne tych materiałów zostały wykorzystane do zrozumienia ich własności fizycznych oraz uzyskania podstawowych parametrów, umożliwiających powiązanie ich z warunkami wzrostu MBE. Materiały te są dobrze znane w formie objętościowej ze względu na ich zróżnicowane właściwości elektroniczne (od półprzewodzących po metaliczne), które są zależne od fazy krystalicznej. Faza metaliczna jest najbardziej interesująca, gdyż posiada właściwości topologiczne z nośnikami chiralnymi i relatywistyczną dyspersją $E(k)$. Właściwości te są związane z brakiem symetrii inwersji lub odwrócenia w czasie w strukturze krystalicznej. Ponieważ technologia wzrostu tych cienkich warstw znajdowała się w stadium początkowym na początku tej rozprawy, a $NiTe_2$ i TaAs zostały zademonstrowane w laboratorium MBE Wydziału Fizyki Uniwersytetu Warszawskiego po raz pierwszy na świecie, głownym celem pracy było przeprowadzenie kompleksowej charakterystyki ich właściwości, tak aby uzyskać wiedzę na temat tych materiałów. Głównym narzędziem były pomiary magnetotransportowe, a także szereg uzupełniających metod eksperymentalnych (XRD, SEM czy rozpraszanie Ramana wykonywane przez Autorkę pracy oraz TEM, ARPES, STM, AFM we współpracy) oraz obliczenia teoretyczne (we współpracy), które zostały wykorzystane do określenia fazy i ujawnienia właściwości cienkowarstwowych warstw $NiTe_2$, $MoTe_2$ i TaAs.

Warstwy $NiTe_2$ wykazały wysoką jakość krystaliczną, gładką morfologię oraz wyraźnie zaznaczone interfejsy pomiędzy poszczególnymi warstwami. W warstwach obecne było znaczne naprężenie, prawdopodobnie wynikające z defektów międzywarstwowych lub atomów międzywęzłowych, a także lokalnych naprężeń związanych z podłożem, co zostało również udokumentowane. Właściwości elektroniczne warstw $NiTe_2$ były determinowane temperaturą podłoża podczas wzrostu - przy niskich temperaturach obserwowano metaliczne $NiTe_2$, natomiast przy wysokich temperaturach ujawniła się faza o charakterze półprzewodnikowym, wynikająca z niedoboru Te. W pomiarach magnetotransportowych najbardziej opornych próbek z metalicznym $R(T)$ zaobserwowano 3D słabą antylokalizację (z ang. weak antilocalization), która w wyższych temperaturach ewoluowała w dodatnią parabolę, sugerując pochodzenie topologiczne. Było to skorelowane z obserwacją stanów topologicznych w widmach ARPES, jednakże nie zaobserwowano innych zjawisk transportowych przewidywanych dla półmetali Diraca, najprawdopodobniej z powodu bardzo dużej koncentracji nośników.

Próbki $MoTe_x$ okazały się znacznie trudniejsze do wzrostu, przy czym tylko jedna próbka zawierała topologiczną fazę 1T′-$MoTe_2$. Niestety faza ta była „ukryta” pomiędzy dwoma ma-

teriałami przewodzącymi, co uniemożliwiało przeprowadzenie wiarygodnej charakterystyki za pomocą pomiarów transportu elektronowego. Niemniej jednak przeprowadzono charakterystykę innych wyhodowanych próbek $MoTe_x$, co pozwoliło lepiej zrozumieć ich właściwości transportowe. W szczególności były to: 2H-$MoTe_2$ dla niskiej temperatury podłoża oraz wiązki nanodrutów 2H-$MoTe_2$ / Mo_6Te_6 przy wyższych temperaturach podłoża. Ze względu na to, że dla cienkich warstw zaobserwowano wrażliwość na powietrze, zaproponowano i przetestowano warstwę ochronną AlO_x, która chroni $MoTe_2$ przed wpływem atmosfery.

Cienkie warstwy TaAs wykazały morfologię nanokolumnarną, skorelowaną z anizotropią przewodnictwa: przewodnictwo było do 5 razy większe dla prądu płynącego wzdłuż nanokolumn niż w poprzek. Struktura krystaliczna poszczególnych nanokolumn była zdominowana przez nietypowe ułożenie atomów (z ang. stacking faults) w porównaniu do tetragonalnego TaAs. Ta struktura atomowa była charakterystyczna dla fazy ortorombowej, co zostało potwierdzone poprzez identyfikację refleksów w dyfraktogramach XRD, które są zabronione dla fazy tetragonalnej. Obliczenia DFT wykazały, że konfiguracja ortorombowa jest energetycznie korzystna dla TaAs i że taka faza jest również półmetalem Weyla. Niskotemperaturowe pomiary magnetotransportowe ujawniły słabą antylokalizację jako jedyny ślad obecności nośników topologicznych. Wszystkie punkty Weyla znajdują się daleko od eksperymentalnego poziomu Fermiego i pozostają nieobsadzone. Wszystkie te fakty pozwalają stwierdzić, że zaobserwowano nową fazę półmetalu Weyla - ortorombowy TaAs (o-TaAs).

The note from the author

The physical dissertation contains the results of the studies on transition metal compounds, characterized by several experimental techniques. The author of the dissertation performed magnetotransport measurements in LMNP and Raman measurements due to courtesy of LaSsO group. SEM images and a part of XRD measurements were made with the kind help of Dr. J. Binder and Dr. M. Tokarczuk, respectively. The other results (TEM, AFM, ARPES, DFT calculations) were made by other associates and their authorship is always noted. In most cases the data were analyzed by the author of the thesis.

Contents

Abbreviations

2D . . . Two dimensional
3D . . . Three dimensional
AAS . . . Arc allowed surfaces
AC . . . Alternating current
AFM . . . Atomic force microscopy
AFS . . . Arc-forbidden surfaces
AH . . . Average humidity
ARPES . . . Angle-resolved photoemission spectroscopy
ASA . . . Atomic sphere approximation
BL . . . Buffer layer
BD(P) . . . Bulk Dirac (point)
BZ . . . Brillouin zone
CFS . . . Crystal-field splitting
CVD . . . Chemical vapor deposition
CVT . . . Chemical vapor transport
DC . . . Direct current
DFT . . . Density functional theory
DiFT . . Discrete Fourier transform
DOS . . . Density of states
DSM(s) . . . Dirac semimetal(s)
DUT . . . Device under test
EDX . . . Energy-dispersive X-ray
E_F . . . Fermi energy
FA(s) . . . Fermi arc(s)
FFT . . . Fast-Fourier transform
FWHM . . . Full width half maximum
HLN . . . Hikami-Larkin-Nagaoka
HR . . . High resolution
IBG(s) . . . Inverted band gap(s)
IS . . . Inversion symmetry
IV . . . Current-voltage
M . . . Magnetization

MBE . . . Molecular beam epitaxy

MOCVD . . . Metal-oxide chemical vapor transport

MR . . . Magnetoresistance

MSA . . . Mobility spectrum analysis

NC(s) . . . Nanocolumn(s)

NLSM(s) . . . Nodal line semimetal(s)

NNH . . . Nearest-neighbor hopping

NMR . . . Negative magnetoresistance

NW(s) . . . Nanowire(s)

PES . . . Photoemission spectroscopy

PMMA . . . Polymethyl methacrylate

PMR . . . Positive magnetoresistance

QPI . . . Quasiparticle interference

RHEED . . . Reflection high energy electron diffraction

RMS . . . Root mean square

SARPES . . . Spin angle-resolved photoemission electron spectroscopy

SEM . . . Scanning electron microscopy

STEM . . . Scanning transmission electron microscope

STM . . . Scanning tunneling microscopy

SRS . . . Spin-rotational symmetry

SS . . . Surface states

TEM . . . Transmission electron microscopy

TH . . . Tkachov-Hankiewicz

TI . . . Topological insulator

TL(s) . . . Trilayer(s)

TMD(s) . . . Transition-metal dichalcogenide(s)

TMP(s) . . . Transition-metal pnictide(s)

TSM(s) . . . Topological semimetal(s)

TSS(s) . . . Topological surface state(s)

TRS . . . Time-reversal symmetry

TrSS(s) . . . Trivial surface state(s)

UHV . . . Ultra-high vacuum

WAL . . . Weak antilocalization

WL . . . Weak localization

WSM(s) . . . Weyl semimetal(s)

VRH . . . Variable range hopping

XPS . . . X-ray photoelectron spectroscopy

XRD . . . X-ray diffraction

Chapter 1

Introduction

1.1 Scientific background and aim of the thesis

Over the past two decades, pioneering work by Geim, and Novoselov has initiated a new research direction, revealing remarkable physical phenomena in two-dimensional materials. A key finding was that the properties of atomically thin systems differ fundamentally from their bulk counterparts (e.g. graphene versus graphite). Such single-layer materials exhibit exceptional optical, mechanical and electronic properties, which together with their unique topological features, establish them as a powerful platform for both fundamental physics and novel applications. Among these systems, topological semimetals (TSMs) have attracted particular attention. In TSMs, charge carriers may possess mobilities significantly higher than in conventional metals [1], resulting in very low resistivities even for ultra-thin layers. Unlike graphene, a subclass of TSMs, Weyl semimetals exhibit large resistivity changes of several orders of magnitude under external magnetic fields [1]. This striking property, combined with other exotic effects such as angle-dependent chiral anomaly [2, 3, 4] and unconventional superconductivity [5, 6, 7], positions TSMs at the forefront of modern condensed matter research.

This research was carried out within the framework of the OPUS 14 project (2017/27/B/ST5/02284) entitled "Molecular beam epitaxy growth and investigations of topological semimetal heterostructures with ferro and antiferromagnets" which focused on the MBE growth and investigations of topological semimetal heterostructures with ferromagnets and antiferromagnets, led by Dr. Janusz Sadowski. The project was devoted to the fabrication and investigation of thin TSM layers, with thicknesses in the 1–50 nm range, grown by molecular beam epitaxy. Owing to the ultra-high vacuum conditions and precise control over crystal growth, MBE provided a promising purity. Within this work, we successfully fabricated for the first time thin, layers of $NiTe_2$ and TaAs. The key objective was to explore the electrical characteristics of the materials, providing essential feedback for the

growth process. A comprehensive range of physical properties was investigated alongside extensive sample characterizations including scanning electron microscopy (SEM), transmission electron microscopy (TEM), X-ray diffraction (XRD), atomic force microscopy (AFM), RHEED, angle-resolved photoemission spectroscopy (ARPES), and Raman spectroscopy to gain a deeper understanding of the obtained films and their underlying physics. Additionally, the work relates to the second project of PRELUDIUM 20 (2021/41/N/ST5/04206) entitled "Thin layers of transition metal dichalcogenides: influence of substrate on structure, morphology, and magnetotransport properties of $MoTe_2$, funded by the National Science Centre (NCN), with Zuzanna Ogorzałek-Sory as the project leader. As a part of this project, we addressed fundamental questions about the relation of the TMDs layer with the substrate and enhanced the understanding of $MoTe_2$ growth mechanisms, material stability and its electronic transport properties.

Considering that modern electronic technology is fundamentally based on thin films, our results demonstrate that the fabrication of high-quality ultra-thin TSMs opens a path toward their integration into next-generation electronic devices.

This doctoral dissertation is divided into ten chapters. All abbreviations used in the dissertation are described just before the Introduction in the Abbreviations section. The first chapter opens the dissertation, presenting scientific background and aim of the thesis and the motivation for the research on the layered materials. It also includes a description of the growth method (MBE) and provides a theoretical introduction to the Dirac and the Weyl semimetals. The second chapter describes the experimental methods used to characterize the studied materials and main experimental setups used for measurements. The third chapter presents elements of basic transport models used to describe the obtained experimental results. The forth chapter presents the description and progress in the sample preparation, which is essential for their correct characterization using magnetotransport studies. Chapters five through seven present the experimental results of selected transition metal compounds, compared with current experimental and theoretical results from other scientific institutions worldwide. The eight chapter includes comment on the MBE growth of transition metal compounds. The ninth chapter presents a summary of all the previous chapters, discusses obtained results and suggests possible paths for further research. The tenth chapter presents the summary of the Author's scientific activity. Appendices A, B, C, D and E provide additional information to experimental methods, $NiTe_2$, $MoTe_2$, TaAs and a short list of the types of characterized materials whose results were not presented in the main part of this dissertation, respectively. The bibliography cited in the dissertation is included at the end.

1.2 Exfoliated materials

Since 2004, when Konstantin Novoselov and Andriej Geim [8] have isolated for the first time one atom-thick layer of graphite - graphene, a new field of two dimensional (2D) physics has opened. Ten years later, and five years after they were awarded the Nobel Prize in physics, ten thousand papers of the graphene-related topics were published each year, revealing many breakthrough discoveries. It turned out that the graphene substantially differs from its bulk form and exhibits new properties, giving an ideal platform for studying a novel physics. Graphene, as a semimetal, exhibits ultra-fast charge- [9] and thermal conductivity [10]. The charge transport can be ballistic in the micrometer range [11] with high carrier mobility exceeding 100 000 cm^2/Vs at room temperature [12, 13]. Due to its tremendous mechanical strength and high Young's modulus [14], graphene can be implemented in the integrated circuits [15] or energy storage devices [16], finding applications in many fields such as electronics, medicine or defense. Exceptional electrical, mechanical, optical, and thermal properties of the graphene pushed interest of scientists to other layered crystals such as mono- or few layers of hexagonal boron nitride (h-BN) or molybdenum disulfide (MoS_2) whose abundance in nature and good stability under ambient conditions [17] hold promise for many applications. Finally, in 2011 first van der Waals (vdW) heterostructure of graphene and h-BN was assembled [18] combining outstanding properties of those two families. In 2013 Geim and Grigorieva [19] published a groundbreaking paper on van der Waals heterostructures. An idea of an artificial material, assembled in a chosen sequence, was defined as atomic-scale Lego. The opportunity to combine different 2D crystals provides new heterostructures with unusual properties. It is possible due to strong in-plane covalent bonding, which hold one monolayer (ML) together and relatively weak van der Waals forces, which on one hand allow an easy exfoliation but on the other, are sufficient to keep the layers together. Since then it evolved to a vast field where different kinds of 2D materials were studied. For instance 2D transition metal carbides and nitrides [20], organic materials [21], transition metal pnictides (TMPs) or transition metal dichalcogenides (TMDs) [22]. Pnictides are of type of MY and dichalcogenides of MX_2. M is a transition metal atom such as Mo, Ni or W while Y belongs to the 15 group of elements, i.e., N, P, As, Sb or Bi. X is a chalcogen atom such as S, Se or Te. The TMDs provide a promising alternative to the graphene-base system due to their richness in terms of optical, electrical and magnetic properties. Most of the TMDs exist in various crystallographic phases and each of them has different electrical properties, from semiconducting (2H) through metallic (1T) to topological type-II Weyl semi-metallic (T_d), having broad application prospects and strongly diverse physics. To prepare layered heterostructures different approaches are used: bottom-up or top-down techniques [17]. A mechanical exfoliation, belonging to the top-down method, is the frequently used one as it is cheap and relatively fast, requiring only a standard Scotch-type tape which is used to peel off the individual flakes from the bulk crystal.

This approach allows to obtain high-quality MLs with greatest versatility. Nevertheless, the thickness and the shape of the exfoliated flakes are difficult to control and the size of the layers ranges from tens to hundreds of micrometers. To increase the efficiency of the procedure, the traditional method of exfoliation were systematically improved, leading to several new methods: gel film-assisted exfoliation [17] with a thermal treatment [23], anode bonding method [24] or metal-assisted exfoliation [17]. With new kinds of exfoliation methods, both the quality and sample size have increased up to even 82 mm^2 [25]. Moreover, with a reasonable repeatability, precision of one ML was achieved. To obtain large flakes, one could also use a chemical vapor deposition (CVD) method (bottom-up approach) in which ML or bilayer (BL) of TMD can be obtained by thermal vaporization of the precursor metal which reacts with the thermally evaporated chalcogen element [17]. In spite of large sizes of the CVD-grown flakes, the quality of the obtained layers is usually poor. Although the above methods are very popular, they show certain drawbacks. The preparation of the samples requires high manual precision and usually consists of multiple processes which is time consuming. Exfoliation and flake transfer may introduce different kinds of defects, like dust particles, leading to numerous imperfections such as folds, ripples or air bubbles [26]. Also, to prevent heterostructures from air degradation, an encapsulation is mandatory. Furthermore, adhesive tapes frequently leave some residues between the layers and on top of them which can significantly change the TMDs' properties. Finally, the heterostructures are microscopic and large amount of manual work is necessary.

To take advantage of the potential of TMDs in an industrial scale, novel approaches and technologies to grow large-scale TMDs are required. There is a number of methods to obtain high quality crystalline TMDs and TMPs materials including self-flux method [27, 28, 29, 30, 31], metal-oxide chemical vapor transport (MOCVD) [32, 33], chemical vapor transport (CVT) [34, 35], CVD [36, 37, 38, 39] and molecular beam epitaxy [40, 41, 42]. The latter method is relatively novel in the context of layered materials, and yet seems very promising as it meets both conditions of the industry and replacement of the silicon-based integrated circuits as it allows to grow high quality and large-scale TMDs, integrated with the commonly available three dimensional (3D) substrates. The large-scale growth would permit TMDs to integrate in the field of nanoelectronics, spintronics, thermoelectric applications and novel applications such as integrated circuits, phase-change memory or valleytronics [43, 44]. The MBE method was used to grow the samples studies in this thesis, including representatives of TMDs family ($MoTe_2$ and $NiTe_2$) and TM pnictide (TaAs). Each of these materials was known to have crystal phase in which it showed topological semimetal properties.

1.3 Dirac and Weyl semimetals

The fundamental electronic properties of topological semimetals, particularly Dirac and Weyl semimetals, which host novel quasiparticles will be addressed in the following section. Based on the band structure, the condensed matter may be classified into insulators and semiconductors, which have a finite band gap between the valence and the conduction bands and metals which have gapless states and an electron delocalization. In the band structure of topological materials, apart from trivial states, there are so called topological states. They are observed where certain energy bands cross forming linear $E(\vec{k})$ dispersion. Some crossings, known as nodal points are topologically protected - they are immune to external perturbations in which crystal symmetry is preserved. Knowing the wavefunctions one can calculate the Chern number, which is non zero for the topological states.

A topological insulator (TI) is an example of material which is characterized by an insulating bulk gap and conducting topological surface (or edge) states. This topological material, which is protected by time-reversal symmetry (TRS) and has a large spin-orbit coupling (SOC), has been theoretically predicted in 1985 by Volkov and Pankratov [45] and then observed in many compounds such as $HgTe_2$ [46], BiSb [47] or Bi_2Se_3 [48]. The conducting surface (or edge) states in TI exhibit a linear energy dispersion $E(\vec{k})$. Both topological surface and bulk states may exist in semimetals called topological semimetals (TSMs). The surface states originate from the topological nature of the bulk band structure, as described by the bulk-boundary correspondence [49]. In topological semimetals, certain energy bands - either degenerate or non-degenerate, cross at isolated points in momentum space, where the band gap locally vanishes. These crossings, known as nodal points, are protected by crystal symmetries and time-reversal symmetry, which prevent the conduction and valence bands from hybridizing and opening a gap. Bulk bands linearly disperse along certain momentum directions in the Brillouin zone (BZ), forming a 3D analogue of graphene's band structure, with Dirac fermions residing in the bulk rather than in a 2D plane. Depending on the band degeneracy and the position of the nodal points in the momentum space, the TSMs can be divided into three classes: nodal line semimetals (NLSMs), Dirac semimetals (DSMs) and Weyl semimetals (WSMs) [50], schematically presented in Figures 1.1(a)-(c).

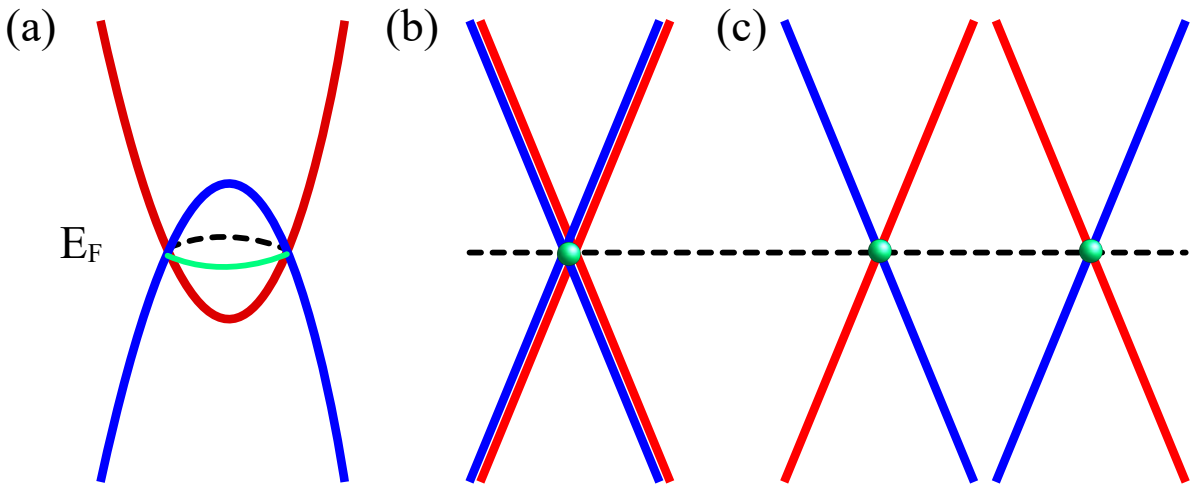

Figure 1.1: Schematic band structure of the (a) nodal line semimetal, (b) Dirac semimetal with four-fold degenerated bands and (c) Weyl semimetal with two Weyl cones of opposite chiralities. The Fermi energy is marked by the black dotted line. The nodal line and nodal points are marked by the green line and points, respectively. The colors represent different spins. [Figure preparation: Z. Ogorzałek-Sory based on [51].]

In 3D systems, the conduction and valence bands can cross either at the discrete points for DSMs and WSMs or along a closed curve for NLSMs. A closed curve, named a nodal line (see Figure 1.1(a)), can be extended over the whole BZ, take the form of a small loop inside the BZ or combine and create a chain consisting of several connected loops (called a nodal chain) [52]). NLSMs, theoretically proposed in 2011 in superlattices of trivial insulators and TIs with a broken TRS, have been experimentally observed shortly afterwards in a few bulk materials such as $PbTaSe_2$ or $PtSn_4$ [53]. Dirac semimetals owe their stability to certain crystal symmetries, such as rotational and translational ones. When both the time-reversal symmetry and inversion symmetry (IS) coexist, a four-fold-degenerate three-dimensional (3D) Dirac point emerges (Figure 1.1(b)). Dirac point represents a degenerate pair of Weyl points carrying opposite chiralities [54]. One Dirac cone is composed of two Weyl nodes of opposite chiralities overlapping in the momentum space. TRS and IS protect the two degenerate nodes from annihilation. Dirac point can be separated in momentum space once either time-reversal or inversion symmetry is broken [54]. This breaking of symmetry allows the Dirac point to split into two Weyl cones with Weyl fermions of opposite chiralities (Figure 1.1(c)). Each Weyl node is characterized by the Berry curvature [55, 56, 57] which characterizes the topology of the band structure. Figure 1.2(a) presents a calculated Berry curvature in momentum space. It can be visualized as a vector field, where the conduction and valence bands of a topological semimetal intersect at Weyl nodes.

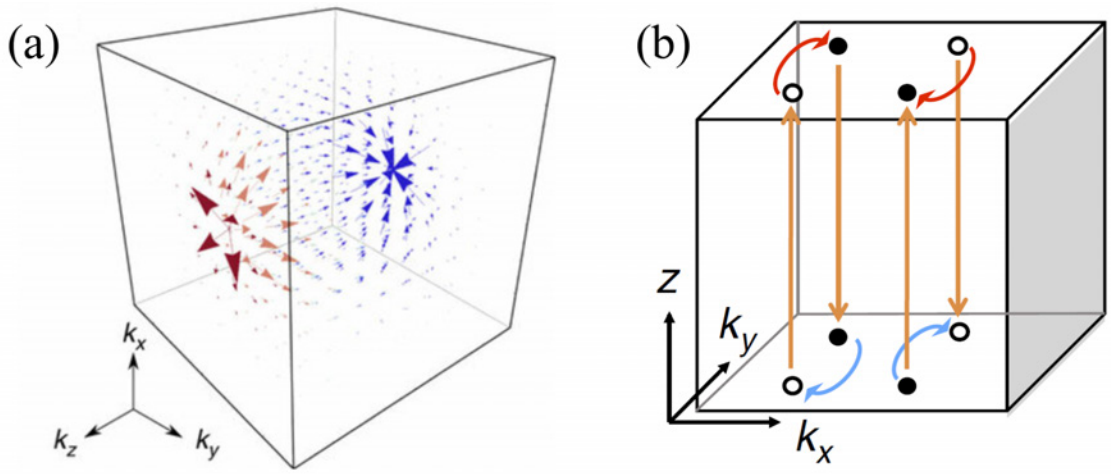

Figure 1.2: (a) The calculated Berry curvature in momentum space [58]. (b) The scheme of the 4 pairs of the Weyl nodes. The Weyl fermion trajectory between the top and the bottom surfaces is marked by the orange arrows. The blue and red arrows show the electron momentum space trajectories tracing out the constant energy contour of the Fermi arcs on the surfaces [59].

Each Weyl point is a monopole of Berry curvature of opposite chiralities. They act as sources (σ^+) and sinks (σ^-) of Berry curvature. They are separated in momentum space but are connected through the crystal boundary by a peculiar surface state called Fermi arcs (FAs). FAs are the direct consequence of the presence of bulk Weyl nodes: they are their projections to the sample surface. Figure 1.2(b) schematically illustrates a closed electron trajectory under a magnetic field, where the electron propagates along the Fermi arc on the top surface, tunnels through a Weyl node into the bulk, and continues along the Fermi arc on the bottom surface, completing a loop. This mechanism underlies the exotic magnetotransport properties observed in Weyl semimetals.

The band dispersion of the TSMs can be described by formula:

$$E_{\pm}(\vec{k}) = \pm U(\vec{k}) + T(\vec{k}) \tag{1.1}$$

where $U(\vec{k})$ describes even, linear dispersion of the cone, which obeys Lorentz invariance, whereas the $T(\vec{k})$ term introduces an odd, linear part and it is responsible for the cone tilting [60]. If $T(\vec{k}) = 0$ the classical topological nature of the type-I cone is observed (Figure 1.3(a) [61]).

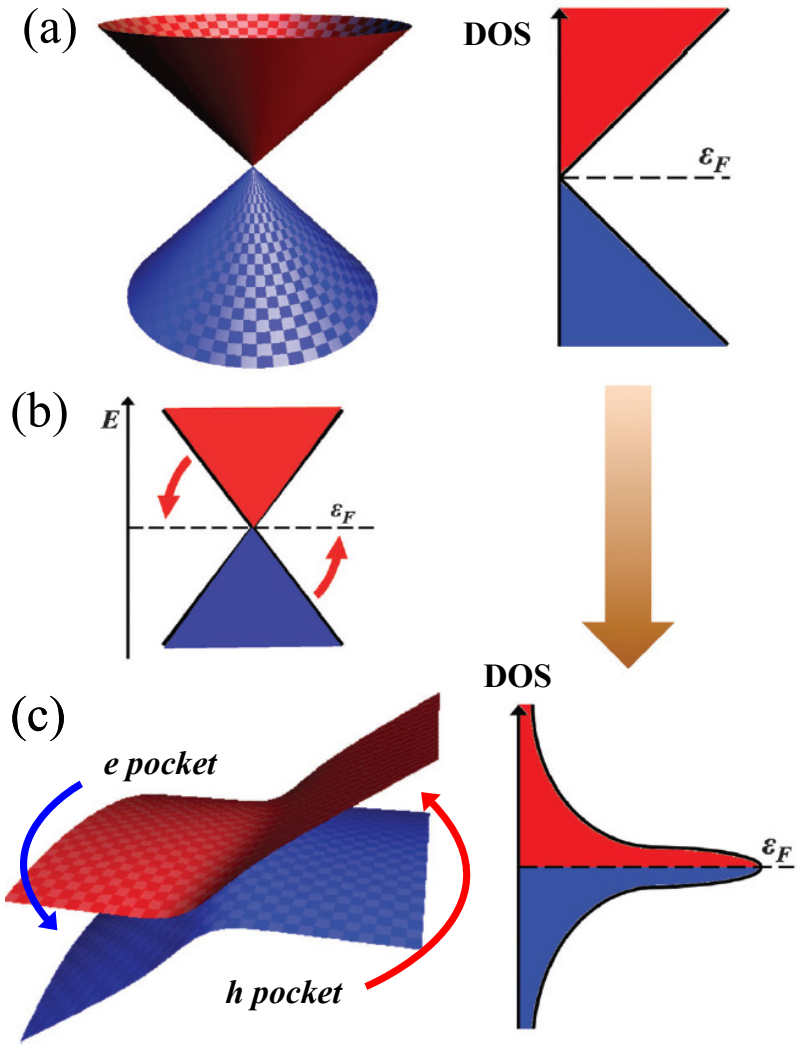

Figure 1.3: The scheme of the (a) an isotropic type-I Dirac cone with a linear dispersion and a vanishing DOS at the Fermi level, (b) tiled Dirac cone, modifying the band structure while preserving linear dispersion and (c) the formation of the type-II flat band with electron (e) and hole (h) pockets, leading to a significant increase in the DOS near the Fermi level [61].

On the other hand, if the $T(\overrightarrow{k})$ term is present the Dirac or Weyl cone is tilted [60]. This tilting causes the original conical dispersion to tip over (see Figure 1.3(b) [61]), creating a type-II Dirac or Weyl nodes. In this regime, the energy bands no longer form an ideal, upright cone but instead form electron and hole pockets (see Figure 1.3(c) [61]) that touch either at the Weyl or Dirac point. Because of this, the bands near the node do not cross at a point but develop finite density of states at the Fermi level, and the dispersion looks "flattened" or strongly anisotropic.

When the Fermi surface lies close to Dirac or Weyl nodes, the charge transport is dominated by relativistic, massless quasiparticles. In particular, type-I Dirac and Weyl semimetals exhibit negative magnetoresistance (NMR) along both in-plane and out-of-plane directions [62], while the magnetoresistance in type-II semimetals is expected to be extremely anisotropic and visible only when magnetic field is parallel to the current flow [62, 63]. This

anomalous reduction of resistance under parallel electric and magnetic fields is commonly attributed to the chiral anomaly (Adler–Bell–Jackiw (ABJ) anomaly), a quantum field theory effect where the conservation of chiral charge is violated in the presence of parallel electric and magnetic fields [64]. In the context of condensed matter, it manifests as a charge pumping between Weyl nodes of opposite chirality caused by electric field, resulting in the observed NMR. As presented in Figures 1.4(a)-(b), if the sufficiently strong magnetic field B is applied, the Landau levels will form.

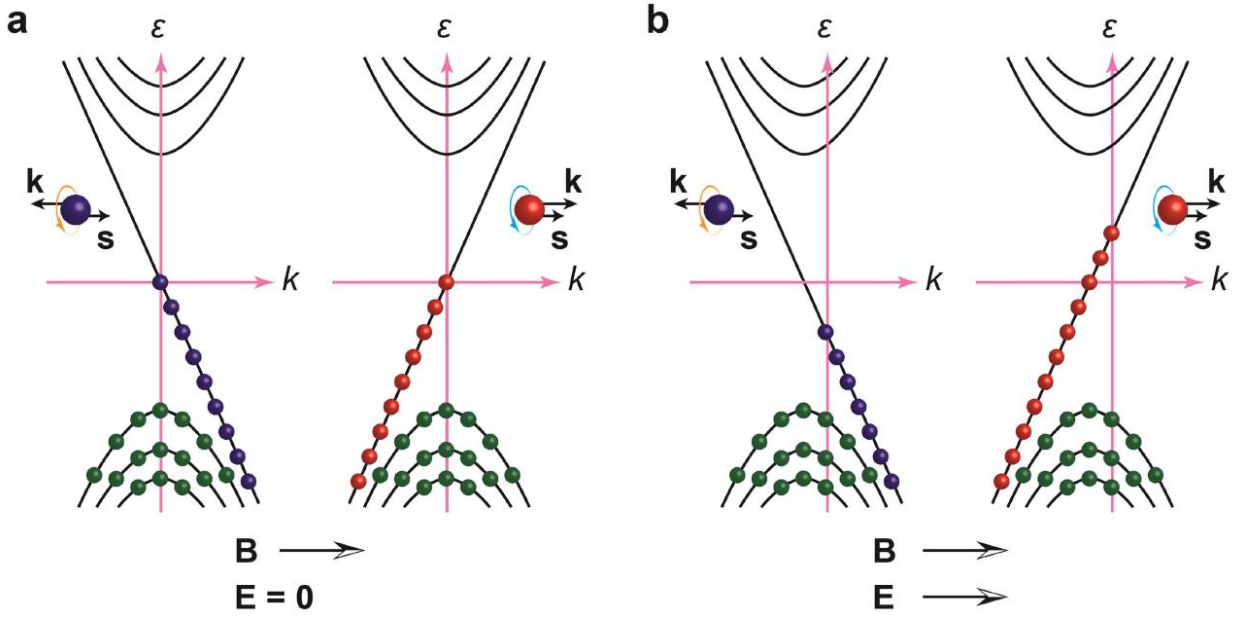

Figure 1.4: The zeroth Landau level carrier imbalance under parallel magnetic and electric fields where (a) E=0 or (b) E≠0 [64].

The reverse slopes of the linear zeroth Landau levels refers to opposite chiralities of the Weyl nodes. If the magnetic field is parallel to the electric field (B ∥ E), it would imply the electron occupancy imbalance at the zeroth Landau level creating electron flow from one node to the other (see Figure 1.4(b)). The observation of NMR is one of the proofs of the Weyl semimetal state. Therefore transport experiments are well suited for the verification of chiral nature of carriers. To observe exotic Fermi arcs and the zeroth Landau level electron occupancy imbalance, the nodes must be close to the Fermi energy of the system. In particular, too high concentration shifts Fermi level far from the Weyl node diminishing Weyl fermion contribution to the electronic transport, eventually leading to the Lifshitz transition[1] [65]. For instance, it has been shown that NMR, ascribed to the chiral anomaly effect, was observed in Na_3Bi with low carrier density ($\sim 10^{17}$ cm^{-3}) [66] whereas it was invisible in the same material with a higher carrier density ($\sim 10^{18}$ cm^{-3}), revealing only a positive MR [67]. Complementary observations have been made by Ch.-L. Zang [68], who showed that there

[1] A Lifshitz transition is a quantum phase transition characterized by a change in the topology of the Fermi surface, such as the appearance or disappearance of Fermi pockets, without involving symmetry breaking.

is no chiral anomaly in the bulk TaAs samples if chemical potential was much higher than the Weyl node.

The complex band structure and Fermi surface of TSMs involve contributions not only from the topological bulk states and topological surface states (TSSs), but also from trivial surface states (TrSSs), all of which affect charge transport.

1.4 Molecular beam epitaxy technique

To reliably probe topological semimetals, high-quality single-crystalline thin films are essential and molecular beam epitaxy has proven to be a powerful technique for the controlled growth of such materials. MBE is a widely used technique of III-V and II-VI compounds growth. It is characterized by very high purity due to ultra-high vacuum (UHV) with a pressure of order of 10^{-11} mbar. The epitaxial growth is performed on many commonly available substrates of certain crystal symmetries such as cubic (GaAs (100)) or hexagonal (GaAs (111)) with a specific lattice parameters which can be adapted with buffer layer. The scheme of the MBE setup with the conventional Knudsen cells is presented in Figure 1.5.

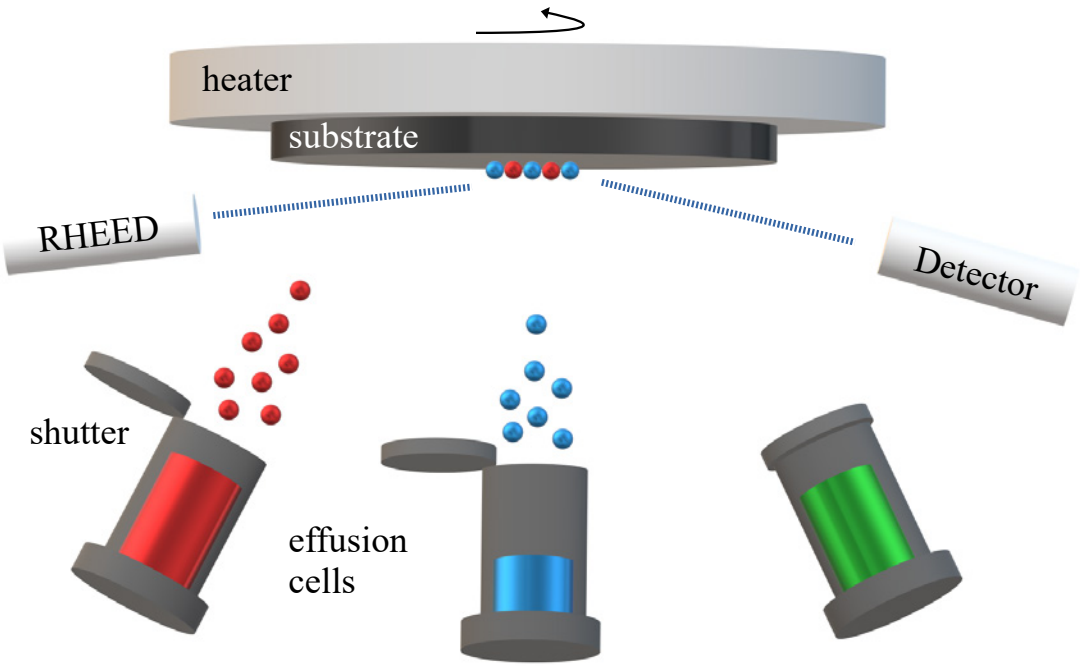

Figure 1.5: The scheme of the MBE setup with the conventional Knudsen cells, equipped with the RHEED tool and the electron detector. [Figure preparation: Z. Ogorzałek-Sory]

On the pre-heated crystal substrate, which can be rotated in the growth process, as marked by the black arrow, the chosen elements are deposited from the effusion cells. The ultra-clean environment usually ensures no interaction between the atoms before deposition at the substrate surface. The quantity of the atom flux can be efficiently controlled by the MBE shutters. This type of the beam source is used for group III elements (Ga, In, Al). For atoms

with low partial pressure (As or Sb), the valved cracker sources are used. The elements from the transition metal group such as Mn, Co, Fe or W whose melting temperatures are very high and the vapor pressures when heated are low, are deposited from the electron beam (e-beam) sources. The substrate temperature (T_s) and the temperatures of the effusion cells are the parameters used for the calibration of the beam flux during the growth. The substrate temperature is measured by a thermocouple placed 1 cm behind the substrate. For some materials, after the growth process an annealing step at a specific annealing temperature (T_a) can be applied, to improve the quality of the layers. The quality and the lattice parameters of the layers are monitored in-situ by reflection high energy electron diffraction (RHEED) tool which is essential for the growth of the large-scale, homogeneous samples. Eventually one can obtain the samples with a well defined, epitaxial relationship to the underlying crystal substrate. Apart from that, in some setups, many other complementary techniques as energy-dispersive X-ray (EDX) spectroscopy or scanning tunneling microscopy (STM) can be employed to probe the surface of the samples which can be transferred through the vacuum suitcase. In principle, highly controllable growth process enables to achieve pure and high quality layers, with low defect contamination. The ability of precise thickness control down to atomic scale and an in-situ surface control inside provide films applicable for many electronic and optoelectronic devices. More information about MBE technique and growth process details can be found in the doctoral dissertation of Dr. Bartłomiej Seredyński entitled "Epitaksja dwuwymiarowych materiałów warstwowych z grupy dichalkogenków metali przejściowych: $MoTe_2$, $MoSe_2$ oraz $NiTe_2$", which was devoted to the growth of TMDs. For the sake of this thesis, MBE growth was performed at the Faculty of Physics of the University of Warsaw in a twin chamber MBE system (SVTA) with one growth chamber dedicated to II-VI and the second one to III-V compounds. Three compounds were grown: $NiTe_2$, $MoTe_2$ and TaAs. Mo and Ta atoms have been evaporated from the electron beam source. Both Ni and Te were evaporated from conventional effusion cells: high-temperature crucible for Ni and low-temperature, dual filament cell crucible for Te. The valved-cracker source was used for As. The substrate holders in the MBE machine allow easy mounting of the relatively large substrates: the whole, half, quarter of 2 inch and 3 inch substrates and the square of 10 mm to 10 mm.

Chapter 2

Experimental methods used

Several experimental methods have been used to characterize the studied layers. Below, the main methodology has been described.

2.1 Raman spectroscopy

The Raman spectroscopy is a technique based on the Raman effect, observed in 1928 by the C. V. Raman and K. S. Krishnan [69].

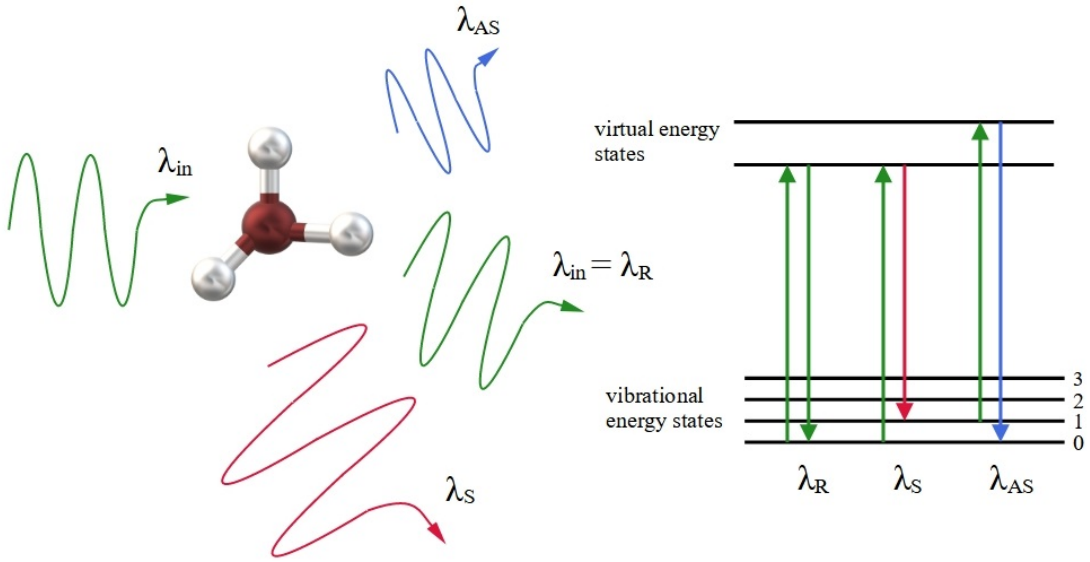

Figure 2.1: The scheme of the scattering processes in the Raman spectroscopy with energy diagrams of the corresponding Reighley (R), Stokes (S) and anti-Stokes (AS) transitions. [Figure preparation: Z. Ogorzałek-Sory]

When incident light of a wavelength λ_{in} scatters on the molecule or crystal, it may be excited to some higher virtual state at a higher energy. The virtual state is not stable and the photon is re-emitted to the vibrational state. In most cases, the re-emitted photon is of the same

wavelength (λ_R) due to the elastic Reighley scattering process. However, it may be inelastically scattered by phonons. Then, the outgoing wavelengths are shorter or longer than the incident beam λ_{in}, corresponding either to phonon emission or absorption, revealing Stokes (λ_S) and anti-Stokes (λ_{AS}) vibrational modes, respectively. The scheme of the Raman scattering processes is shown in Figure 2.1. This scattered light form the Raman spectrum. The Raman spectroscopy technique is used to measure the vibrational energy modes of a sample. As the phonon spectrum is very specific characteristics of crystals, Raman spectroscopy allows for primary sample verification. The position of the vibrational modes enables to optically characterize the studied material, its homogeneity, morphology and sample phase identification which is crucial and nontrivial in TMDs family.

Raman spectroscopy studies were performed at the Faculty of Physics, University of Warsaw, using the Horiba system, available in the LaSSo group. The spectra were collected using 532 nm laser excitation, focused by means of a 100x magnification long working distance objective and grating with 1800 lines\mm. The spot radius of the focused beam was 1 μm. The excitation power focused on the sample was kept below 300 μW during all measurements to avoid local heating.

2.2 X-Ray diffraction - XRD

X-ray diffraction (XRD) is an experimental technique allowing crystal structure characterization. The XRD uses an X-ray monochromatic electromagnetic wave with the wavelength λ_x which is of order of the distance between the atomic layers (d). When the incident beam strikes a sample, it is diffracted onto the subsequent atomic layers (see Figure 2.2(a)).

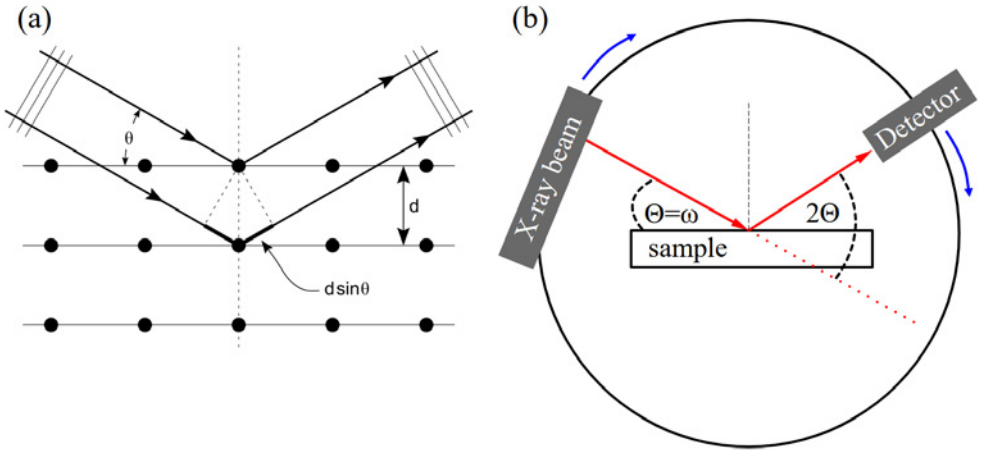

Figure 2.2: Scheme of the (a) sample subjected to X rays obeying Bragg's law [70] and (b) the experimental configuration. [Figure (b) preparation: Z. Ogorzałek-Sory]

If the Bragg's law is met, i.e.

$$n \cdot \lambda_x = 2 \cdot d \cdot sin\Theta, \tag{2.1}$$

where n in an integer and Θ is an angle of incidence, the constructive interference of the electromagnetic waves occurs, providing a maximum in the scattered rays. The XRD allows to find the distance between the atomic planes and depending on the chosen reflex, allows to find lattice parameters, the thickness of the studied layer, its quality and to identify the crystallographic phase of the studied material. Advanced equipment allows to perform asymmetrical measurements revealing also in-plane lattice parameters. To fulfill the Bragg's condition the X-ray beam and/or detector are rotated, changing ω and 2Θ angles, as presented in Figure 2.2(b).

The XRD studies were performed in two locations. The preliminary studies were performed at the Faculty of Physics, University of Warsaw by Dr. Mateusz Tokarczyk (some together with the author) with a Panalytical X'pert diffractometer equipped with a parallel beam Bragg X-ray mirror in front of the Cu X-ray tube (very weak Cu K and W L lines may be present) with a small angular step size (0.005^o). The detector optics are dedicated to thin-film analysis (Soller slits). More advanced studies with the asymmetrical reflections were made at the Institute of Physics, Polish Academy of Sciences by Dr. Jarosław Domagala with the Panalytical Empyrean high resolution diffractometer using (Cu $K_{\alpha 1}$) line of $\lambda_x = 1.5406\ \mathring{A}$ with a hybrid two-bounce Ge (220) monochromator. Some measurements were also performed with a high-resolution X-ray diffractometer Philips X'Pert.

2.3 Atomic force microscopy - AFM

The atomic force microscopy (AFM) is an experimental technique which allows sample topography reconstruction. Invented in 1986 by the IBM [71], together with the scanning tunneling microscopy (STM), belongs to the scanning probe microscopy (SPM) group. Figure 2.3 presents the scheme of the atomic force microscopy technique which explains its principle of operation [72].

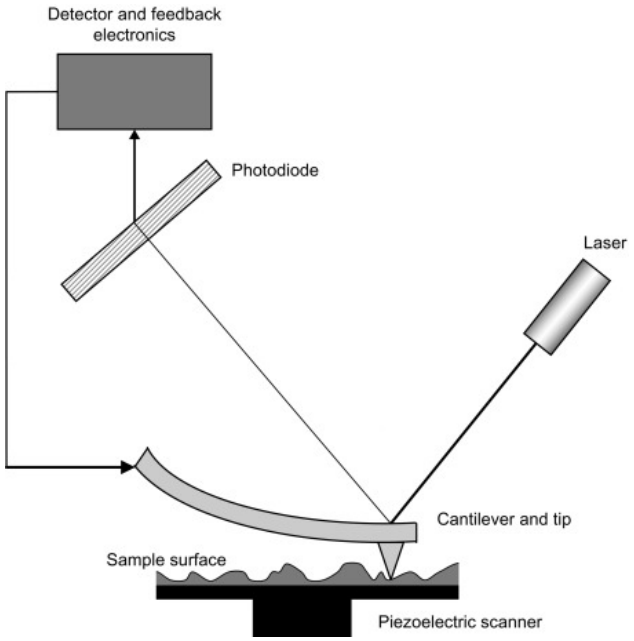

Figure 2.3: Scheme of the atomic force microscopy technique [72].

The sample is placed on the piezoelectric scanner which can move the sample in the x, y and z (normal to the sample surface) directions. The topography of the sample is measured by the cantilever, terminated by the sharp tip. The AFM analyzes the deflection of the cantilever with the tip upon interaction between the tip and the atoms of the sample surface. In general, the cantilever can operate in the three working modes: the contact one or the non-contact and the tapping ones, depending on what type of the interaction forces are measured. In the contact, non-contact and tapping modes the short-range repulsive, long-range attractive and both forces alternately are measured, respectively. In the tapping mode, the cantilever scans the sample topography oscillating in some frequency. The change of the sample topography influences the position of the cantilever. The cantilever deflection is measured by the reflected laser beam with a photodiode and it is processed by the feedback electronics, which control the piezoelectric scanner. Theoretically, the AFM resolution in the z or x and y directions can reach 0,01 nm and 0,1 nm, respectively [73], however it is usually lower and limited by the working mode, the tip shape and the type of the studied material and its roughness [74]. The AFM technique offers fast topography detection of all materials both on conducting and insulating substrates. The samples do not require surface preparation and can be characterized in vacuum, ambient or liquid environments.

Selected samples were characterized at the Faculty of Physics, University of Warsaw by Dr. Rafał Bożek and Dr. Marta Borysiewicz, using the Digital Instruments MultiMode AFM and Bruker Dimension Icon AFM models.

2.4 Scanning electron (SEM) and transmission electron (TEM) microscopy

The scanning electron microscope (SEM) and transmission electron microscope (TEM) serve for advanced surface and bulk samples characterization [75]. To improve the imaging resolution both techniques use accelerated beams to probe the studied specimen. Typically, in SEM imaging the electrons are accelerated by voltage of $U \sim 15$ kV, giving 0.01 nm of de Broglie wavelength, sufficiently low to image the surface with the resolution of around few nm. The scheme of the SEM is shown in Figure 2.4(a).

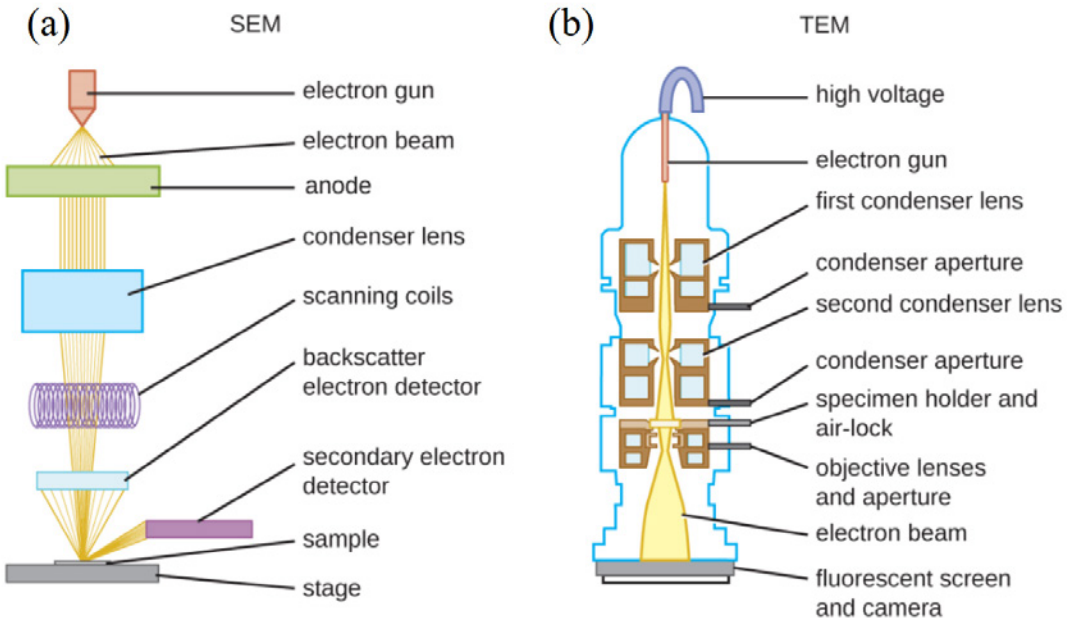

Figure 2.4: Scheme of the scanning (a) and transmission (b) electron microscope [75].

Electron beam from electron gun (arising from heating a tungsten filament) is accelerated by the anode and formed by condenser lens. The scanning magnetic coils allow deflecting the electron beam to map the sample surface. The surface image is collected from reflected electrons through both back-scattered and secondary ones. In TEM imaging, the electron beams are transmitted through ultra-thin specimens, prepared from the studied sample. The TEM technique is much more advanced than SEM imaging and requires proper sample preparation. In this case, very thin lamella is made with the focused ion beam technique. The scheme of the TEM equipment is shown in Figure 2.4(b). The acceleration voltages in TEM imaging are considerably higher than in the SEM technique, giving 0.002 nm of de Broglie wavelength which allows the identification of individual atoms. The TEM can also operate in scanning mode (STEM), in which a finely focused electron probe is rastered across the sample. The transmitted signal is collected point by point as a function of the probe position [76]. Multiple STEM detectors can be used simultaneously, including the high-angle

annular dark-field (HAADF) detector, which provides enhanced Z-contrast, particularly useful for distinguishing high-Z atoms embedded in a low-Z matrix.

Studied samples were characterized by SEM at the Faculty of Physics, University of Warsaw by author and Dr. Johannes Binder, using the Helios Nanolab 600 model. The STEM characterization was performed by Dr. Sławomir Kret, MSc Wikotoria Zajkowska-Pietrzak and Dr. Anna Kaleta at the Institute of Physics, Polish Academy of Sciences using Titan Cubed 80-300 transmission electron microscope. The scanning transmission electron microscopy - high angle annular dark field detector (STEM-HAADF) images were acquired with 197 mrad outer and 80 mrad inner HAADF detector collection angles. Helios Nanolab 600 scanning electron microscope equipped with Focused Ion Beam mode was used for classic lamella preparation using platinum Gas Injection System.

2.5 Angle-resolved photoemmission spectroscopy - ARPES

The angle-resolved photoemission spectroscopy (ARPES) is an essential tool for the material band structure analysis. Widely used technique for the band structure analysis is a photoemission spectroscopy (PES). The PES is based on the photoelectric effect, described in 1905 by Einstein, in which the material's electrons are excited by photons and have enough energy to escape to the vacuum. The photo-excited electrons are then detected by the electron energy analyzer. The scheme of the photoemission effect in PES is presented in Figure 2.5 [77].

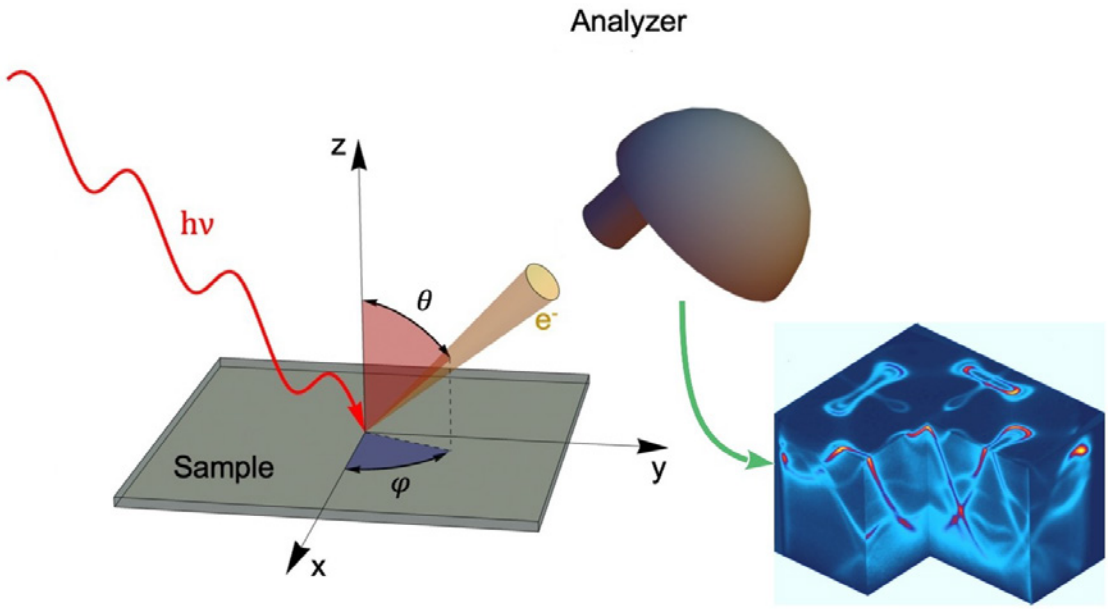

Figure 2.5: The scheme of the (angle-resolved) photoemission spectroscopy [77].

As the total energy in the system must be conserved, the kinetic energy of the emitted electrons (E_k) must be equal to the incident photon energy ($h\nu$), reduced by the initial

binding energy (E_B) of the corresponding bound electronic state and the work function (Φ) of the material [78]:

$$E_k = h\nu - E_B - \Phi \tag{2.2}$$

In an angle-resolved (AR) PES, apart from the energy of electrons, the electron momentum (k) can be also traced, providing the energy band dispersion E(k) of the studied material. It is possible to define an electron momentum, knowing its emission angle (θ), relative to the surface normal. As the parallel component of the electron momentum ($k_\parallel$) is conserved [78], one can easily determine it by changing the polar angle of the incident light (θ):

$$k_\parallel = \frac{\sqrt{2 \cdot m \cdot E_k}}{\hbar} \cdot \sin(\theta), \tag{2.3}$$

where m is the electron mass. In the case of the perpendicular component ($k_\perp = k_z$), one should known the experimentally found inner potential (V_0) of the material [78]:

$$k_\perp = k_z = \sqrt{\frac{2 \cdot m}{\hbar^2}(E_k \cos^2(\theta) + V_0)} \tag{2.4}$$

The electrons k_x and k_y momenta can be determined by taking the azimuthal (ϕ) angle:

$$k_x = \frac{\sqrt{2 \cdot m \cdot E_k}}{\hbar} \sin(\theta)\cos(\phi) \tag{2.5}$$

$$k_y = \frac{\sqrt{2 \cdot m \cdot E_k}}{\hbar} \sin(\theta)\sin(\phi) \tag{2.6}$$

The selected $NiTe_2$ sample was characterized by ARPES studies by Dr. Janusz Sadowski and Dr. Piotr Dziawa in the National Synchrotron Radiation Centre SOLARIS of the Jagiellonian University in Krakow, using URANOS beamline.

2.6 Magnetotransport measurements

The main experimental methods used for the transition metal compounds characterization were magnetotransport measurements, performed at wide temperature range (from T=1.4 K to T=300 K) in magnetic field (B) up to B=12 T and with various current to magnetic field direction configurations. The description of main magnetotransport effects studied is presented in further subsection.

2.6.1 The classical Hall effect and the magnetoresistance effect

One of the main experimental transport methods used in this PhD dissertation is the Hall effect. It was discovered in 1879 by Edwin Herbert Hall, during his PhD studies at Johns

Hopkins University in Maryland, USA. Edwin Hall observed that when an electric current (I) was passing through the conductor and the magnetic field was applied perpendicular to the current flow, a perpendicular to both I and B, voltage difference, called Hall voltage ($V = U_H$) was created [79]. The slope of the Hall voltage - Hall coefficient, allows not only to distinguish the type of the carrier but also to determine the carrier concentration in the sample specimen. The scheme of the sample geometry, being a conducting slab of the length L, the width W and the thickness d, in the Hall effect experiment is presented in Figure 2.6.

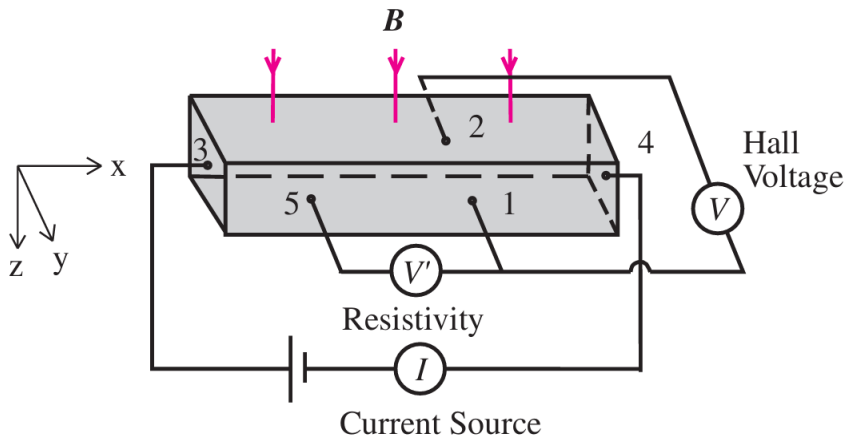

Figure 2.6: The geometry of the sample used in the Hall effect experiment [80].

In the classical Drude model, the electrical motion is described by equation of motion 2.7

$$m \cdot \dot{\vec{v}} + \frac{m}{\tau} \cdot \vec{v} = -e \cdot \vec{E} \tag{2.7}$$

where m is an effective mass, v - a drift velocity, τ - a relaxation time, e - the elementary charge $e = 1.602176634 \cdot 10^{-19}\ C$ and E an electric field. In the presence of magnetic field B, the equation of motion takes the form of Formula 2.8:

$$m \cdot \dot{\vec{v}} + \frac{m}{\tau} \cdot \vec{v} = -e \cdot [\vec{E} + (\vec{v} \times \vec{B})] \tag{2.8}$$

where $-e \cdot [\vec{E} + (\vec{v} \times \vec{B})]$ is the Lorentz force acting on electron. For the static case, when $\dot{\vec{v}} = 0$, the equation represents the Formula 2.9

$$\frac{m}{\tau} \cdot \vec{v_D} = -e \cdot [\vec{E} + (\vec{v_D} \times \vec{B})] \tag{2.9}$$

where $\vec{v_D}$ is the Drude velocity. After calculating the cross product of the $[\vec{E} + (\vec{v_D} \times \vec{B})]$ with the use of the standard basis vectors, one obtains the following Formulae 2.10-2.12 for x, y and z components:

$$\frac{m}{\tau} \cdot v_{Dx} = -e \cdot [E_x + (v_{Dy} \cdot B_z)] \tag{2.10}$$

$$\frac{m}{\tau} \cdot v_{Dy} = -e \cdot [E_y - (v_{Dx} \cdot B_z)] \tag{2.11}$$

$$\frac{m}{\tau} \cdot v_{Dz} = -e \cdot [E_z] \tag{2.12}$$

Knowing that

$$\overrightarrow{j} = -e \cdot n \cdot \overrightarrow{v_D} \tag{2.13}$$

$$\overrightarrow{v_{Dz}} = \frac{-e\overrightarrow{E_z}\tau}{m} \tag{2.14}$$

where the $\overrightarrow{j}$ and n are the current density and the carrier concentration, respectively, the perpendicular components of the current density (2.15-2.17) are:

$$j_x = (\frac{ne^2\tau}{m}) \cdot E_x - (\frac{eB_z}{m})\tau j_y \tag{2.15}$$

$$j_y = (\frac{ne^2\tau}{m}) \cdot E_y + (\frac{eB_z}{m})\tau j_x \tag{2.16}$$

$$j_z = (\frac{ne^2\tau}{m}) \cdot E_z \tag{2.17}$$

Using magnetic field conductivity σ_0 and the cyclotron frequency ω_c:

$$\sigma_0 = \frac{e^2 \cdot \tau \cdot n}{m} \tag{2.18}$$

$$\omega_c = \frac{e \cdot B_z}{m} \tag{2.19}$$

2.15-2.17 may be written as::

$$j_x = \sigma_0 \cdot E_x - \omega_c \cdot \tau \cdot j_y \tag{2.20}$$

$$j_y = \sigma_0 \cdot E_y + \omega_c \cdot \tau \cdot j_x \tag{2.21}$$

$$j_z = \sigma_0 \cdot E_z \tag{2.22}$$

The solutions of these equations are 2.23-2.25:

$$j_x = \frac{\sigma_0}{1 + (\omega_c \cdot \tau)^2} \cdot (E_x - \omega_c \cdot \tau \cdot E_y) \tag{2.23}$$

$$j_y = \frac{\sigma_0}{1 + (\omega_c \cdot \tau)^2} \cdot (E_y + \omega_c \cdot \tau \cdot E_x) \tag{2.24}$$

$$j_z = \sigma_0 \cdot E_z \tag{2.25}$$

giving $\overrightarrow{j} = \hat{\sigma} \cdot \overrightarrow{E}$ and the magnetoconductatance tensor $\hat{\sigma}$ (2.26):

$$\hat{\sigma} = \frac{\sigma_0}{1 + (\omega_c \cdot \tau)^2} \cdot \begin{pmatrix} 1 & -\omega_c \cdot \tau & 0 \\ \omega_c \cdot \tau & 1 & 0 \\ 0 & 0 & 1 + (\omega_c \cdot \tau)^2 \end{pmatrix} \tag{2.26}$$

As the magnetic field acts only on particles moving perpendicularly to the magnetic field direction, the in-plane magnetoconductatance tensor $\hat{\sigma}$ may be simplified to two-dimensional form in the plane $\perp$ B:

$$\hat{\sigma} = \frac{\sigma_0}{1 + (\omega_c \cdot \tau)^2} \cdot \begin{pmatrix} 1 & -\omega_c \cdot \tau \\ \omega_c \cdot \tau & 1 \end{pmatrix} = \begin{pmatrix} \sigma_{xx} & -\sigma_{xy} \\ \sigma_{xy} & \sigma_{xx} \end{pmatrix} \tag{2.27}$$

where:

$$\sigma_{xx} = \frac{n \cdot e^2 \cdot \tau}{m} \cdot \frac{1}{1 + (\omega_c \cdot \tau)^2} \tag{2.28}$$

$$\sigma_{xy} = \frac{n \cdot e^2 \cdot \tau}{m} \cdot \frac{\omega_c \cdot \tau^2}{1 + (\omega_c \cdot \tau)^2} \tag{2.29}$$

In the magetoresistivity ($\hat{\rho}$) description:

$$\hat{\rho} = (\hat{\sigma})^{-1} \tag{2.30}$$

thus:

$$\hat{\rho} = \frac{1}{\sigma_{xx}^2 + \sigma_{xy}^2} \cdot \begin{pmatrix} \sigma_{xx} & -\sigma_{xy} \\ -\sigma_{xy} & \sigma_{xx} \end{pmatrix} \tag{2.31}$$

The resisitivity tensor components may be experimentally probed, measuring sample resistance R and transverse voltage (U_T). As there is no current flow along the y direction in the steady state in the classical Hall measurement configuration:

$$\begin{pmatrix} j_x \\ 0 \end{pmatrix} = \begin{pmatrix} \sigma_{xx} & -\sigma_{xy} \\ -\sigma_{xy} & \sigma_{xx} \end{pmatrix} \cdot \begin{pmatrix} E_x \\ E_y \end{pmatrix} \tag{2.32}$$

$$\begin{pmatrix} E_x \\ E_y \end{pmatrix} = \begin{pmatrix} \rho_{xx} & \rho_{xy} \\ -\rho_{xy} & \rho_{xx} \end{pmatrix} \cdot \begin{pmatrix} j_x \\ 0 \end{pmatrix} \tag{2.33}$$

The off-diagonal magnetoresistivity component (ρ_{yx}) is known as Hall resistivity. Additionally, $\rho_{xy}(B) = -\rho_{yx}(B)$. The matrix equation 2.33 can be explicitly written in the following forms:

$$E_x = \rho_{xx} \cdot j_x \tag{2.34}$$

$$E_y = -\rho_{xy} \cdot j_x \tag{2.35}$$

The ρ_{xx} element of the magnetoresistivity tensor is measured by the ratio between the longitudinal electric field E_x and the current density j_x in the x direction while the component ρ_{xy} is measured by the ratio between the transverse electric field E_y and the current density j_x in the x direction. Assuming that there is one type of carriers in the system and the relaxation time τ is independent of the energy E, the components of the magnetoresistivity tensor are equal to:

$$\rho_{xx} = \frac{m}{n \cdot e^2 \cdot \tau} = \frac{1}{e \cdot n \cdot \mu} \tag{2.36}$$

$$\rho_{xy} = \frac{B}{e \cdot n} \tag{2.37}$$

The magnetoresisitivity tensor components allow to calculate the carrier concentration n and carrier mobility μ. Additionally, one can see that in the classical Hall approximation, the ρ_{xx} component does not depend on the magnetic field so material shows no magnetoresistance (MR). However, taking the statistical approach, the Boltzmann equation reveals that real metals and semiconductors show a positive magnetoresistance with $\rho_{xx}(B) > \rho_{xx}(B = 0)$ [81]. One often refers to MR value defied as:

$$MR(B)\ (\%) = \Delta\rho(B)_{xx}/\rho_{xx}(B = 0) = [\rho(B)_{xx} - \rho_{xx}(B = 0)/\rho_{xx}(B = 0)] \cdot 100\% \tag{2.38}$$

Taking 2.35 and 2.37, one can obtain transverse electric field:

$$E_y = \frac{B}{n \cdot e} \cdot j_x \tag{2.39}$$

Taking the sample thickness d, one obtains the Hall voltage:

$$U_H = \frac{B}{n \cdot e} \cdot I \cdot \frac{1}{d} \tag{2.40}$$

with the Hall coefficient:

$$R_H = \frac{1}{n \cdot e} \tag{2.41}$$

A common sample geometry used in the Hall effect experiment is the 6-contacts Hall-bar one, presented in Figure 2.7(a). The current is passing through the sample from the higher (1) to the lower (6) contacts and two pairs of the longitudinal ($U_2 - U_3$ and $U_4 - U_5$) and transverse ($U_2 - U_4$ and $U_3 - U_5$) voltages are measured.

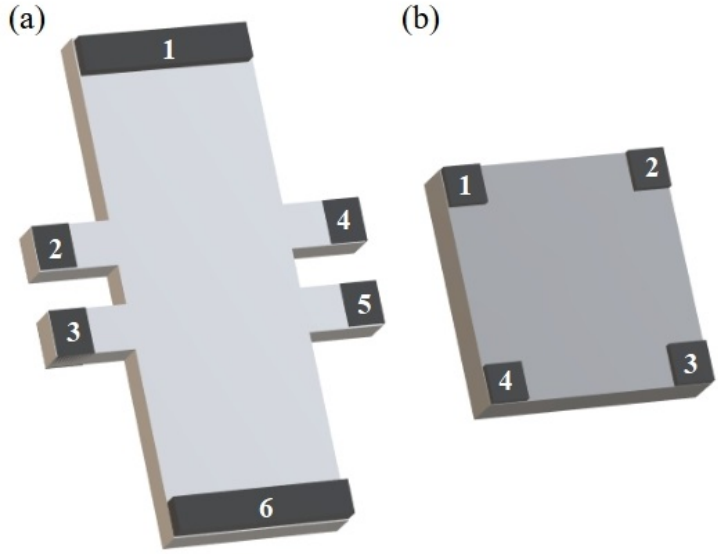

Figure 2.7: The sample geometries used in the resistivity tensor measurements in the the two and four-probe measurements. The scheme of (a) the 6-contacts Hall-bar and (b) the 4-contacts van der Pauw configurations. The dark gray ares at the edges represent contacts. Subsequent digits number subsequent contacts. [Figure preparation: Z. Ogorzałek-Sory]

This type of configuration was used most often during the PhD studies. The other geometry used is the van der Pauw configuration, presented in Figure 2.7(b). Similarly to the Hall-bar configuration, the current passes between the 1 and 4 contacts and the voltage between 2 and 3 contacts is measured, then all contacts permutations are needed to find $\hat{\rho}$. Although the van der Pauw measurements seem to be easier to perform, several further conditions have to be satisfied in order to obtain the correct resistivity values: (1) the sample must have not only a flat shape and uniform thickness but also must be homogeneous, (2) all four contacts must be located at the edges of the sample and (3) the areas of all contacts should be at least an order of magnitude smaller than the area of the entire sample. Therefore the majority of data were obtained for Hall-bar structures. Van der Pauw configuration was used once during the PhD studies and has given comparable results against the Hall-bar geometry.

Due to sample inhomogeneity and the lack of a well-defined measurement geometry, the longitudinal and transverse voltage signals are typically contaminated by admixtures of transverse and longitudinal components, respectively. To accurately extract the individual resistivity components, the data were always processed by symmetrization for the longitudinal resistivity (ρ_{xx}) and antisymmetrization for the transverse (Hall) resistivity (ρ_{yx}).

2.7 Experimental set-ups

2.7.1 VTI Oxford Instruments

Magnetotransport measurements were performed in Oxford Instruments cryostat with the Variable Temperature Insert (VTI) with a superconducting coil up to B=12 T, temperature range from T=1.4 K to T=300 K. Figure 2.8(a) presents the simplified scheme of the cryostat.

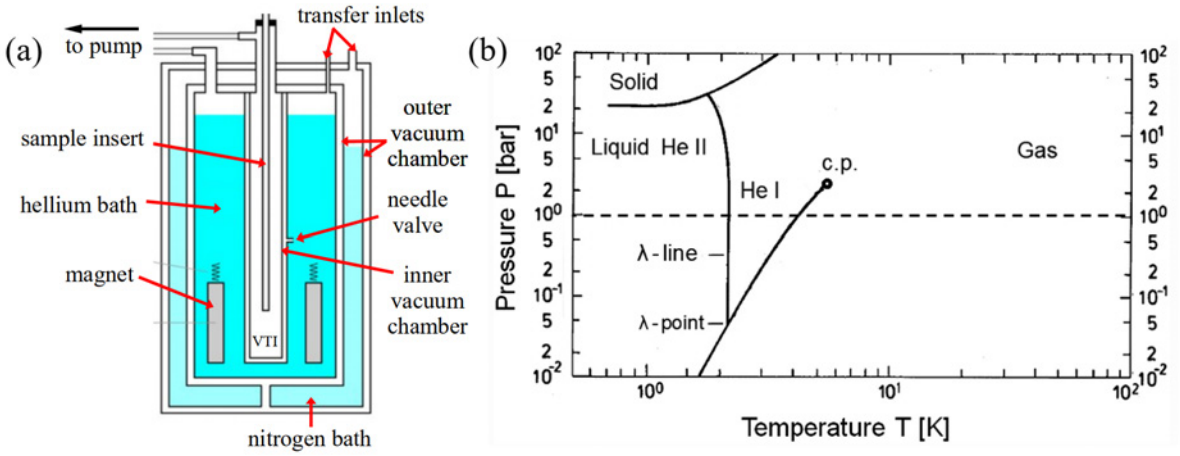

Figure 2.8: (a) Simplified scheme of the cryostat with the Variable Temperature Insert (VTI) [82]. (b) Pressure–temperature phase diagram of ^{4}He in a double logarithmic diagram. The dashed horizontal line marks atmospheric pressure [83].

The cryostat is composed of two main vacuum chambers: the outer and the inner one, which both insulate from hot environment. The whole system is cooled with liquid nitrogen, introduced between the outer vacuum chambers and the liquid helium-4, introduced between the inner vacuum chambers which forms the main bath area. The main bath and the VTI area are connected in two places: at the top of the cryostat and at the bottom of the VTI area with needle valve. The former allows to introduce atmospheric pressure to the VTI space and the latter to establish the helium pressure around the sample. The liquid helium flowing through the needle valve is heated at heat exchanger in a range from 300 K to 4.2 K. To obtain lower temperatures, the needle valve should be shut a little to obtain the pressure sufficient to go down on the lambda line of the helium-4 phase diagram as presented in Figure 2.8(b). Following that, the operational basic temperature of 1.4 K can be achieved. In the present setup, the vacuum pump is operated continuously from the beginning of the experiment, regardless of the temperature setpoint. Maintaining a reduced and stabilized pressure (of order of 30 mbar) in the VTI space ensures efficient and rapid control of the temperature throughout the entire temperature range. This pressure regulates the liquid helium evaporation rate and the cooling efficiency, thus enabling a fast system response to temperature setpoint changes. Figure 2.9(a) shows the photo of cryostat used in which all temperature- and magnetic field-dependent electric measurements were carried out.

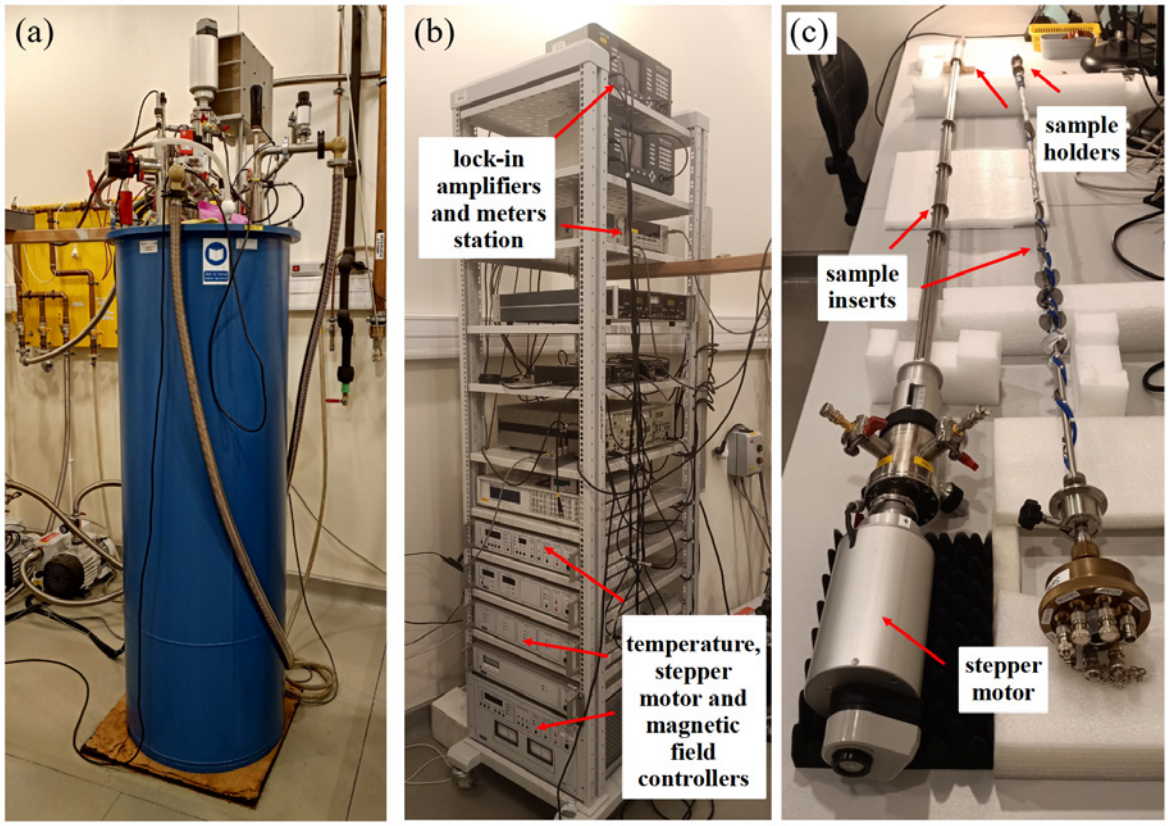

Figure 2.9: The photos of the (a) Oxford Instruments cryostat with Variable Temperature Insert (VTI) and superconducting coil. (b) VTI controlling station with temperature, stepper motor, magnetic field controllers and lock-in amplifiers and other equipment. (c) VTI sample holders.

The cryostat is equipped with multifunctional supplies allowing control of the following parameters. Among others, they include:

1. ITC503 temperature controller enabling temperature control from 300 K to 1.4 K.
2. IPS120-10 superconducting magnet power supply powering the magnet and controlling magnetic field sweep rate from 0.99 T/min. down to 0.001 T/min.
3. SMC4 stepper motor controller enabling sample rotation versus magnetic field vector.

The VTI station with temperature, stepper motor, magnetic field controllers, lock-in amplifiers and meters equipment are presented in Figure 2.9(b). The samples are mounted in the sample holders, located at the end of the sample inserts which are introduced to the VTI area. The photos of the two main VTI inserts are presented in Figure 2.9(c). Two different sample inserts were used. One with Swedish rotator, allowing sample rotation, which it is presented on the left side in Figure 2.9(c). The motor controller allowed sample positioning with an accuracy of 1 degree. Thus, all the magneto-electric configurations, with the in-plane and out-of-plane magnetic field directions versus the crystallographic axes of the studied layers, could be achieved. The photo of the sample holder with an exemplary sample on the carrier chip, used in angle-resolved insert is presented in Figure 2.10(a).

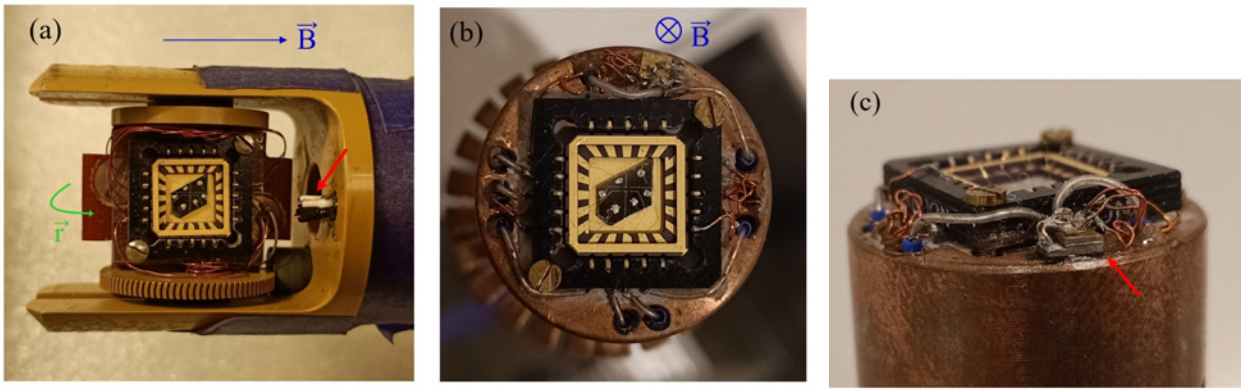

Figure 2.10: The photos of the sample holders in the inserts with (a) a Swedish rotator and (b) high-thermal stability. The rotation axis, position of the thermometer and the direction of the positive magnetic field were marked by the green, red and blue arrows, respectively. (c) The side photo of the insert with high-thermal stability with the indicated position of the thermometer, marked by the red arrow.

The positive magnetic field vector B and the axis of the rotation r of the sample holder are marked by the blue and the green arrows, respectively. Usually, in the in-plane measurements, the current path was along the magnetic field direction to fulfill the conditions of the chiral anomaly effect. Alternatively, for the Hall measurements studies, the sample had to be rotated for 90 degrees. The position of the Cernox thermometer, controlling the sample temperature, is marked by the red arrow.

The second insert with high-thermal stability, was equipped with an additional heater. Massive metallic pedestal ensures thermal stability and allows for precise temperature control with a stability better than a few tens of mK. The photo of the insert and sample holder with an exemplary sample on the carrier chip are presented on the right side in Figure 2.9(c) and in Figures 2.10(b)-(c). The positive magnetic field vector B is marked by the blue arrow. In this case, the Cernox thermometer is placed much closer to the sample as it is marked by the red arrow in Figure 2.10(c). The thermometer placed in the vicinity of the sample allows precise temperature reading. Such a good temperature accuracy leveled the influence of the temperature response in the Hall measurements, especially in the samples with the high Hall concentration, where the Hall coefficient is usually very small. In this case any instabilities of the temperature could falsify the real change of the transverse resistance by adding to the signal the temperature response of the longitudinal contacts.

Specific insert design required an increased caution while sample mounting. The sample and the thermometer are protected by the cap, as presented in Figure 2.11(a).

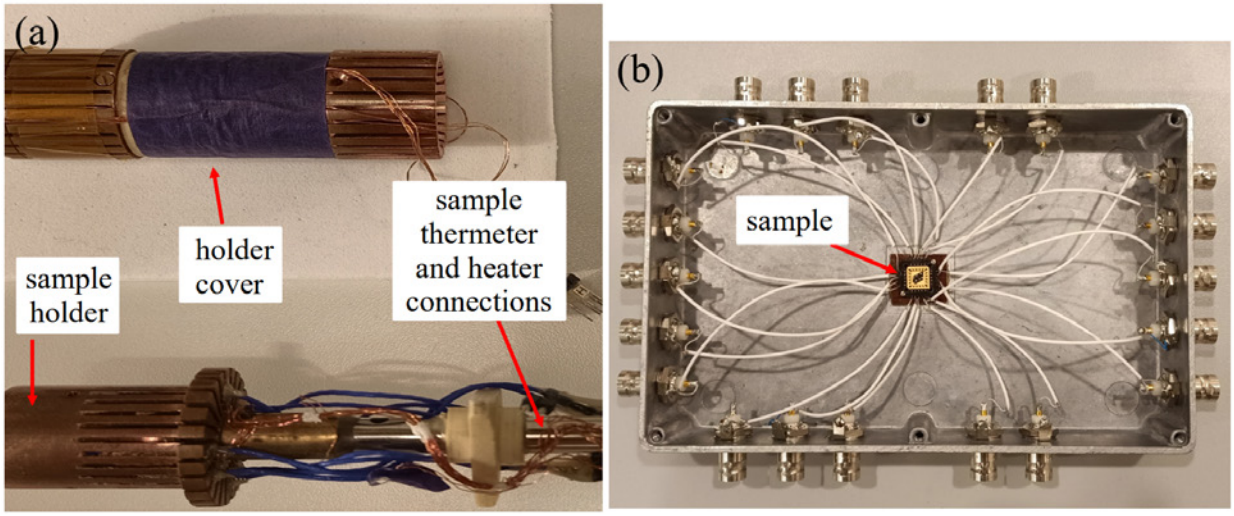

Figure 2.11: The photos of the (a) cap and sample holder with an additional heater and precise-thermometer, (b) test box for the room temperature, two- or four-probe electrical characterization.

The ground potential in the sample could be established with the use of the BNC jumper. To minimize the noise and dust influence, the BNC female connector outputs which were not used in the experiments were covered with the BNC connector covers. Before any magnetotransport studies, all the samples were electrically characterized at room temperature by two-probe and four-probe voltage-current characteristics. Every time each sample was placed in the specifically designed test box, presented in Figure 2.11(b) and terminated with the BNC female connector outputs, allowing easy current and voltage connections.

2.7.2 Desiccator set-up with temperature and humidity sensors

For the studies of air-sensitive samples under controlled atmospheric conditions, a special desiccator was developed by Dr. A. Kwiatkowski and MSc J. Mierzejewski at the Faculty of Physics, UW. The desiccator was equipped with electrical feedthroughts for humidity and temperature sensors and for samples to set the electric current and to measure the longitudinal resistances using four-probe method. To perform measurements on samples subjected to the same experimental conditions, two samples were placed in series with the external current source. Simultaneously, the temperature and humidity sensors measured the exact temperature and humidity value at the vicinity of the samples. Detailed descriptions of the experiments and a photograph of the desiccator can be found in Section 6.2.3.2 and in the inset of Figure 6.25.

Additional information concerning supporting experimental setup is provided in Appendix A.

Chapter 3

Elements of electronic transport models

In the following chapter, elements of fundamental charge transport models are introduced and discussed in the context of their application to the theoretical interpretation of the experimental results.

3.1 Band transport

In a non-disordered semiconductors there is a well-defined energy structure of energy bands, separated by the energy gap. In the band transport, the conduction occurs due to delocalized, free carriers in the valence or conduction bands leading to the p-type or n-type conduction, respectively. The conductivity of free carriers depends on their concentration and mobility. Both usually have strong temperature dependencies, as presented in Figures 3.1(a)-(b). Figure 3.1(a) shows free electron density as a function of temperature for a n-doped silicone sample [84]. At low temperature all electrons are in the valence band, localized on atoms / donors. Along with temperature increase, the number of the electron excited to the conduction band (holes in the valence band) rises as the impurities get ionized. The number of the free carriers is approximately constant as it is limited by the dopant concentration. If the temperature is high enough, band to band transitions come into play. If an electron from the valence band gains enough energy (through e.g. the photon absorption or thermal excitation), the band-to-band transition can occur. In this case, the concentrations rise informs about the energy gap of the material.

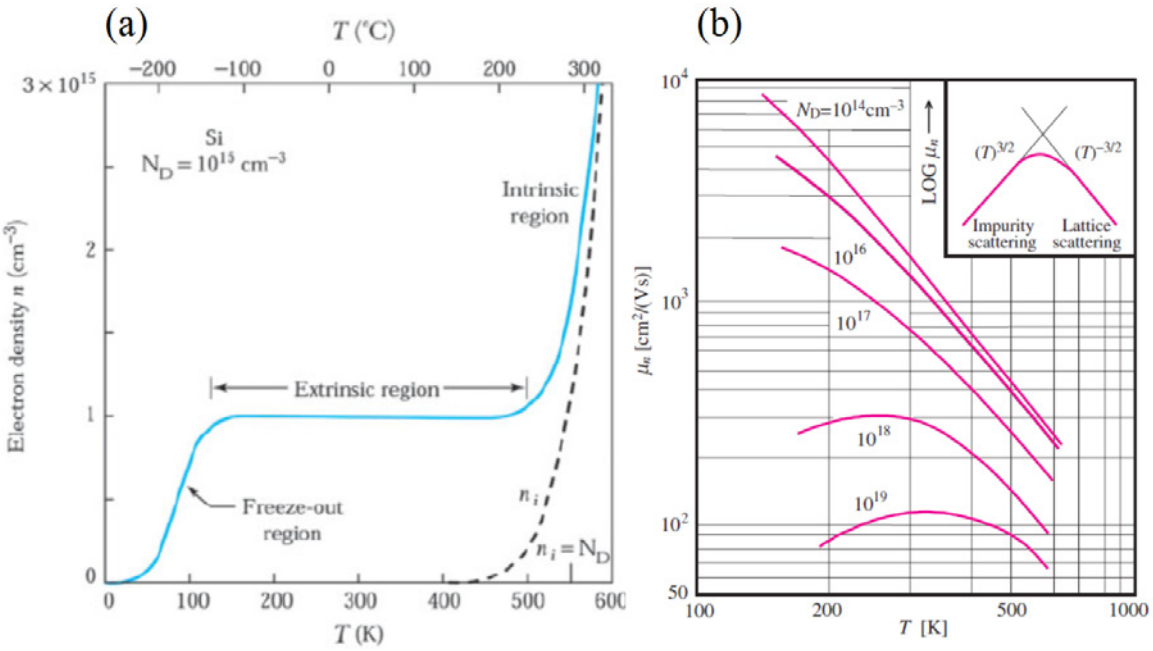

Figure 3.1: (a) The free electron density as a function of temperature for a silicone sample with a concentration of n=10^{15} cm^{-3} [84]. (b) The temperature dependence of mobilities for n-type silicone samples with different electron concentrations. The inset presents the temperature dependence of the electron mobility, limited by lattice and impurity scattering processes [80].

At the same time, carriers in a semiconductor are scattered by their interaction with various excitations such as phonons, ionized impurities or defects [80]. As shown in Figure 3.1(b) the carrier mobility is limited by the impurity scattering at low temperatures, whereas phonon scattering leads to the mobility decrease at high temperatures, leading to the $\sim T^{3/2}$ and $\sim T^{-3/2}$ dependencies, respectively. When phonon term is taken into account

$$\sigma(T) = \sigma_0 \cdot exp(-E_A/k_BT), \tag{3.1}$$

where E_A stands for activation energy. We adapt this formula for the purpose of $\rho(T)$ analysis, where no information about the carrier concentration was experimentally available, in the form:

$$\sigma(T) = \sigma_0 \cdot exp(-T_0/T)^x \tag{3.2}$$

where T stands for temperature, x=1 (other values of exponents will apply for hoping conductivity, as it will be shown), T_0 [85] is a parameter related to activation energy: $T_0 = E_A/k_B$, where k_B is the Boltzmann constant. Using the above formula, one can determine the activation energy (E_A) of the studied layer.

3.2 Charge transfer in disordered materials - the hopping regime

3.2.1 The charge transfer through the localized states

In the disordered materials, with numerous dopants, vacancies or defects, the energy band structure is more complex and localized states appear in the gap among which the hopping transport may occur. Figure 3.2(a) schematically shows the density of states of a noncrystalline semiconductor as a function of energy described by ϵ_v and ϵ_c mobility edges in the conduction band and the valence band, respectively.

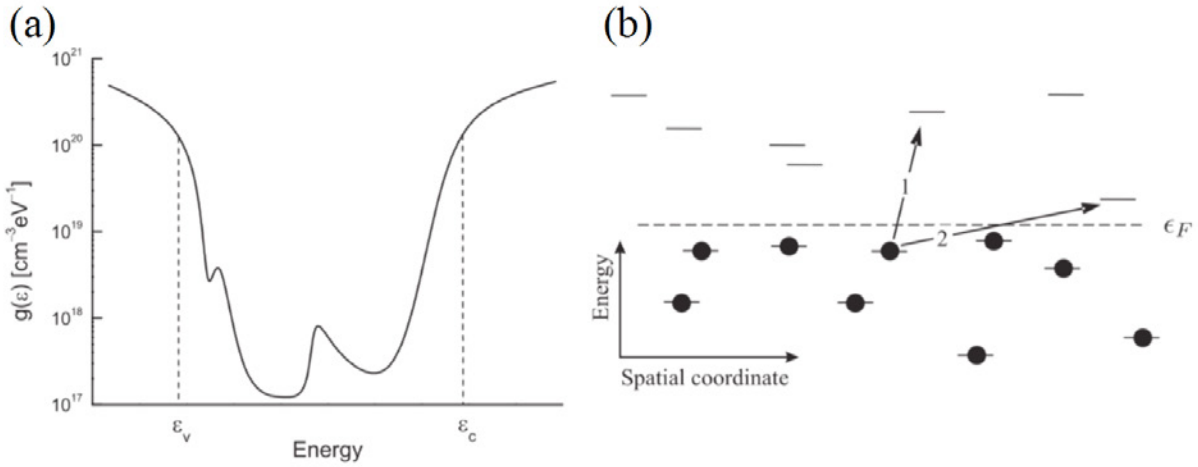

Figure 3.2: The scheme of (a) density of states of a noncrystalline semiconductor with the corresponding ϵ_v and ϵ_c mobility edges in the conduction band and the valence band, respectively and (b) the two alternative hopping transitions between occupied (filled circles) and unoccupied states (dashes). The position of the Fermi level is marked by the dashed line. Hoppings (1) and (2) correspond to the nearest-neighbor and variable-range hopping regimes, respectively [86].

Figure 3.2(b) presents the scheme of the two alternative hopping transitions between occupied states, marked by the filled circles, and unoccupied ones, marked with dashes. The hopping transition depends on the energy difference between the initial and final states and on the physical distance between defects. If two states are close to each other, electrons would pass from one to another (1) if the energy difference is not too large. This transport regime is called nearest-neighbor hopping (NNH). However, if the energies of the nearest-neighboring sites are much different, the probability of hopping decreases. In that case, the electron would tunnel to defects of similar energies, even though they are further apart (2), however still with accessible tunneling distance. This transport regime is called variable range hopping (VRH) [86]. Usually, the NNH regime dominates at higher temperatures, when thermal energy is sufficient enough to allow carriers to pass to the nearest state. One the other hand, the VHR becomes more relevant at low temperatures, when the hopping between longer distances is more energetically favorable.

3.2.2 The Mott-Davis and the Efros-Shklovskii models

Both NNH and VRH regimes were primarily developed by Sir Nevill Mott [87] who proposed that the locallized carrier of the energy E_i, can absorb the energy $W \sim k_B \cdot T$ and tunnel (hopp) to another empty locallized state of the energy $E_j = E_i + W$. The probability p_t of the tunneling is described by [88]:

$$p_t = v_{ph} \cdot exp(-2\alpha R) \cdot exp(\frac{-W}{k_B T}) \tag{3.3}$$

where R, W and α define the distance and the energy between two states and wave function decay rate, respectively. The transfer between the localized states is due to electron-phonon interactions and p_t is proportional to the phonon dispersion coefficient v_{ph}. As presented in Figure 3.3, for $k_B T >> W$, the third therm of equation 3.3 is close to 1. As a result, the p_t strongly depends on the distance R, as presented in the inset of Figure 3.3.

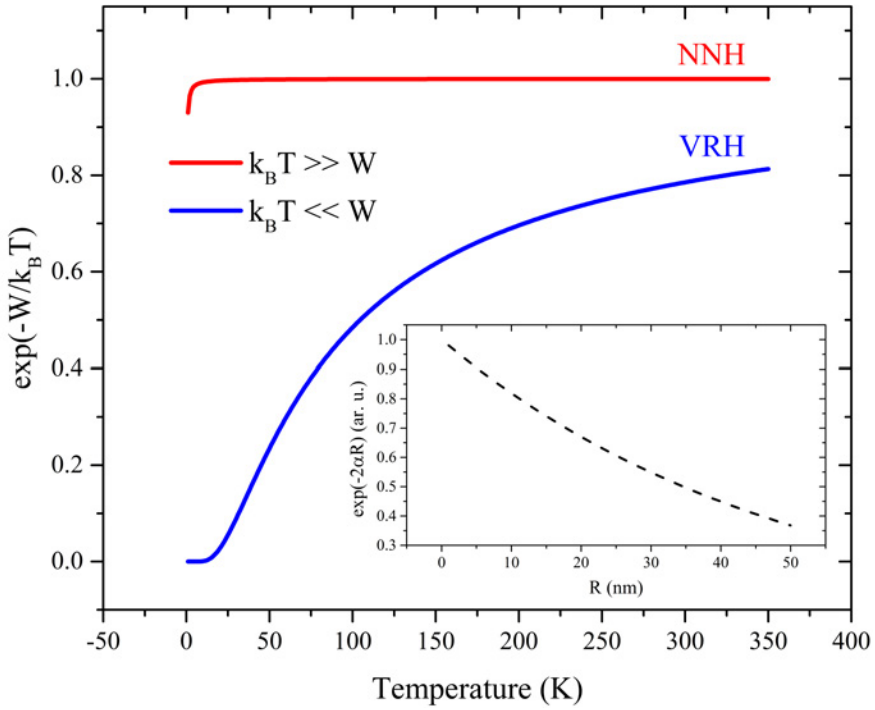

Figure 3.3: The tunneling probability p_t components for various $k_B T$ regimes.

For $k_B T << W$, the electron is more likely to hop to much more distant state if only it is more energetically matched. In VRH, the electrical conductivity typically follows the Mott law for which the conductivity is described by equation 3.2 with $x = -\frac{1}{4}$ and $x = -\frac{1}{3}$ for 3 and 2 dimensional systems, respectively, according to $x = \frac{1}{1+d}$ [85, 86].

In the Mott-Davis model, the electrostatic interactions between the carriers are not taken into account. On the other hand, Efros and Shklovskii [89] considered electron transfer between the occupied donor state E_i and the empty E_j, which are at a r_{ij} distance from each

other. Taking into account the Coulomb interactions between the donor states, the required energy for hopping is equal:

$$W = E_1 - E_2 - \frac{e^2}{4 \cdot \pi \cdot \epsilon_0 \cdot \epsilon_r \cdot r_{12}} \tag{3.4}$$

where e is the elementary charge, ϵ_0 - absolute permittivity and ϵ_r - relative permittivity. The last part of the equation describes the Coulomb energy between the electron that has hopped to state j and the positively charged donor ion left behind at state i. In the Efros-Shklovskii model, the temperature dependence of the conductivity is described by the equation 3.2 with $x = -\frac{1}{2}$, irrespectively of dimension [85, 86]. For the Efros-Shklovskii model the T_0 parameter equals to:

$$T_0 = \beta \cdot \frac{e^2 \cdot \alpha}{4 \cdot \pi \cdot \epsilon_0 \cdot \epsilon_r \cdot k_B} \tag{3.5}$$

where β is of order of unity. Based on T_0 parameter, which can be determined experimentally, one can calculate the temperature-driven wave function decay rate (α), the optimal hopping distance (d_{opt}):

$$d_{opt} = 0.25 \cdot \alpha^{-1} (\frac{T_0}{T})^{\frac{1}{2}} \tag{3.6}$$

and the optimal hopping energy (E_h):

$$E_h = 0.5 \cdot k_B \cdot (T_0 T)^{\frac{1}{2}} \tag{3.7}$$

The optimal hopping distance describes the average distance an electron hops between localized states to minimize the total energy cost. The optimal hopping energy expresses the average energy difference between the initial and final localized states during a hop. Both optimal hopping distance and energy are very useful in the charge transport mechanism analysis in disordered materials. For instance, the d_{opt} can be related to the grain boundaries of the system and the E_h to the shallow impurity level values.

3.3 Weak localization effect

The physics of disordered thin films can be surprising and may reveal peculiar resistance anomalies. One such example is the observation of a resistance change upon application of a perpendicular magnetic field in a thin Cu film with a thickness of 80 $\AA$ [90]. According to the classical single-band Boltzmann transport theory, the magnetoresistance of metal should be field independent, as the product of the cyclotron frequency and the elastic scattering time ($\omega_c \cdot \tau$) was smaller than unity, which places the system deep in the regime where the magnetic field is expected to have negligible influence on charge transport. This discrepancy suggests

the presence of quantum interference effects or other mechanisms beyond the scope of the semiclassical description. Similar observations have been made later in other materials such as pure thin film of magnesium for which the magneto-resistance curves have been shown in Figure 3.4(a) in the upper panel with a typical resistance increase in a small magnetic field range [90, 91].

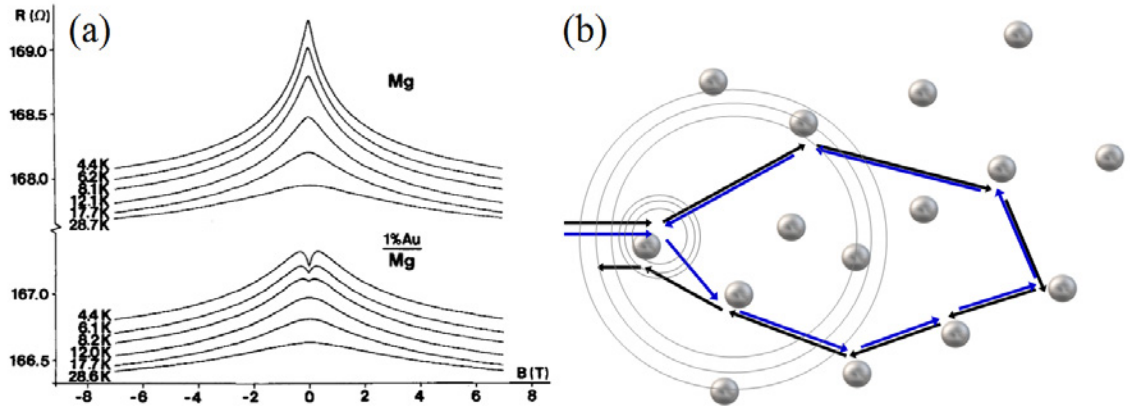

Figure 3.4: (a) The magneto-resistance curves for different temperatures measured for pure Mg (upper panel) and Mg with 1% of Au (lower panel) [90]. (b) A possible closed loop path of the conduction electron in a disordered system. The silver balls represent impurities in the system. [Figure (b) preparation: Z. Ogorzałek-Sory]

Such a phenomenon is called a weak localization (WL) and it is a conductivity correction originating from the quantum interferences in diffusion regime. The charge carriers in (thin) disordered materials can be described by the two main parameters: the mean free path (l_e) and the phase coherence length (l_ϕ). The mean free path describes the average distance a charge carrier travels between scattering events that alter its momentum. It includes both elastic and inelastic scattering processes on static and dynamic centers. The phase coherence length defines the average distance over which carriers maintain their phase before it is lost due to inelastic scattering events. The phase coherence length is directly related to the electron-phonon coupling and electron-electron interactions. The quantum diffusion regime is satisfied if the mean free path is significantly smaller than the phase coherence length. In this regime, inelastic scattering events must be suppressed [92]. Therefore, interference phenomena are observed at very low temperatures when the lattice vibrations are limited. The quantum correction can be described by the electron interferences. In a semi-classical regime charge scattering leads to randomized paths and some of them involve closed loops. The scheme of the diffusion path of the conduction electron in the disordered system is presented in Figure 3.4(b). As illustrated, there is a finite probability of the scattered electron taking a path of a closed loop which is marked by the black arrows. However, with the same probability electron can perform a time-reverse loop which is marked by the blue arrows. In a quantum diffusion regime, when the l_e is much smaller than a system size and l_ϕ,

electrons can suffer from scattering but still can maintain their phase coherence. Due to the wave–particle duality nature of the electron, one can imagine the constructive interference of the electron loops leading to the enhanced back-scattering and a decrease in conductivity. As the weak localization effect strongly depends on the inelastic scattering events, the increase of the temperature would systematically decrease its amplitude which can be seen in the upper panel of Figure 3.4(a). Furthermore, the quantum correction can be suppressed by the applied magnetic field as the electrons acquire additional phase form the magnetic field.

3.4 Weak antilocalization effect

In contrast, the presence of the spin–orbit coupling causes the destructive quantum interference which leads to an opposite phenomenon called the weak antilocalization (WAL) [90, 93]. Following this, the relation between the symmetry classes and the WL or the WAL effects can be determined. The general symmetry classification includes the orthogonal, symplectic and the unitary classes. If there is no time-reversal symmetry and no spin-rotational symmetry (SRS), the system belongs to the unitary classes and neither WL nor WAL effects are expected. For the systems with both TRS and SRS, WL effect is predicted. If only the TRS exists, the system is classified as the symplectic class where WAL effect is expected [92]. The evidence of the WAL effect is the resistance drop in a small magnetic field range as presented in the lower panel of Figure 3.4(a). Magnesium is a light metal (of the standard atomic weight of 24,31 u [94]) and has a very small spin-orbit coupling. On the other hand, the introduction of the small amount of gold, which is a strong spin-orbit coupler (with the standard atomic weight of 196,97 u [94]) generates huge changes in the magneto-resistane curves. As for the WL effect, the WAL can be also suppressed by both temperature increase and the applied magnetic field. A precise temperature dependence of the WAL effect is used to determine the scattering mechanisms in the studied layers. Initially, the WAL effect was attributed only to the SOC interactions. Later it has been proved that WAL effect can originate also from the non-trivial Fermi surface being an evidence of the intrinsic topology of the material: electron gains additional phase $= \pi$ from the Berry curvature of the host k-space [95, 96]. In the last decade, the WAL effect was widely observed in many TIs and TSMs. Dirac and chiral fermions fingerprints were captured in many exotic TMDs and pnictides, for instance: $Bi_{0.97}Sb_{0.03}$ [97, 98], $ZrTe_5$ [99] or TaAs [68, 100].

Quantum conductivity correction can be theoretically described by the 2D Hikami-Larkin-Nagaoka (HLN) formula, proposed in 1980 [101]:

$$\Delta\sigma_{\perp}(B) = N \cdot \alpha \cdot \frac{e^2}{2\pi^2 \cdot \hbar} \cdot \left[\Psi(\frac{1}{2} + \frac{B_{\perp}}{B}) - ln\frac{B_{\perp}}{B}\right] \tag{3.8}$$

where

$$B_{\perp} = \frac{\hbar}{4 \cdot |e| \cdot l_{\phi}^2}, \tag{3.9}$$

here N is a number of independent coherent channels, contributing to the total conductivity, α is a symplectic universality class and for WAL takes the value $-\frac{1}{2}$ and 1 for WL [101]. Ψ is the digamma function [101]. The relative change of the conductivity is defined as:

$$\Delta\sigma = \sigma_{\perp}(B) - \sigma_{\perp}(B_0), \tag{3.10}$$

where $\sigma_{\perp}(B_0)$ is the conductivity of the sample in zero magnetic field.

Fitting the quantum correction provides insight into the phase coherence length in the system. The 2D conductivity contribution of the WAL effect is observed in the experiment with the magnetic field perpendicular to the layer ($B_{\perp}$). In particular, the WAL effect should vanish for a 2D system, when the parallel component of the magnetic field ($B_{\parallel}$) is introduced. However angle-resolved measurements do not always show simple 2D scenarios. Frequently, the WAL effect does scale with perpendicular magnetic field, suggesting a 3D contribution or highly-coupled upper and lower 2D TSSs. That interaction can be indeed very strong and delocalized deep into the bulk states. In order to probe the spatial extent of topological surface state inside the sample (λ), Tkachov and Hankiewicz [102] proposed WAL model in the parallel magnetic field:

$$\Delta\sigma_{\parallel}(B) = N \cdot \alpha \cdot \frac{e^2}{\pi \cdot h} \cdot \ln(1 + \frac{B^2}{B_{\parallel}^2}) \tag{3.11}$$

where

$$B_{\parallel} = \frac{\hbar}{\sqrt{2} \cdot |e| \cdot \lambda \cdot l_{\phi}}, \tag{3.12}$$

λ parameter is interpreted as decay length of the wave function of topological surface states. The conductivity enhancement in the presence of the parallel magnetic field can also be a 3D response of the system. Here, Hai-Zhou Lu and Shun-Qing Shen have proposed a formula to fit the magnetoconductivity arising from the weak (anti-)localization in three dimensions [103]:

$$\Delta\sigma_{\perp}(B) = C_1 \cdot \frac{B^2 \cdot \sqrt{B}}{B_c^2 + B^2} + C_2 \cdot \frac{B_c^2 \cdot B^2}{B_c^2 + B^2}, \tag{3.13}$$

where C_1 and C_2 are the fitting parameters, positive for the WL effect and negative for WAL effect. Similarly, to the $B_{\perp}$, the critical field B_c is related to the phase coherence length according to the $B_c = \frac{\hbar}{4 \cdot |e| \cdot l_{\phi}^2}$ relation.

Chapter 4

Sample preparation

4.1 Electric contacts

In order to characterize transport properties of the studied samples, electrical contacts had to be prepared. This is a challenge by itself and there is number of papers devoted solely to the contact formation to those materials. We used two types of contacts, depending on the resistivity of the studied layers.

For more resistive samples (typically for $MoTe_2$ layers), the indium contacts were deposited through the shadow mask in the Hall-bar six-terminal contacts geometry. The manually made silver paste contacts were not ohmic giving nonlinear current-voltage (IV) characteristics. The work function of clean $MoTe_2$ stays in a range between Φ=4.1 eV [104] to Φ=4.8 eV [105], depending on the purity and it can be much higher for the oxidized layers e.g. Φ=5.6 eV reported for $MoTe_2$ with MoO_3 oxides [106]. On the other hand indium has quite low value of work function (compared to Cr (Φ=4.5 eV) or Pd (Φ=5.3 eV) [107]) which is very close to the work function of $MoTe_2$. Such small differences in the work functions are a primary reason for good ohmic contact to $MoTe_2$. Indium and indium/gold combinations have been shown to form low resistance contacts to many 2D materials, including $MoSe_2$, which is hard to contact otherwise [105]. Indeed, the two-probe IV characteristics of $MoTe_2$ with indium contact gave a linear output. However, there is a potential drawback of In, as it has a superconducting character at low temperatures.

The shadow masks, designed in the AutoCad-type program, were made from 0.3 mm-thick stainless-steel and cut by the laser. During the PhD studies, different types of the shadow mask have been designed. For instance, the first one, presented in Figure 4.1(a), contained only the circular pads. Figure 4.1(b) shows the photo of the first $MoTe_2$ sample, grown on ZnTe buffer and SI GaAs (111)B substrate with the indium contacts, deposited through the first shadow mask.

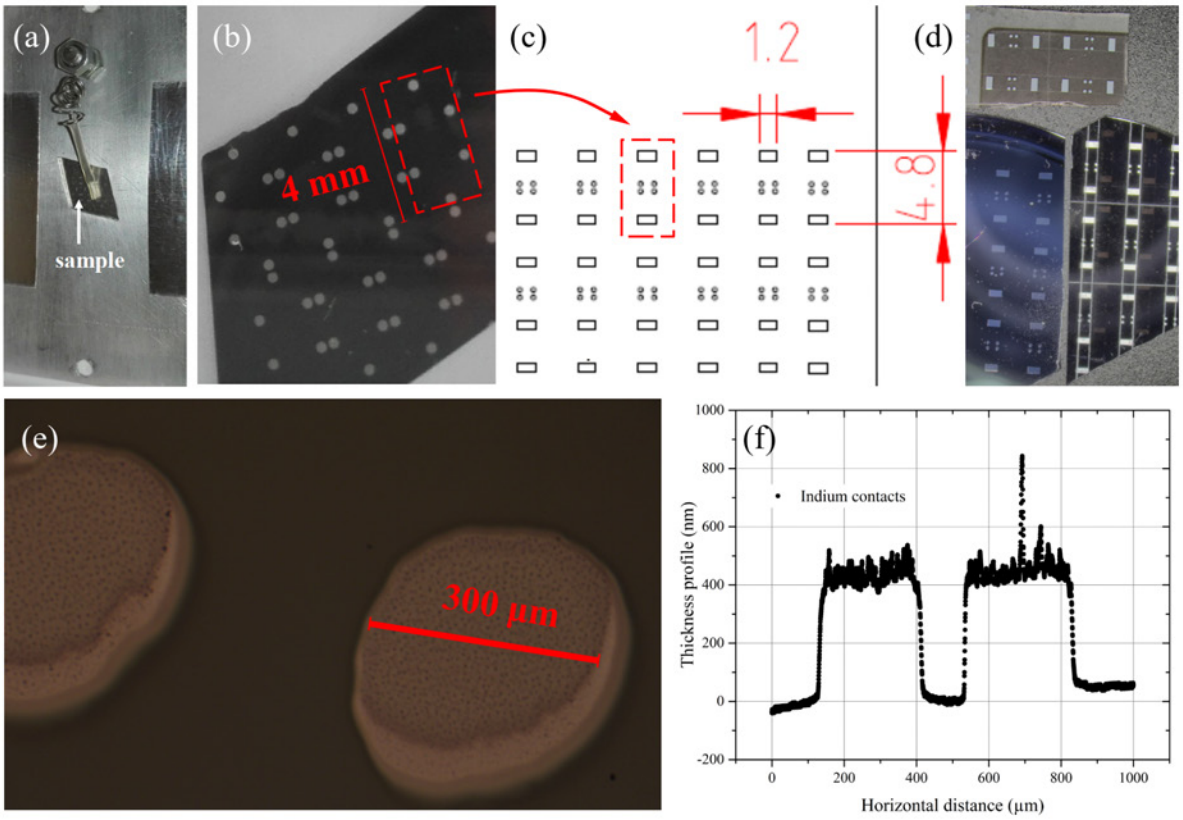

Figure 4.1: The photos of the (a) first shadow mask used for the indium contact deposition and (b) $MoTe_2$ sample, grown on ZnTe buffer and SI GaAs (111)B substrate with the indium contacts. (c) The scheme of one of the subsequent shadow masks, used for the indium ohmic contacts deposition and (d) the indium ohmic contacts deposited through the shadow mask on $MoTe_2$ layers grown on GaAs (111)B or sapphire substrates with manually traced geometry lines with the use of the diamond scribing pen. (e) The magnified photo of the indium contacts of 300 μm diameter. (f) The typical thickness profile of the indium contacts deposited through the shadow mask.

To improve sample geometry and the electric field distribution, the subsequent masks have been changed. The final version of the shadow mask was designed to obtain the most favorable Hall-bar configuration with a more beneficial length to width (L/W) ratio. Figures 4.1(c)-(d) presents the scheme of the final shadow mask and the optical image of the GaAs (111)B and sapphire substrates with the deposited indium contacts on top of the different TMDs, respectively. Figure 4.1(e) shows the magnified image of the indium contact. The nominal diameter of the circle contact is 300 μm. The deposition process was performed in ultra-high vacuum conditions. The average thickness and the width of the indium contacts, established from the mechanical profilometer scans, was 200 to 400 nm (depending on the deposition process) and 300 μm, respectively. Typical surface scan of the indium contacts is shown in Figure 4.1(f). Although the contact surface roughness is quite large, the diameters of the indium contacts are in good agreement with the specification of the designed mask. Indium contacts were deposited with the help of Prof. Krzysztof Korona from Faculty of Physics, University of Warsaw.

For less resistive samples (such as $NiTe_2$ or TaAs layers), the electric contacts were made manually, using silver paste. In that case, the Hall-bar geometry was defined by the special scriber, a machine developed for the realization of the project. The detailed procedure was described in the section 4.2.

4.2 Preparation of the sample and geometry definition

Each sample has to be fixed and connected to the specifically designed sample holder. The studied layers were connected either manually using silver paste or to the indium contacts made before. In both cases, the golden wires, outgoing the chip, were prepared before to do so. They were attached to the chip with the help of the Kulicke & Soffa Industries Inc. 4500 manual wire bonder machine. Details on bonding are presented in Appendix A.

The wafers with the pre-defined geometry by the indium contacts, deposited through the shadow mask, had to be cut into individual samples. The samples grown on the relatively soft substrates could be cleaved manually. Those grown on harder ones like sapphire, usually required other technique. For them, the cutting process was made with the use of the Buehler Isomet low speed saw. Details on that process is described in Appendix A. There were certain limitations related to sample cutting and defining sample geometry. In order to improve the defining sample geometry, scribing procedure was applied. This type of technique, in a manual version, was used in macroscopic film measurements [108], as presented in Figure 4.2(a). In our case, the diamond scribing pen with an accuracy of a few μm, scribes pre-designated path. To define the geometry, both current path and voltage pads needed to be isolated to form symmetric channels. Although it could be done using a diamond scribing pen as presented in Figure 4.2(a), the repeatability of the process would be low. Alternatively it can be done with a use of the scriber which is presented in Figure 4.2(b). The prototype model was made by Dr. Artur Broda from the Łukasiewicz Research Network and a new upgraded machine was produced for the needs of this project. Its functionalities were tuned during the exploitation. The whole process was semi-automatized and personally designed Hall-bars geometries could be patterned on the sample. Figure 4.2(c) shows a scheme of the sample with the defined Hall-bar geometry, obtained using scribing machine. Typical width and the length of the Hall-bar geometry used in sample electrical characterization were 100 μm and 320 μm, respectively. The narrowest current channel width and length, tested electrically, were 70 μm and 220 μm, respectively.

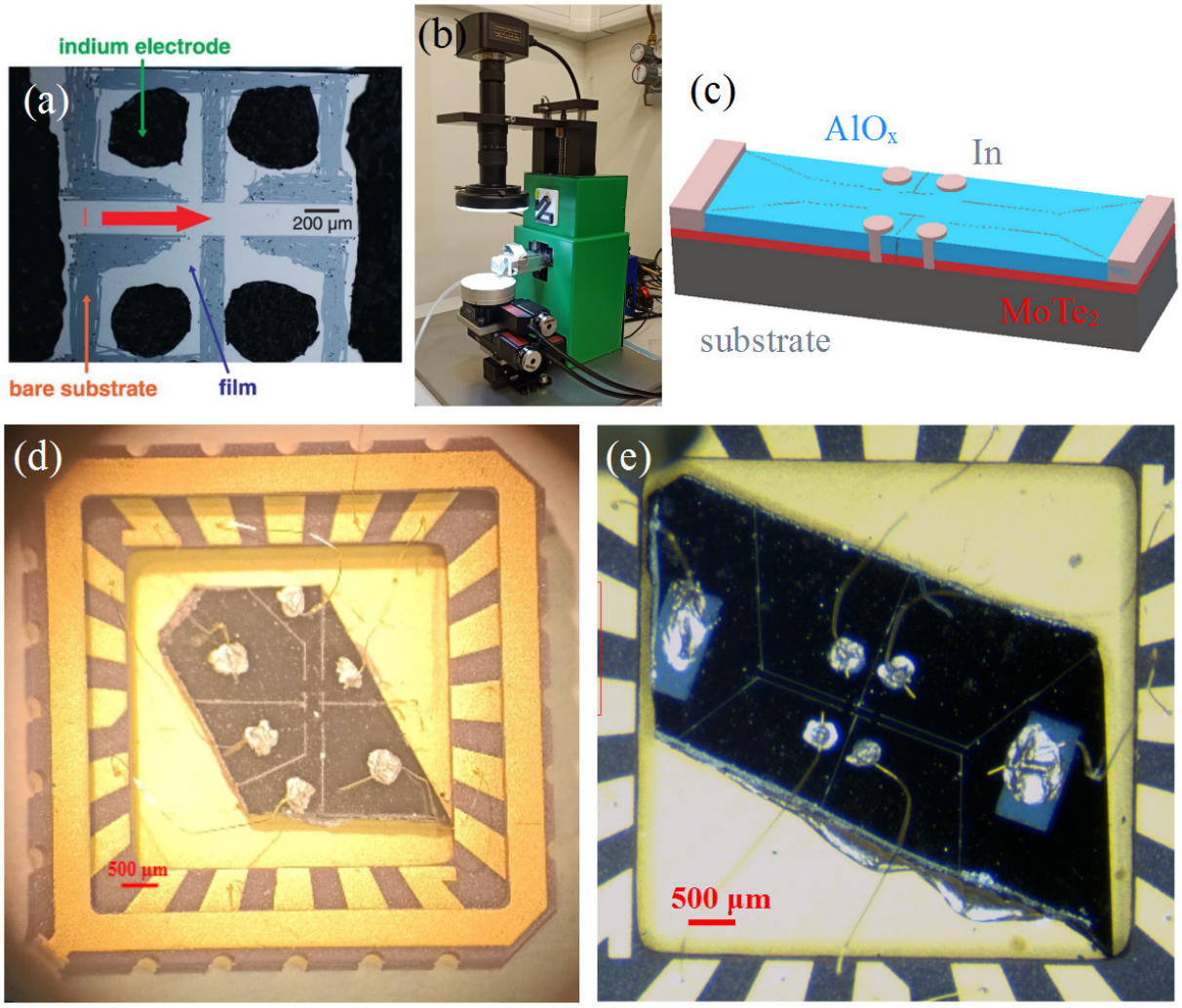

Figure 4.2: The photos of the (a) Hall-bar device made from a $Cr_{0.15}(Bi_{0.1}Sb_{0.9})_{1.85}Te_3$ film [108] and (b) a solvent-free scriber, made by the Łukasiewicz Research Network. (c) The scheme of the top view of $MoTe_2$ sample, capped with AlO_x, deposited In contacts and with a defined geometry. The optical images of (d) $NiTe_2$ and (e) $MoTe_2$ samples with the defined Hall-bar geometry and placed on the chip carrier for the electric measurements with manually made contacts or deposited through the shadow mask, respectively.

The use of the scribing machine allowed not only to decrease sample time preparation but also to avoid sample cutting. Moreover, this technique does not require any surface treatment nor coverage with resist, which was shown to influence the sample properties, by e.g. doping [109]. Since the current path was precisely aligned, the electric contacts, made manually with the silver paste, could be placed anywhere in the defined pads area. The scribing process eliminated the inhomogeneities of the current flow and significantly diminished the longitudinal voltages contributions to the transverse voltages. Figures 4.2(d)-(e) present the optical images of the $NiTe_2$ and $MoTe_2$ samples with the defined Hall-bar geometry with the use of the scriber and placed on the sample holder for electric measurements.

Chapter 5

$NiTe_2$

5.1 State of knowledge

5.1.1 Crystal structure

Nickel ditelluride ($NiTe_2$) belongs to the 2D transition metal dichalcogenides. It has a trigonal centrosymmetric structure with $P3\bar{3}m1$ space group [110] with unit cell parameters a = b = 3.8581(2) $\AA$ and c = 5.2644(3) $\AA$ for the bulk crystal [111]. It is a Dirac semimetal of the second type, in which the three-fold C_3 rotation symmetry protects Dirac cones and prevents gap opening in the system [63]. Typically $NiTe_2$ crystallizes in the tetragonal, 1T-phase which is thermodynamically stable, however, hexagonal, 2H-phase was also observed [112]. The top and the side views of the tetragonal 1T-$NiTe_2$ are presented in Figures 5.1(a)-(b) with the primitive unit cell marked with the yellow, solid line.

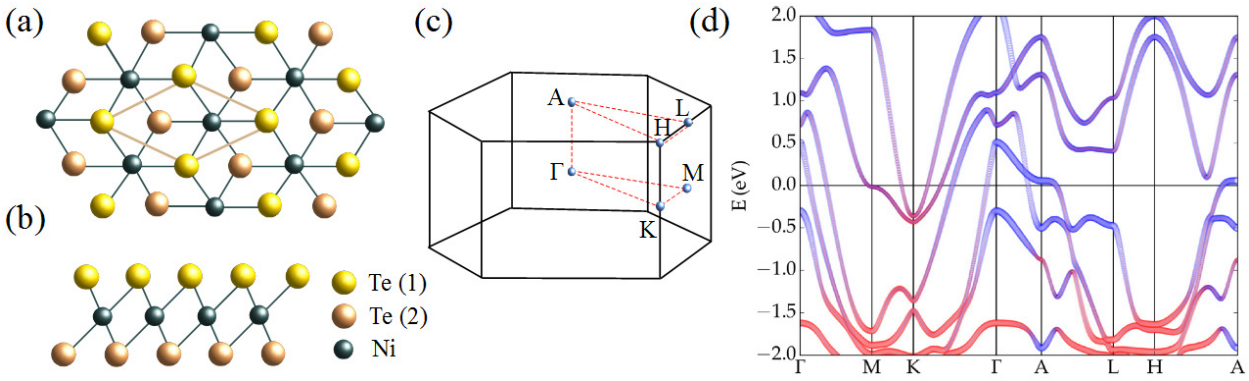

Figure 5.1: Atom arrangement in 1T-$NiTe_2$. Scheme of $NiTe_2$ bulk crystal structure in the (a) top and (b) side views. (c) First Brillouin zone of $NiTe_2$ with the high-symmetry points and paths between them. (d) Bulk $NiTe_2$ electronic band structure [63].

Each slab of $NiTe_2$ is composed of one trilayer. Every Ni atom (dark green) is sandwiched between the upper (yellow) and the lower (orange) layer of Te atoms - Te (1) and Te (2), respectively. Every tri-layer is connected with the subsequent ones by weak van der Waals forces, while the intralayer bonds are strong and covalent. Due to the layered structure and

weak interlayer coupling, $NiTe_2$ can be easily exfoliated. Figure 5.1(c) presents BZ of the bulk $NiTe_2$. The blue balls and red lines between them represent the high-symmetry points (Γ, A, M, K, L and H) and the paths connected to them, respectively.

5.1.2 Historical background

Although the huge interest in $NiTe_2$ as a 3D DSM began in 2018, the first experimental and theoretical studies on this material date back to 1955 when E. Uchida and H. Kondoh [113] have grown single crystals of $NiTe_x$ from the mixture of powders of Ni and Te and measured their magnetic properties. They observed that for a molar content x of Te atoms $x < 0.65$, $NiTe_2$ behaves as a ferromagnet. On the other hand, the paramagnetic behavior appeared for the molar content of $x > 0.7$. Later in 2020, Pauli-like paramagnetism of $NiTe_2$ was independently proven by Q. Mao et al. [114] and W. Zheng et al. [115] who showed a small and nearly temperature independent magnetic susceptibility (χ) of $NiTe_2$. Since 1970, experimental research on $NiTe_2$ focused on its crystal structure, based on the XRD studies and its thermodynamic properties [116, 117, 118]. In 1982 Orders et al. [119] presented the angle-resolved ultraviolet photoelectron spectra from the valence bands of $NiTe_2$ and determined its empirical band structure along high symmetry directions of the BZ revealing without going into details some crossings deep in the valence band along the $\Gamma \rightarrow K$ direction. Later, in 1986 and 1996, first G. Guo and W. Liang [120], next W. Bensch et al. [121] have presented the band structures and the DOS of $NiTe_2$. Both works showed a complicated Fermi surface of the $NiTe_2$ and a large DOS at the Fermi energy. For the first time it has been noticed that Te-p states contribute by more than 50% to the DOS at E_F. However, at this time, the Dirac band dispersion of the $NiTe_2$ has not been investigated from a topological perspective. After this, subsequent studies on the TMDs of a form of TMX_2 (TM = Pd, Pt; X = Se, Te) have started [62, 122, 123, 124, 125, 126, 127, 128, 129, 130, 131, 132], which were first predicted and then experimentally shown to host type-II Dirac fermions. $NiTe_2$ was also expected to host relativistic type-II Dirac fermions. Moreover, first-principle calculations showed that type-II Dirac node was located just above the E_F, being much closer to E_F than in other type-II Dirac transition metal di-tellurides like $PdTe_2$ or $PtTe_2$ [110]. Figure 5.1(d) shows an electronic band structure of bulk $NiTe_2$ [63]. Zero energy is set at E_F. At energies close to $E \sim 1.4$ eV and $E \sim 0.1$ eV, one can see the type-I and type-II Dirac nodes, respectively, both located along $\Gamma \rightarrow A$ direction. The exact value of energy of type-II Dirac point slightly differs for various calculations. For example Gosh et al. [133] predicted that the Dirac cone position stays at 20 meV above the E_F while Mukherjee et al. [134] calculated that value to equal 76 meV. Relatively large energy discrepancy led Nurmamat et al. [135] to recalculate the electronic band structure of $NiTe_2$ for both experimental and relaxed lattice parameters. They showed that the energy position of $NiTe_2$ type-II Dirac cone crucially depends on lattice

parameters revealing the shift with energy of the Dirac cone from 72.6 meV above the E_F to 57 meV below the E_F when lattice parameter is decreased. At lower energies additional topological band crossings of type I can be found, for instance at E∼-1.5 eV and type II along the $\Gamma \rightarrow K$ direction, accompanied by a number of trivial bands.

5.1.3 Band structure theory and experiment

The electron configurations of Ni and Te atoms are $[Ar]4s^2 3d^8$ and $[Kr]5s^2 4d^{10} 5p^4$, respectively, meaning that the covalent bonds are between electrons from Ni-3d orbital and electrons from Te-5p orbital (see Figure 5.2(a)).

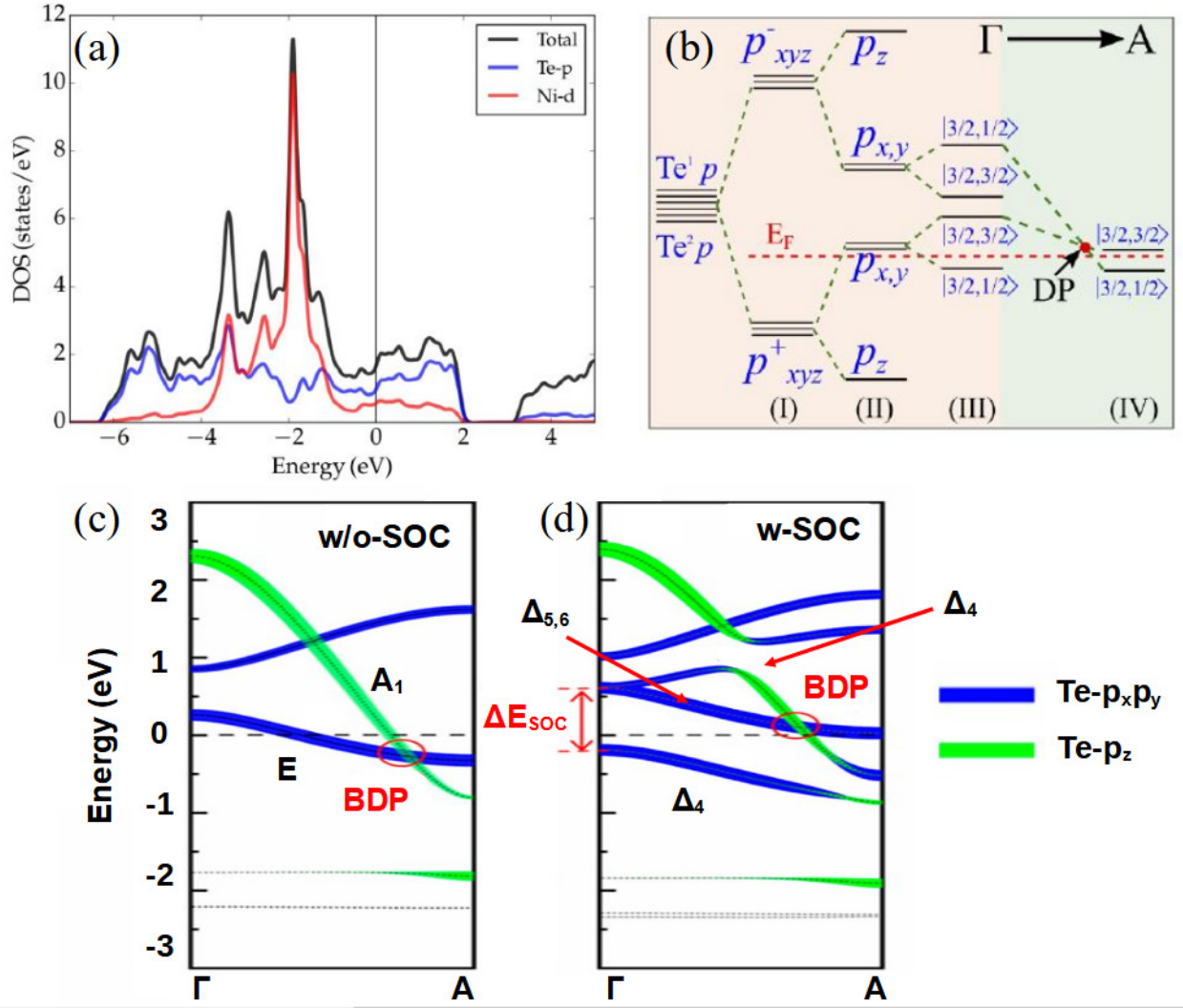

Figure 5.2: (a) The projection of the total DOS and Te-p and Ni-d orbital contributions for the bulk $NiTe_2$, marked by the black, blue and red curves, respectively [63]. The zero energy (E=0 eV) defines the E_F position. (b) The scheme of the evolution of the Te 5p orbitals in $NiTe_2$ into (I) bonding and antibonding states, orbitals' splitting in the presence of the (II) CFS and (III) SOC and (IV) the formation of the bulk Dirac point [133], please mind that this part referes to the A point of the BZ. The orbital-resolved band structure of $NiTe_2$ along $\Gamma \rightarrow A$ direction (i.e. along k_z) (c) without and (d) with the SOC [136].

The nonzero density of states at E=0 eV reveals semimetallic nature of $NiTe_2$ with a total

DOS of 1.67 states/eV derived from 59% from Te-5p orbitals and 34% from Ni-3d orbitals. As presented in Figure 5.2(b) due to the crystal-field splitting (CFS), the triply-degenerate orbitals of Te-$p_{x,y,z}$ split into Te-p_z and Te-$p_{x,y}$ orbitals. Usually, the topology of the Dirac or Weyl semimetals is driven by the SOC interactions which lift degeneracy of the bands, leading to topological band crossings. Due to heavy Te atoms (twice as heavy as Ni ones), the SOC interactions are present in this material leading to the Te-$p_{x,y}$ orbitals splitting. Going along $\Gamma \rightarrow A$ direction one can observe the formation of the bulk Dirac nodes [133, 134]. In the case of $NiTe_2$, the SOC interactions are responsible for the Dirac cone energy and momentum shifts. As presented in Figures 5.2(c)-(d), whether SOC is present or not, the bulk Dirac points always exist [136]. Figures 5.2(c)-(d) present the orbital-resolved band structure of $NiTe_2$ along $\Gamma \rightarrow A$ direction for Te-p_xp_y and Te-p_z orbitals marked by the blue and the green curves, respectively. Figure 5.2(c) shows band structure without SOC interactions where the A_1 band and doubly-degenerate E band cross each-other below the E_F forming bulk Dirac point (BDP). The introduction of the SOC interactions, as presented in Figure 5.2(d), splits the E-band into Δ_4 band, shifted below the E_F, and into doubly-degenerate $\Delta_{5,6}$ band, shifted above the E_F and the A_1 band splits and forms the anticrossing forming BDP just above the E_F (marked with a red circle). A splitting of the Te-p_z orbital into bonding and antibonding states decreases from Γ to A direction leading to a strong band dispersion in the k_z directions [136, 137].

A strong k_z dependence of the bulk Fermi surface can be observed in the calculated in-plane $NiTe_2$ ($k_x - k_y$) maps, presented in Figures 5.3(a)-(e), where different colors indicate different k_z values [135].

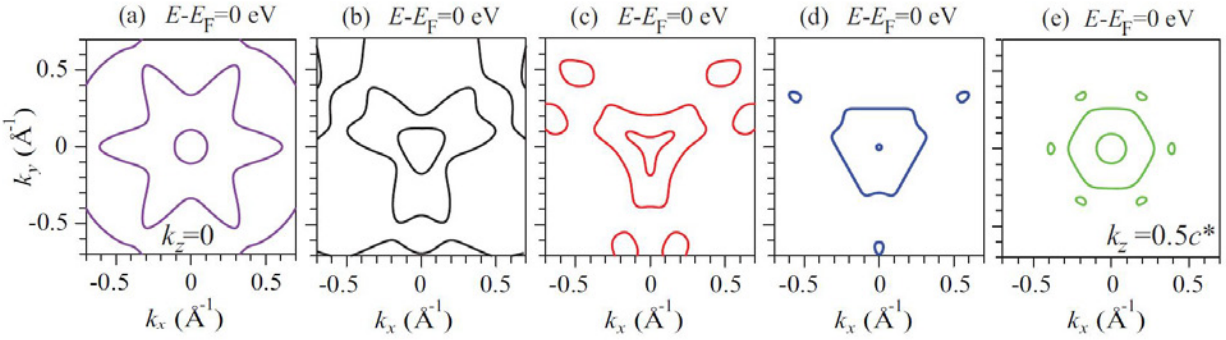

Figure 5.3: (a)-(e) Cuts through Fermi surfaces at various k_z along the $\Gamma \rightarrow A$ direction in the BZ [135].

Experimentally the band structure can be probed in angle-resolved photo emission experiment. The 3D character of the Fermi surface is seen even in very thin samples. In particular, Hlevyack et al. [30] have performed systematic ARPES studies on the MBE-grown $NiTe_2$ samples changing their thickness from one trilayer to five TLs (results are included Figure B.2 in Appendix B). They observed a clear topology evolution while changing the thickness of the samples: as the film thickness increased, the dimensionality crossover from the ultra-thin

film to bulk-like regime occurred, leading to the gap closing at the Γ point ($k_{\|} = 0\ \AA^{-1}$) giving rise to the TSS.

Gosh et al. observed a strong 3D character of the Fermi surface, measuring band structure of $NiTe_2$, along $\bar{K} \leftarrow \bar{\Gamma} \rightarrow \bar{K}$ direction and taken for different k_z values, as shown in Figures 5.4(a)-(e) [133].

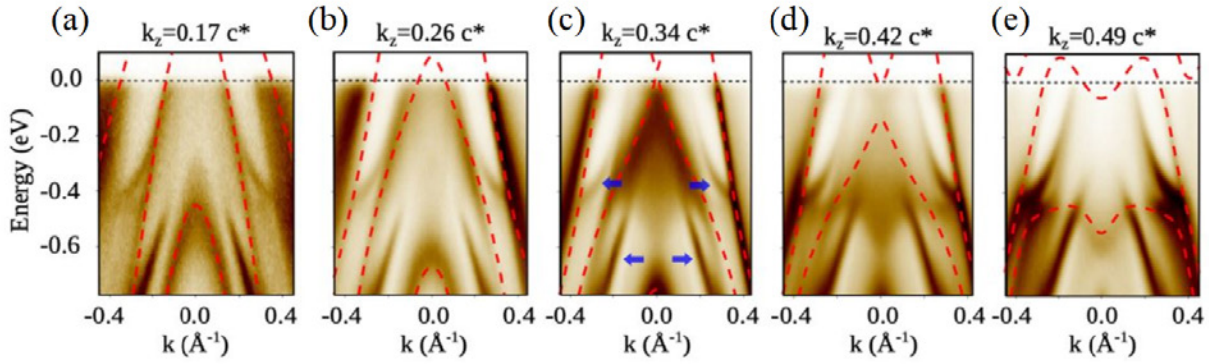

Figure 5.4: Measured $NiTe_2$ band dispersion along in-plane $\bar{K} \leftarrow \bar{\Gamma} \rightarrow \bar{K}$ directions for different k_z values with the calculated bulk states marked by the red dashed lines and indicated surface states, marked by the blue arrows [133]. The bars denote that the points are projections of the corresponding bulk high-symmetry points into the surface.

They showed also band dispersion and the corresponding DFT surface states calculations along $\bar{K} \leftarrow \bar{\Gamma} \rightarrow \bar{K}$ directions [133], presented in Figures 5.5(a)-(b), revealing that most of the observed states are the surface ones (marked by the red arrows).

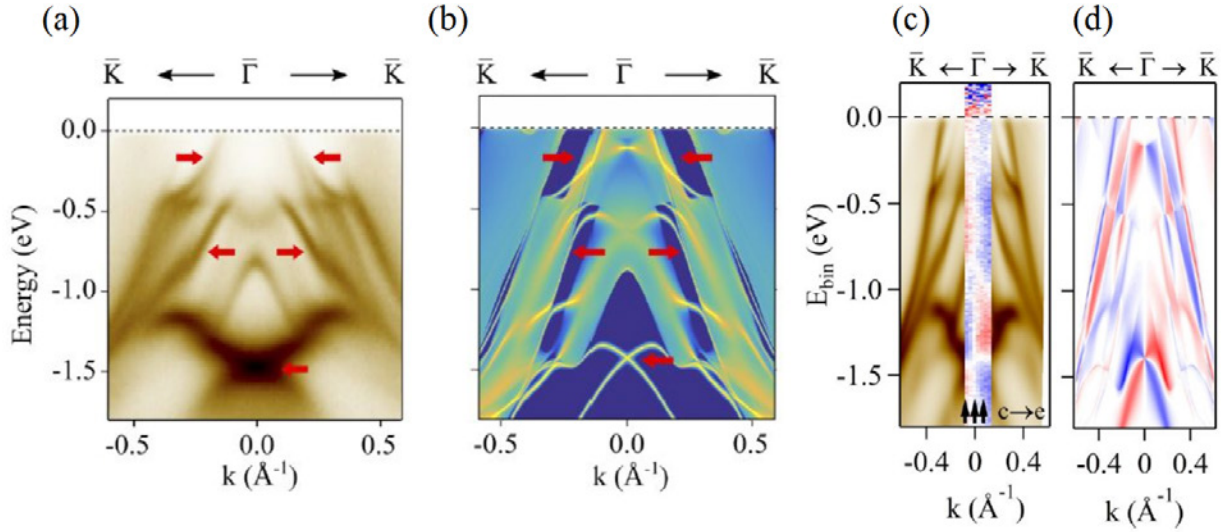

Figure 5.5: The measured (a) and calculated (b) $NiTe_2$ band dispersion for $\bar{K} \leftarrow \bar{\Gamma} \rightarrow \bar{K}$ directions. The measured (c) and calculated (d) spin texture for the bands along $\bar{K} \leftarrow \bar{\Gamma} \rightarrow \bar{K}$ directions. Both data were taken for the energy hv = 24 eV [133].

Figures 5.5(c)-(d) present the spin-resolved ARPES studies showing the measured and calculated spin textures. The topological nature of the surface states is manifested by two

opposite spin polarizations visible for example at the $\bar{\Gamma}$ point at $-1.5\ eV$, where the surface state bands cross. In 2020, Mukherjee et al., have performed similar ARPES experiments on bulk $NiTe_2$, grown by chemical vapour transport [134] (results are included in Figure B.1 in Appendix B). They showed similar ARPES results and corresponding DFT calculations for the bulk system and for the slab surface, containing 10 primitive unit cells of $NiTe_2$ stacked along the [001] direction. ARPES data were in good agreement with the DFT calculations and showed the surface origin of the topological states (TSS1 and TSS2). Compared to the results of the Gosh et al. [133], the TSS2 state at the Γ point was shifted slightly towards E_F reaching -1.4 eV.

5.1.4 Modification of $NiTe_2$ by ad-atoms, doping and pressure

Recent DFT calculations have shown that by introducing strain to the $NiTe_2$ one can tune the energy and position in the momentum space of the Dirac crossing [63]. Figure 5.6 presents theoretical calculations of E(k) of Dirac node position upon pressure.

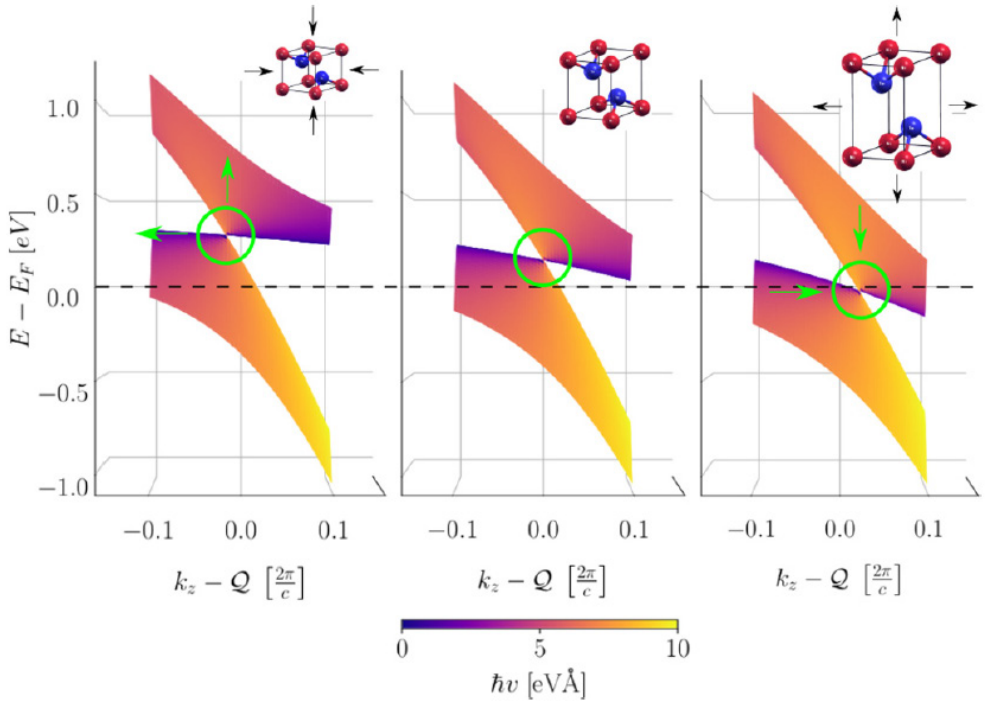

Figure 5.6: The E(k) dependence of Dirac cone for isostatic compressive pressure (left panel), the undeformed structure (middle panel) and for the isostatic tensile pressure (right panel). Zero energy defines E_F. The absolute value of the velocity at each point is indicated by colors. $\mathcal{Q}$ describes the out-of-plane momentum component (k_z) of the Dirac node, and its value is derived from parameters of effective Hamiltonian [63].

For the undeformed structure (middle panel), the Dirac cone position is located above the E_F at k_Z=0. By applying isostatic compressive strain (left panel) or tensile strain (right panel) strain to $NiTe_2$ elementary cell, the Dirac cone position moves away from (or gets closer to)

the E_F. Moreover, both compressive and tensile strains shift the Dirac cone position versus the k_Z wave vector.

The elementary cell deformation can be introduced by intercalations, placing additional atoms in the interlayer gap of TMDs. Ferreira et al., have shown that a monotonic evolution of a and c lattice parameters is possible by "chemical doping" of the alkali atoms (Li, Na, K). For instance, incorporation of the Li atoms, i.e. $Li_{0.25}NiTe_2$, lead to 3% of deformation along the c axis and 1.2% of deformation along the a axis. The type-II Dirac cone (shifted below E_F at E ~-0.2 eV) and its topology were preserved [63]. In contrast, Gosh et al., have underlined that bulk doping is substantial to obtain the bulk Dirac point energy shift. For instance, as shown by Gosh et al., surface deposition of alkali metals (such as potassium) leads to electron doping, which preserves the bulk Dirac point energies while shifting only the surface states [133].

The properties of $NiTe_2$ may be varied also by other factors. One of them is disorder. Wang et al. [138] have studied the influence of atomic defects in freshly cleaved $NiTe_2$ surface.

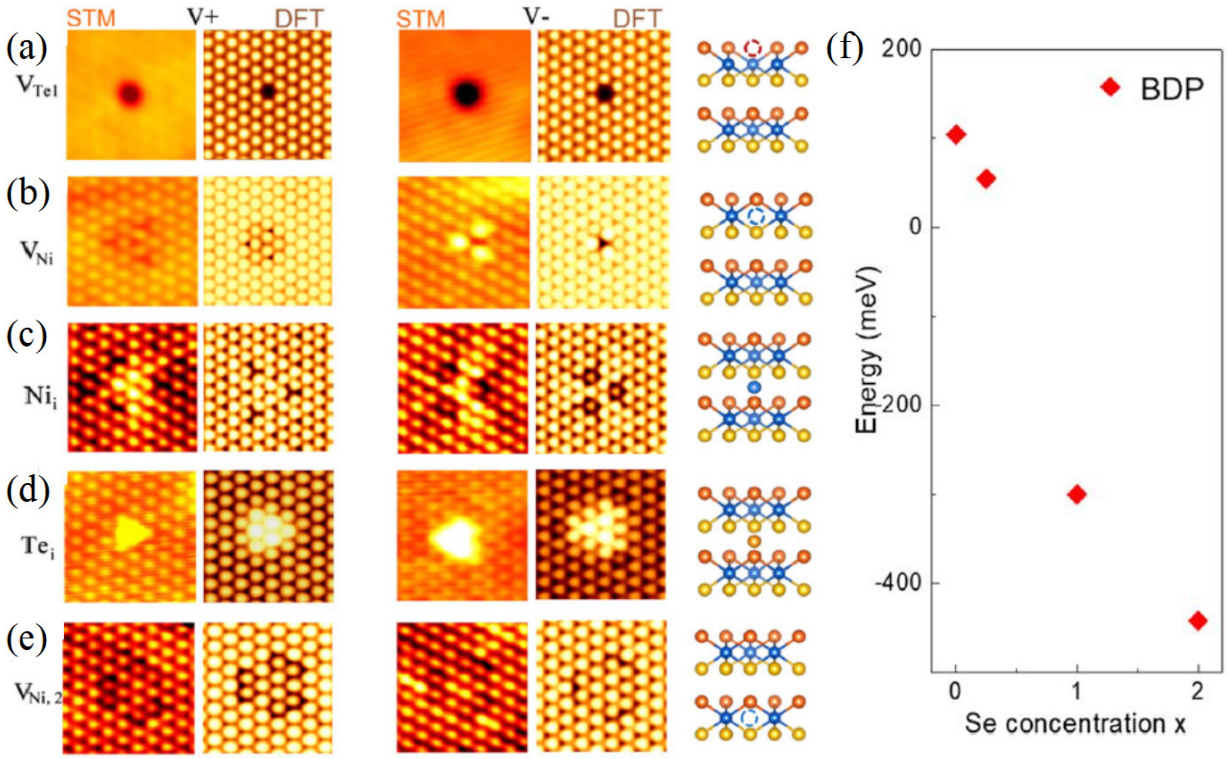

Figure 5.7: (a)-(e) The STM topographies and corresponding DFT simulations of the $NiTe_2$ defects [138]. (f) The bulk Dirac point energy as a function of the Se concentration in the $NiTe_{2-x}Se_x$ alloy [136].

They observed that the $NiTe_2$ surface exhibits different defects as Ni or Te vacancies (V_{Ni}, V_{Te}) and Ni or Te intercalations (Ni_i, Te_i). Figures 5.7(a)-(e) show the visualizations of the atomic defects by the atomically-resolved scanning tunneling microscopy (STM). In particular, they found that formation energy of the Ni intercalation (Ni_i) is lowest of all considered here. Therefore those defects are predominant, with the density reaching $6.4 \cdot$

10^{12} cm^{-2}. Although the defect concentration was high, the experimental ARPES results and the corresponding DFT calculations have shown that the TSSs are robust against the observed defects, confirming they were related to band topology [49].

The DFT calculations and corresponding ARPES and STM results have been made by Lam et al. [136], who has shown that by increasing the Se content in a single $NiTe_2$ crystal and creating the $NiTe_{2-x}Se_x$ alloy, one can decrease the SOC strength and tune the Dirac cone position versus E_F. It is shown in Figure 5.7(f) [136].

Qi et al. [139] compressed a single crystal of $NiTe_2$ by applying pressures up to 60 GPa. They observed a change of electrical properties. Figure 5.8(a) presents the pressure-dependent lattice parameters a and c and c/a ratio variation for a single crystal of $NiTe_2$ which shows a compressive strain of 8% and even 16% for a and c lattice parameters, respectively.

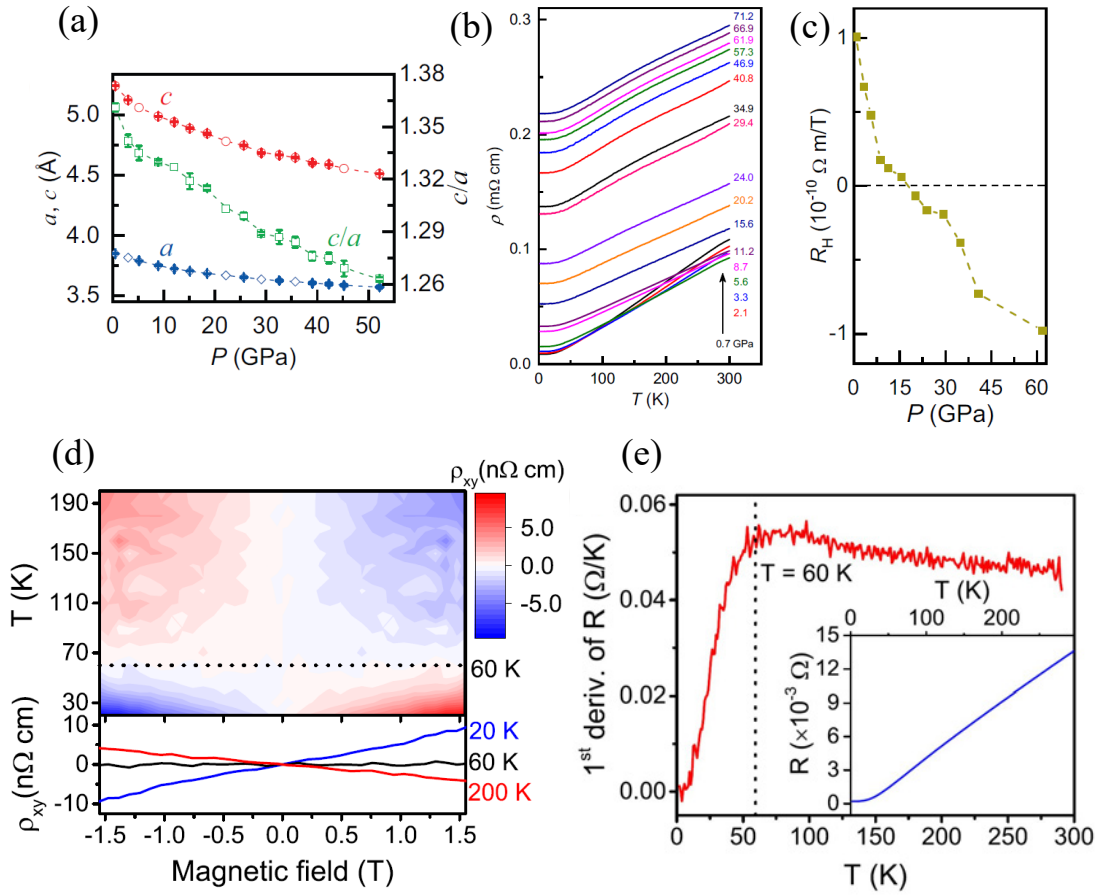

Figure 5.8: (a) Lattice parameters a, c and c/a evolution with pressure. (b) Longitudinal resistivity as a function of temperature at various pressures. (c) Hall coefficient variation as a function of pressure at T=10 K [139]. (d) Hall resistivity as a function of the magnetic field at different temperatures [140]. (e) First derivative of resistance dependence on temperature of the single crystal $NiTe_2$ with a kink at T=60 K. Inset: R(T) dependence [140].

The authors have observed a significant variation of the resistivity dependence on temperature, shown in Figure 5.8(b). Although the residual resistivity ratio - RRR (which as it will be shown further, assesses the quality of the studied crystal) is not high (1 to 10), the

resistivity of the sample increases by a factor of 3 under pressure (from more metallic to more resistive). Moreover, the compressive strain has induced a change of the Hall coefficient, from positive to negative, as presented in Figure 5.8(c). This was interpreted as a change of the charge carrier type in the studied sample. This behavior was viewed as a signature of the pressure-driven Liftshitz transition in the studied system. Indeed, there are many papers showing a Liftshitz transition in TMDs induced not only by temperature [64] or applied pressure [139], but also by magnetic field [141] or by photo-excitation [142].

Electronic and topological transitions can also be reflected in other parameters of the sample. For instance, along with the discovered Hall coefficient change, Qi et al. [139] have also observed a kink in the c/a ratio dependence at the similar pressure value (compare Figures 5.8(a) and 5.8(c).

Another work, presented by Cheng et al. [140] seems to be crucial as well, as they demonstrated a temperature-driven electronic and topological transition of $NiTe_2$ showing the flip of the sign of the Hall coefficient at the temperature equal 60 K, as presented in Figure 5.8(d). They have carefully examined the resistance dependence on temperature where at low temperature they have observed a resistance upturn at 60 K. It in seen seen as a peak in the first derivative of resistance on temperature as shown in Figure 5.8(e). Similar results, as will be demonstrated later, were also observed in this dissertation.

The above results show that the electric properties of $NiTe_2$ strongly depend on the stoichiometry and on lattice parameters. Recent papers show that magnetic properties of $NiTe_2$ strongly depend on doping as well. Bulk crystal of $NiTe_2$ is not known to be a superconductor, however theoretical calculations show that the monolayer form of $NiTe_2$ can be an intrinsic superconductor with a critical temperature (T_c) $T_c \sim 5.7$ K as shown by F. Zheng et al. [143]. They also demonstrated that a bilayer of the $NiTe_2$ intercalated with lithium is found to display two-gap superconductivity with a $T_c \sim 11.3$ K and a superconducting gaps of ~ 1.9 meV and ~ 3.1 meV. Similar results have been reported by Lima et al. [144] who investigated the effect of titanium doping on physical properties of single crystal $NiTe_2$. They showed that $Ti_{0.1}NiTe_{1.5}$ exhibits superconducting properties with a T_c close to 4 K.

5.1.5 Fingerprints of Dirac fermions

The existence of the highly mobile Dirac fermions may lead to quantum oscillations originating from Landau quantization of DOS in the presence of the magnetic field. The oscillations can be observed not only in the longitudinal magnetoresistance (in the form of the Shubnikov de-Haas oscillations [145]) but also in magnetization (M) signal known as the de-Haas van Alphen oscillations [146, 110, 115]. Such result is presented in Figure 5.9(a) [115], where magnetization component shows oscillating character for B > 15 T.

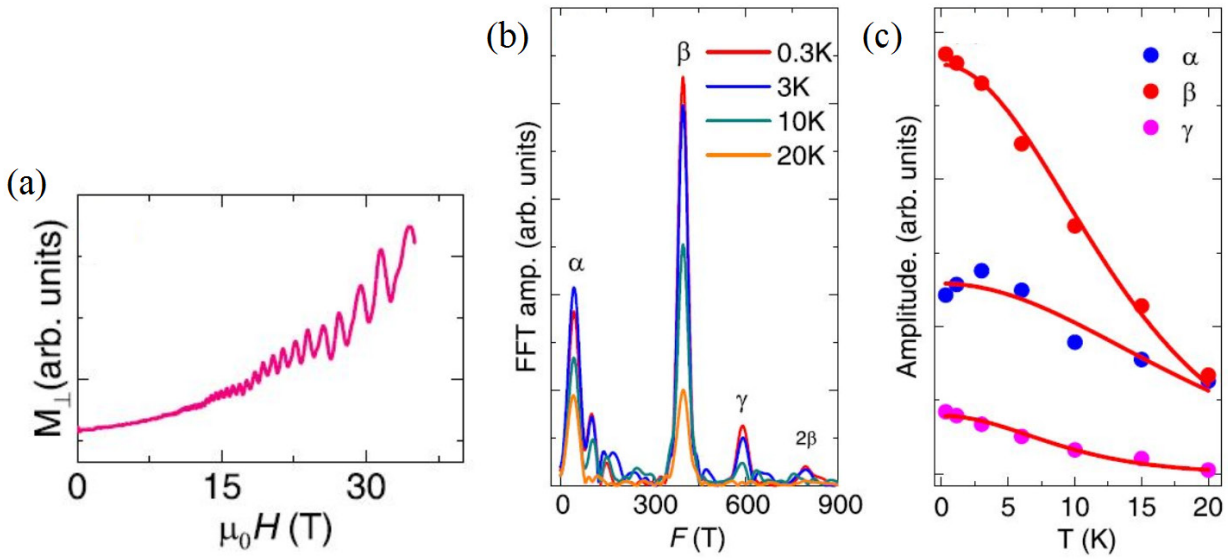

Figure 5.9: (a) The magnetization oscillations (or the de-Haas van Alphen oscillations) measured in a torque magnetometry. (b) The FFT of the de-Haas van Alphen signal, revealing frequency dependence of the oscillations. (c) The temperature dependency of the de-Haas van Alphen F amplitude oscillations [115] with the red fitted curves from the Lifshitz-Kosevich model [146].

Figure 5.9(b) shows the fast Fourier transform (FFT) of the magnetization signal peaked at frequency (F) values, directly related to the Fermi surface cross-section. The temperature dependence of the FFT peaks (see Figure 5.9(c)) allows one to calculate carrier effective mass in the sample [146]. Moreover, from the value of the Berry phase oscillations one may conclude if the carriers are topological or trivial.

Up to now the topological features of the $NiTe_2$ carriers in the magnetotransport measurements have not been intensively explored yet. W. Zheng et al., observed a 600% increase of the MR at T = 2 K under B=9 T [115] for their best sample. Although they have obtained carrier mobilities over 2000 $cm^2/V \cdot s$ at T=2 K, which were considerably higher than reported by Xu et al. [110], they have not observed Shubnikov-de Haas oscillations. Even if the Dirac fermions exist in the sample, their contribution to the electrical transport was limited due to high E_F relative to the BDP's energy position. The complex $NiTe_2$ Fermi surface can lead to the intricate electrical results where the relativistic carriers coexist with the trivial ones, forming parallel conductivity channels. For instance, Liu et al. [147] have shown that the planar Hall effect, observed in the single crystal $NiTe_2$, usually being an evidence for the chiral anomaly in topological semimetals [28, 148], originates from the trivial orbital magnetoresistance.

5.2 Experimental results

This chapter presents experimental finding for MBE-grown $NiTe_2$. As outlined in section 5.1, mechanical and magnetotransport properties of the $NiTe_2$ layers have not been fully inves-

tigated yet. Still, there is a lack of the systematic experimental studies of $NiTe_2$ layers with different thicknesses and various growth parameters. Moreover, the studied layers had a drawback of tiny samples, imposed by the growth method. With this in mind, MBE technique was applied, which allows a large-scale samples and precise growth control. To our knowledge it was the first time the MBE technique was used for $NiTe_2$ growth. The growth procedures of the pioneering samples can be found in the paper of Seredyński et al. [42] and in the PhD thesis of Dr. Bartłomiej Seredyński, which focuses on crystal continuity and morphology [149]. In this PhD dissertation, structural and transport studies are performed on the following samples: UW1650, UW1651, UW1712, UW1721, UW1722, UW1723, UW1724, UW1745, UW1746, UW1747, UW1748, UW1997B, UW1849, UW1999 and UW2001. Majority of them were grown by Dr. Wojciech Pacuski and Dr. Bartłomiej Seredyński from the Faculty of Physics, University of Warsaw.

5.2.1 Substrate

To satisfy requirement of a small lattice mismatch between the $NiTe_2$ and the substrate, a nearly lattice-matched 3D substrate of GaAs (111)B has been used for the $NiTe_2$ growth [42]. To avoid any parallel conduction, the samples dedicated for transport experiments were grown on semi-insulating (SI) substrate. As shown in Figure 5.10, the lattice shown hexagonal symmetry complying with the $NiTe_2$ symmetry.

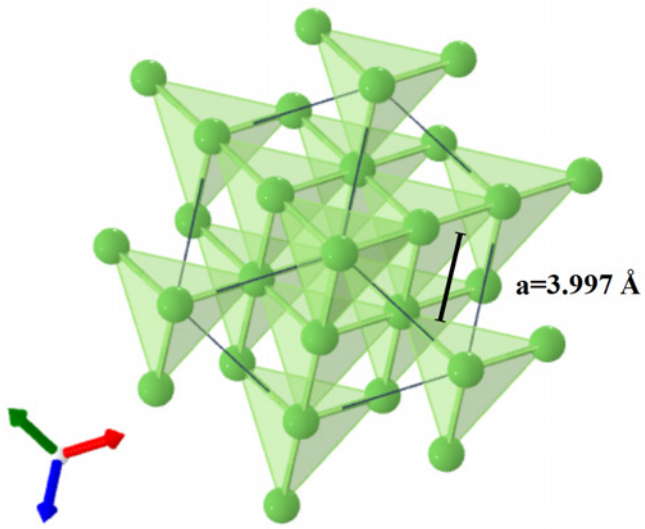

Figure 5.10: The scheme of the top view of the GaAs (111), used as a substrate for the $NiTe_2$ MBE growth [150].

The in-plane lattice parameter of the GaAs (111)B is a=3.997 $\AA$ [151] giving a tensile strain to $NiTe_2$ resulting from the 3.5% mismatch. The linear thermal expansion coefficient for the GaAs substrate is $\alpha_T = 5.73 \cdot 10^{-6}\ K^{-1}$ [152] being very close to the in-plane linear thermal

expansion coefficient of $NiTe_2$. Taking into account the temperature-evolution of the both materials, the low- and room-temperature in-plane strains in the $NiTe_2$ are 3.59% and 3.6%, respectively, revealing that the temperature practically does not impact the strain in the layer during cooling process. This was confirmed by James et al. [112] who showed a small both in-plane and out-of-plane lattice parameters evolution based on XRD measurements while heating $NiTe_2$ sample from T=20 K to T=300 K.

5.2.2 Growth parameters and sample characterization

To choose optimal growth conditions for high-quality continuous $NiTe_2$, numerous samples of various thickness were grown at various substrate temperatures (T_S). The T_S has been controlled using one- or two-steps heating processes. In the former, the T_S has been constant and stayed within a range (130 ^{o}C to 430 ^{o}C). In the second case, initial temperature was set to T_{S1}=180 ^{o}C and in the middle of process, it was ramped up to T_{S2}, either to 230 ^{o}C, 430 ^{o}C or 530 ^{o}C. The thickness of the samples varied from 15 nm to 500 nm.

5.2.3 TEM and STM analysis

The thickness of the layers and its homogeneity were monitored during the growth with a use of RHEED which allows a precise control of a sample thickness. The morphology and structure of $NiTe_2$ layers were investigated post-growth, by the FEI Titan 80-300 transmission electron microscope operating at $U \sim 300$ kV. Figures 5.11(a)-(b) present the high-resolution scanning transmission electron microscope (STEM) cross-section images of samples on SI GaAs (111)B substrate and $NiTe_2$ layers of (a) 15 nm and (b) 55 nm grown at T_S = 230 ^{o}C and T_S = 180 ^{o}C, respectively. At a small scale the layers are smooth and homogeneous and of a high quality, without any islands, with clear interfaces between the layers and the substrate and with a perfect arrangement of the Ni and Te atoms in 1T-phase, as clearly revealed in the zoomed red frames in Figures 5.11(a)-(b). The 15 nm-thick $NiTe_2$ is continuous, however for the thicker 55 nm-thick sample, the length of the unperturbed layer reached only up to hundreds of nm (Figure 5.11(c)), revealing gaps of a few tens of nm, in which $NiTe_2$ was missing. Figures 5.11(d)-(e) show the TEM image cross-section and corresponding strain field analysis showing misfit dislocations and strain originating from the GaAs substrate. Figure 5.11(f) presents the scanning tunneling microscopy image of the top of 55 nm-thick $NiTe_2$ at the atomic resolution proving hexagonal structure of $NiTe_2$ [42].

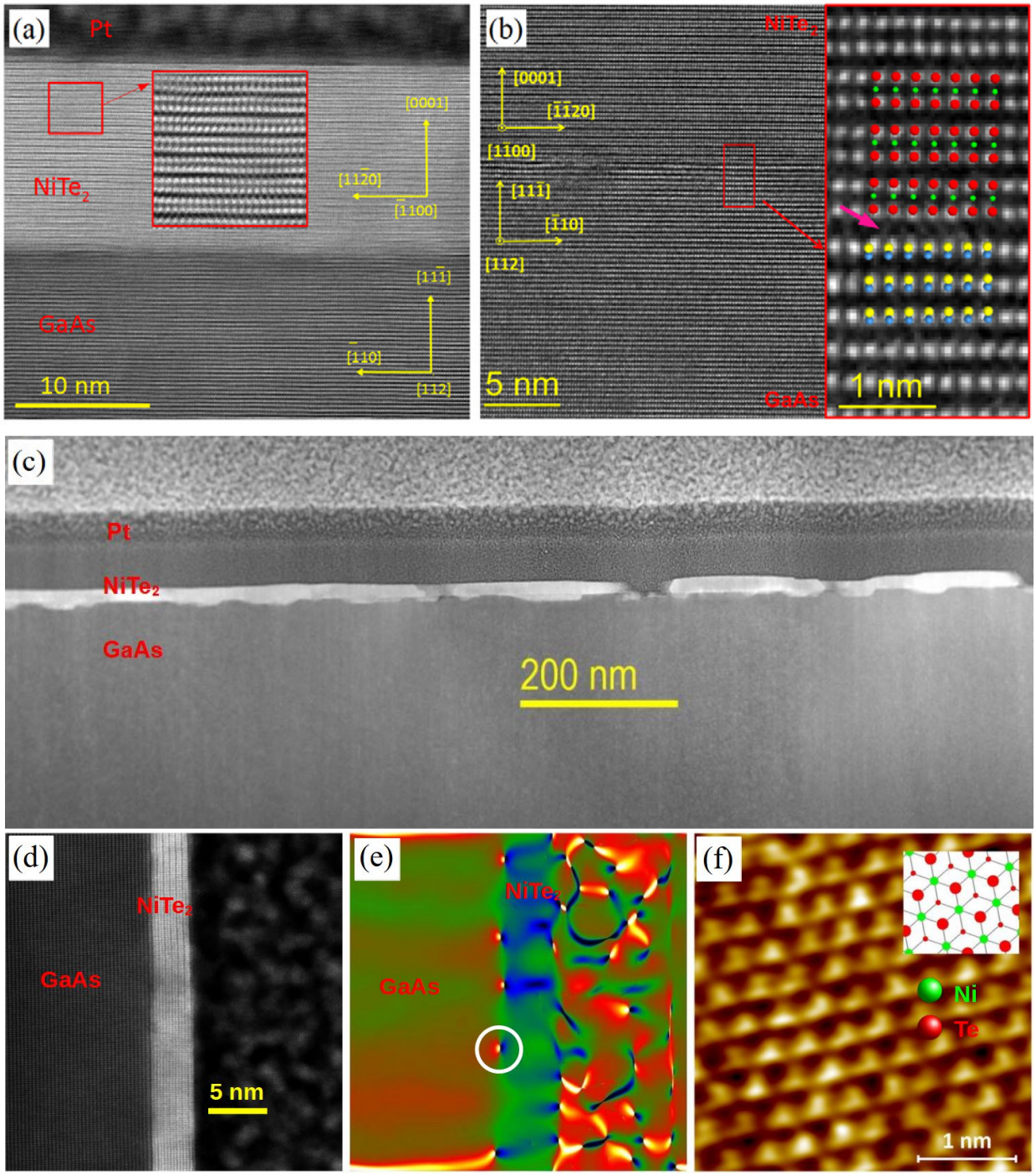

Figure 5.11: High-resolution STEM image (made in the high angle annular dark field (HAADF) detector mode) of cross-sections of the $NiTe_2$ layers on SI GaAs (111)B substrate of (a) 15 nm (UW1651) and (b) 55 nm (UW1723) thick [42]. The Ni, Te, Ga and As atoms are marked with the green, red, blue and yellow balls, respectively. The large-area profile of (c) 15 nm (UW1651) $NiTe_2$. The HR TEM image cross-section of (d) 2 nm (UW1650) $NiTe_2$ and (e) the corresponding strain field originating from the GaAs (111)B substrate. [TEM images were taken by Dr. S. Kret and MSc W. Zajkowska-Pietrzak, Institute of Physics, PAS]. (f) The scanning tunneling microscopy image (made with the bias $V_b = +10$ mV and current $I_t = 1.5$ nA) of 55 nm (UW1723) thick $NiTe_2$ grown at $T_S = 180\ ^oC$ [42]. [The image was taken by Dr. R. Bożek, Faculty of Physics, UW].

As it will be shown further, the substrate temperature significantly changes morphology of the $NiTe_2$ layers. For instance, the TEM cross-section images showed that $NiTe_2$ samples

grown using two-steps heating process with final temperature T_{S2} equal or higher than 430 ^{o}C, were tellurium deficient. It gave rise to semiconducting behavior of the longitudinal resistivity dependence on temperature. Additionally, it should be noted that although the subsequent TLs of $NiTe_2$ are supposed to be coupled only by weak van der Waals forces, some unidentified bright echo spots are visible in the STEM-HAADF image (see the pink arrow in the zoomed frame in Figure 5.11(b)). The observed spots evidence the unknown electron densities present in the system. They might reflect some inner parts of layer being covalently bonded. As the procedure involves the epitaxial growth of a vdW material on a conventional 3D substrate, the question rises if the growth is a pure vdW-like, or whether it shows some covalent character. The influence of the quasi-vdW epitaxy on TMDs growth is tackled in more details in Chapter 8. The bright spots may also originate from defects and intercalates at $NiTe_2$ layers. The above remarks highlight a need for future extended investigations of the nature of atomic interactions in the MBE-growth of van der Waals materials.

5.2.4 XRD analysis

The crystal structure of $NiTe_2$ layers was identified with the use of the symmetrical X-ray diffraction measurements. Figures 5.12(a)-(c) shows an $\omega - 2\Theta$ scan of the XRD pattern for the $NiTe_2$ layers, grown at three different T_S, on GaAs (111) substrate. One can see diffraction on (111) and (222) GaAs planes. For all $NiTe_2$ samples, the XRD peaks are sharp and narrow. Positions are well indexed, i.e. (001), (002), (003) and (004), indicating high quality of the layers. The apparent differences between $NiTe_2$ and GaAs (111) peak intensities result from the use of samples of different sizes. Note that the intensities are presented in arbitrary units and cannot be directly compared across samples. The high quality of the $NiTe_2$ layers was also evidenced by the symmetric and periodic Laue oscillations visible around (001) reflection, presented in Figure 5.12(d). The Laue oscillations, known as the thickness fringes, are visible only in high-quality multilayers [153]. The inset of Figure 5.12(d) shows the position of the thickness fringes versus its index and a linear fit, presented by the red curve. It gives information on the distances Θ between the thickness fringes and estimation of the layer thickness. Using the Scherrer equation, one can calculate the average thickness of the layers (d_S): $d_S = \lambda_x/(2 \cdot cos(\Theta) \cdot \Theta)$, where λ_x is the X-ray wavelength (λ_x = 1.54 $\AA$), one obtains d_S=(56.4 ± 0.4) nm.

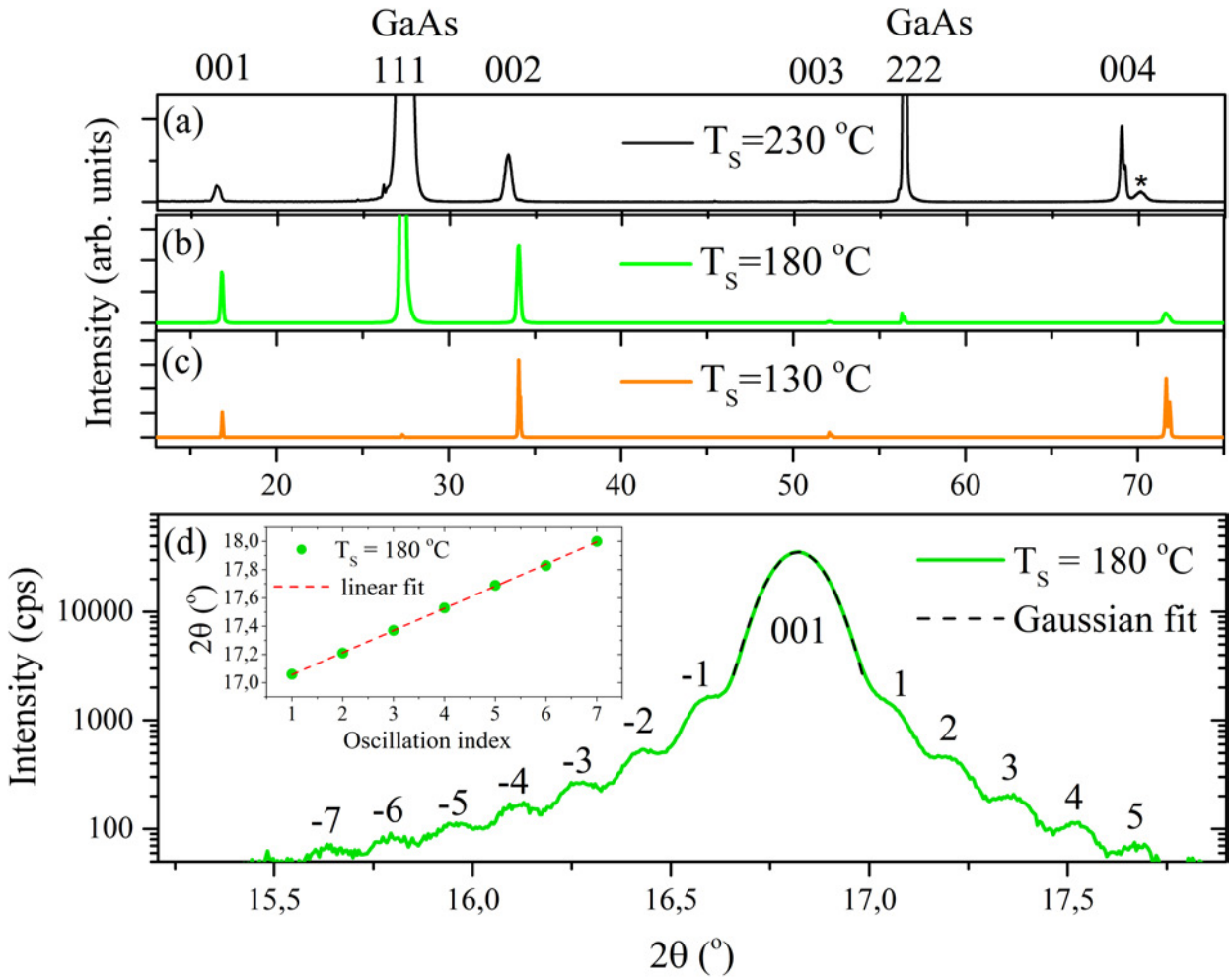

Figure 5.12: The X-ray diffraction pattern. The relative intensity of the $\omega - 2\Theta$ scan for $NiTe_2$ samples grown at various substrate temperatures: (a) T_S = 230 ^{o}C (UW1651), (b) T_S = 180 ^{o}C (UW1723) and (c) T_S = 130 ^{o}C (UW2001). Peak marked with asterisk in the black curve comes from the silicon sample holder. (d) The $\omega - 2\Theta$ scan for $NiTe_2$ sample grown at T_S = 180 ^{o}C with visible thickness fringes marked with indexes and Gaussian fit of the (001) peak (black dashed curve). Inset: the 2Θ position of the fringes with a linear fit, presented with the red, dashed line. [The data were measured by Dr. M. Tokarczuk, Faculty of Physics, UW. The data analysis and Figure preparation: Z. Ogorzałek-Sory]

The position and the full width at half maximum (β) obtained from the Gaussian fit to the (001) peak, marked by the black dashed curve in Figure 5.12(d) also allows to calculate the thickness (d_X) of the studied layers. Assuming $d_X = K \cdot \lambda_x / (\beta \cdot cos(\theta))$, where K is a dimensionless shape factor with a value close to unity, the average thickness of the $NiTe_2$ sample, grown at T_S = 180 ^{o}C, is d_X=(55.3 ± 0.2) nm. Both d_S and d_X values are in a very good agreement with the nominal thickness (see TEM results in Figure 5.11(c)). Moreover, from the Bragg's law to the (00l) planes, the interplanar spacing (c lattice parameter of the studied layers) was determined. Figure 5.13(a) presents the relative intensity of the $\omega - 2\Theta$ scan for $NiTe_2$ samples grown at three T_S, limited to the 001 peak data, with fitted Gaussian distributions, marked by the red dashed curves.

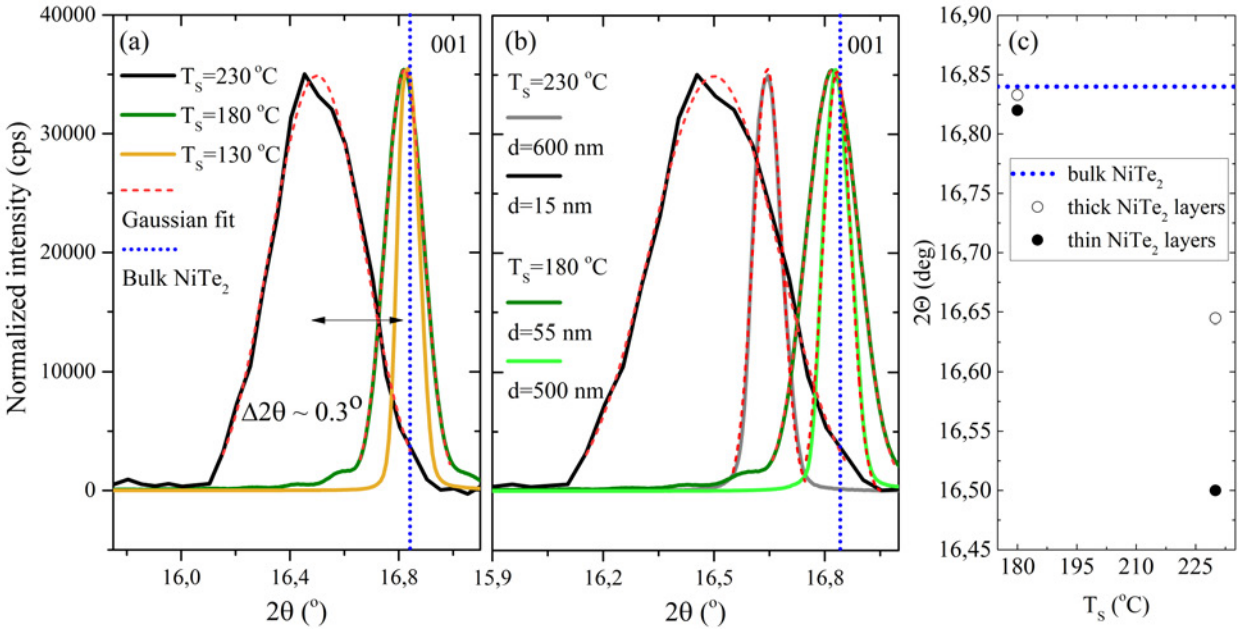

Figure 5.13: X-ray diffraction pattern of 001 reflection for samples grown (a) at three various substrate temperatures and (b) at T_S = 230 ^{o}C (UW1651), T_S = 180 ^{o}C (UW1723) and T_S = 130 ^{o}C (UW2001) for three sample thicknesses. The Gaussian distribution fits and 001 reflections for bulk $NiTe_2$ [111] marked by the dashed, red and dotted blue curves, respectively. (c) The 2Θ position of the 001 peak for the ensemble of the samples, grown at two various substrate temperature. [The data were measured together with Dr. M. Tokarczuk, Faculty of Physics, UW. The data analysis and Figure preparation: Z. Ogorzałek-Sory.]

The vertical blue dotted line shows the position of the 001 peak for bulk $NiTe_2$ sample [111]. It is clearly visible (see also Figures 5.12(a)-(c)) that the position of the 001 changes for different samples. The difference between the positions of the bulk and $NiTe_2$ sample, grown at T_S = 230 ^{o}C, is quite considerable and equals 0.3^o. As the T_S rises, the 001 peak shifts to the smaller angles. The position of the 00l peak reflects the interplanar spacing, and its shift indicates that the c lattice parameter differs from the bulk value (it is larger for all the studied layers). It evidences tensile strain along c axis of the studied layers. As a first approximation, one can assume that it is the T_S which influences the strain in the layers. Figure 5.13(b) shows the ω–2Θ scans for samples grown at two different substrate temperatures: T_S = 180 °C and T_S = 230 °C. At each temperature, two samples were grown one with a thickness on the order of tens of nanometers, and one on the order of hundreds of nanometers. The comparison of the grey and light green curves, which present the results for the samples grown at different substrate temperatures but of similar thicknesses confirms the hypothesis that lower T_S shifts the position of the 00l peak to the higher angles. However, one should not forget that the critical thickness of the MBE-grown $NiTe_2$ layers is still not known yet. The 001 peak positions for the thin samples are always shifted to lower angles in respect to to the bulk value. On the other hand, the 001 peak position for the thick samples are much closer to the 00l position of the bulk value (see Figure 5.13(c)). It shows that this is not the substrate temperature alone that influences the strain in the studied layers, but

also the layer thickness. Knowing that the influence of the T_S and layer thickness on the lattice parameter c is visible, a relation between the thickness of the grown layers and lattice parameters was found. Figures 5.14(a)-(c) show the evolution of the 001 peak position and c and a lattice parameters, obtained from symmetrical and asymmetrical reflections in the XRD studies, as a function of the thickness of the $NiTe_2$ layers, presented in panels by the (a) black, (b) orange and (c) blue points, respectively.

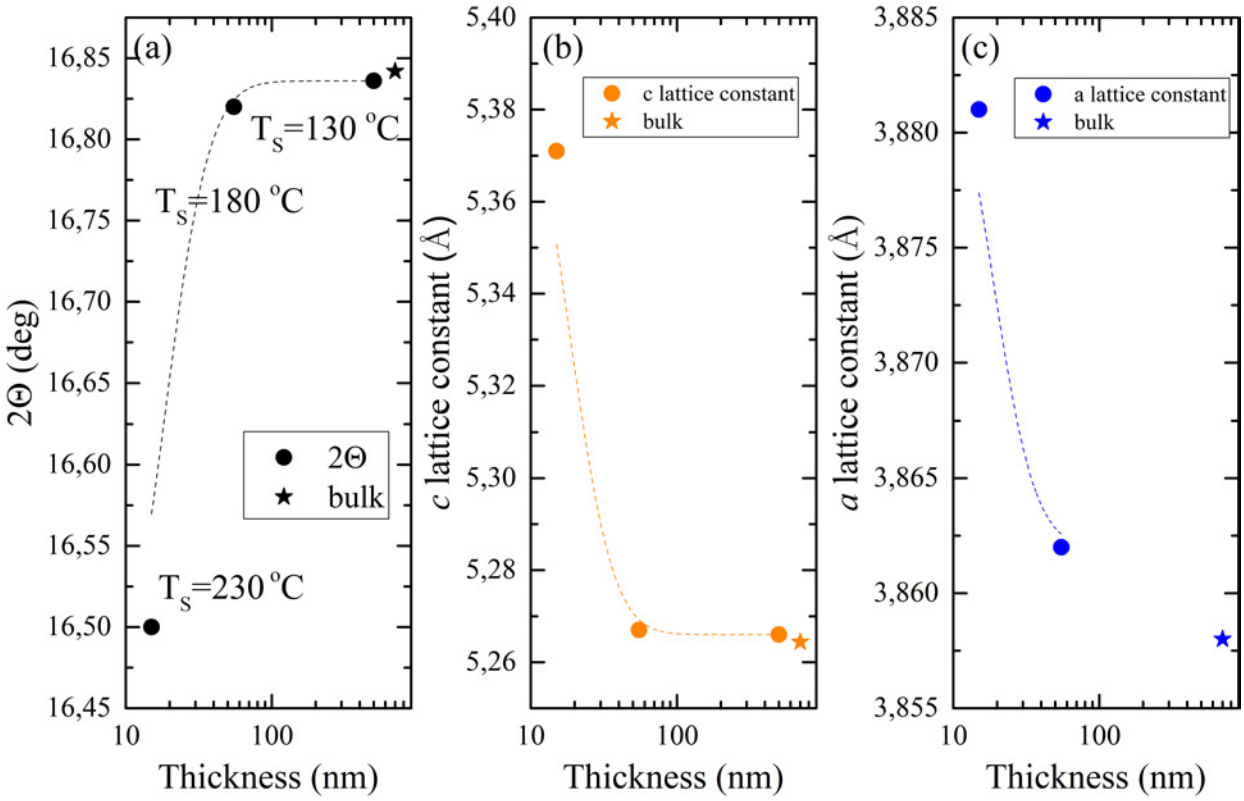

Figure 5.14: (a) The 2Θ 001 peak position variation as a function of layer thickness. (b)-(c) Lattice parameters (out-of-plane c and in-plnae a) values as a function of $NiTe_2$ thickness. [The symmetrical data were measured together by the Author with Dr. M. Tokarczuk, Faculty of Physics, UW. The asymetrical data were measured by Dr. J. Domagala, Institute of Physics, PAS. The data analysis and Figure preparation: Z. Ogorzałek-Sory.]

The asterisks depict the 2Θ, c and a values for bulk material [111]. Although the thickness of the layers was changed simultaneously with the T_S, one can notice a trend between the 2Θ, c and a values and sample thickness. The experimental 2Θ, c and a values get closer to the theoretical ones for the samples with the thickness larger than 500 nm.

Another factor imposing strain to the studied $NiTe_2$ layers is the substrate quality: preparation and the presence of the buffer layer (see Figure 5.11(e)). Figures 5.15(a)-(d) show relative intensities of the $\omega - 2\Theta$ scans for layers of different thicknesses with and without GaAs buffer layer (BL). Figures 5.15(a)-(b) present a shift in the 001 reflection obtained for layers of different thicknesses. It shows that the strain can be tuned with the use of the buffer. The shift of the 001 peak is reduced for sample with buffer layer and stays closer to the bulk value (marked with the blue dashed line).

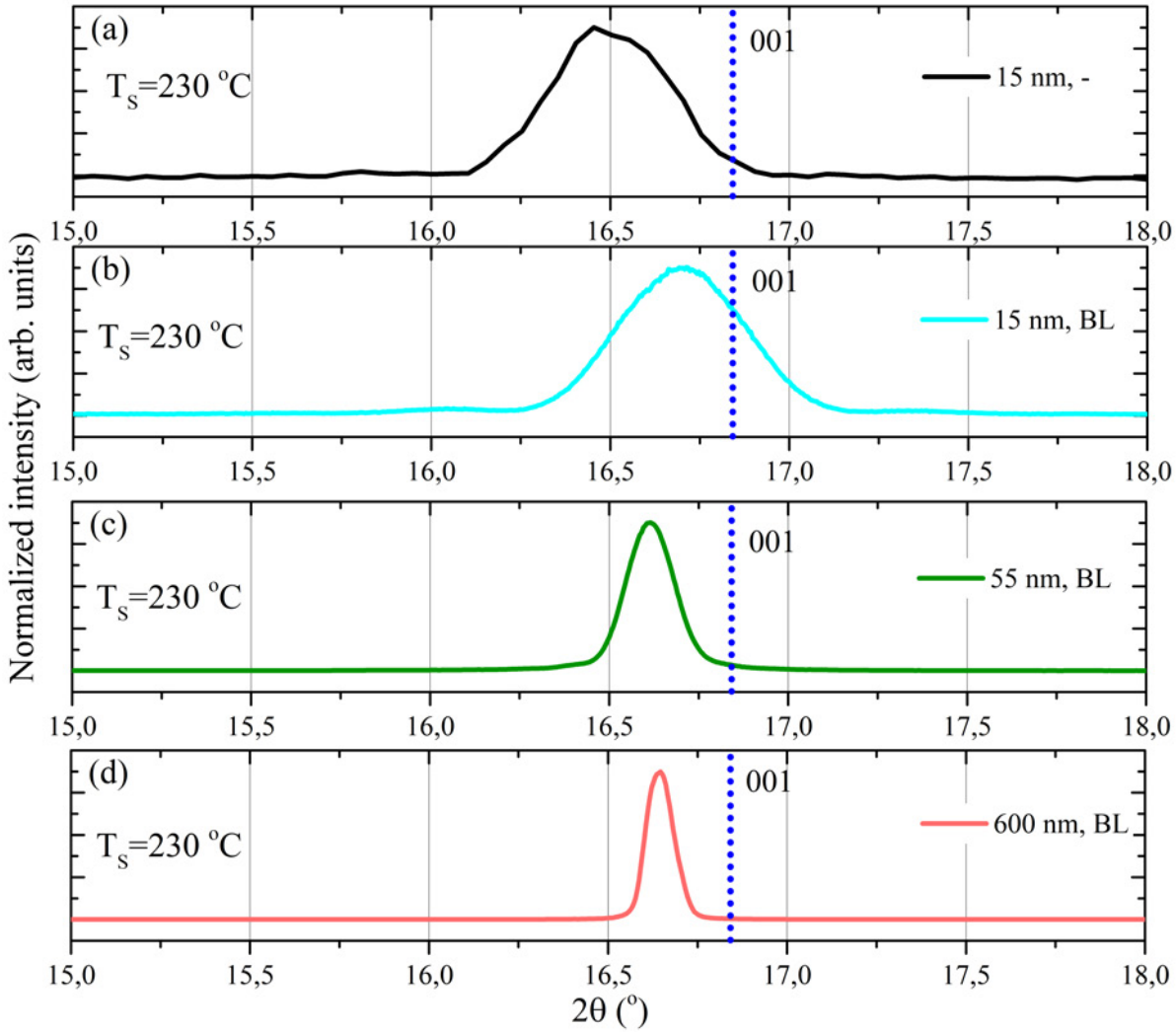

Figure 5.15: The X-ray diffraction characterization. Normalized intensities of the $\omega - 2\Theta$ scans for samples (a) without (UW1651) and (b) with (UW1712) the GaAs buffer and for the samples with the buffer with (c) thin (UW1713) and (d) thick (UW1748) $NiTe_2$ layer. The thickness of the buffer layer was equal 150 nm. All samples have been grown at T_S = 230 ^{o}C. The blue, dashed line corresponds to the theoretical value of the bulk $NiTe_2$ 001 peak. [The data were taken by Dr. M. Tokarczuk, Faculty of Physics, UW. The data analysis and Figure preparation: Z. Ogorzałek-Sory.]

Moreover, thicker samples are less strained, as presented in Figures 5.15(c)-(d). The width of the peak is much smaller as the samples are thicker. Still, the strain is observed. To trace the dependence of the 001 peak position on sample growth parameters, the results of the normalized intensities of the $\omega - 2\Theta$ scans (Figure 5.15(a)-(d)) are presented in one panel in Figure 5.16.

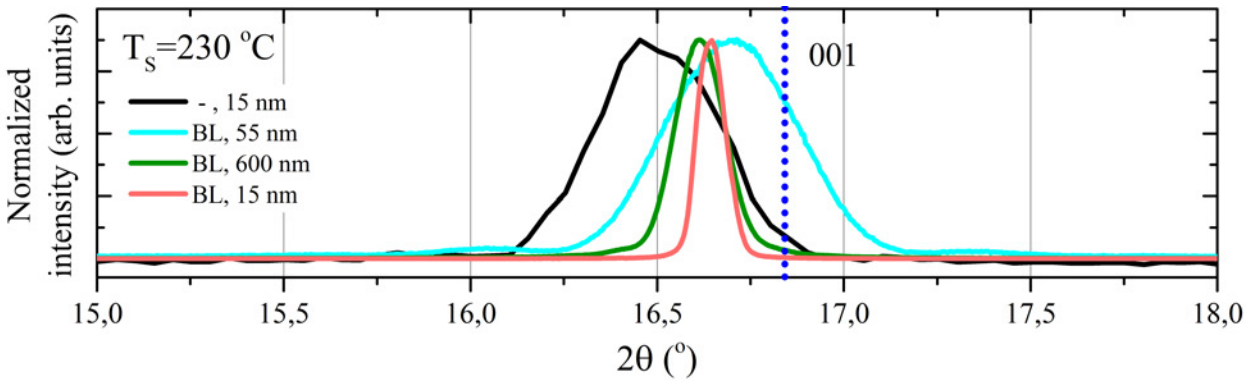

Figure 5.16: The X-ray diffraction characterization. Normalized intensity of the $\omega - 2\Theta$ scans for samples grown at T_S = 230 ^{o}C, with different thicknesses and GaAs buffer. The blue, dashed line corresponds to the theoretical value of the bulk $NiTe_2$ 001 peak. [The data were taken by Dr. M. Tokarczuk, Faculty of Physics, UW. The data analysis and Figure preparation: Z. Ogorzałek-Sory.]

The result does not show clear dependence on the growth parameters. Unfortunately a series of sample with only one parameter varied (thickness or T_S) was not available. Moreover, samples grown at one T_S were not obtained in the same growth process. It depicts possible limitations of this analysis.

To summarize, both T_S and sample thickness are main factors to tune tensile strain in the layers. However, as it has been stated in the section 5.2.3, there are some bright clearings in the zoomed frame of the Figure 5.11(b) of the $NiTe_2$ STEM image, suggesting that the interactions between the substrate and the transition metal compound layers grown by the MBE technique are complicated and they are seem not to be limited only to the pure out-of-plane weak van der Waals forces. With this in mind, a possible hypothesis of the role of T_S is that defects, intercalants, or impurity atoms in the van der Waals gap are introduced and are responsible for the observed tensile strain.

The obtained findings highlight an existence of external factors responsible for the tensile strain present in the $NiTe_2$ layers. Nevertheless, they still require more research and theoretical support to model STEM results. The list of the in-plane and the out-of-plane lattice parameters values obtained from X-ray diffraction measurements for the two selected and most strained samples are presented in Table 5.1.

Table 5.1: The $NiTe_2$ in-plane and out-of-plane lattice parameters from the symmetrical and asymmetrical X-ray diffraction measurements for two different samples. [The data were mesured by Dr. J. Z. Domagala, Institute of Physics, PAS]

Sample	a (Å)	a_{bulk}(Å)	Tensile strain [%]	c (Å)	c_{bulk}(Å)	Tensile strain (%)
T_S = 230 ^{o}C d=15 nm	3.881	3.858	0.59	5.371	5.264	2.03
T_S = 180 ^{o}C d=55 nm	3.862	3.858	0.1	5.267	5.264	0.05

Based on lattice parameters, the in-plane and out-of-plane strain was calculated ($((a - a_{bulk})/a_{bulk})$). Compared to the bulk values of the $NiTe_2$ lattice parameters ($a_{bulk} = b_{bulk}$ and

c_{bulk}), both the in-plane (a=b) and the out-of-plane (c) values of the lattice parameters are considerably tensile strained. Preliminary analysis of the change of lattice parameter c comes form increased interlayer or intralayer distances is presented in Figure B.3 in Appendix B. Tensile strain in both in-plane and out-of-plane directions contradicts elastic deformation of the lattice parameter of the unit cell, where the in-plane compression is accompanied by the out-of-plane contraction. The in-plane lattice parameters a and b are equally strained maintaining $NiTe_2$ C_3 rotational symmetry. As the type-II Dirac node crossing is symmetrically allowed and protected against hybridization and gap-opening mechanisms due to the C_3 rotational symmetry, the topology of the $NiTe_2$ layers should be not lifted [63].

5.2.5 ARPES analysis

The electronic band structure of the MBE $NiTe_2$ comes from preliminary ARPES measurements. The sample was 35 nm-thick $NiTe_2$ (i.e. 65 MLs), grown at T_S = 160 ^{o}C on the conducting GaAs (111)B substrate. Figures 5.17(a)-(c) present selected first derivatives over momentum of the ARPES maps along $K \leftarrow \Gamma \rightarrow K$ directions in the (k_x, k_y) plane, for three photon energies: 95 eV, 115 eV and 120 eV.

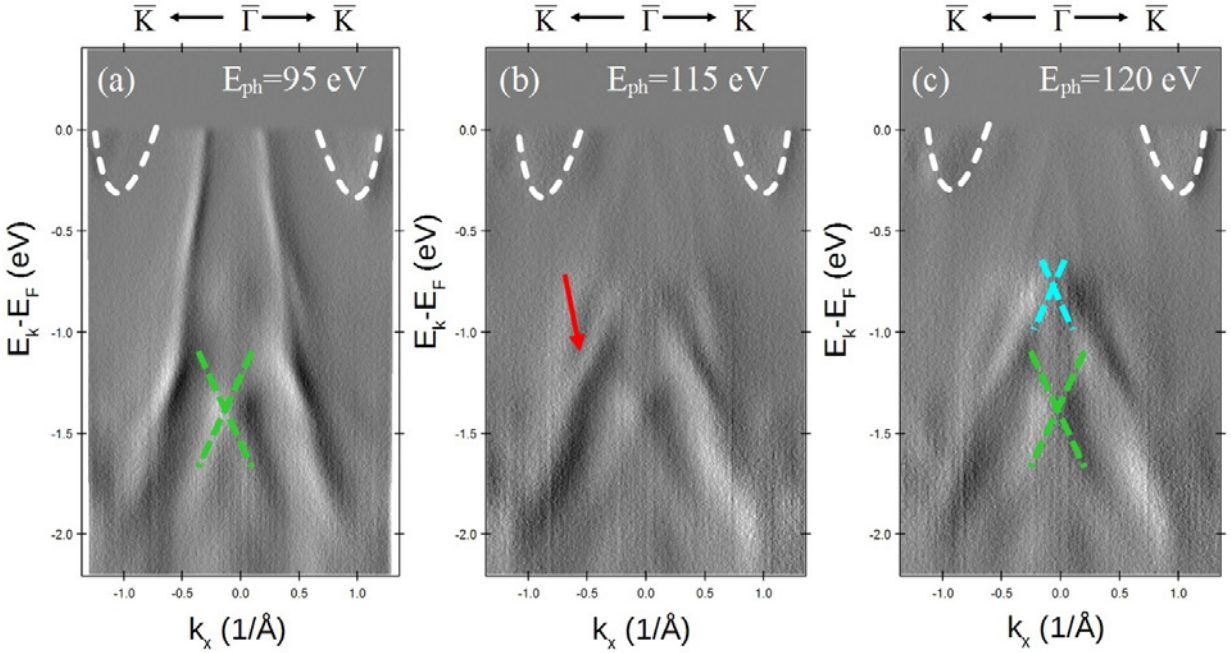

Figure 5.17: ARPES surface states spectra along $K \leftarrow \Gamma \rightarrow K$ directions for the 35 nm-thick $NiTe_2$ sample, grown at T_S = 160 ^{o}C taken for the photon energy (a) E_{ph}=95 eV, (b) E_{ph}=115 eV and (c) E_{ph}=120 eV. White parabolas show trivial electron pockets, and green and blue curves show the surface states (TSS1 and TSS2, respectively). The red arrows indicate the other SS, consistent with [135]. [The data were measured by Dr. J. Sadowski and Dr. P. Dziawa, Institute of Physics, PAS at National Synchrotron Radiation Centre SOLARIS, Jagiellonian University, Kraków, Poland. The data analysis and Figure preparation: Z. Ogorzałek-Sory, P. Dziawa.]

ARPES spectra exhibit a complex structure with numerous bands and multiple band cross-

ings. In particular, one can distinguish the electron pockets it the vicinity of the K points, marked with white dashed curves for all photon energies. Linear E(k) dependencies are visible in certain parts of the map: at $E_k - E_F \sim$ -0.8 eV and $E_k - E_F \sim$ -1.4 eV at Γ point ($k_x = 0$ $\AA^{-1}$), which can be attributed to the topological surface states TSS1 and TSS2, schematically marked with the blue and green dashed lines, respectively. The energies and momenta of the TSS1 and TSS2 are in a good agreement with the previously reported data by Gosh's [133] (-1.4 eV), Xu's [110] (-1.5 eV) or Hlevyack's [30] (-1.5 eV). Except TSS1 and TSS2, several other SS can be identified, for instance the one marked by the red arrow, which is consistent with the previously reported surface states [135]. The SS was also captured in the constant energy $k_x - k_y$ maps (Figures 5.18(a)-(c)) measured in the vicinity of Fermi energy for different energies in respect to the Fermi level: -0.01 eV, -1.1 eV and -1.5 eV.

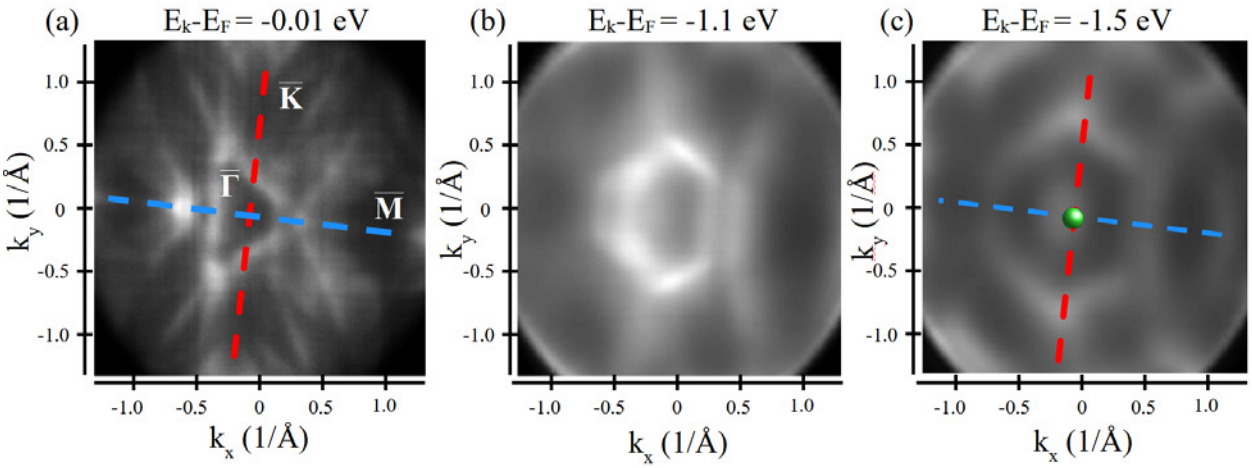

Figure 5.18: ARPES $k_x - k_y$ constant energy maps, taken with a photon energy E_{ph}=100 eV for (a) $E - E_F$=-0.01 eV, (a) $E - E_F$=-1.1 eV and (c) $E - E_F$=-1.5 eV. The high-symmetry $\bar{K} \leftarrow \Gamma \rightarrow \bar{K}$ and $\bar{M} \leftarrow \Gamma \rightarrow \bar{M}$ directions are marked with red and blue dotted lines, respectively. The green sphere points to the position of the TSS2. [The data were measured by Dr. J. Sadowski and Dr. P. Dziawa, Institute of Physics, PAS at National Synchrotron Radiation Centre SOLARIS, Jagiellonian University, Kraków, Poland. The data analysis and Figure preparation: Z. Ogorzałek-Sory, P. Dziawa.]

Red and blue curves mark the $\bar{K} \leftarrow \Gamma \rightarrow \bar{K}$ and $\bar{M} \leftarrow \Gamma \rightarrow \bar{M}$ directions, respectively. Close to E_F (Figure 5.18(a)) one can observe a small triangle around Γ point. By increasing the cutting energy, the pattern changes its shape to a hexagonal one. By reaching the cutting energy of $E_k - E_F$=-1.5 eV, a small circle at Γ point ($k_x = k_y = 0$ $\AA^{-1}$) appears, schematically marked by the green sphere (Figure 5.18(c)), accompanied by the hexagonal outer pattern. The small circle corresponds to the TSS2, clearly seen in the energy band dispersions at Γ point ($k_x = 0$ $\AA^{-1}$). The results qualitatively agree with the Fermi surface cuts presented by Nurmamat et al. [135]; however, supplementary DFT modeling is needed to precisely identify these features.

ARPES spectra revealed a complex band structure with a pronounced three-dimensional character of the Fermi surface. The results show a strong k_z dependence, similarly to the

constant energy surfaces maps observed before [135]. Multiple Weyl cones were identified, confirming that MBE-$NiTe_2$ shows topological bands. However one should note that they are all located deep within the valence band, suggesting their limited contribution to electrical transport properties of samples.

5.2.6 Electrical characterization

In this chapter electrical characterization of the studied samples is presented. All $NiTe_2$ samples were characterized by the IV characteristics and resistivity tensor measurements in a wide temperature range and in a magnetic field up to B=12 T. The samples were cleaved and the Hall-bar geometry was defined by the scriber (described in Chapter 4). Ohmic contacts were made manually with a silver paste. The photo of $NiTe_2$ sample placed in the sample holder is shown in Figure 4.2(d). Figure 5.19(a) presents the scheme of the sample used for transport measurements.

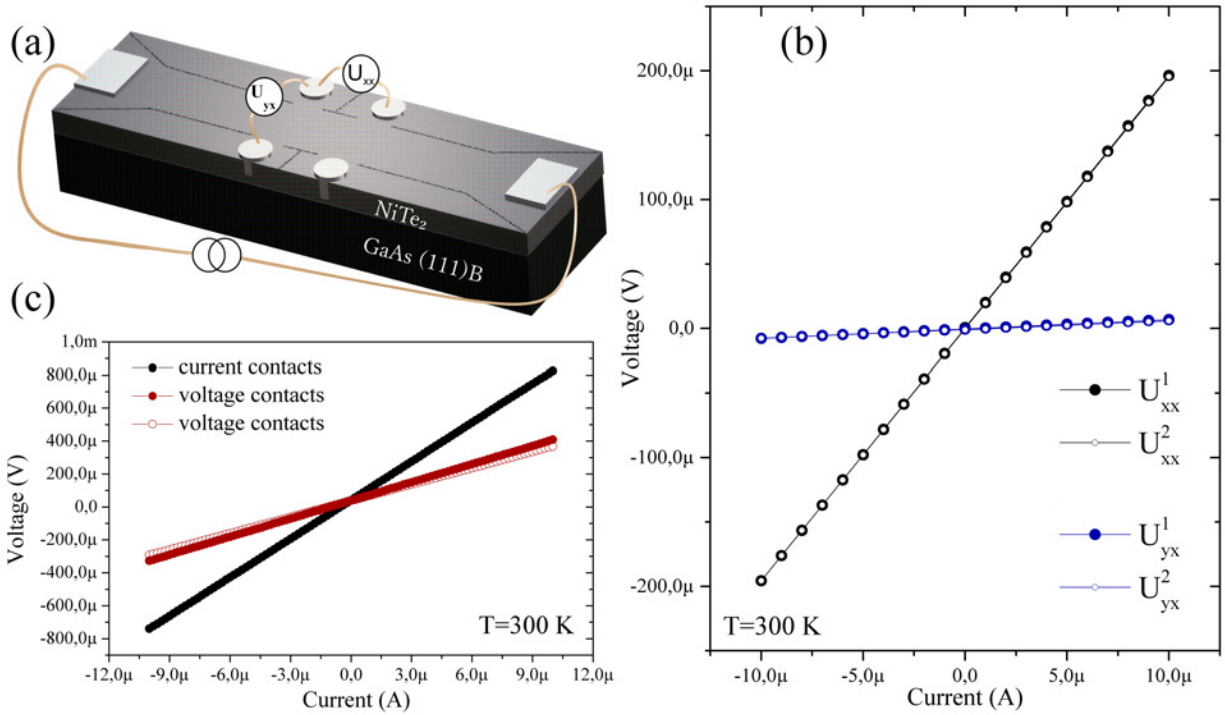

Figure 5.19: Electrical studies of $NiTe_2$. (a) The scheme of the $NiTe_2$ sample and the electronic connections for longitudinal (U_{xx}) and transverse (U_{yx}) voltages. (b) Room temperature four-probe current-voltage characteristics for two pairs of longitudinal and transverse voltages. (c) Room temperature two-probe current-voltage characteristic for the current contacts and voltage contacts.

The direct current was passed along the sample and the longitudinal (U_{xx}) and transverse (U_{xy}) voltages were measured along the current path. Figure 5.19(b) shows a typical four-probe current-voltage characteristics of the $NiTe_2$ sample, for two pairs of the longitudinal (U_{xx1} and U_{xx2}) and transverse (U_{xy1} and U_{xy2}) voltages, marked by the black and blue curves, respectively. Due to a precise Hall-bar geometry, both pairs of the longitudinal and transverse voltages are practically the same, giving almost zero-voltage response in the transverse

signals. Those results evidence also homogeneity of the sample. The slope of the IV characteristic defines the resistance of the studied layers. Similar linear results of the IV characteristics were also obtained in the two-probe measurements. Figure 5.19(c) presents the two-probe current-voltage characteristic, for current contacts and two pairs of longitudinal (voltage) contacts. The linear IV characteristics of both voltage and current contacts, down to helium temperature, prove ohmic contacts to the studied layers.

Figure 5.20(a) shows the dependence of longitudinal resistivity on temperature $\rho(T)$, normalized to the values at room temperature, for a few selected samples, grown in one- or two-steps growth processes, controlled by T_S.

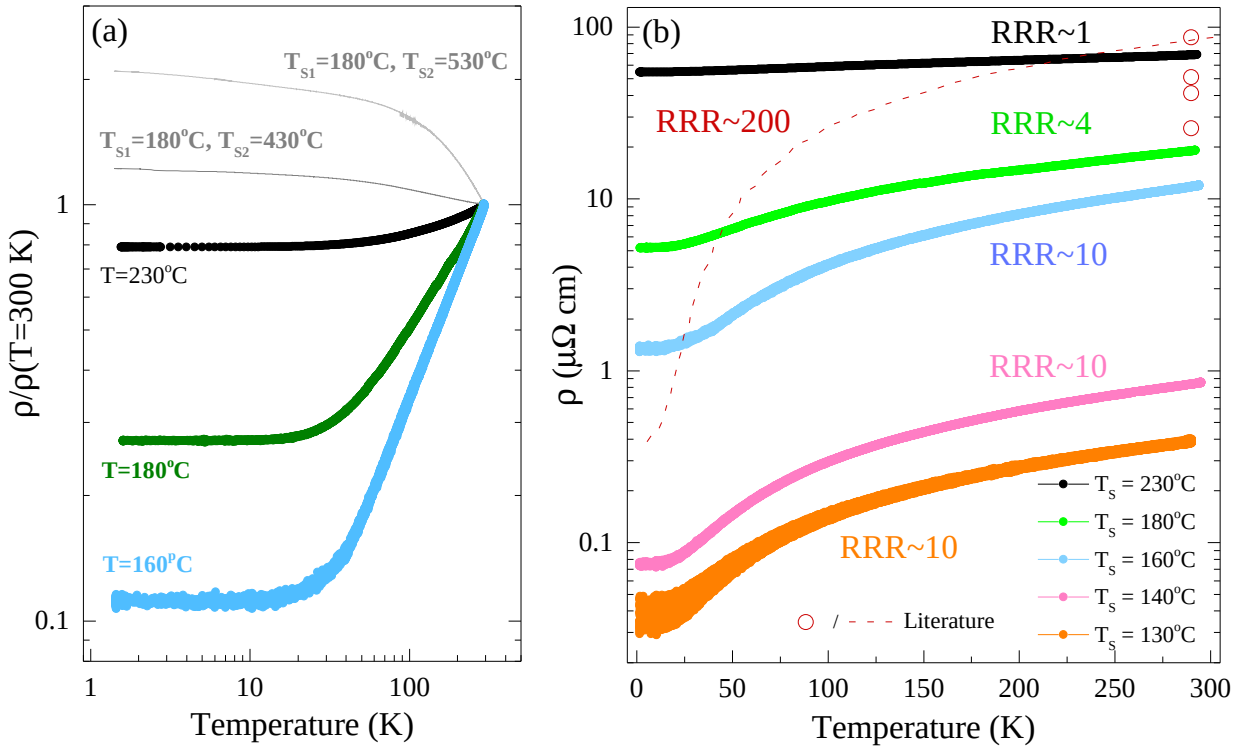

Figure 5.20: Electrical studies of $NiTe_2$. (a) Normalized longitudinal resistivity as a function of temperature for samples obtained in one and two-steps growth processes. (b) $NiTe_2$ longitudinal resistivity as a function of temperature for various substrate temperatures with a corresponding RRR parameters. Red empty points and red dashed curve presents literature resistivity data for samples grown by other techniques [110, 115, 147].

For the samples grown in a two-steps growth process, with the final substrate temperature equal or higher than $T_{S2} = 430\ ^oC$, a non-metallic resistivity dependence is observed, shown by the light and dark gray curves. This kind of dependence is not expected for metallic $NiTe_2$ layers. Based on the TEM studies (see Figures 8.2(d)-(e)) this peculiar $\rho(T)$ dependence with a rise of resistivity at low temperature correlated with Te deficiency for samples grown at $T_{S2} = 430\ ^oC$ and from a complete absence of the tellurium in sample grown at $T_{S2} = 530\ ^oC$. The samples grown in one step growth process and at lower temperature, exhibit expected metallic $\rho(T)$ dependence with a resistivity drop and a characteristic resistivity saturation at liquid helium temperatures, as shown by the black, green and blue curves for the samples

grown at T_S = 230 ^{o}C, T_S = 180 ^{o}C or T_S = 160 ^{o}C, respectively. The figure of merit of $\rho(T)$ curves is residual resistivity ratio (RRR). It is defined as the ratio of the room temperature resistivity to the low temperature resistivity. For high quality metallic samples it may reach thousands [154]. The character of the $\rho(T)$ dependence evolves for different T_S. As the T_S decreases, the RRR factor increases. Figure 5.20(b) shows the $NiTe_2$ longitudinal resistivity as a function of temperature for samples grown at various T_S, with the corresponding RRR parameters. The room temperature resistivity values for the bulk $NiTe_2$ grown by other techniques were pointed by the red empty points [110, 131, 147]. They show the same order of magnitude as the studied MBE-grown layers. Although the MBE-grown $NiTe_2$ layers are of high quality, as evidenced by the STEM images and XRD analysis, the RRR parameter values of all studied layers stay relatively low. It slightly rises when T_S is reduced, reaching 10 at maximum for samples grown at T_S < 160 ^{o}C. The highest values of RRR parameters for $NiTe_2$ layers reached 200-380 [115, 110] as presented by the red dotted curve in Figure 5.20(b) [131]. Undoubtedly, the appropriate choice of the T_S is crucial to obtain not only the proper stoichiometry of the $NiTe_2$ compound but also to increase the value of its RRR.

Figure 5.21(a) presents the room temperature transverse resistivity of $NiTe_2$ layers, grown at various T_S. A room temperature negative Hall resistivity was observed.

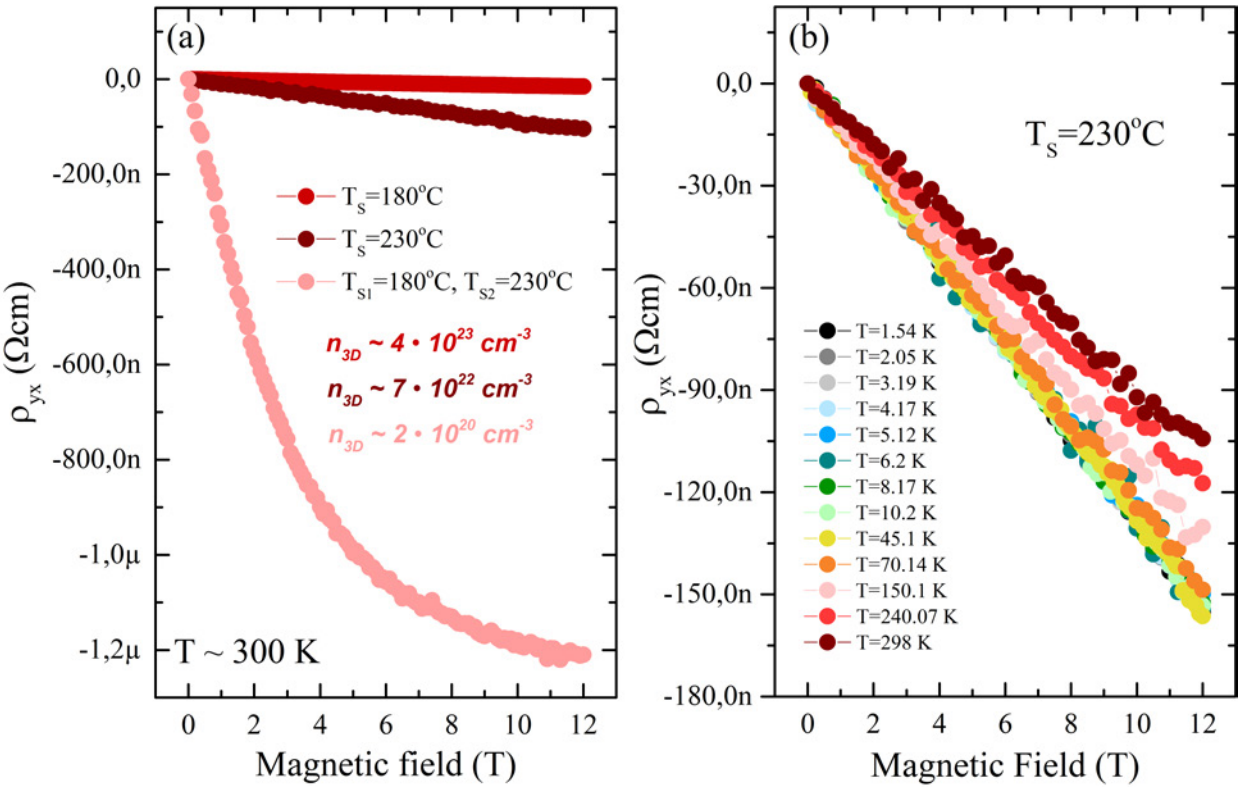

Figure 5.21: Electrical studies of $NiTe_2$. (a) The room temperature Hall resistivity of the $NiTe_2$ layers grown at different T_S, revealing various Hall concentrations. (b) The Hall resistivity of the substantially strained $NiTe_2$ layers, grown at T_S = 230 ^{o}C (UW1651) for different temperatures.

By increasing the value of T_S one can increase the Hall resistivity and decrease the Hall

concentration by three orders of magnitude, possibly paving a way to control the position of the E_F which seems to be very crucial for the magnetotransport studies in the systems with the Dirac fermion carriers. The further decrease of T_s increased much Hall carrier concentrations making the Hall coefficient for those samples unmeasurable. Magentoresistance for the samples grown at the lowest T_s stays positive and parabolic, with no traces of Shubnikov-de Haas oscillations, reaching 3% at 12 T.

The presentation and analysis of resistivity tensor measurements is performed for two samples: one grown at 230 ^{o}C, second at 180 ^{o}C. Figure 5.21(b) presents transverse resistivity dependence on magnetic field for various temperatures for a sample grown at T_S = 230 ^{o}C. The linear Hall response may evidence one type of the carriers. The linear Hall signal may also originate from the multicarrier transport with the carriers of similar concentrations and low mobilities of arbitrary sign. Figure 5.22(a) presents the map of the transverse Hall resistivity as a function of the magnetic field for different temperatures.

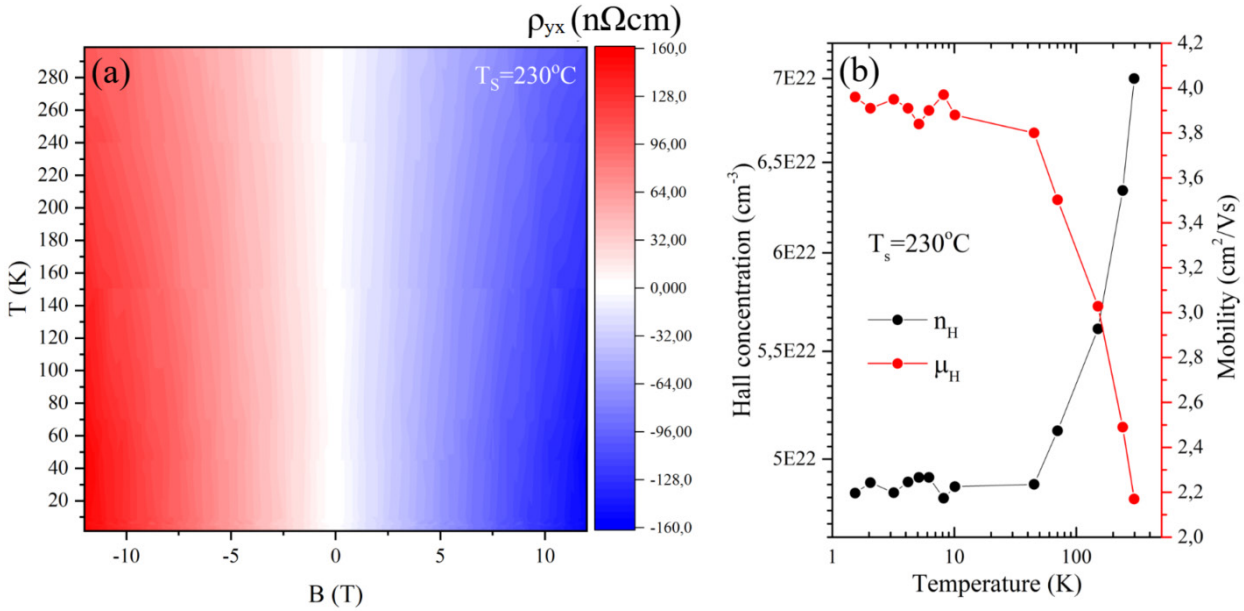

Figure 5.22: Electrical studies of $NiTe_2$. The Hall resistivity as a function of magnetic field and temperature for the sample grown at T_S = 230 ^{o}C (UW651). The Hall concentration (left axis) and the Hall mobility (right axis) of the $NiTe_2$ layers grown at T_S = 230 ^{o}C (UW1651).

The slope of the Hall resistivity practically does not change with the increasing temperature. It shows that the carrier concentration is nearly constant over the entire temperature range. The values of Hall concentrations and mobilities are presented in Figure 5.22(b).

The electron concentration is of order of $n_H \sim 10^{16}$ cm^{-2} ($n_H \sim 10^{22}$ cm^{-3}) and it is nearly constant over the entire temperature range. The electron mobility stays relatively low and saturates at 4 cm$^2/V \cdot s$ at liquid helium temperature. Figure 5.23(a) shows the longitudinal resistivity at T=3.85 K. Relative change reaches only 0.17% at magnetic field B=12 T. None of the quantum effects, such as Shubnikov–de Haas oscillations nor chiral anomaly, were identified.

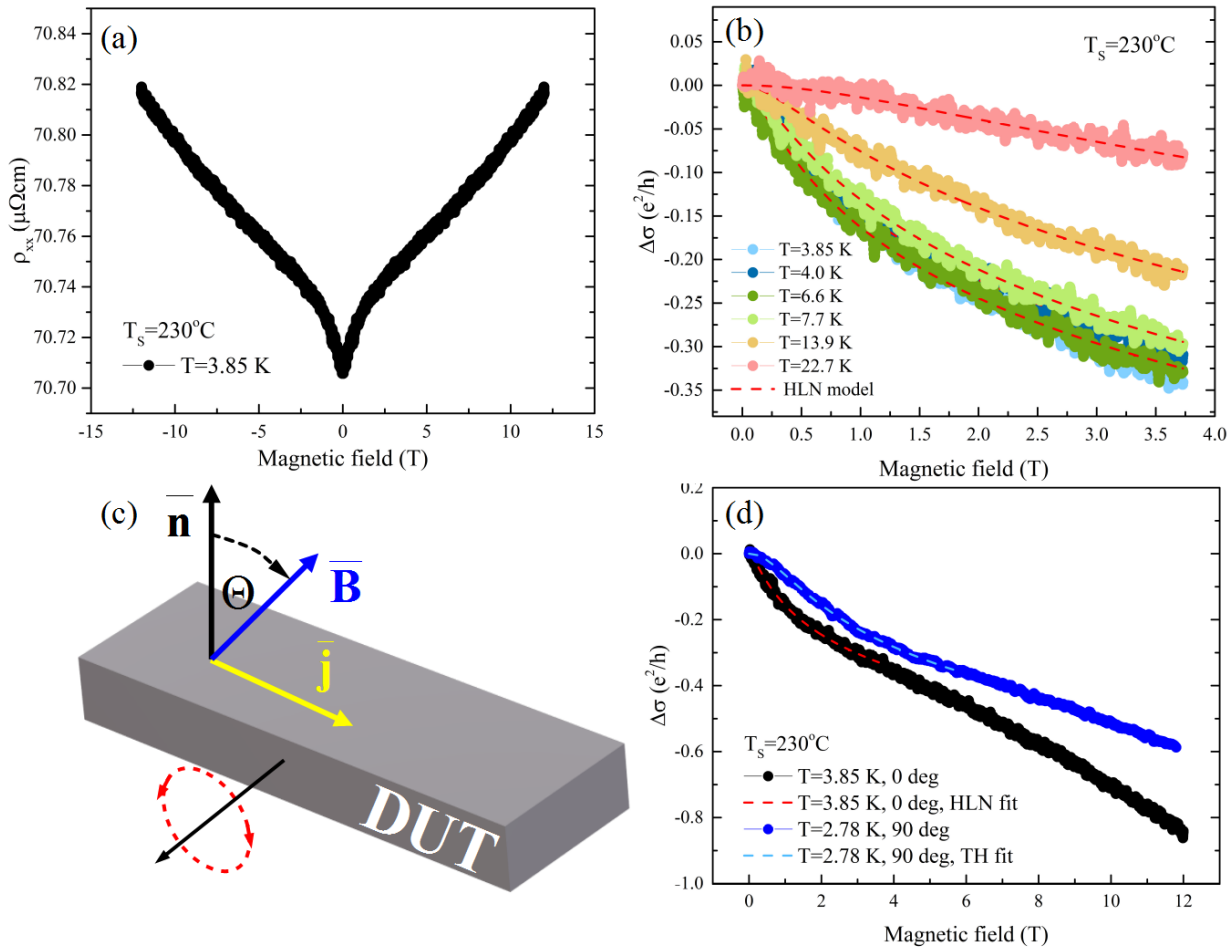

Figure 5.23: Electrical studies of $NiTe_2$. (a) The longitudinal resistivity at T=3.85 K as a function of the perpendicular magnetic field for a sample grown at T_S = 230 ^{o}C. (b) The temperature dependence of the magnetoconductance for the sample grown at T_S = 230 ^{o}C. (c) The scheme of the sample in the experiment with rotation of sample plane in magnetic field. The n, $\vec{B}$ and $\vec{j}$ axes define vector along c lattice parameter, magnetic field and current direction, respectively. (d) The magnetoconductance dependence in two magnetic field positions versus current direction.

Figure 5.23(a) shows small resistivity drop observed at close to B=0 T. The observed drop may be ascribed to the WAL effect, which is often seen in topological semimetals and may be a fingerprint of the Dirac fermions. Figure 5.23(b) shows the temperature dependence of the observed WAL effect in the form of magnetoconductance, expressed in conductance units. As expected, the WAL effect shows a strong temperature behavior and it vanishes above T=25 K. The amplitude of the WAL effect is relatively small, reaching 0.4 e^2/h at B=4 T. To describe the observed effect, the Hikami-Larkin-Nagaoka model has been applied to the data (see section 3.4), as presented by the red, dashed curves in Figure 5.23(b). In order to verify the dimensionality of the studied system and to evaluate if the WAL effect originates only from the TSSs, the Hall effect was measured in two configurations: with B in the plane of the layer and perpendicular. Figure 5.23(c) shows the experimental configuration. As presented in Figure 5.23(d), the WAL effect is observed in both in-plane and out-of-plane magnetic field configurations, revealing that the observed effect is rather 3D, originating not

only from the TSSs but also from bulk states. Figures 5.24(a)-(b) show the results of the 2D HLN fit: number of the conducting channels (N) and the phase coherence length (l_ϕ) as a function of temperature.

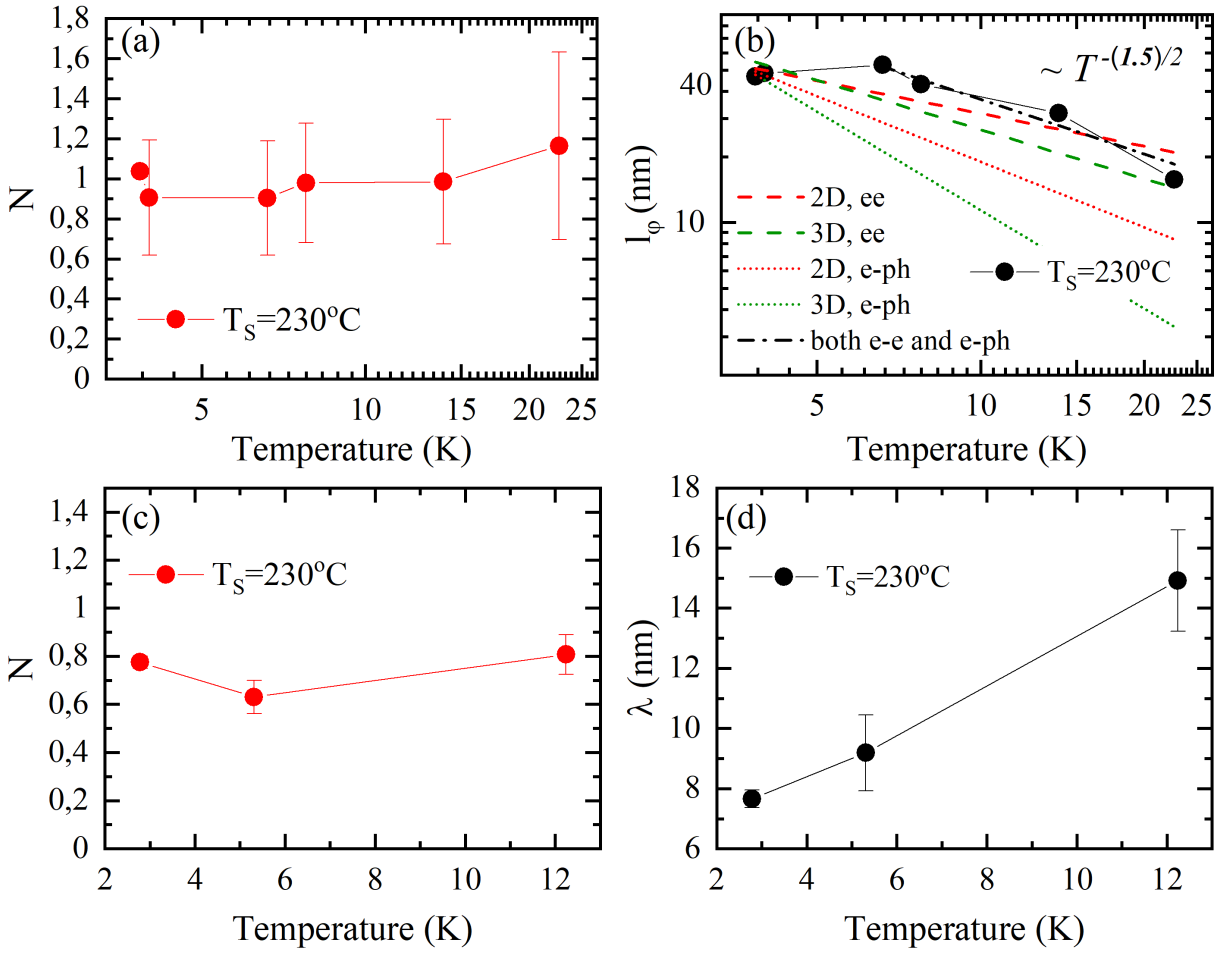

Figure 5.24: Electrical studies of $NiTe_2$. Temperature dependence of the (a) number (N) of the conducting channels and (b) the phase coherence length (l_ϕ), for the sample grown at T_S = 230 ^{o}C, obtained from the 2D Hikami-Larkin-Nagaoka model. The colored, dashed lines in (b) show the theoretical dependencies for 2D or 3D electron-electron or electron-phonon interactions [155, 156, 157]. Temperature dependence of the (c) number (N) of the conducting channels and the (d) decay length (λ) parameters, for the sample grown at T_S = 230 ^{o}C, obtained from the Tkachov-Hankiewicz model.

The number of the conducting channels is close to one. The phase coherence length is of order of a few tens of nm at low temperatures and it decreases to 10 nm at T=25 K. The green and red dashed and dotted curves show theoretical temperature dependencies of phase coherence length predicted for 3D and 2D electron-electron (e-e) and electron-phonon (e-ph) interactions, respectively [155, 156, 157]. The scattering due to e-ph interactions leads to a faster phase coherence length decrease than experimentally observed. In the case of $NiTe_2$ layers, the e-e interactions seem to be responsible for the scattering processes. However, the dependence of the phase coherence length is neither 2D nor 3D as presented by the dashed or dotted green curves, respectively. The most accurate fit corresponds to the theo-

retical description of the both e-e and e-ph interactions, as presented by the black, dashed line. The extracted temperature dependence of the phase coherence length gives $l_\phi \propto T^{-p/2}$ with $p = 1.5$, corresponding to $l_\phi \propto T^{-0.75}$. This is consistent with the Nyquist dephasing, suggesting that the electron transport exhibits a quasi-3D character rather than purely 2D behavior [158].

To describe the influence of the bulk states, the magnetoconductance data were modeled with the use of the Tkachov-Hankiewicz model. Figures 5.24(c)-(d) show the results of the number of the conducting channels (N) and the decay length of the wave function (λ) of topological surface states. Similarly to the results obtained from the Hikami-Larkin-Nagaoka model, the number of the conducting channels is close to one. On the other hand, the decay length of the wave function is of order of dozens of nm being of order of the thickness of the studied layer. It means that the TSSs of the opposite sides of the sample are not independent. Moreover, they overlap with the bulk states.

Quite different results were obtained for the sample, grown at $T_S = 180\ ^oC$. Figures 5.25(a)-(b) show the resistivity tensor results: the normalized longitudinal and transverse resistivities for various temperatures. Here MR is much larger, reaching almost 8% at liquid helium temperature at B=12 T. At low magnetic fields, the MR has a parabolic character which changes to linear at higher magnetic fields. We attribute it rather to the disordered structure of the studies layers than its topological properties.

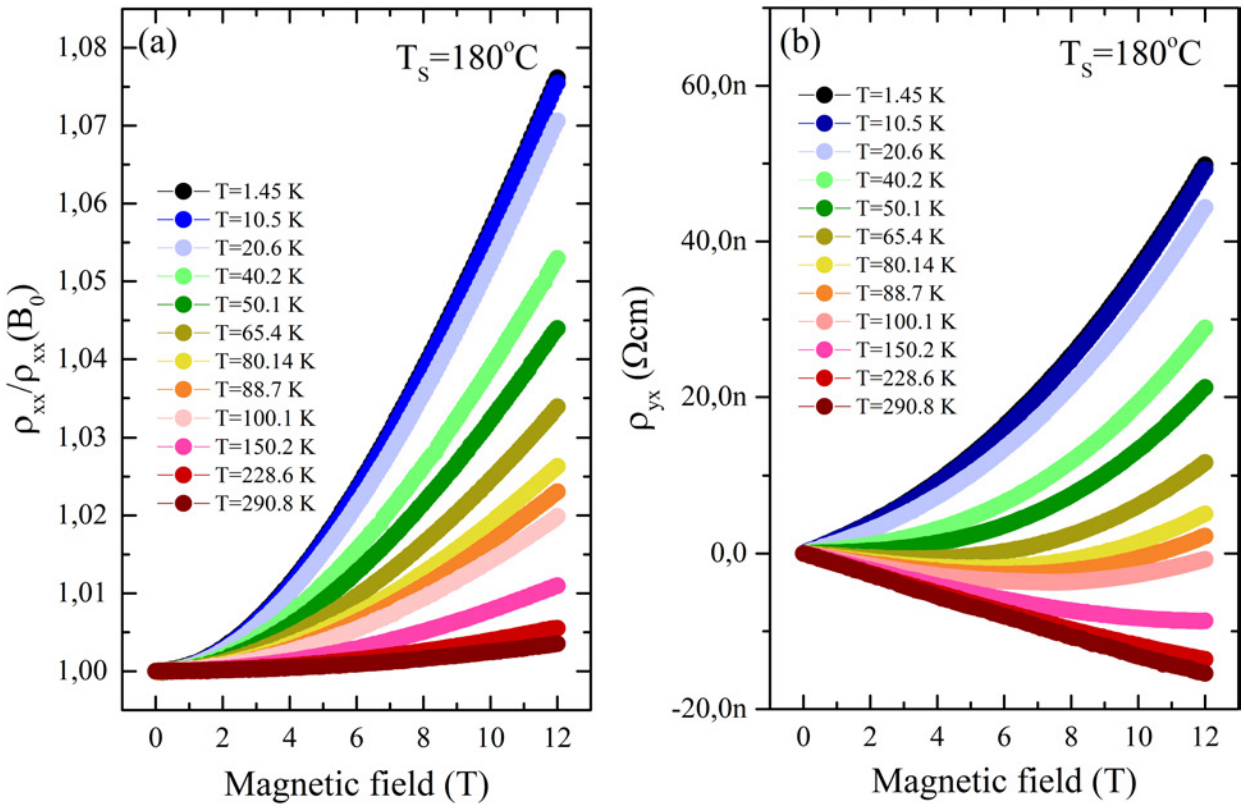

Figure 5.25: Electrical studies of $NiTe_2$. (a) Normalized longitudinal resistivity at various temperatures and (b) transverse resistivity at various temperatures for sample grown at $T_S = 180\ ^oC$ (UW1723).

The linear and negative room-temperature Hall resistivity changes to non-linear and positive when the temperature is decreased. The non-linear response may be interpreted in terms of multicarrier charge transport. Due to the much lower resistivity (compared to the sample grown at T_S = 230 ^{o}C), the conductivity of the studied layers is much higher. Figure 5.26 shows a normalized magnetoconductance in the small magnetic field range. Left and right axes present the same magnetoconductance data in the $sq./\Omega$ and e^2/h units, respectively, showing the amplitude of measured signal. The conductivity of the layers is high and it was not possible to observe small conductivity corrections related to WAL effect (compare with the Figure 5.23(b)).

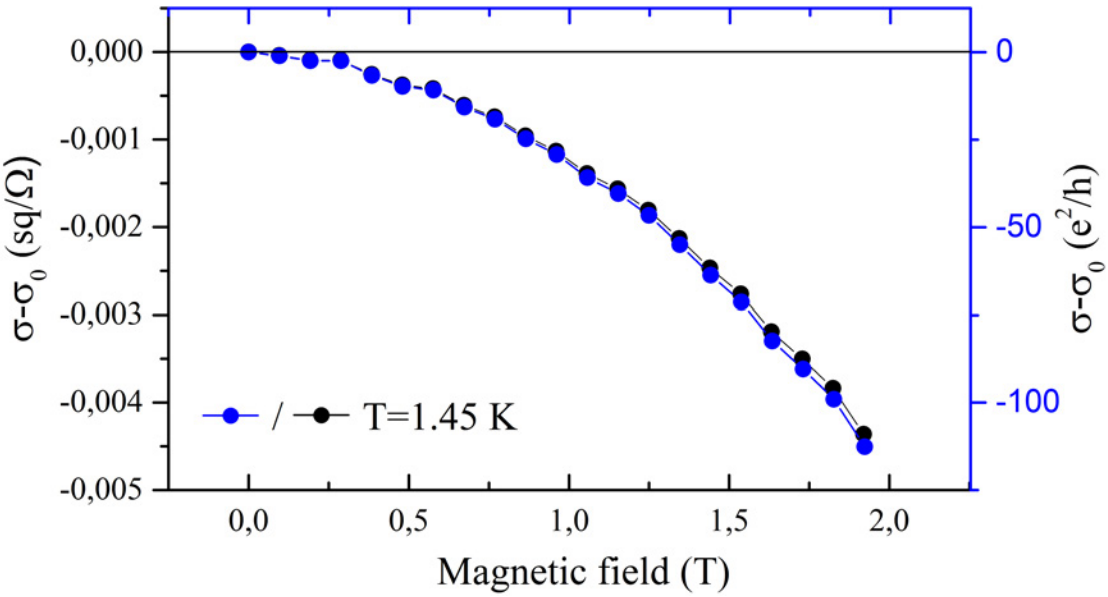

Figure 5.26: Electrical studies of $NiTe_2$ grown at T_S = 180 ^{o}C (UW1723). The magnetoconductance dependence on B at T=1.45 K. The black dotted line depicts the zero magnetoconductance value.

The longitudinal and transverse experimental data were modeled by 2-channel conductivity. The fitted curves are presented with the red dashed lines in Figures 5.27(a)-(b) with the corresponding experimental conductivity tensor.

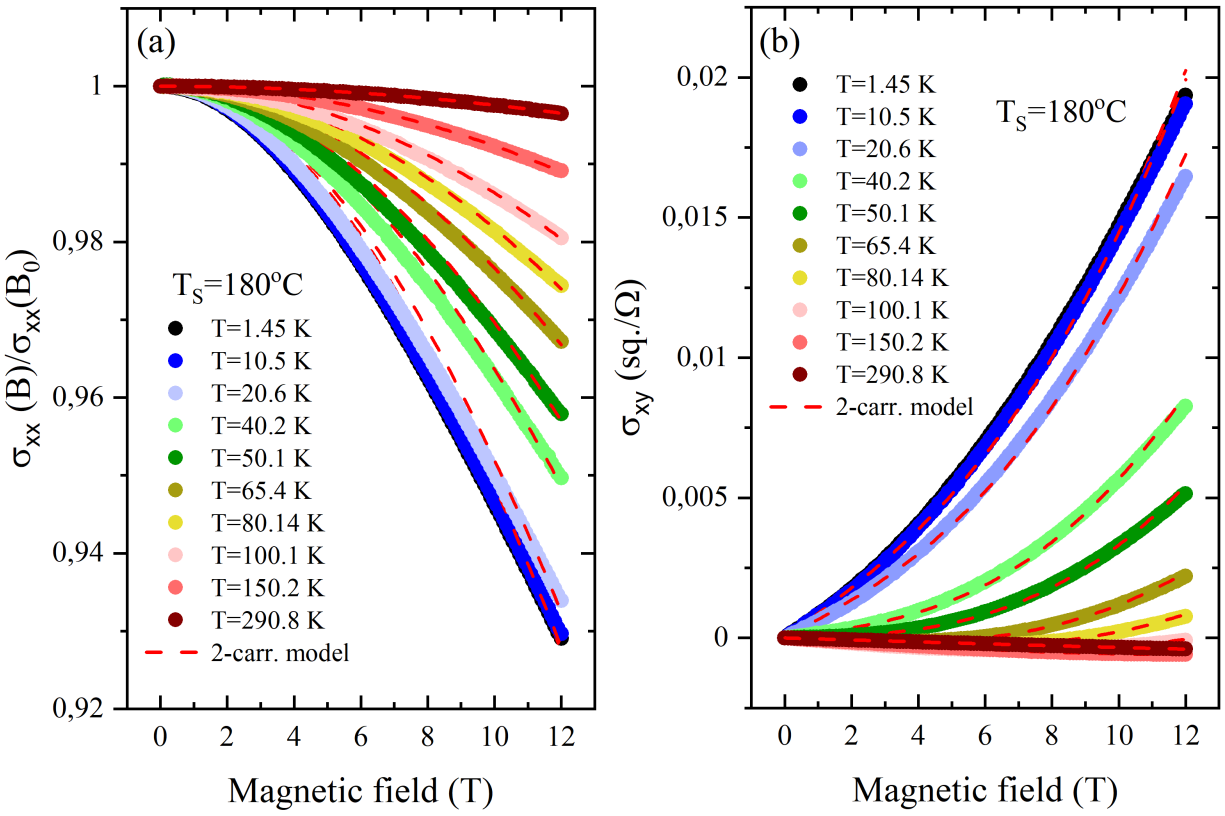

Figure 5.27: Electrical studies of $NiTe_2$. The (a) longitudinal and (b) transverse magnetoconductance dependence on magnetic field for various temperatures for the sample grown at T_S = 180 ^{o}C (UW1723). The red dashed curves show the 2-carrier model fits.

There is a relatively good matching of the fit and data. In 2-channel conductivity we used the following parameters of mobilities and concentrations: μ_1, n_1, μ_2, n_2. Figure 5.28 shows the parameters of the fits. The left axis of Figure 5.28 shows the mobility dependence on temperature for the two types of the carriers, marked with the red points. At low temperatures, mobility of electrons and holes reaches 200 $cm^2/V \cdot s$ and 280 $cm^2/V \cdot s$, respectively. They decrease starting from 20 K to around 50 $cm^2/V \cdot s$ at room temperature. Similar mobility results can be obtained using $\Delta R/R_0 \sim \mu^2 B^2$ estimation, where the μ and R_0 define the average mobility and the zero-magnetic field resistance, respectively. The average mobility, presented by the green points, is reaching almost 250 $cm^2/V \cdot s$ at low temperature, being between the mobility values of the electron and holes, obtained from the 2-channel conductivity. The right axis of Figure 5.28 shows the results of the temperature dependence of carrier concentration for the electrons and holes.

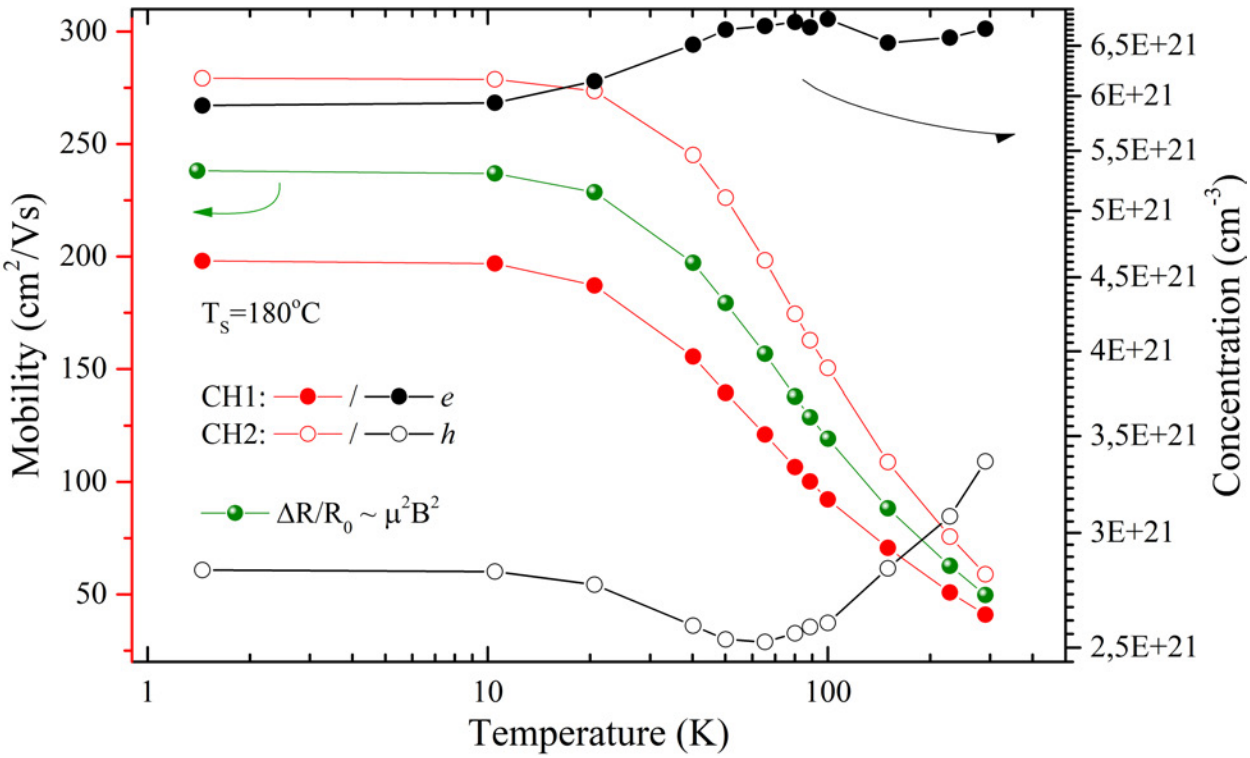

Figure 5.28: Electrical studies of $NiTe_2$. Mobility and carrier concentration of $NiTe_2$ layer grown at T_S = 180 ^{o}C, obtained from the 2-channel conductivity. The green dots correspond to the $NiTe_2$ mobility obtained from $\Delta R/R_0 \sim \mu^2 B^2$ estimation.

It seems that the charge transport in the sample is governed by the two types of carriers: electrons and holes, marked by the full and empty points, respectively. Both concentrations are similar, of order of several 10^{21} cm^{-3}, and similarly to the sample grown at T_S = 230 ^{o}C show only a tiny variation over the entire temperature range. The obtained results of the change of the sign of the Hall conductivity are similar to those by Cheng et al., [140] (see Figure 5.8) and can be explained in the context of the temperature-induced Liftshitz transition [145].

Following the approach of Chi et al. [64] an average temperature of transition T_p was found from the first derivative of ρ_{xx} over temperature as presented in Figure 5.29(a).

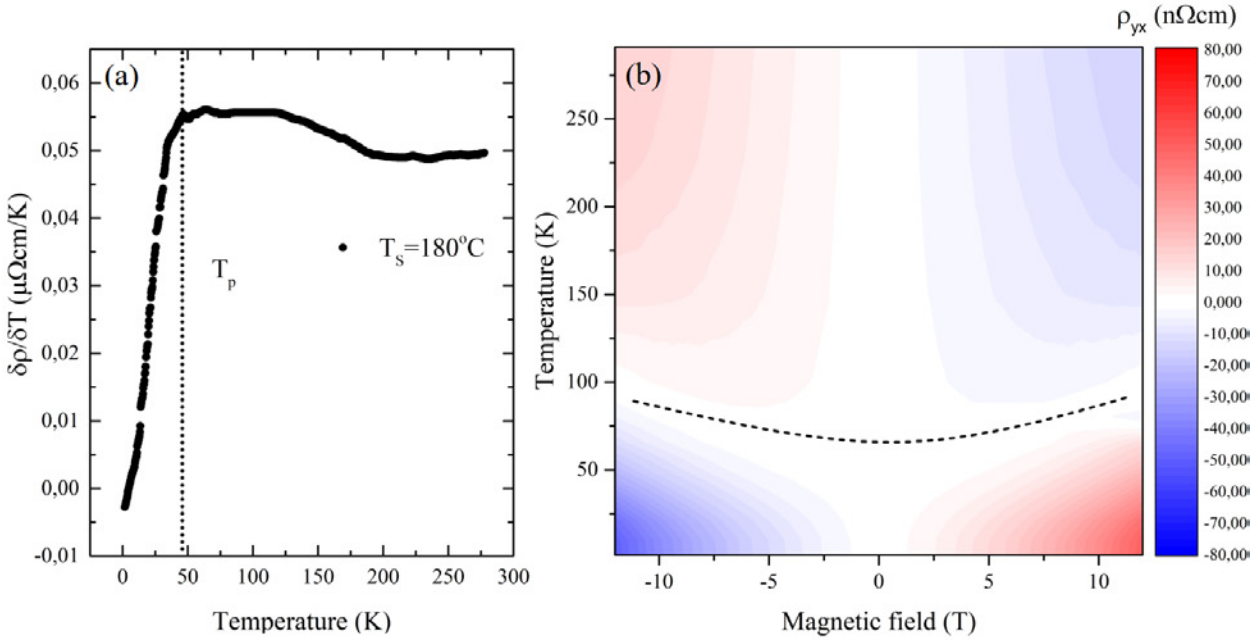

Figure 5.29: Electrical studies of $NiTe_2$. (a) The first derivative of the sample resistivity as a function of temperature where the gray shadow background depicts the temperature transition (T_p). (b) Hall resistivity as a function of magnetic field and temperature. Dashed black line shows the temperature range where the Hall resistivity changes sign.

One can notice a similar dependence of the $\frac{\delta\rho_{xx}}{\delta T}$ as observed in the literature data (see Figure ??(a)). The dotted black line shows the approximate temperature where the anomaly in the temperature-dependent resistance appears. The estimated T_p is in a good agreement with the temperature value for which the Hall resistivity slope changes sign. The temperature dependence of the transverse magnetoresistivity in the form of a map is presented in Figure 5.29(b). The change of the Hall resistivity slope is schematically marked by the black dashed line. The T_p appears to be slightly higher than for Cheng et al. data [140]. This may be due to the different value of carrier concentration in the studied sample. The difference between the T_p values fits the theorem proposed by Chi et al. [64], who has shown the relationship between T_p and the carrier concentrations in $ZrTe_5$ (see Figure ??(b)).

Figure 5.30 shows the mobility dependence on temperature for electrons and holes referred to the basic scattering mechanisms. The dashed gold and magenta lines show the theoretical mobility dependencies for the acoustic [159] and piezoelectric phonons [159], respectively. The best fit is obtained for both scattering mechanisms [160], following $\sim T^{-1}$ dependence. Although the $\sim T^{-1}$ dependence is frequently observed in the literature, it does not strictly comply with Matthiessen's rule, yet it often provides a reasonable approximation.

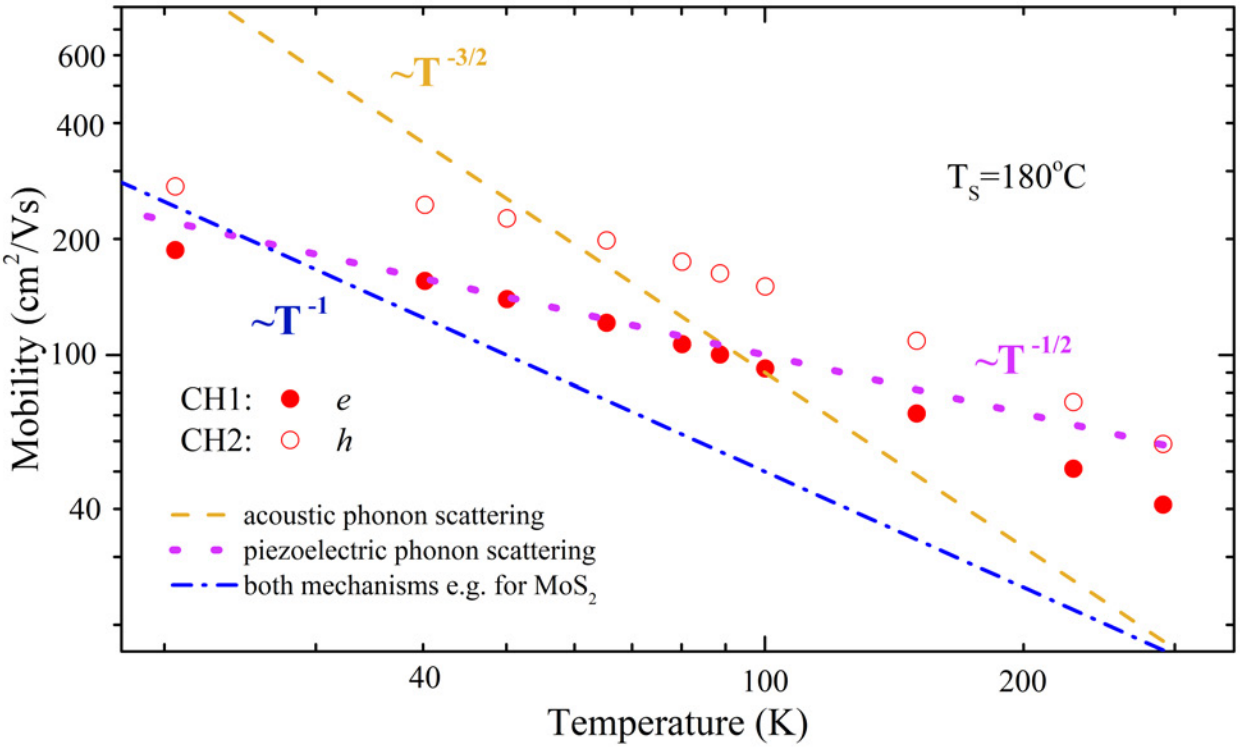

Figure 5.30: Electrical studies of $NiTe_2$. Temperature dependence of mobility of the $NiTe_2$ layer grown at T_S = 180 ^{o}C, referred to the basic scattering mechanisms [159, 160].

The longitudinal and transverse magnetoconductance can be also modeled with the use of the mobility spectrum analysis (MSA), which allows to obtain the spectrum of carrier mobilities in a conducting material. Figure 5.31(a) shows the conductivity density as a function of carrier mobility for liquid helium- and room-temperature conductivity tensors data, presented by the blue and red curves, respectively.

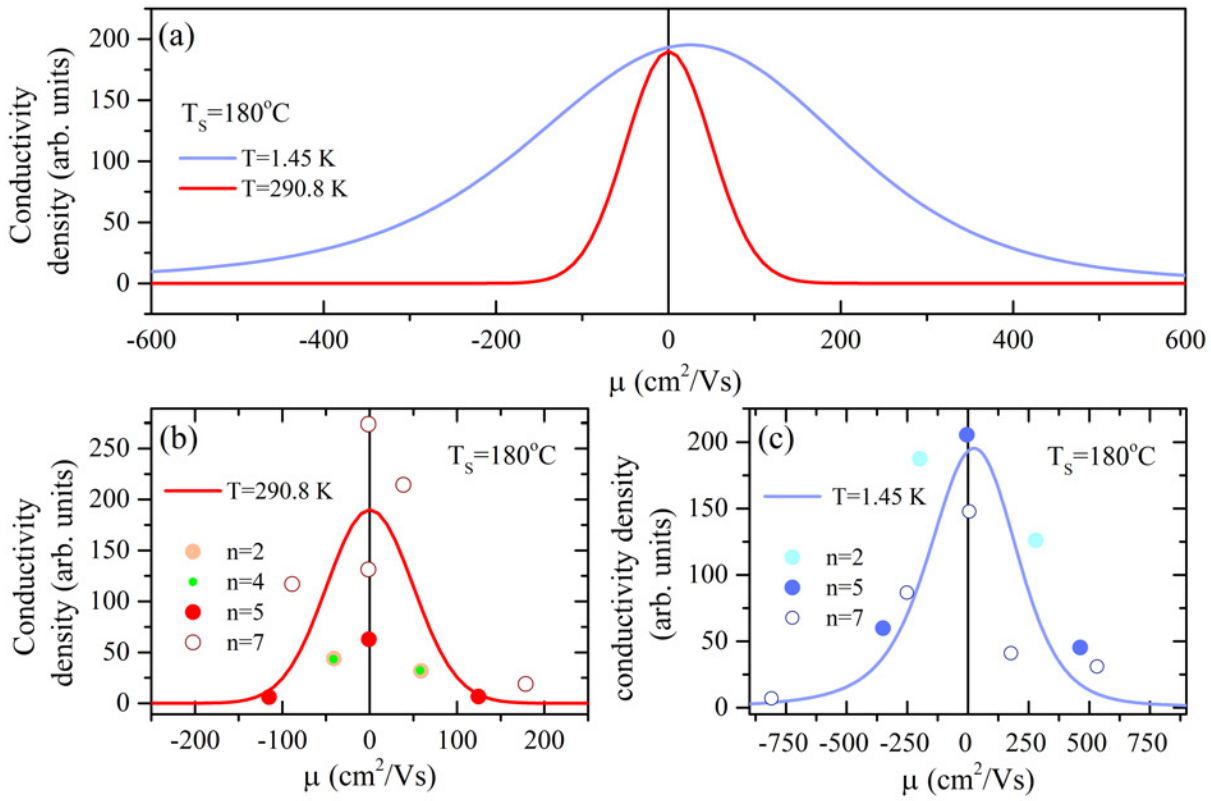

Figure 5.31: Electrical studies of $NiTe_2$. (a) Room- and liquid helium-temperature mobility spectrum analysis for the sample grown at T_S = 180 ^{o}C with the coherent multiband discrete (b) or continuous (c) pictures. The inset in (a) shows the zoomed conductivity density dependencies in the small mobility range. [The continuous mobility spectrum was calculated by Prof. M. Baj, Faculty of Physics, UW, descrete by the author of the thesis. Figure preparation: Z. Ogorzałek-Sory.]

Negative values of mobility correspond to electrons and positive values to holes. If the conductivity density takes a shape of the Dirac delta, symmetrical to zero mobility, it means that the longitudinal part of the conductivity is constant and there is no transverse signal. Here the conductivity density takes the shape of a broad peak, which reflects the presence of MR in the system, as presented in Figure 5.25(a). At liquid helium temperature, the conductivity density peak broadens meaning that the MR increases. Moreover a conductivity density shifts to positive values indicating that the hole carrier contribution is dominating. Although the MSA has been performed in a wide mobility range ($\sim \pm 15\ 000\ \mathrm{cm}^2/V \cdot s$) and with one and two millions of iterations for the room- and liquid helium-temperatures, respectively, the MSA did not reveal any additional high-mobility peaks for this sample. The obtained results are in a good agreement with the 2-channel conductivity model which gives similar values of the carrier mobilities and carrier concentrations for both electron and hole carriers. The continuous mobility spectra can be also estimated by larger number of discrete conductivity channels, as presented in Figures 5.31(b)-(c) for room- and liquid helium-temperature data, respectively. The mobility spectra are modeled with different numbers of carriers from n=2 to n=7. The modeled curves are zoomed to smaller values of the carrier mobilities and not

all the points are visible in the presented Figures. Independently of the number of discrete conductivity channels, all points are grouped around zero mobility and reflect the curves obtained from the mobility spectrum analysis.

The transport properties of $NiTe_2$ strongly depend on the substrate temperature (T_S), which affects the homogeneity of the sample, the resistivity behavior, the carrier concentration, and the mobility. Metallic behavior and higher residual resistivity ratios are observed for samples grown at lower T_S, while Te-deficient samples exhibit non-metallic behavior. Hall effect measurements confirm electron-type conduction with low mobility and nearly temperature-independent carrier concentration. A weak anti-localization effect is detected in some samples, indicating a 3D character and the interplay between surface and bulk states. For other samples, multicarrier transport with a temperature-induced Lifshitz transition is observed. The mobility spectrum analysis supports the two-channel transport model, with no evidence of high-mobility carriers.

5.2.7 Theoretical description of the influence of strain in $NiTe_2$

As has been shown by Ferreira [63] and by Nurmamat [135] the electronic properties of $NiTe_2$, strongly depend on the lattice parameters. To address the influence of strain in $NiTe_2$ we have invited to collaboration Pedro P. Ferreira (University of Sao Paulo and Institute of Theoretical and Computational Physics), Antonio L. R. Manesco (Kavli Institute of Nanoscience), Christoph Heil (Institute of Theoretical and Computational Physics) and Luiz T. F. Elen (University of Sao Paulo). Here preliminary theoretical results are presented, and the work is still in progress.

Figure 5.32 shows the map, where the intensity is the Dirac cone energy in respect to E_F as a function of in-plane and out-of-plane lattice parameters. As one can see, strain can efficiently shift the Dirac cone center towards the Fermi level.

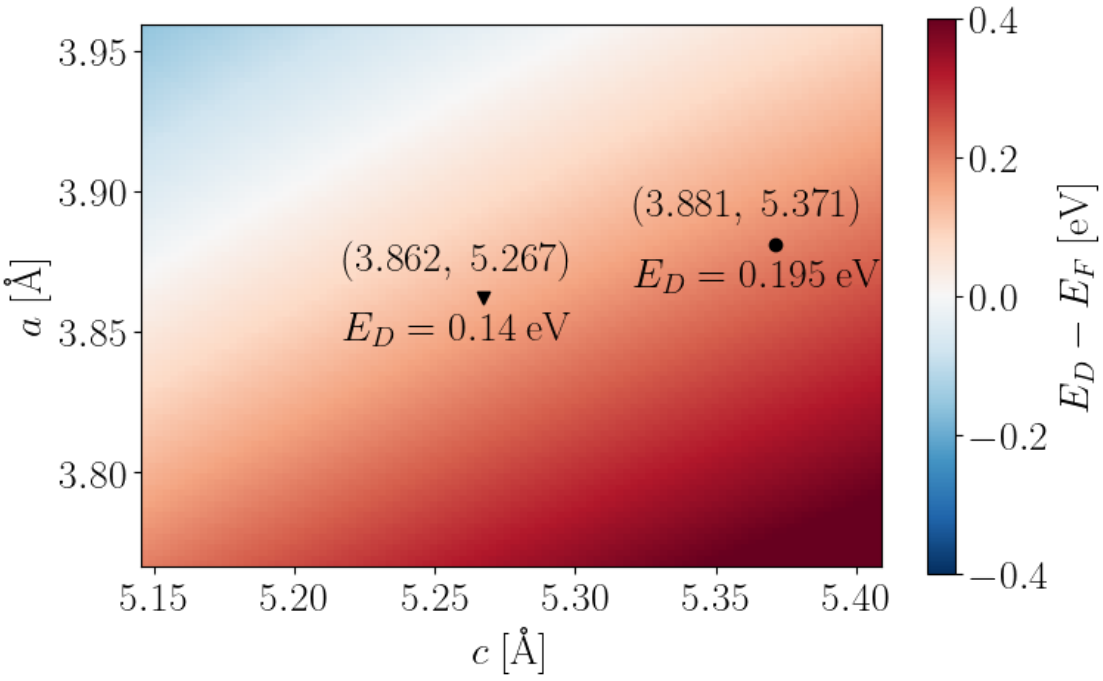

Figure 5.32: Dirac cone energy (E_D) in respect to the Fermi level for different $NiTe_2$ a and c lattice parameters, assuming intrinsic carrier concentration. Black triangle and square present the position of the E_D for samples grown at T_S = 180 ^{o}C and at T_S = 230 ^{o}C, respectively, based on their lattice parameters [161].

The positions of the E_D in respect to E_F of the two samples, grown at T_S = 180 ^{o}C and at T_S = 230 ^{o}C are shown by the black triangle and square, respectively. The position of the Dirac cones equal $E_D - E_F$ = 140 meV and $E_D - E_F$ = 195 meV for layers grown at T_S = 180 ^{o}C and at T_S = 230 ^{o}C, respectively. The results show that the E_D for both samples is far from the Fermi energy.

To obtain a picture of energy bands, which includes changes of the lattice parameters, Pedro P. Ferreira, Antonio L. R. Manesco, Christoph Heil and Luiz T. F. Elen performed electronic structure calculations using the Kohn-Sham scheme [162] within the framework of density functional theory [163]. Figure 5.33(a) shows bulk band diagram, calculated assuming two sets of lattice parameters, for samples grown at T_S = 230 ^{o}C and at T_S = 180 ^{o}C. They are marked by the blue and the red curves respectively.

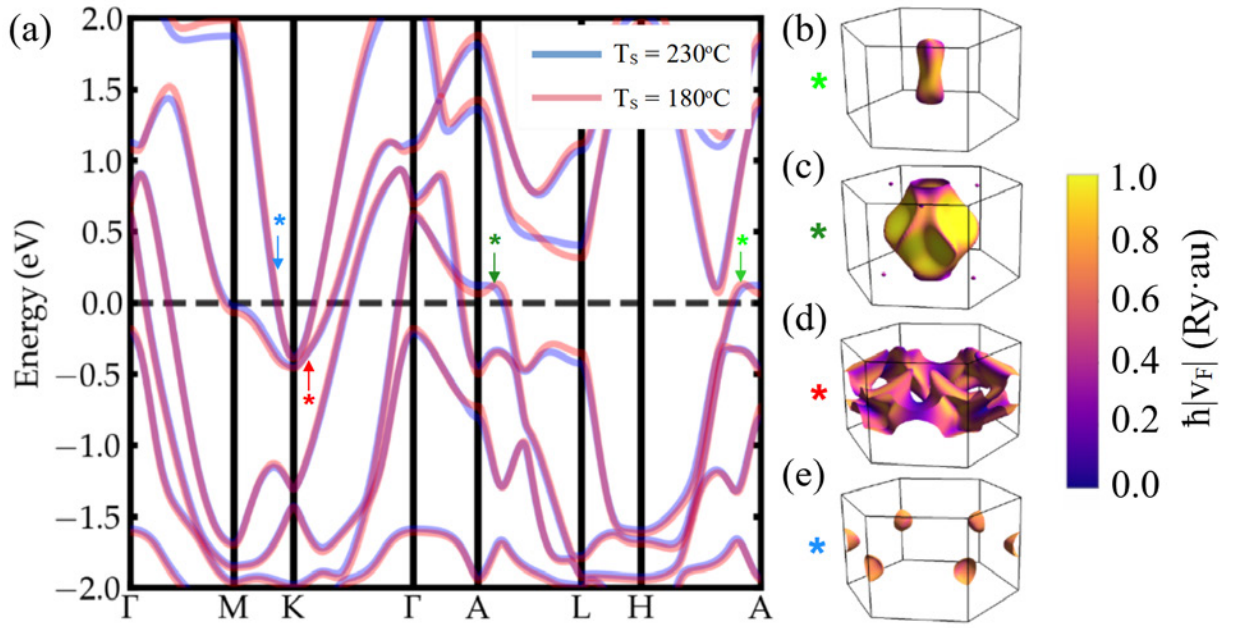

Figure 5.33: The bulk band diagram for the samples grown at T_S = 230 ^{o}C and at T_S = 180 ^{o}C, marked by the blue and the red curves respectively, with the SOC included. The blue, red and the dark and light green arrows show four independent and disconnected bands which cross the Fermi level. The zero energy defines the position of the E_F for the charge neutral cells. (b)-(e) Fermi surfaces of sample grown at T_S = 230 ^{o}C of four independent and disconnected bands which cross the Fermi level. The color map indicates the magnitude of the Fermi velocity [161].

Compared to the unstrained $NiTe_2$, the tensile-strained samples have similar electronic band structure with type-II bulk Dirac points. The energy of type-II bulk Dirac point slightly differs for the two samples studied. The Dirac cone is located between Γ and A points at E = 210 meV for the sample grown at T_S = 230 ^{o}C and at E = 135 meV for the sample grown at T_S = 180 ^{o}C. In the unstrained case, the Dirac cone is located at E = 150 meV. Surprisingly, although both samples are tensile-strained, E_D shifts either below or above the energy of the unstrained Dirac cone.

From the band structure one can see that there are four independent and disconnected bands which cross the Fermi level. There are two Te-p hole pockets at the zone center, marked by the dark and light green asterisks, and two hybridized Te-p and Ni-d electron pockets around the K high-symmetry point in Brillouin zone (BZ), marked by the blue and red asterisks. These numerous bands contribute to the overall sample conductivity. Moreover, it can be seen, that bands close to the Dirac point (with dark green astrisk) transform with strain and the hole and electron pockets form for the samples grown at T_S = 180 ^{o}C. This stays in a good correspondence to the results of multicarrier conductivity (or mobility spectrum analysis), where both electron and holes were identified. The 3D Fermi surfaces of the four independent and disconnected bands which cross the Fermi level are shown in Figures 5.33(b)-(e). Additional calculations of the phonon band structure are included in chapter B in section B.5 in Figure B.4.

Chapter 6

$MoTe_2$

6.1 State of knowledge

6.1.1 Crystal structure

Molybdenum ditelluride ($MoTe_2$) belongs to the family of transition metal dichalcogenides. It exists in several crystallographic phases: hexagonal 2H, monoclinic 1T′, octahedral 1T and orthorhombic T_d which emerges below T=260 K as a result of 1T′ to T_d transition. The schemes of the 2H (including $2H_c$ and $2H_a$ stacking sequences), 1T, 1T′ and T_d phases are presented in Figures 6.1(a)-(e).

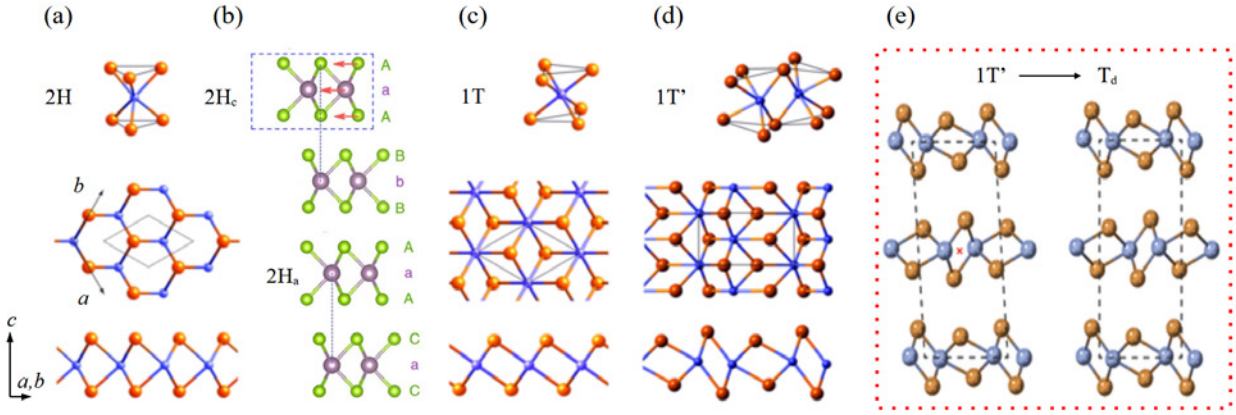

Figure 6.1: The 3D schemes of the (a) 2H, (b) $2H_c$ and $2H_a$ [164] (c) 1T and (d) 1T′ phases of $MoTe_2$. The middle and the lower panel show top and side views of the $MoTe_2$ structure, respectively [165]. (e) The symmetry difference and phase transition from 1T′− to T_d-MoTe_2 [166]. The blue (violet) and the orange (green) balls correspond to Mo and Te atoms, respectively. The light blue and dashed black lines depicts the unit cells of each phase. An inversion center in 1T′−phase is indicated by a red cross mark.

Among various TMDs, $MoTe_2$ holds a special place as its each phase exhibits different electrical properties, from semiconducting (2H) through metallic (1T) to topological type-II Weyl semi-metallic state for T_d phase. The 2H-$MoTe_2$ is an indirect band gap semiconductor with

the energy gap $E_g \sim 1$ eV for the bulk material [167]. It has the hexagonal crystal structure with a honeycomb in-plane atom arrangement (see Figure 6.1(a)) and it belongs to the space group $P6_3/mmc$ [168]. For the 2H phase, two stacking sequences are possible: $2H_a$ and $2H_c$. In contrast to the $2H_a$ phase, in the $2H_c$ structure each successive $MoTe_2$ layer is systematically shifted relative to the previous one [164]. The octahedral 1T-phase, presented in Figure 6.1(c), has metallic properties but it is not thermodynamically stable [169] and gives rise to monoclinic and also metallic 1T′-phase belonging to the space group of $P2_1/m$ [170] as shown in Figure 6.1(d). This phase undergoes another reversible phase transition to the orthorhombic T_d phase which belongs to the space group $Pmn2_1$ [170]. The 1T′ phase is monoclinic with the stacking angle of $\sim 93.9^o$ (instead of 90^o for T_d phase), whereas the T_d phase is orthorhombic (see red cross mark and the comparison of the back dashed lines depicting unit cells in Figure 6.1(e)). Due to the lack of the inversion symmetry T_d-phase exhibits topological properties [7]. The type of the crystal structure, type of the conduction and lattice parameters for various $MoTe_2$ phases are summarized in Table 6.1.

Table 6.1: The type of the crystal structure, type of the conduction and lattice parameters for three main stable $MoTe_2$ crystallographic phases.

$MoTe_2$ phase	Crystal structure	Type of conduction	a (Å)	b (Å)	c (Å)
2H [171]	hexagonal	semiconductor	3.52	3.52	13.966
1T′ [7]	monoclinic	metal	6.320	3.469	13.86
T_d [172]	orthorhombic	Weyl semimetal	6.340	3.501	14.15

The most interesting of the $MoTe_2$ phases is an orthorhombic T_d one. In 2015 $T_d - MoTe_2$ has been theoretically predicted [173, 174, 175] and in 2016 experimentally shown [176] to possess peculiar Fermi arcs states, which are topologically protected surface states, typical for Weyl semimetals. The physical properties of the $T_d - MoTe_2$ include many features, unique for topological semimetals. The exotic properties of charge carriers, which are chiral, helical and have a linear E(k) dependence lead to many novel physical phenomena such as giant magnetoresistance [177, 178], planar Hall effect [4, 179], chiral anomaly [180], quantized anomalous Hall effect [181] or negative magnetoresistance [182]. Due to strong spin-orbit coupling, $1T' - MoTe_2$ was used in hybrid heterostructures with e.g. permalloy ($Ni_{81}Fe_{19}$) to switch current-induced magnetization (at room temperature in the absence of an external magnetic field [183]). Owing to its numerous remarkable properties, it paves the way for novel applications in electronics [184], spintronics [185], optoelectronics [186, 187], sensing [34] and flexible electronics [188]. It should be noted that 1T′-phase is less stable than 2H under ambient conditions [189]. The ground-state energy differences between 1T′ and 2H monolayers is only 43 meV per unit cell [189] (which is considered small in the context of thermodynamic phase stability), and semiconducting 2H-phase is favored by means of thermodynamics. Its band gap can be tuned from direct to indirect depending on the thickness of the layer. 1 ML has the narrowest direct bandgap of $E_g \sim 1.1$ eV [190] among Mo- and W-based TMDs,

being a good candidate for the future near-infrared electronics and optoelectronic applications. Even though the electronic transport in the semiconducting phase is dominated by nonrelativistic carriers, still 2H-$MoTe_2$ exhibits interesting features, e.g. hidden in the bulk spin-polarized bands [191, 192] or highly tunable nonlinear Hall effect induced by the spin-orbit coupling [193]. Out of all TMDs, $MoTe_2$ has gained attention due to small free energy differences between its semiconducting and semi-metallic phases at room temperature [194] and between semi-metallic and topological phase at low temperatures [195, 196]. It opened a path to new potential applications in phase-change memory and low power electronics. Phase diversity of the $MoTe_2$ layers, combined with the molecular beam epitaxy growth bring a perspective of phase-engineering and heterostructures and hybrid structures growth for studying fundamental and novel physics.

6.1.2 Phase engineering

The studies of the $MoTe_2$ phases date back to 1970 were the first measurements on the bulk $MoTe_2$ had been performed. One of the earliest studies was conducted by M. B. Vellinga et. al. [197] who examined the homogeneity of $MoTe_x$, where x was changed from x=1.75 to x=2. They have found that $MoTe_2$ undergoes a phase transition at about 820-880 ^{o}C from the low-temperature semiconducting and diamagnetic 2H to the high-temperature metallic and paramagnetic 1T$'$. They also demonstrated that 1T$'$ can be stabilized at room temperature by quenching: rapidly cooling the sample from high temperature down to room temperature. Upon reheating, this metastable phase transforms back to the low-temperature semiconducting 2H at around 500 ^{o}C. In 1978, Clarcke et al., studied bulk $MoTe_2$ phase-transition at much lower temperatures [198]. They had performed a systematic XRD measurements in which they observed a temperature-driven change of the $MoTe_2$ reflections. Figure 6.2(a) presents (1 0 16) and ($\bar{1}$ 0 16) reflections during the heating and cooling cycles with a visible reflection splitting at around 250 K. A precise measurements of the c lattice parameters and the angle between c and a axes during $MoTe_2$ phase transition were performed.

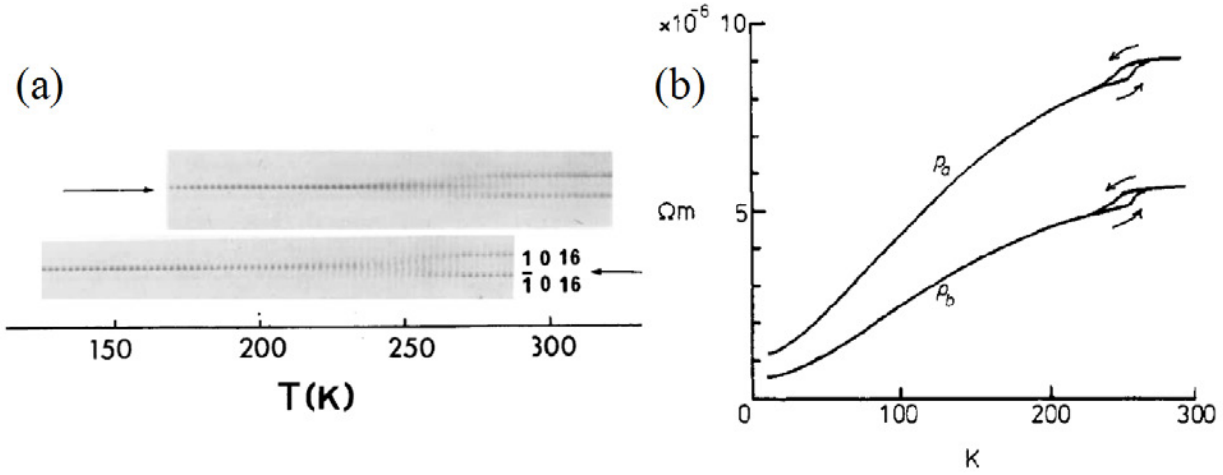

Figure 6.2: (a) The (1 0 16) and ($\bar{1}$ 0 16) reflections during the heating and cooling cycles [198]. (b) The temperature dependence of the two in-plane resistivity ρ_a and ρ_b components [199].

Clarke et al. described their discovery as a structural phase transition, and although unaware of topological aspect, they had observed for the first time a phase transition between 1T′ and T_d phases. Hughes et al., have also observed a temperature-driven $1T' - T_d$ phase transition, but in electrical measurements [199]. Figure 6.2(b) show the temperature dependence of the in-plane resistivity ρ_a and ρ_b components with a visible hysteresis around T=250 K. They also observed an in-plane anisotropy of the resistivity with the ρ_b being almost twice lower at room temperature than ρ_a. The discovered anisotropy originated from the formation of the zig-zag chains of Mo atoms along which the conduction took primarily place in bands formed from the Mo d-levels [199].

Recently, about 2016, research on the $MoTe_2$ layers has focused again on the 2H and 1T′ phases, looking for the possibilities to make heterostructures and hybrid structures. The phase transition in $MoTe_2$ layers from 2H to 1T′ has been achieved through several techniques, including electrostatic doping [200], strain engineering [201], CVD [36], CVT [202] or using a two temperature zone tube furnace [203]. Alternatively, it seems that laser irradiation is the fast and clean technique to obtain the phase transition in the $MoTe_2$ layers. Figure 6.3(a) shows the Raman spectra for a 9 nm-thick $MoTe_2$ flake before and after laser irradiation, marked by the black and red curves, respectively.

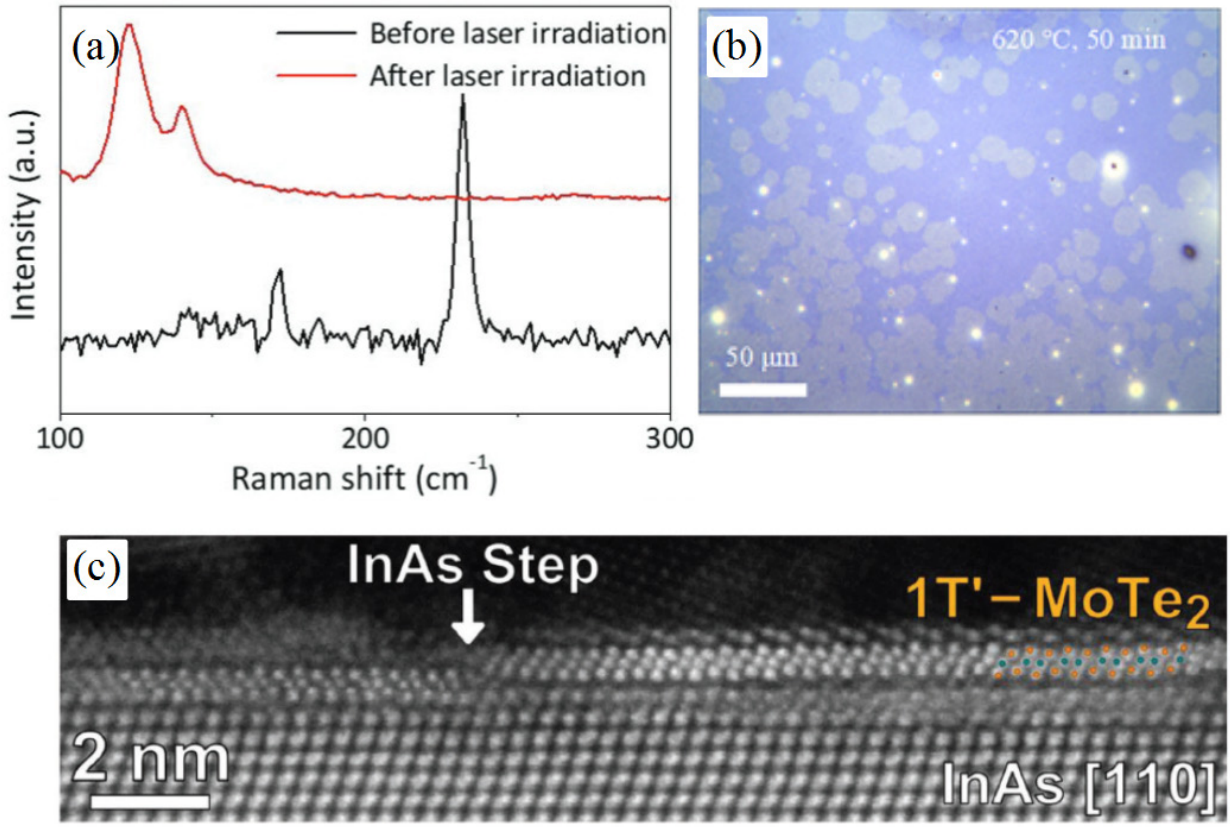

Figure 6.3: (a) The Raman spectra of the 9 nm-thick $MoTe_2$ flake on top of silicon substrate before (black curve) and after (red curve) laser irradiation revealing 2H and 1T′ phases, respectively [204]. (b) The optical image of the 1T′–2H $MoTe_2$ homojunction grown at T=620 ^oC on Si/SiO_2 substrate using a two temperature zone tube furnace [203]. (c) The TEM cross-section image of the MBE-grown 1T′ – $MoTe_2$ on InAs (111) substrate. [100] $MoTe_2$ is parallel to [11$\bar{2}$] InAs, and [010] $MoTe_2$ is parallel to [01$\bar{1}$] InAs [172].

By a proper adjustment of the laser power and irradiation time, Tan et al. [204] controlled the phase transition of $MoTe_2$ layers. Although the above techniques were fast, the obtained 1T′–2H $MoTe_2$ homojunctions were usually small with selective phase surfaces not exceeding tens of μm (see circular spots in Figure 6.3(b)). Recently, Tsipas et al. have carried out a successful MBE growth of the 1T′ – $MoTe_2$ on InAs (111) substrate [172]. Surprisingly, the orthorhombic T_d phase was observed at room-temperature. Stability of T_d phase was attributed to influence of strain coming from the substrate. Figure 6.3(c) shows the TEM cross-section image of the MBE-grown 1T′ – $MoTe_2$ on InAs (111) substrate [172]. The phase of $MoTe_2$ was proven by the STM and ARPES studies, however no magnetotransport measurements have been performed. Although the successful large-scale growth of the 1T′ – $MoTe_2$ on InAs (111) substrate opens huge perspectives in $MoTe_2$ phase engineering, the conducting InAs substrate introduces parallel conducting channel which much impedes $MoTe_2$ signal separation. Moreover, InAs shows high carriers mobility and strong SOC interactions therefore separation of effects (such as WAL, NMR or the Shubnikov-de Haas oscillations which are also expected for Weyl semimetals [205]) coming from $MoTe_2$ layer is

challenging, if not impossible.

6.1.3 Bulk and surface Weyl fermions in 1T′ – /T_d phase

Figure 6.4(a) shows the scheme of the 3D bulk and (001) surface Brillouin zones of the T_d – $MoTe_2$. There are four pairs of Weyl points W1 and W2.

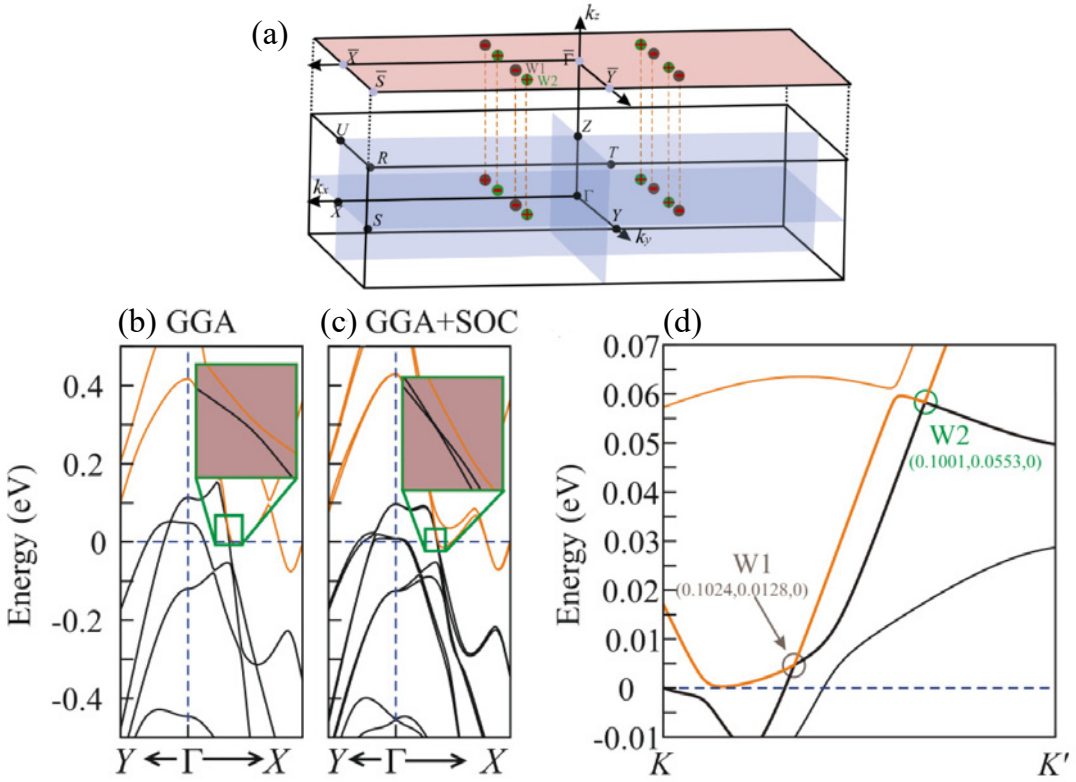

Figure 6.4: (a) The scheme of bulk and (001) surface Brillouin zones of the T_d – $MoTe_2$ with four pairs of the Weyl points W1 and W2. Band structure of the T_d–$MoTe_2$ along $\Gamma \rightarrow Y$ and $\Gamma \rightarrow X$ high symmetry points (b) without and (c) with SOC effects. (d) The band structure of the T_d – $MoTe_2$ along $K \rightarrow K'$ (aside from the high symmetry $\Gamma \rightarrow X$ line), showing W1 and W2 points in the k_x, k_y plane [173].

The topological properties of T_d phase are mainly associated with SOC effects which give rise to the linear band crossings in the $MoTe_2$ band structure (compare Figure 6.4(b) and Figure 6.4(c)). Band structure of the T_d – $MoTe_2$ along $K \rightarrow K'$ reveals W1 and W2 points in the (k_x, k_y) plane [173] which form significantly tilted Weyl cones as presented in Figure 6.4(d). This type of tilted linear crossing is characteristic for type-II Weyl semimetal. The results of the first experimental observation of the hole and electron pockets in $MoTe_2$ band structure, as well as the Fermi arcs, are presented in Appendix C in section C.1.

6.1.4 Electric properties of 1T′ and T_d phases

The 1T′ to T_d phase transition of $MoTe_2$ can be observed by resistivity measurements. Figure 6.5(a) shows resistivity as a function of temperature for the 1T′-phase while cooling and warming, presented by the black and red curves, respectively.

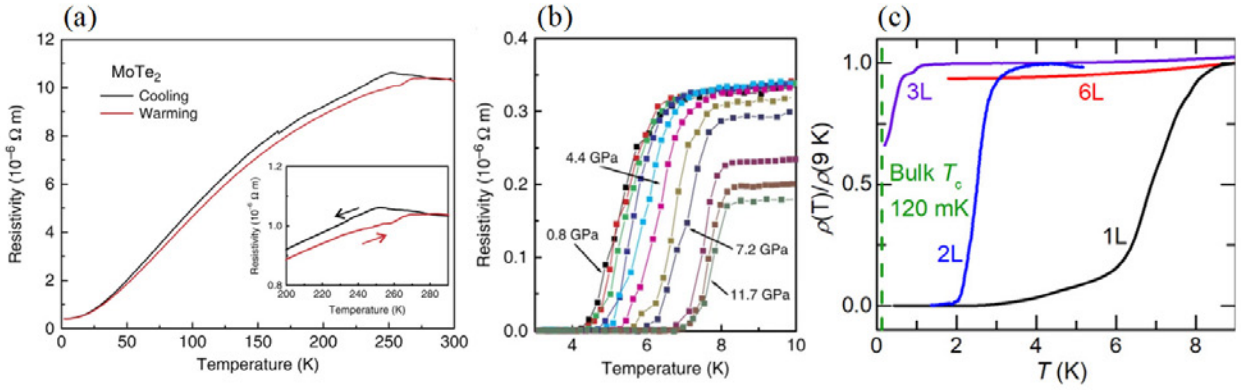

Figure 6.5: (a) The resistivity as a function of temperature for 1T′−$MoTe_2$. Inset: the zoomed region of resistivity hysteresis close to T=250 K showing temperature-driven phase transition between 1T′ and T_d phases. (b) The low-temperature resistivity as a function of temperature for $T_d - MoTe_2$ for pressures of 0.7-11.7 GPa [7]. (c) The normalized resistivity as a function of temperature for bulk, 6, 3, 2 and 1 layers of $T_d - MoTe_2$ [206].

One can see that below T∼ 260 K a large hysteresis occurs (see data magnification shown in the inset in Figure 6.5(a)) which is the main evidence of the phase transition. Below T∼ 260 K 1T′−metallic phase changes to T_d−Weyl semimetallic one. Similar (and better) results have been obtained in the 80' (see Figure 6.2(b)). Moreover, $T_d - MoTe_2$ was observed to show pressure- and thickness-dependent superconductivity. Figures 6.5(b)-(c) show longitudinal resistivity as a function of temperature for various pressures and sample thickness, respectively. With increasing pressure the T_C shifts to higher temperatures, whereas the increase the thickness of the layers leads to T_C decrease. The observed temperature hysteresis, along with the strong thickness-dependent and pressure-driven enhancement of T_C, are indicative of $T_d - MoTe_2$ topological character.

6.1.5 The stability of the TMDs including $MoTe_2$ layers

The problem of the stability of the molybdenum- or hafnium-based TMDs has been spotted shortly after the "rediscovery" of $MoTe_2$ [207, 208], becoming a substantial challenge to overcome. The well-known sensitivity of transition metal dichalcogenides to atmospheric conditions [209, 210] opens up opportunities for sensing applications [211, 212, 213]. However, this potential is often limited by unintentional doping from ambient oxygen [214], which frequently leads to sample degradation or irreversible changes.

The degradation of $MoTe_2$ caused by oxygen exposure has been investigated using various experimental techniques and evidenced by Raman scattering [215], transmission electron or

atomic force microscopy studies [207], X-ray photoelectron spectroscopy [216, 211, 213] and photoluminescence methods [217]. Figure 6.6(a) presents an example of the surface roughness evolution for the molybdenum-based TMDs [207] kept in air at atmospheric pressure.

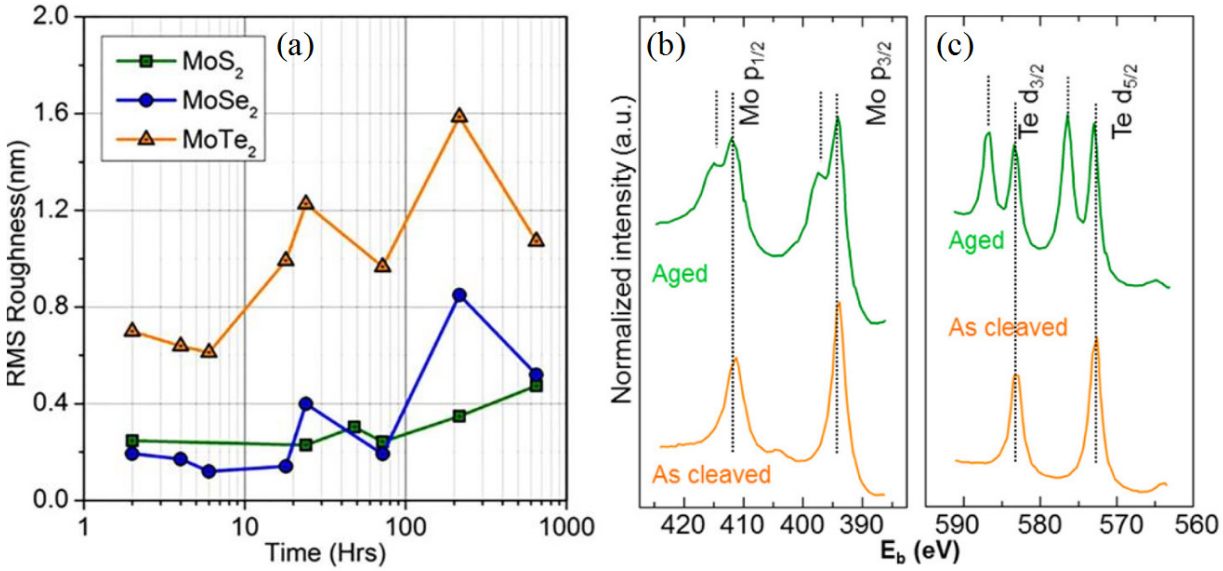

Figure 6.6: (a) The surface roughness trends for the molybdenum-based TMDs [207]. The normalized X-ray photoelectron spectroscopy spectra for as cleaved bulk crystals (orange curves) and kept in air for a week (green curves) around (b) Mo 3p and (c) Te 3d peaks [217]. $MoTe_2$ flakes were exfoliated from 2H bulk crystals.

For all the TMDs, surface roughness has increased even by 100%. Some variation is observed in the RMS data, which may be attributed to several factors, such as misalignment caused by AFM tip replacement or the disappearance of loosely bound surface features. Despite this "noise," the overall trends remain reliable, showing a general increase in surface roughness over time. Similar observations of $MoTe_2$ degradation have been made by Chen et al. [217], who measured the X-ray photoelectron spectroscopy surfaces spectra for the as-cleaved and aged $MoTe_2$, presented in Figures 6.6(b)-(c). For the as-cleaved layer, narrow and single binding energies (E_b) peaks, described by (b) Mo 3p and (c) Te 3d states, are visible, shown by the orange curves. For the aged sample, marked by the green curves, new lines appear at E_b=415 eV, E_b=398.5 eV, E_b=587.2 eV and E_b=576.6 eV. These four new states correspond to oxidized forms of Mo and Te atoms, revealing the formation of MoO_3 and TeO_2 compounds. The X-ray photoelectron spectroscopy data showed that the oxygen atoms interact at the Te-defect sites, forming Mo–O and Te–O bonds [217].

The structural instability and the surface decomposition was also observed by the STM and Raman studies [218, 216]. Figure 6.7(a) presents the Raman spectrum of the E^1_{2g} peak intensity for a few monolayers of 2H-$MoTe_2$ flakes [216].

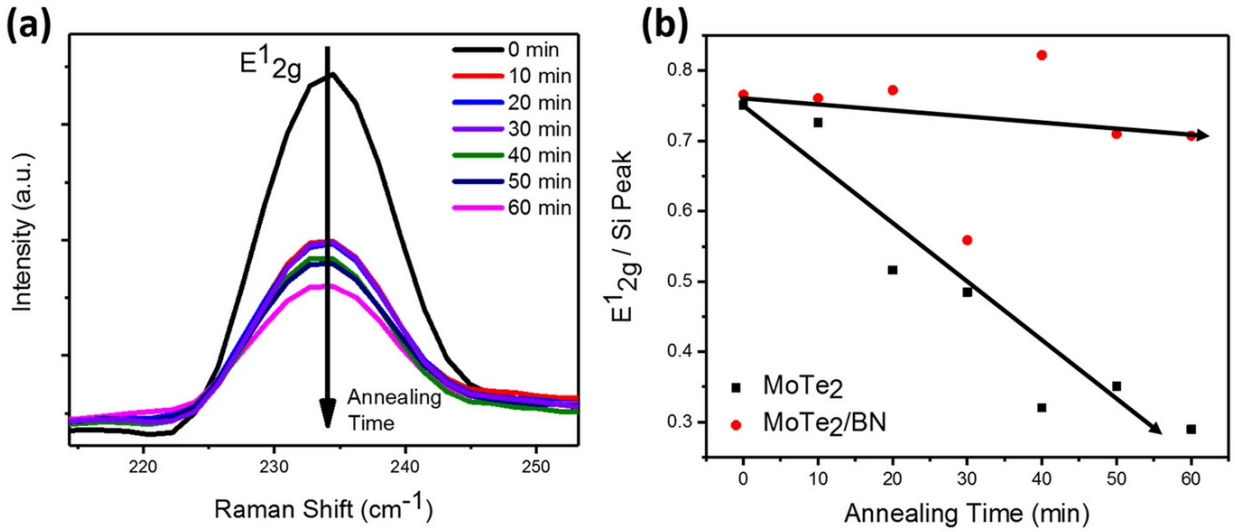

Figure 6.7: (a) The E^1_{2g} Raman peak intensity for a few monolayers of 2H-$MoTe_2$ at T=100 ^{o}C in air for subsequent time intervals. (b) The relative intensity of the E^1_{2g} peak as a function of annealing time for pristine 2H-$MoTe_2$ (black squares) and $MoTe_2$ capped with BN capping layer (red squares) [216].

$MoTe_2$ flakes were kept at T=100 ^{o}C in air. Along with the annealing time, the intensity of the E^1_{2g} Raman mode exhibited a continuous decline with the major drop in the first 10 minutes, proving a very fast degradation of $MoTe_2$ layers and its surface oxidation. To prevent $MoTe_2$ from this degradation Sirota et al. have proposed BN capping [216]. Figure 6.7(b) shows that the capped $MoTe_2$ layers exhibit a much lower rate of the E^1_{2g} Raman mode decay. The question of the stability is especially significant for the ultra-thin, few monolayer thick samples. In the last few years, several attempts were made to enhance TMDs' stability. Among others, the polymethyl methacrylate (PMMA) coverage [209], the Al_2O_3 or AlO_x passivation [219, 220] or an amorphous-BN encapsulation [216, 213] were reported. The proposed methods are used only for the individual, exfoliated flakes and were performed in glovebox. None of these methods has given a reproducible and large-scale surface protection until now.

6.1.6 The influence of the substrate on $MoTe_2$ nucleation

Several attempts have been made to grow $MoTe_2$ by MBE, yet the influence of the substrate on its nucleation and growth remains under debate [39]. For example, Fraser et al., have shown that when Mo is used as a seed layer, semiconducting 2H-phase is the only product, whereas MoO_3 leads to preferential growth of metallic 1T′ – $MoTe_2$ [221]. In turn, Hynek et al. have examined two different substrates: sapphire Al_2O_3 (0001) and amorphous SiO_2. They have shown that the chemical composition of the substrate is more important than the surface topography and crystallinity, with high quality 2H-$MoTe_2$ films formed on Al_2O_3 (0001) in contrast to mixed phase 2H/1T′ – $MoTe_2$ formed on SiO_2 [39]. The procedure

proposed by Hynek et al. included tellurization of MoO_x, deposited on substrates by atomic layer deposition (ALD) technique. However, the process of ALD is time-consuming which is known to be its major limitation. In particular, over 130 ALD cycles allowed to obtain only 7 to 8 layers of $MoTe_2$. Besides, the obtained films yielded only 40% of surface coverage, they were non continuous and not appriopriate for macroscopic transport studies.

The influence of the substrate and the effusion cells parameters on $MoTe_2$ nucleation have not been documented in such detail yet. At the beginning of this thesis, the process of targeted phase growth of MoTe2 films on different substrates in MBE had not yet been established, nor were the electronic properties of MBE-grown MoTe2 thin films known. With this in mind, the nucleation of $MoTe_2$ by changing the temperature of the substrate (T_s), temperature of the tellurium effusion cell (T_{Te}) or annealing impact were examined.

6.2 Experimental results

To achieve a relatively small in-plane lattice mismatch between the layer and the substrate and maintain crystal symmetry between hexagonal $MoTe_2$ and the substrate, crucial for energy gap and phase engineering, various substrates have been employed for MBE growth. $MoTe_2$ layers have been grown on: cubic, hexagonal or trigonal substrates with different lattice parameters such as SI GaAs (001), SI GaAs (111)B, sapphire (0001), ZnTe and InAs (111). Growth conditions were varied with the following parameters: substrate temperature (T_S), tellurium effusion cell temperature (T_{Te}), and annealing temperature (T_A). During the PhD studies, the $MoTe_2$ samples of the following numbers have been investigated experimentally: UW0885, UW0996, UW0997, UW0998, UW1004, UW1009, UW1080, UW1087, UW1090, UW1112, UW1170, UW1173, UW1175, UW1176, UW1178, UW1180, UW1182, UW1187, UW1189, UW1193, UW1316, UW1317, UW1337, UW1341, UW1420, UW1423, UW1428, UW1431, UW1432, UW1433, UW1439, UW1440, UW1441, UW1540, UW1541a, UW1541b, UW1542s, UW1542b, UW1547, UW1548, UW1551, UW1560, UW1791, UW1792, UW1793, UW1797, UW1798, UW1799, V168, UW1800, UW1801, UW1802. Some of the layers were grown by Dr Bartłomiej Seredyński and contributed to his PhD thesis on epitaxy, some were obtained by Dr Janusz Sadowski and Dr Wojciech Pacuski. In this PhD dissertation the main results of the selected $MoTe_2$ samples have been presented.

6.2.1 Growth parameters and $MoTe_x$ characterization

Figures 6.8(a)-(g) show scanning transmission electron microscope (STEM) images of the cross section of $MoTe_2$ samples grown at two different T_S, on sapphire or on GaAs (111)B substrates.

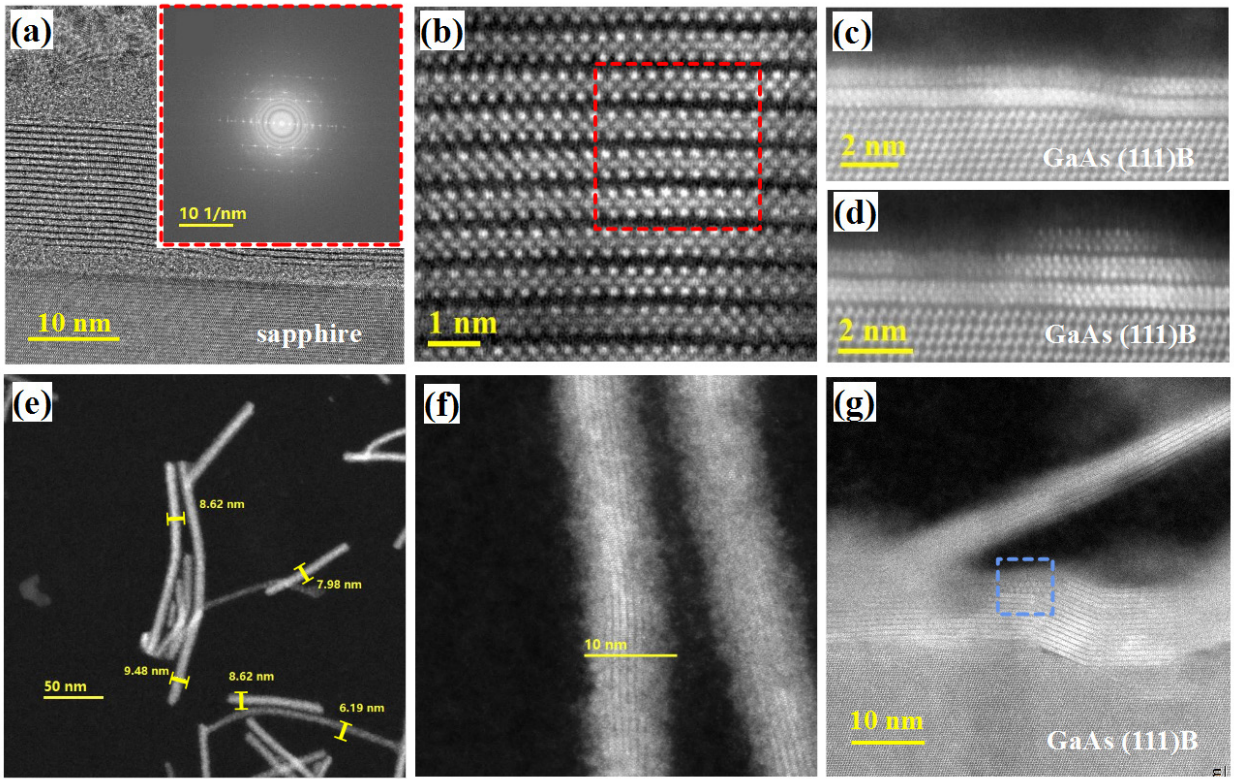

Figure 6.8: Structural characterization of $MoTe_x$. The scanning transmission electron microscope images of the $MoTe_x$ layers, grown at T_S = 270 ^{o}C (UW0997, UW1420, (a)-(d)) and and at T_S = 350 ^{o}C (UW1004, UW1178, (e)-(f)) on ((a)-(b), (e)-(f)) sapphire and ((c)-(d), (g) GaAs (111)B substrates. The nominal thicknesses of $MoTe_2$ layers grown on sapphire were 20 MLs and 2 MLs (UW1420) and 100 MLs (UW1178) on GaAs (111)B substrate. Inset of (a): the FFT of (b) the STEM image of 20 MLs of $MoTe_2$ evidencing six-fold symmetry. 2 MLs of $MoTe_2$ (c) covering atomic step of the GaAs (111)B substrate and (d) starting formation of the third layer. The NWs (e)-(f) not annealed and (g) annealed after the growth. The Mo_6Te_6 crystal is marked by the blue, dashed box. [TEM images were taken by Dr. S. Kret and Dr. A. Kaleta, Institute of Physics, PAS. Data analysis and Figure preparation: Z. Ogorzałek-Sory.]

Figures 6.8(a)-(b) present the pictures of the 20 MLs of $MoTe_2$ grown at T_S = 270 ^{o}C on sapphire substrate. The layers show a perfect arrangement in $2H_c$-phase (see Figure 6.1(b)). There is no clear interface between the layer and the substrate (the epitaxial growth is proceeded by 3 nm rough interface). The $MoTe_2$ layers are continuous, however the length of the unperturbed layer reaches only 10 nm. Also, certain mosaicity and grain boundaries are occasionally observed (see Figures 8.2(a)-(b) in Chapter 8). The inset in Figure 6.8(a) presents a fast Fourier transform analysis of the image captured in Figure 6.8(b), as marked by the red, dashed box, which reveals six-fold symmetry spots, arising from the hexagonal planes and perfect crystal structure. Figures 6.8(c)-(d) show TEM images of 2 MLs, grown at T_S = 270 ^{o}C, revealing the high quality of the studied layers and their continuity across substrate atomic step. In Figure 6.8(d) a nucleation of the third layer can be seen.

The growth at a higher substrate temperature (T_S = 350 ^{o}C) resulted in different processes of the layer nucleation. The 2D, layer-by-layer growth was disturbed and the samples

grew in a 3D growth mode. As evidenced by TEM, tangled nanowires (NWs) were grown in this case. Figures 6.8(e)-(g) show STEM images of the single NWs grown on (e)-(f) sapphire and (g) SI GaAs (111)B substrates with the nominal thicknesses of the $MoTe_x$ of 20 MLs and 100 MLs, respectively. Each nanowire exhibits a well-defined layer-by-layer atomic structure. Typically, NWs are 10-20 nm wide and up to 1 μm long. In Figure 6.8(g), one can see that the initial $MoTe_2$ layers grow in the Frank-van der Merwe mode. It is disturbed by atomic step or other surface inhomogeneity which probably induces the NWs formation. Surprisingly, in all NWs new features appear, marked with the dashed blue box in Figure 6.8(g). They are identified as the Mo_6Te_6 state and form 1D NWs [218, 222, 223, 224, 225]. Similar nanowire structures were previously observed in MBE-grown samples [224] and in CVD-grown films on Si_3N_4 [225] and Si/SiO_2 substrates [226]. Figures 6.9(a)-(b) show the schemes of the (a) Mo_6Te_6 structure and the fragment of the (b) Mo_6Te_6 NW, where the blue and orange balls represent Mo and Te atoms, respectively. This phase reveals different stoichiometry as ratio between Mo and Te atoms is one. This shows that the surface was Te-deficient during the growth.

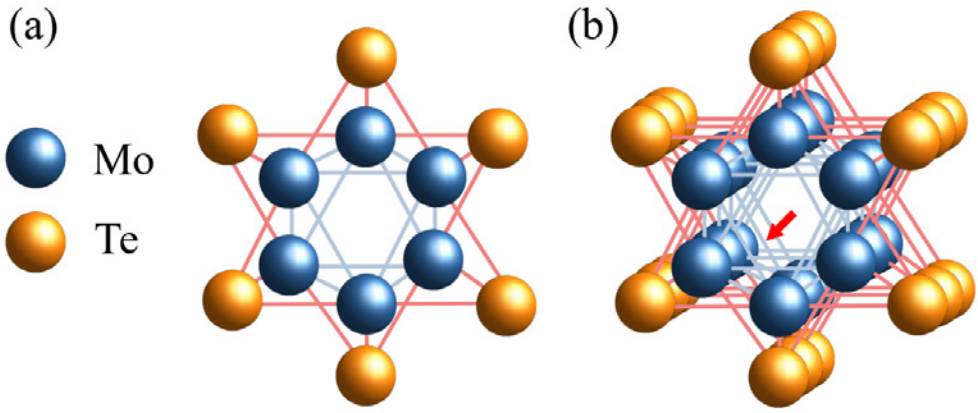

Figure 6.9: The scheme of the (a) Mo_6Te_6 structure and (b) Mo_6Te_6 NW in the ball-and-stick model. Blue and orange balls represent Mo and Te atoms, respectively. The red arrow shows the NW's long axis direction.

Figures 6.10(a)-(c) show additional SEM images of the NWs grown on (a) sapphire and (b)-(c) SI GaAs (111)B substrates, respectively, revealing that time of growth, proportional to the nominal layer thickness, influences the density and size of the NW.

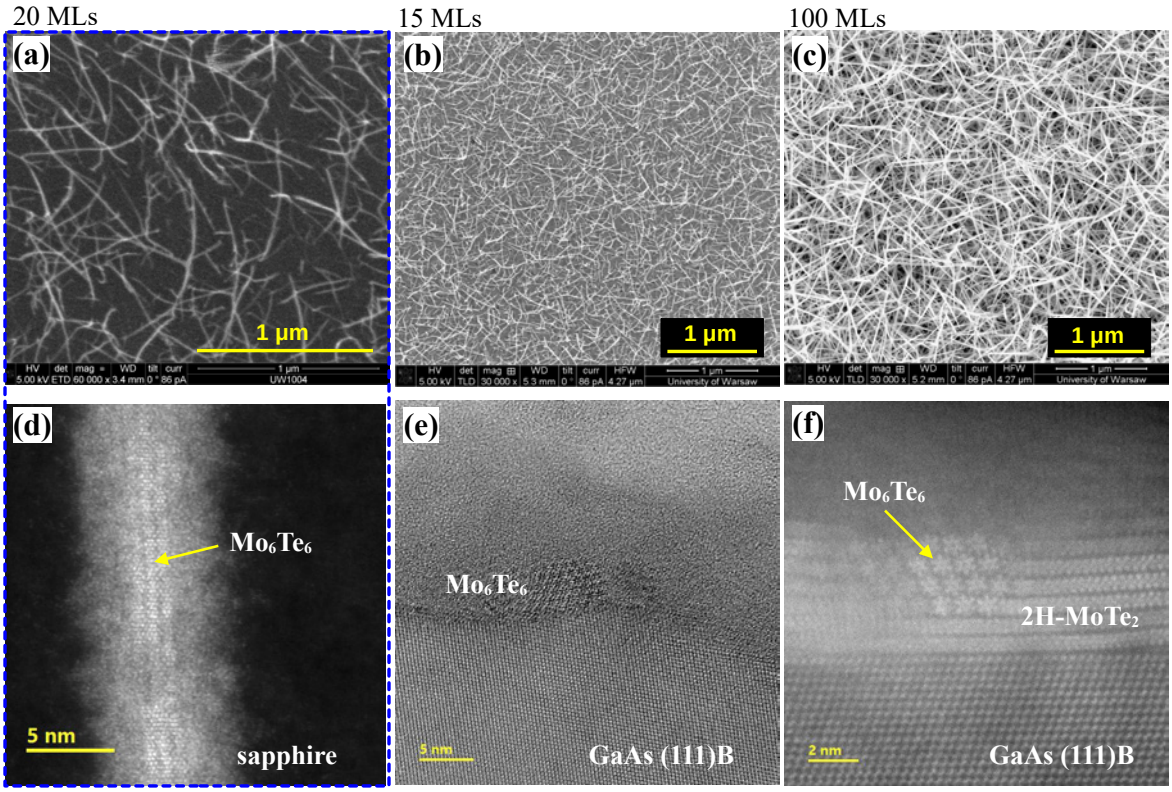

Figure 6.10: Structural characterization of NWs. The scanning electron microscopy images of samples of the nominal thickness of (a) 20 MLs (UW1004) grown on sapphire, (b) 15 MLs (UW1170) and (c) 100 MLs (UW1178), grown on GaAs (111)B at T_s = 350 ^{o}C. The corresponding (d)-(f) TEM cross-sections for samples shown in (a)-(c). [SEM images were made by the Author, with the kind help of Dr. J. Binder, Faculty of Physics, UW. The TEM images were taken by Dr. S. Kret and Dr. A. Kaleta, Institute of Physics, PAS. Figure preparation: Z. Ogorzałek-Sory.]

Furthermore, as the nominal thickness of the layer increases, the length of the NWs increases as well. Figures 6.10(d)-(f) present the corresponding STEM images of NWs. In all NWs the Mo_6Te_6 phase is observed. Although the samples were grown at the same substrate temperature of T_S = 350 ^{o}C, the real substrate temperature can be slightly different between the sapphire and GaAs (111)B. These substrates have different energy gaps and thus the infrared absorption spectra (A(%)) substantially differ i.e. $A_{GaAs} \sim 55\%$ [227] and $A_{sapphire} \sim 15\%$ [228]. Consequently, the real substrate temperature for the sapphire substrate can be slightly lower (than that registered by a thermocouple). In addition, two types of sapphire substrates of different dimensions were used in the experiment: thick square 1 x 1 cm^2 and thin 2" wafer. All these differences can influence the growth conditions and thus introduce changes between those materials.

In addition to the substrate temperature, T_A does not affect the surface morphology in the first-order approximation, but it slightly modifies the surface density of the NWs. Figures 6.11(a)-(b) present the scanning electron microscopy images of $MoTe_2$ NWs grown on sapphire substrate at T_S = 350 ^{o}C (UW1317), annealed either at (a) T_A = 400 ^{o}C or (b)

T_A = 500 ^{o}C for 10 minutes.

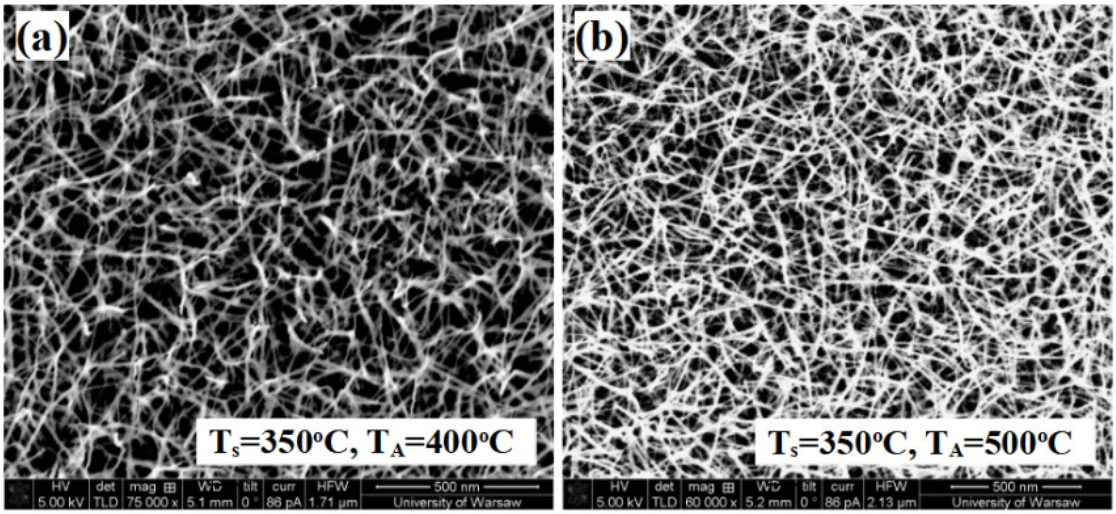

Figure 6.11: Structural characterization of NWs. The scanning electron microscopy images of the NWs grown on sapphire substrate at T_S = 350 ^{o}C (UW1317) and annealed at (a) T_A = 400 ^{o}C and (b) T_A = 500 ^{o}C. [SEM images were made by the Author with the kind help of Dr. J. Binder, Faculty of Physics, UW]

The samples morphology remains the same, but density of NWs is higher for sample annealed at a higher temperature. Although the density of the NWs increases with T_A, the dimensions of the NWs remain the same. Further annealing of the samples (at T_A = 650 ^{o}C) likely leads to sample degradation, as suggested by additional Raman measurements showing the absence of characteristic peaks (data not shown in this dissertation).

It is shown here that the intensity of the Mo and Te fluxes used during the growth is another yet factor responsible for Mo_6Te_6 growth. Similar $MoTe_x$ morphology selection, from the NW-like to the layer-by-layer growth mode, can be achieved with the tellurium source temperature (T_{Te}) variation. Figures 6.12(a)-(b) show scanning electron microscopy images of $MoTe_x$ layers grown on a sapphire substrate at T_S = 270 ^{o}C at two, different tellurium fluxes, defined by Te cell temperature T_{Te} = 360 ^{o}C (UW1431) and T_{Te} = 385 ^{o}C (UW1428). For T_{Te} = 360 ^{o}C the surface of the $MoTe_x$ is homogeneous, while for T_{Te} = 385 ^{o}C NWs appear.

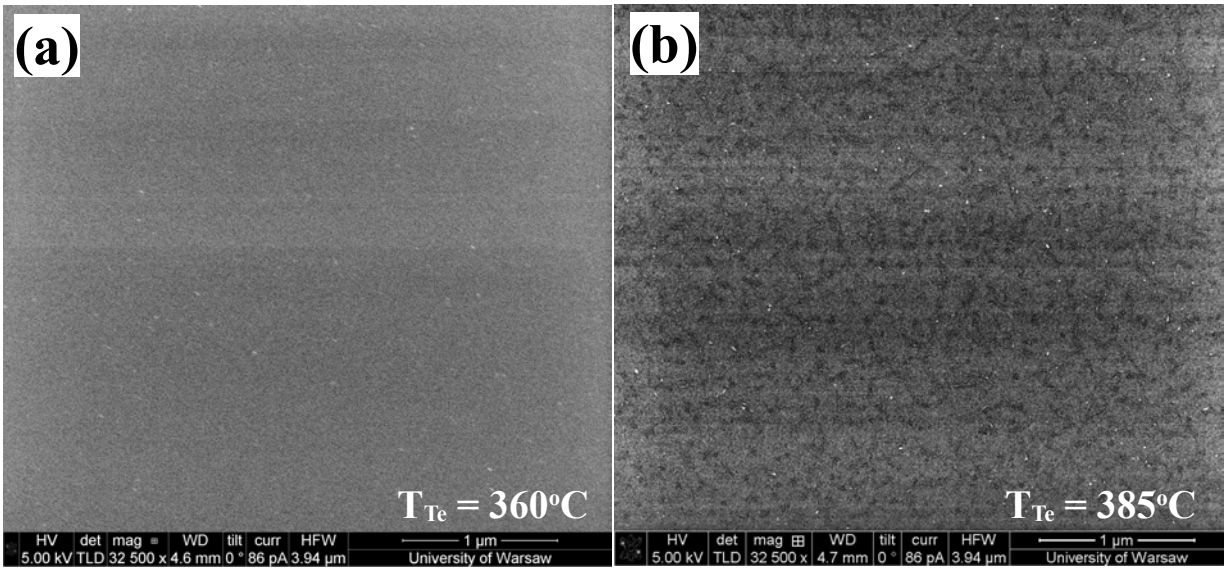

Figure 6.12: Structural characterization of $MoTe_x$. Scanning electron microscopy images of $MoTe_x$ layer of a nominal 10 MLs thickness, grown on a sapphire substrate at T_S = 270 ^{o}C with (a) T_{Te} = 360 ^{o}C (UW1431) and (b) T_{Te} = 385 ^{o}C (UW1428), evidencing different surface patterns. [SEM images were made by Z. Ogorzałek-Sory with a kind help of Dr. J. Binder, Faculty of Physics, UW].

The vibrational characteristics of the selected layers were examined using Raman spectroscopy. Figure 6.13(a) shows a relative intensity of the Raman scattering spectrum of the $MoTe_x$ layers of the nominal thickness of 10 MLs, grown on sapphire substrate at T_S = 270 ^{o}C.

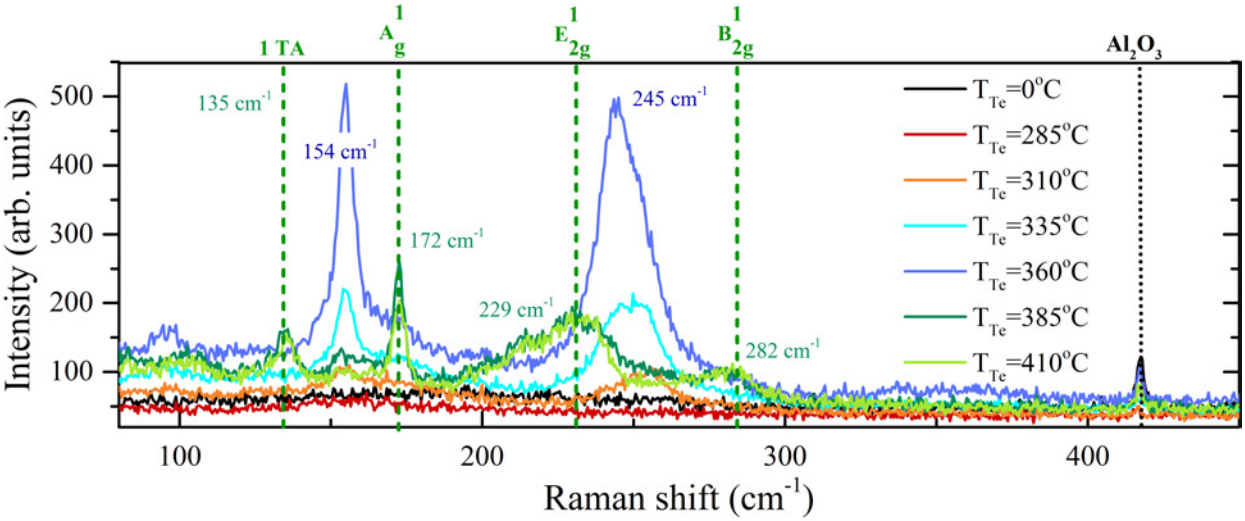

Figure 6.13: Optical characterization of $MoTe_x$. The Raman spectrum of $MoTe_x$ layers, grown at T_S = 270 ^{o}C on sapphire substrate with the molybdenum power P_{Mo}=180 W, for various Te cell temperatures (T_{Te}). 1 TA represents the transverse acoustic phonon excitation at 135.2 cm^{-1}. The peak from the sapphire substrate is marked by the black, dashed line.

The $MoTe_x$ layers were grown with a constant power of molybdenum source P_{Mo} and various tellurium fluxes, as marked in the legend. The black curve presents the results for pure Mo sample, grown without any tellurium. The increase of T_{Te}, apart from the evident changes in the surface morphology (see Figures 6.12(a)-(b)), reveals the presence of the Raman modes

at 150 cm^{-1} and 250 cm^{-1}. For higher T_{Te} the Raman modes shift to higher energies. All the curves group into two classes revealing presence of NWs and regular 2H-phase. The Raman modes for the 2H and NWs phases were marked by the green and blue captions, respectively. The transition between the phases takes place at approximately T_{Te} = 370 ^{o}C. The curves corresponding to the two boundary T_{Te} values, between which the phase transition occurs, are presented in 6.14(a)-(c). Green and blue vertical lines show Raman modes for 2H-phase and NWs, respectively. Panel (b) displays literature data (see blue dashed line) for NWs [218].

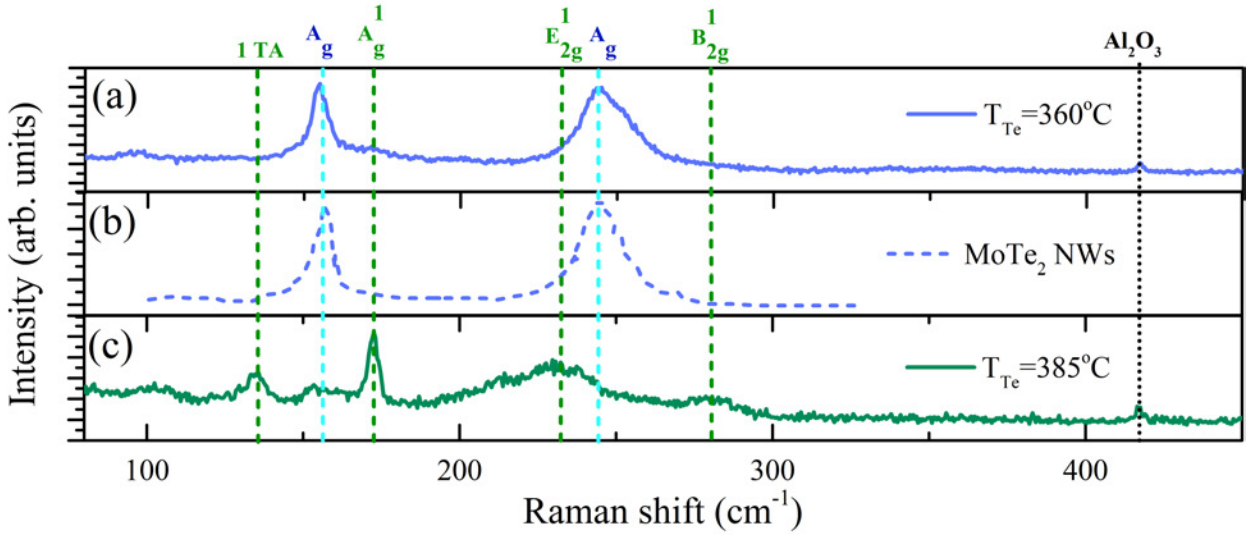

Figure 6.14: Optical characterization of the MoTe$_x$. The intensity of the Raman shift of the 10 MLs MoTe$_x$ for (a) T_{Te} = 360^{o}, representing MoTe$_2$ NWs, (b) literature spectrum for NWs [218] and (c) T_{Te} = 385^{o} with A_g, E_{2g} and B_{2g} modes, representing semiconducting 2H phase. 1 TA represents the transverse acoustic phonon excitation at 135.2 cm^{-1}. The peak from the sapphire substrate is marked by the black, dashed line.

The Raman spectrum for T_{Te} below 360 ^{o}C is shown in Figure 6.14(a) and it is consistent with the literature result for NWs, presented in Figure 6.14(b) [218]. The increase of tellurium temperature above T_{Te} = 370 ^{o}C (Figure 6.14(c)) results in the two-dimensional growth of 2H-MoTe$_2$. The spectrum consists of several clearly-resolved peaks nicely corresponding to the literature values, marked with vertical green lines as A_g, E_{2g} and B_{2g} at 172 cm^{-1}, 234.2 cm^{-1} and 281.7 cm^{-1}, respectively [229]. Similar observations have been made recently by Ohtake et al. [230] who has shown that the MBE-grown MoTe$_2$ films on GaAs (111)B substrate under the Te-rich condition are mainly composed of a semiconducting phase, while under the Te-deficient conditions, the 2H-MoTe$_2$ phase evolves into nanowire-like structure owing to the desorption of Te atoms [230]. Similarly to the results of Ohtake et al., Te-deficient growth conditions also lead to the NW-like structure while under Te-rich conditions to the 2D (thin film) growth. Table 6.2 shows the summary of the most important MBE growth parameters (T_S, P_{Mo}, T_{Te} and T_A) influencing the structural properties of MoTe$_x$ grown on sapphire or SI GaAs (111)B substrates.

Table 6.2: The influence of the MBE growth parameters (i.e. T_S, P_{Mo}, T_{Te} and T_A) on the structural properties of $MoTe_x$ grown on sapphire (S) and SI GaAs (111)B (G) substrates. The T_S marked with the stars indicate the nominal temperatures (not corrected to the infrared absorption of the substrate). ID - insufficient data.

Sample (substrate):	Morphology	Mo_6Te_6	T_S (^{o}C)	P_{Mo} (W)	T_{Te} (^{o}C)	T_A (^{o}C), time (min.)
UW0997 (S) / UW1420 (G)	2D	-/-	270	160	380 / 385	~ 400, 10 / 450, 10
UW1004 (S)	3D: NWs	+	350*	160	380	-
UW1170 (G) / UW1178 (G)	3D: NWs	+/+	350	160	380/400	- / 440, 10
series with various T_{Te} (S)	2D/3D	ID	270*	180	310 - 385	400, 10

The richness of the MBE growth parameters makes $MoTe_2$ a difficult to grow in a reproducible manner. Slight parameter deviations strongly influence the quality of the grown layers changing their morphology. Examples of additional $MoTe_x$ morphologies, obtained for various growth parameters, are presented in Appendix C in Figure C.2. The obtained results show that the change in morphology is directly related to substrate temperature T_S, tellurium effusion cell temperature T_{Te} and the annealing temperature T_A. Our results show that the phase evolution is, to a certain extent, independent of the substrate selection.

Figure 6.15 shows the profiles of the RHEED intensities at different stages of the growth: violet, black and blue curves present data for pristine SI GaAs (111)B substrate and 2 MLs of $MoTe_2$ before and after annealing, respectively.

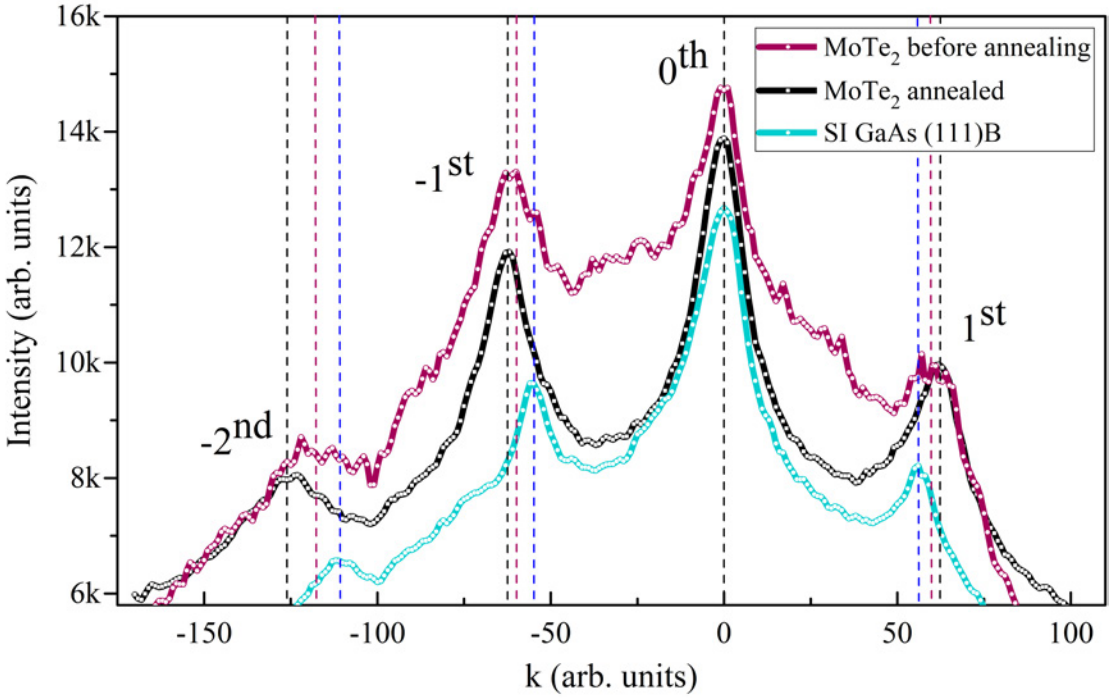

Figure 6.15: The profiles of RHEED intensities for GaAs (111)B substrate, the as-grown and the annealed $MoTe_2$ [40]. [RHEED data were taken by Dr. W. Pacuski and Dr. B. Seredyński, Faculty of Physics, UW. The data analysis and Figure preparation: Z. Ogorzałek-Sory.]

The systematic studies showed that a post-growth annealing of the $MoTe_2$ layers influences its lattice parameters. Indeed, after the annealing, a tiny difference of the positions of the RHEED intensities was observed. By taking the lattice parameter of GaAs as a reference [231], an in-plane lattice parameter a of $MoTe_2$ was estimated. The value of the lattice parameter for the as-grown sample equaled to (3.69 ± 0.01) $\AA$. It is larger than the value reported for the unstrained bulk $MoTe_2$: (3.519 ± 0.001) $\AA$ [232]. It evidences the presence of tensile strain in the system. However, the sample lattice parameter changed after annealing to (3.59 ± 0.01) $\AA$, a value much closer to the one, reported for relaxed $MoTe_2$. This result indicates that the post-growth annealing is an efficient way for strain relaxation in the $MoTe_2$ layer [40].

Although post-growth annealing reduces the strain, one should be aware that the interactions between the GaAs substrate and the $MoTe_2$ layer or between the subsequent $MoTe_2$ layers may not be purely van der Waals-like. Figure 6.16 presents the HR scanning transmission electron microscope image of 2 MLs of $MoTe_2$, grown on GaAs (111)B substrate.

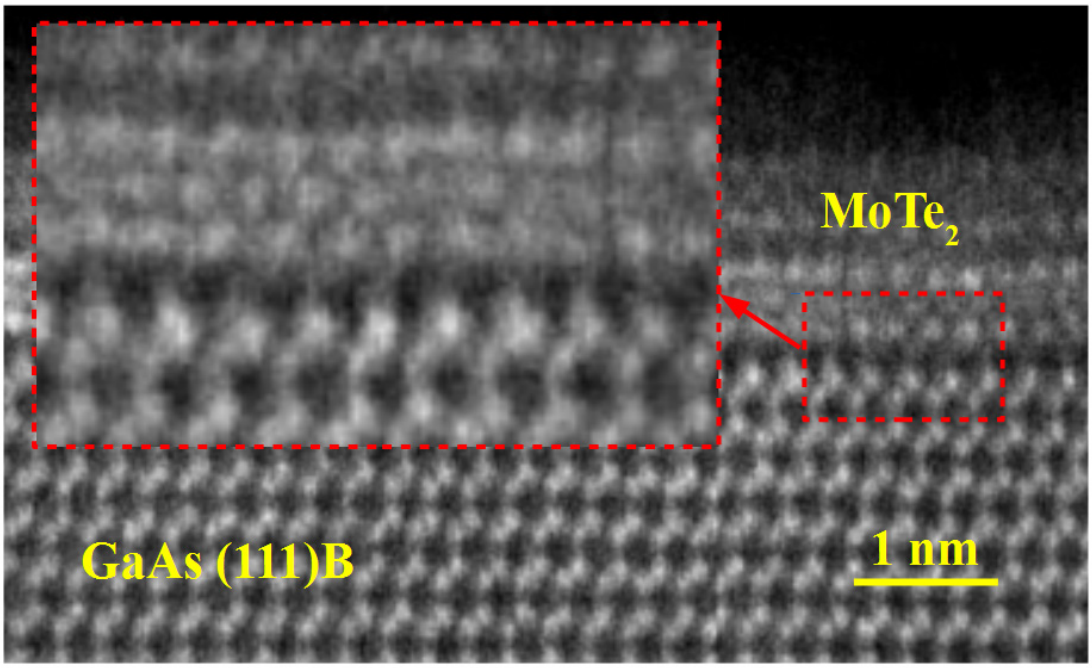

Figure 6.16: Structural characterization of $MoTe_2$. The scanning transmission electron microscope image of the $MoTe_2$ layers grown on GaAs (111)B substrate at T_S = 270 ^{o}C (UW1420). [TEM images were taken by Dr. S. Kret and Dr. A. Kaleta, Institute of Physics, PAS. The data analysis and Figure preparation: Z. Ogorzałek-Sory.]

Numerous links between the substrate and the $MoTe_2$ layers are present, reveling bonds between those two materials. During the PhD studies, several attempts have been made in order to exfoliate the MBE-grown $MoTe_2$ layers into single flakes. In spite of different types of adhesive tapes used, no $MoTe_2$ layers have been successfully exfoliated. It was the case even for the thick films, where substrate-layer interactions should be absent or at least significantly reduced.

In order to verify the quality of the MBE-grown $MoTe_x$ layers, samples were characterized by the XRD measurements. Figure 6.17 shows the $2\Theta - \omega$ scans for three different types of $MoTe_x$ layers: 20 MLs grown on sapphire (grey curve), 2 MLs grown on SI GaAs (111)B and capped with AlO_x (blue curve) and NWs (pink curve).

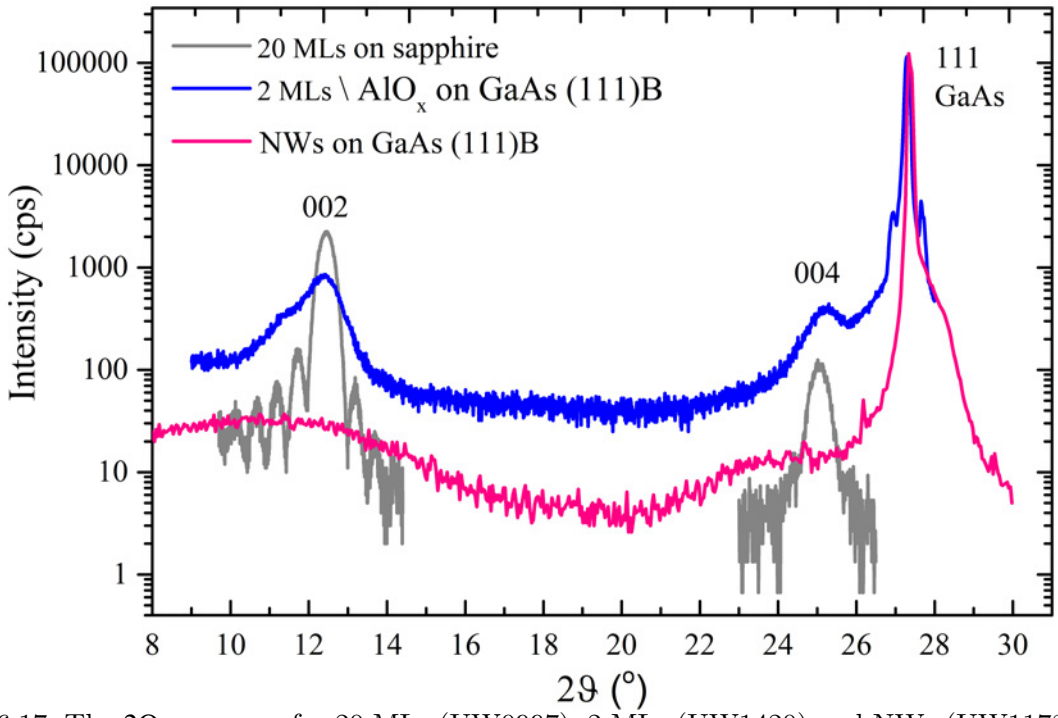

Figure 6.17: The $2\Theta - \omega$ scans for 20 MLs (UW0997), 2 MLs (UW1420) and NWs (UW1178). [The XRD characterization was made together with Dr. M. Tokarczyk, Faculty of Physics, UW. The data analysis and Figure preparation: Z. Ogorzałek-Sory.]

As one can see, for 2 MLs and 20 MLs the 002 and 004 reflections of $MoTe_2$ are well resolved. The reflections for the NWs are broad with very broad peak at $2\Theta = 11.5^o$, possibly originating from the Mo_6Te_6 phase. For the samples grown on GaAs substrates, the 111 GaAs reflection is visible around $2\Theta = 27^o$. The thick sample has the narrowest 002 peak with additional peaks, evidencing high quality of the crystal. The 2 MLs-thick sample has broader 002 peak, as expected. Figure 6.18 shows the zoomed 002 peak spectrum for 20 MLs, where the subsequent satellite peaks are indexed.

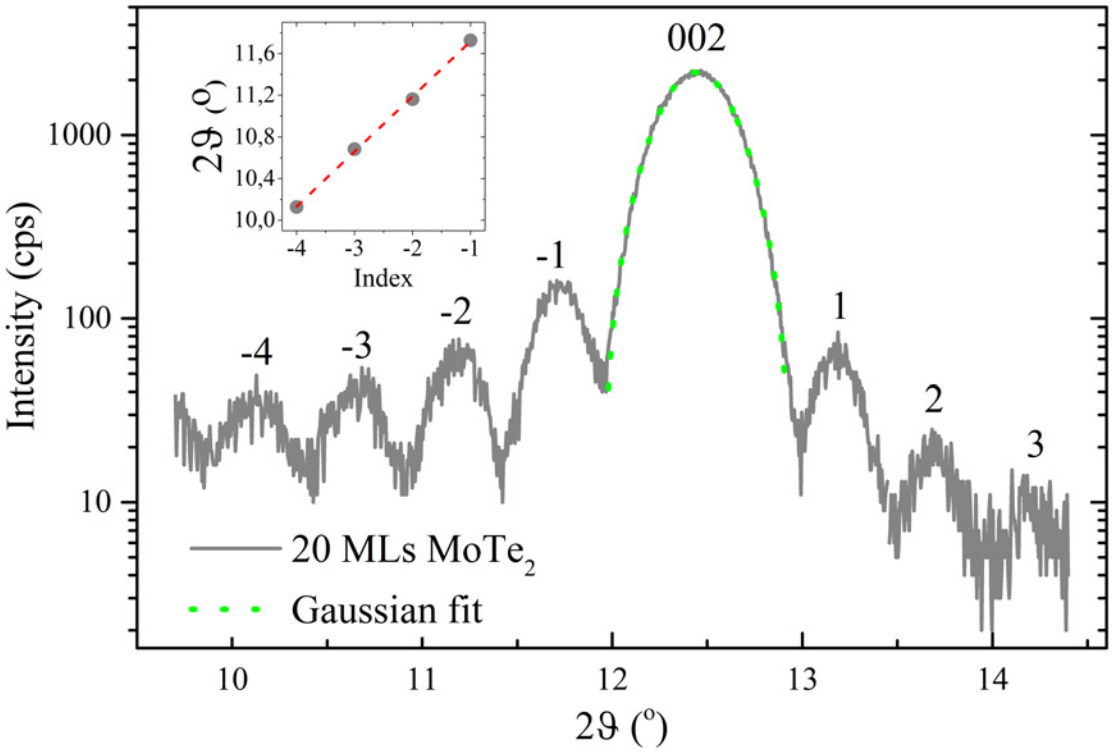

Figure 6.18: The $2\Theta-\omega$ scan for 20 MLs (UW0997). Inset: the periodicity of the $2\Theta-\omega$ oscillations. [The XRD characterization was made together with Dr. M. Tokarczyk, Faculty of Physics, UW. The data analysis and Figure preparation: Z. Ogorzałek-Sory.]

The position and the full width at half maximum (β) obtained from the Gaussian fit, (presented by the green, dashed line) to the 002 peak allowed to calculate the thickness from the Scherrer equation (d_X). Assuming $d_X = K \cdot \lambda_x/(\beta \cdot cos(\Theta))$, where K is a dimensionless shape factor with a value close to unity, the average thickness of $MoTe_2$ is d_X = (17.6±0.1) nm, which nicely agrees with the nominal thickness of the sample and the STEM images in Figure 6.8(a). Around 002 peak symmetric and periodic Laue oscillations are visible, which are known as thickness fringes and are seen only in high-quality multilayers. The positions of the satellite peaks (see the inset of Figure 6.18) allowed to calculate the average thickness of the samples d_S. Assuming $d_S = \lambda_x/(2 \cdot cos(\Theta) \cdot \Delta\Theta)$, d_S = (16.7±0.4) nm which also corresponds to STEM image (see Figure 6.8(a)).

Figure 6.19 shows the reflectometry studies for 2 MLs and 20 MLs along two directions, marked by the blue, gray and red curves, respectively.

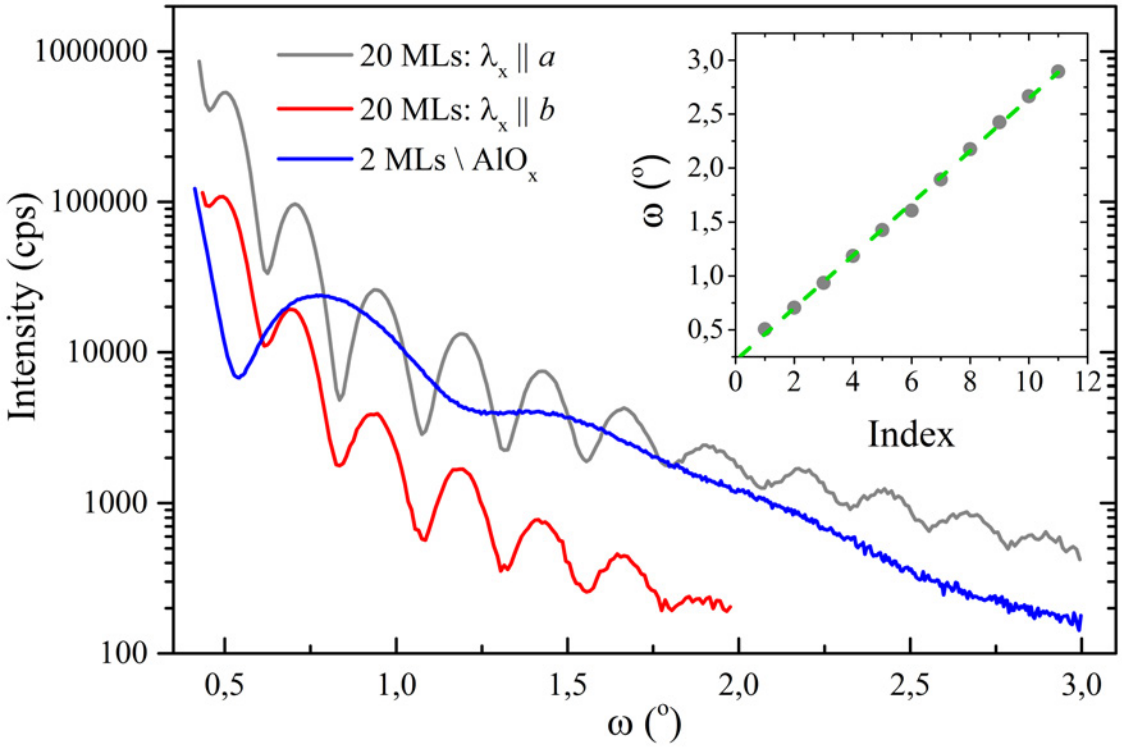

Figure 6.19: The reflectometry for 2 MLs (UW1420) and 20 MLs (UW0997) with the Kiessig oscillations in two orientations of X-ray beam versus sample. Inset: The periodicity of the Kiessig oscillations. [The XRD characterization was made together with Dr. M. Tokarczyk, Faculty of Physics, UW. The data analysis and Figure preparation: Z. Ogorzałek-Sory.]

The high quality of the samples allowed to observe multiple, periodic Kiessig oscillations. The 20 MLs-thick sample was measured along two in-plane crystallographic directions (a and b), with respect to the X-ray beam source wavelength (λ_x= 1.54 Å). The oscillations visible along two directions of the sample indicate its excellent homogeneity. The periodicity of the Kiessig oscillations gives information about the average thickness of the sample (d_K). It is presented in the inset of Figure 6.19(b). Assuming $d_K = \lambda_x/2 \cdot \Delta\Theta$, where $\Delta\Theta$ is the period of the Kiessig oscillations, d_K = (18.2±0.2) nm, which nicely corresponds to the nominal thickness (see STEM image in Figure 6.8(a) where the thickness was estimated to equal ~ 15 nm). Although the sample exhibits structural disorder such as grain boundaries (see Figure 8.2(a)), it still shows high structural quality and notable uniformity, as evidenced by X-ray diffraction and reflectometry.

6.2.2 Electrical characterization of NWs

To address NWs electrical properties, selected samples were characterized by resistivity tensor measurements. Figure 6.20(a) presents the electrical characterization of NWs, grown either on sapphire or SI GaAs (111)B substrates (see Figures 6.10(a)-(c)). It shows the resistivity dependence as a function of temperature $\rho(T)$ measured for three samples containing NWs of the nominal thickness of 15 MLs (UW1170), 20 MLs (UW1004) and 100

MLs (UW1178), marked by the light, medium and dark blue curves, respectively.

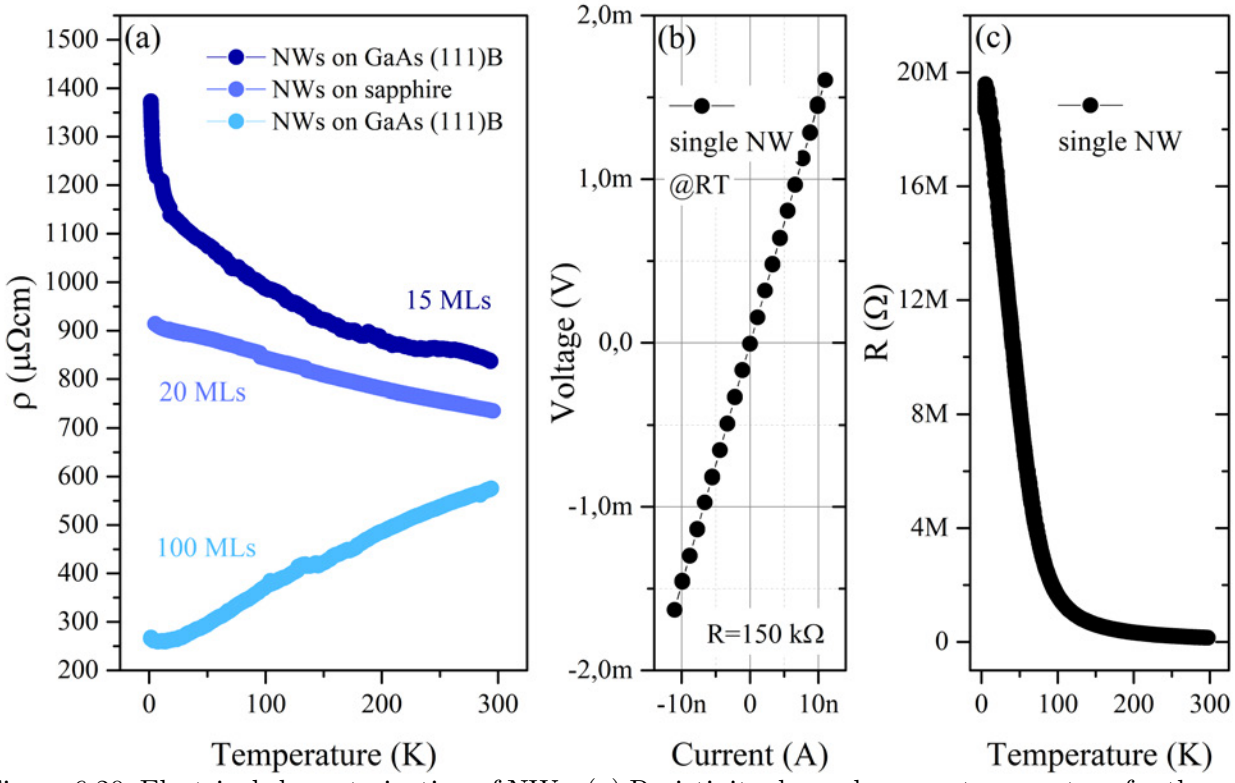

Figure 6.20: Electrical characterization of NWs. (a) Resistivity dependence on temperature for three samples of NWs of different nominal thicknesses. (b) Room temperature two-probe voltage-current characteristic for individual NW. (c) The two-probe longitudinal resistances of the single NW (of a length of 1.37 μm). [The samples of single NWs were made by MSc J. Polaczyński, Institute of Physics, PAN]

For the thinnest sample (15 MLs), the $\rho(T)$ dependence shows a rise of resistivity at low temperature. Qualitatively, this kind of dependence is expected for the 2H-semiconducting phase. For the sample of the nominal thickness of 20 MLs, the $\rho(T)$ dependence is almost constant. Along with the increase of the thickness of the NWs, the temperature resistivity trend changes, leading to the metallic behavior. The RRR for the thickest sample (100 MLs) does not exceed 2 revealing large inhomogeneities and thus poor metallic properties of the studied layers. Along with the increase of the nominal thickness of NWs, not only the quantity of the NWs per unit area increases (see Figures 6.10(a)-(c)), but also sample electrical properties dramatically change: a trend of thickness-dependent temperature resistivity dependence is observed changing from semiconducting-like to metallic-like behavior. As this is a macroscopic response of a thin layer (15 MLs), which has fewer nanowires per unit area and of smaller sizes may indeed be less conducting than thicker one.

To investigate the electric properties of the individual NW, the thickest sample with longest NWs, was selected for processing. The process of sample preparation was done by MSc J. Polaczyński from the Institute of Physics, Polish Academy of Sciences, Warsaw, Poland. The NWs were separated to reach individual wires in an ultrasonic bath. Despite

significant thickness of the sample, the NWs were strongly tangled making this task extremely difficult. Eventually, a few NWs, about 1 μm long, were successfully transferred onto Si/SiO_2 substrate with previously prepared gold paths. The sample prepared for transport measurements consisted of a few single NWs, each connected to three or four electric gold contacts. Connecting wires to contacts pads were made at the Faculty of Physics University of Warsaw by Z. Ogorzałek-Sory and Dr. M. Borysiewicz. Because of the electrostatic fragility of the NWs, the sample handling was made under constant electrical grounding. Then the sample was manually cleaved and fixed on the carrier chip, which was initially electrically grounded. The current-voltage characteristics and temperature dependency resistance were measured, using currents smaller than 12 nA. Although many precautions preventing the electrical discharge to NWs were made, most of the electric contacts were damaged. Eventually, the room temperature voltage-current characteristic and dependence of resistance on temperature were measured by two-probe measurements. Figure 6.20(b) shows two-probe voltage-current characteristic for single NW. The linearity of the current–voltage characteristic confirms the formation of ohmic contacts. The room-temperature resistance reaches 150 kΩ. Figure 6.20(c) presents dependence of resistance on temperature in linear scale. Resistance of single NW increases to 19.5 MΩ at 5 K. One can clearly observe a substantial difference between the characters of the curves of the single NW and the macroscopic sample. The metallic behavior of the macroscopic sample, presented by the light blue curve in Figure 6.20(a), changes to the semiconducting-like one for a single NW. Regardless of the NW structure, the system consists of an initial continuous conducting layer from which a network of tangled NWs emerges. Therefore, a direct comparison between bulk NWs and a single NW is considerably more complex.

Due to high inhomogeneity of the NWs and $MoTe_x$ layers and possibly substantial high carrier concentration, the transverse component of the resistivity tensor was immeasurable.

6.2.2.1 Peculiar resistivity features

Although indium is a good candidate for forming ohmic electrical contacts to $MoTe_2$, one must be aware of its superconducting nature below $T \sim 3.4$ K [233] and its low critical field of $B_C \sim 30$ mT [234]. This is particularly important for low-temperature magnetotransport measurements, where the superconducting phase of indium may interfere with quantum effects expected in topological materials, including Weyl semimetals. Additional results of the unidentified features in the longitudinal resistivity are presented in Appendix C in section C.3.1 in Figure C.3.

6.2.3 Electrical characterization of $MoTe_2$ layers

6.2.3.1 In-situ capping of $MoTe_2$ layers

Being aware of the low stability of the $MoTe_2$ layers, the development of an effective capping procedure was essential. An in-situ capping of the wafer after the MBE growth of a TMD material was undertaken. Two identical samples were grown [40]: after the growth one of the wafers was moved to the III–V MBE growth chamber, vacuum connected to the II–VI one, for aluminum layer deposition. The thin 3 nm aluminum layer was deposited from the conventional high temperature effusion cell on an unheated sample. The aluminum flux intensity was relatively low and corresponded to the growth rate of $0.5\ \mathring{A}\ s^{-1}$. After the growth, the sample was exposed to the ambient atmosphere. It resulted in a formation of an insulating oxide AlO_x, serving as a capping layer [235]. Figures 6.21(a)-(b) show TEM cross-section images of the 2 MLs of the 2H-$MoTe_2$ (UW1420) grown on SI GaAs (111)B substrate, capped with AlO_x layer. Below AlO_x cap, homogeneous 2 MLs of 2H-$MoTe_2$ are identified (see Figure 6.21(b)). TEM results show that AlO_x capping is continuous and homogeneous and the thickness of oxide equals 5 nm. We used 3 nm of Al, because thicker layer risks not to be fully oxidized, leading to the formation of Al layer which may form parallel conducting layer contributing to the electric transport. On the other hand, too thin Al layer may show some discontinuities, and not cover fully the $MoTe_2$ surface as it will be shown further. The In contacts, visible at the top of AlO_x were deposited through a shadow mask (see 4.1 section and Figures 4.1(a)-(f)). The TEM analysis revealed that locally AlO_x layer is pierced by indium: green arrow in Figure 6.21(a) shows the area of electric contact. Due to the high speed of the In deposition process (i.e. hundreds of nm in a few or tens of seconds) In atoms brought high kinetic energy, passing through the AlO_x layer providing electric contact to the layer beneath. The electric connection to $MoTe_2$ was also proven by the energy-dispersive X-ray spectroscopy (EDS) scans of the atomic profiles along the growth axis, shown in Figure 6.21(c). The data is presented in atomic percentages, normalized to 100%. The results show the presence of both Mo and Te elements, between the GaAs (111)B substrate, and the AlO_x capping layer. Moreover, a finite amount of indium atoms can be also resolved in the $MoTe_2$ region. It confirms that AlO_x capping layer does not prevent metal from forming the electric contact to $MoTe_2$ layer. The research shows an efficient way to protect large-scale samples for long-term usage and operation. The procedure of AlO_x capping is fast, relatively cheap and effective. Basically, it can be applied to all transition metal compounds.

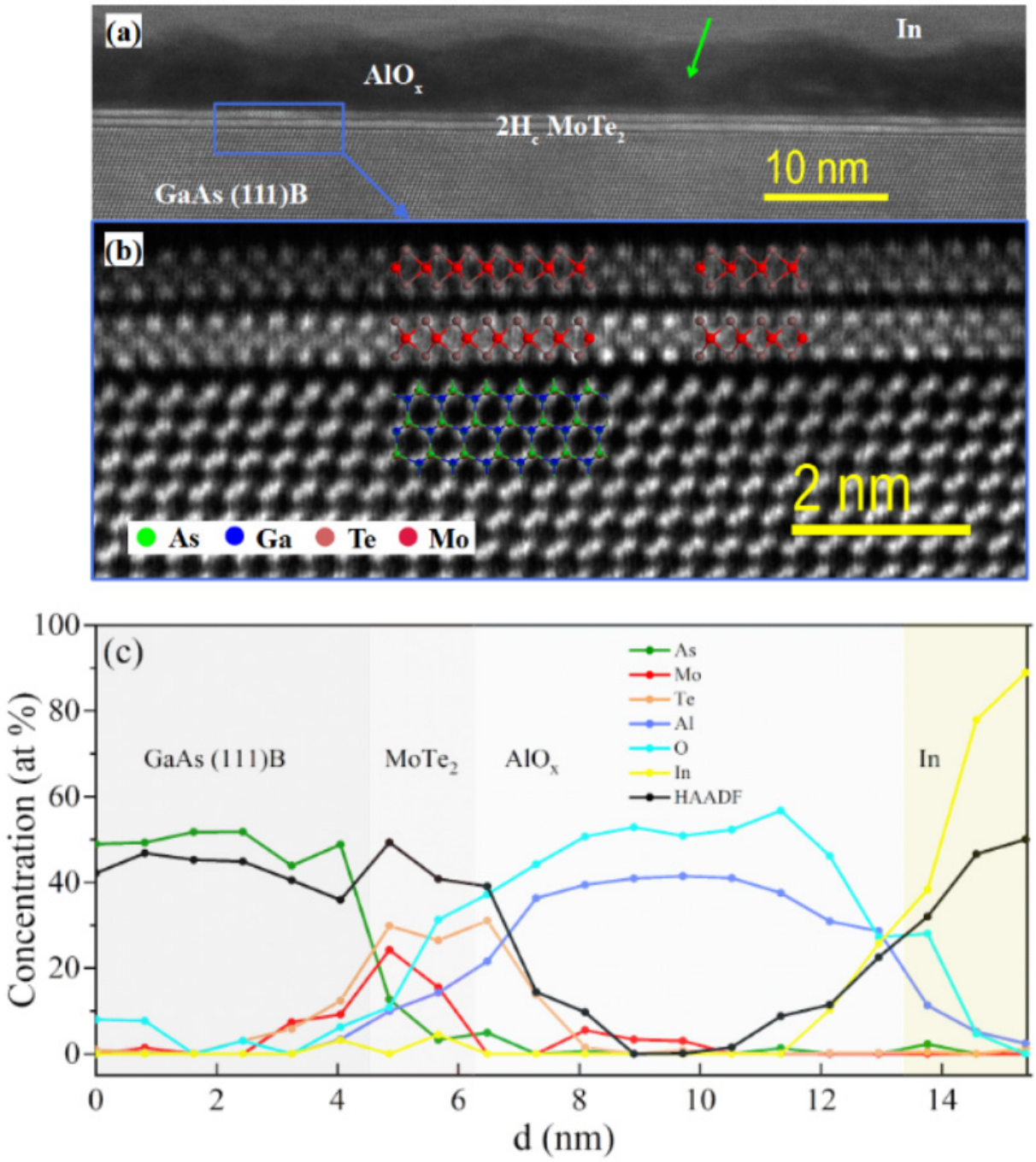

Figure 6.21: Structural characterization of $MoTe_2$ layers. The high-resolution scanning transmission electron microscope images of the cross-section of the AlO_x capped 2 MLs of 2H-$MoTe_2$ with In contact. (a) High quality continuous 2H-$MoTe_2$ layer, 75 nm long. The green arrow shows the area of possible electric contact to the 2H-$MoTe_2$. (b) The zoomed details from the blue frame from the subfigure (a). (c) The profiles of elemental distribution for sample cross-section obtained by EDS. The black curve represents the normalized $[0\bar{1}00]$ STEM-HAADF signal [40]. [TEM images and EDS studies were taken by Dr. S. Kret and Dr. A. Kaleta, Institute of Physics, PAS.]

6.2.3.2 $MoTe_2$ grown on different substrates

To compare the electrical properties and environmental stability of uncapped and capped $MoTe_2$ grown on GaAs (111)B (see Figures 6.21(a)-(b)), and investigate a possible influence of capping on the properties of $MoTe_2$, a set of two identical samples, with and without the AlO_x capping layer, were characterized by R(T) studies. Figure 6.22(a) presents the scheme of sample configuration for measurements.

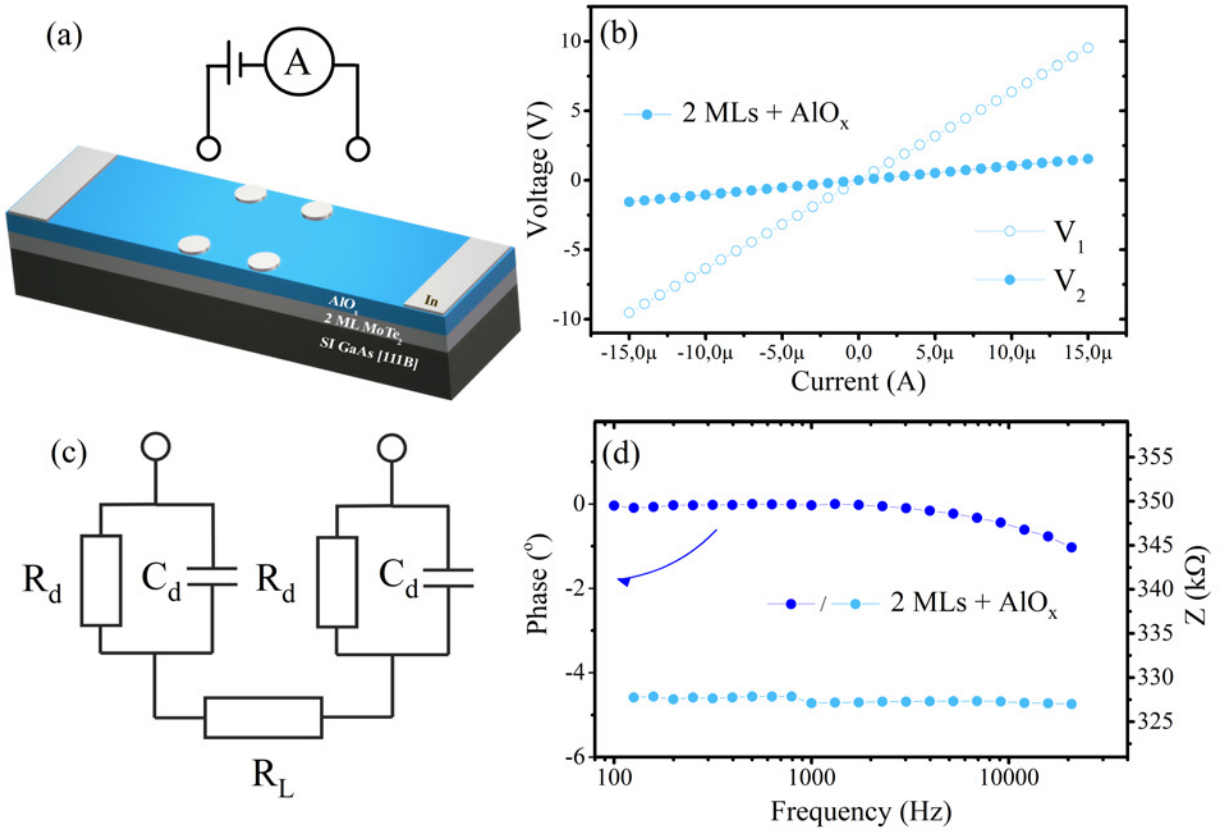

Figure 6.22: Electrical characterization of $MoTe_2$ layers. (a) Sample configuration for two-probe current voltage characteristics. (b) The room-temperature two-probe current–voltage characteristics were measured for two pairs of contacts: V_1 – current (source–drain) contacts used for supplying current and V_2 – voltage contacts positioned along the sample (Hall bar configuration). (c) The electric circuit of the sample with dielectric layer. (d) The phase (left axis) and the impedance magnitude (right axis) as a function of the frequency for 2 MLs of $MoTe_2$ with AlO_x cap.

As shown in Figure 6.22(b) the voltage-current characteristics are linear, proving the formation of the ohmic contacts to the layers beneath. The quality of the contacts, deposited on AlO_x, which in principle could give capacitive (instead of resistive) coupling, was additionally tested by capacitance studies. Figure 6.22(c) shows the scheme of electric circuit of the dielectric AlO_x layer (with a resistance R_D and a capacity C_D) and $MoTe_2$ layer (described by the resistance R_L). Figure 6.22(d) shows the amplitude and phase of the impedance measured between two top contacts. The magnitude of impedance is approximately constant in the whole studied frequency range. Moreover, its value reasonably corresponds to the value

of sample resistance (a few tens of kΩ). The phase of the impedance, close to zero, reveals direct contact in spite of a thin AlO_x layer, indicating that such a thin dielectric layer does not prevent from formation of ohmic contacts to the layer below [40].

Figures 6.23(a) shows the longitudinal resistivity as a function of temperature for two samples studied: 2 MLs of uncapped and capped with AlO_x, presented by black and blue curves, respectively.

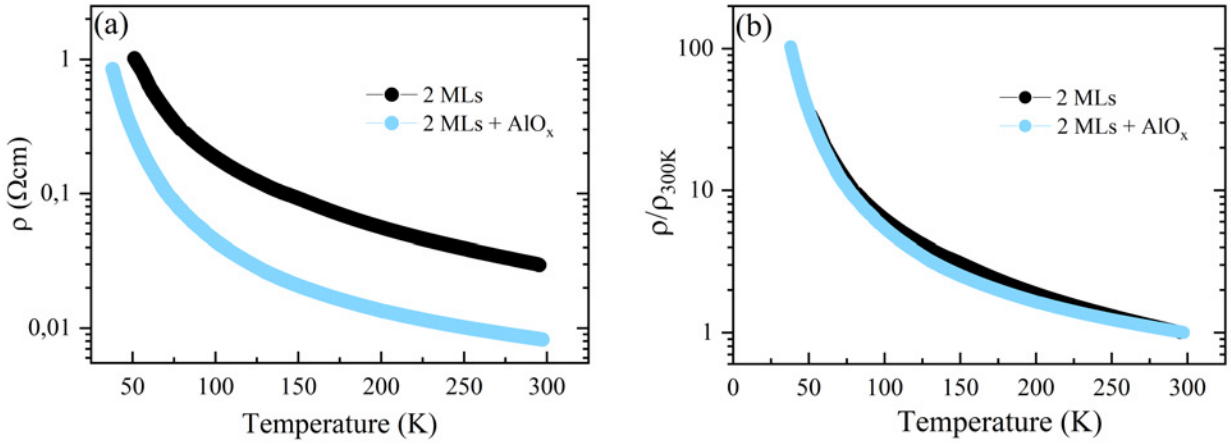

Figure 6.23: Electrical characterization of $MoTe_2$ layers. (a) The longitudinal resistivity and (b) resistivity normalized to room temperature value as a function of temperature for the capped and uncapped samples, marked by the blue and black curves, respectively.

At room temperature there is a large difference between the longitudinal resistivities of studied layers. As it will be shown further, the resistivity difference is most probably associated with the uncapped sample degradation due to the surface oxidation during wiring the sample. Both samples have a similar semiconducting-like behavior with the resistivity rise at low temperature, expected for the 2H-phase. As shown in Figure 6.23(b), where resistivity is normalized to room temperature value, character of $\rho(T)$ is almost identical. In order to understand the resistivity dependencies on temperature, two models of charge transport were taken into account: band transport and hopping, described by equation 3.2. The data was analyzed by plotting them according to different models in appropriate coordinates, and linearity of the resulting curves was used to assess the probable transport mechanism. Figures 6.24(a)-(d) show the dependence of the inverse temperature to the power of a chosen x, as a function of the natural logarithm of conductivity for the capped and uncapped samples, respectively.

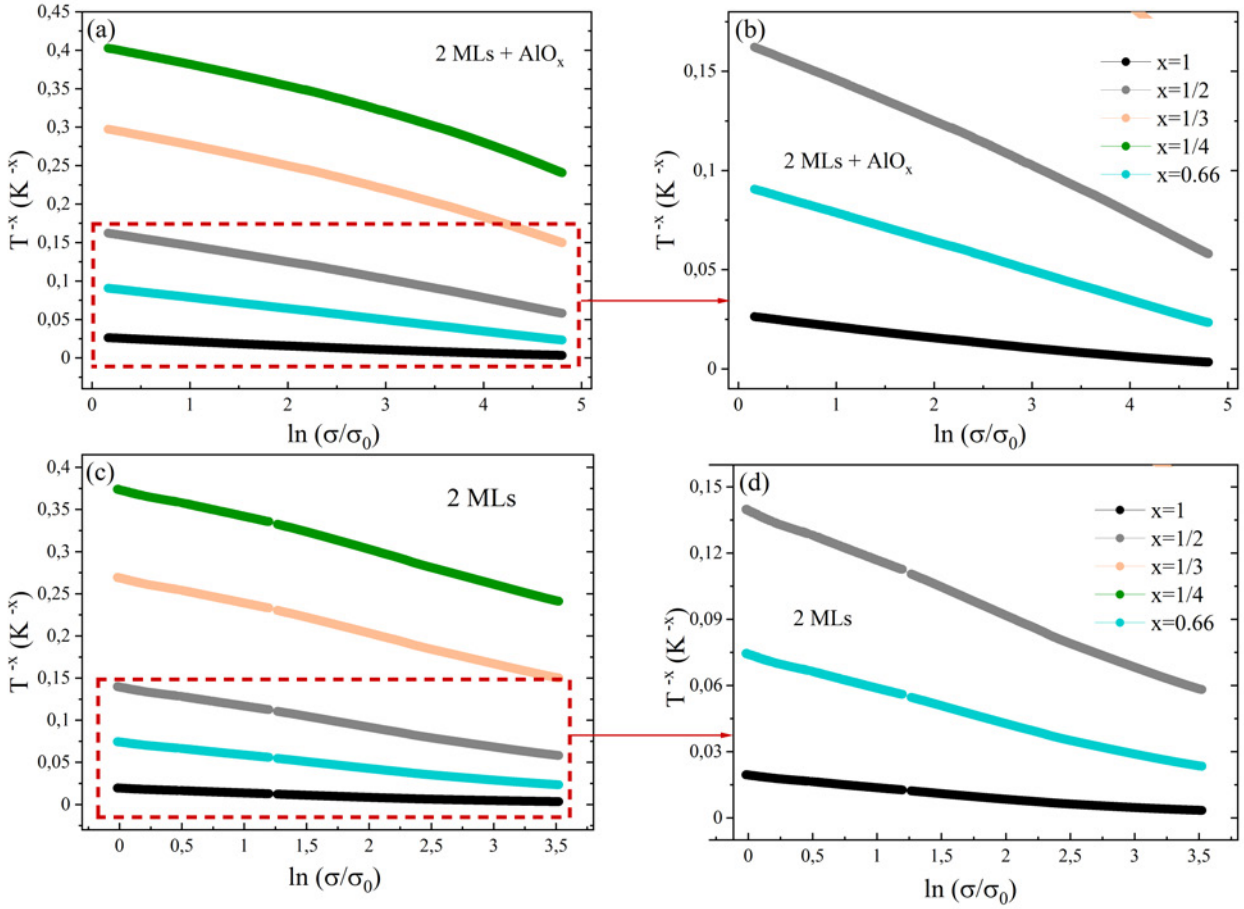

Figure 6.24: Electrical characterization of $MoTe_2$ layers. The conductivity models for the (a)-(b) capped and (c)-(d) uncapped $MoTe_2$ samples. The green and orange colors correspond to the Mott VRH for 3D and 2D systems, respectively. Grey and black curves correspond to the Efros-Shklovskii VRH and band transport model, respectively. The light blue curve corresponds to anomalous exponent of $x \sim 0.66$.

The dependencies for 2D and 3D Mott-Davis VHR models are presented by orange and green curves, respectively. Both curves are far from linear meaning that the models do not correspond to the data. The data points for band transport and Efros-Shklovskii models, presented by black and grey curves, form a line. The zoomed data in red boxes are shown in right panels. The best model description for both samples is obtained for $x \sim 0.66$, as shown by blue curves. This value does not correspond to any well-known model. Comparable values of the x parameter have been also reported for thin metallic layers such as Bi, Ag, Pb and Pd [236] and explained by quantum percolation in a granular network films [237]. Similar value of x has been shown for thin layers with a high dielectric constant, sandwiched between two materials with low dielectric constants. Peculiar conductivity temperature dependence was described with $x \sim 0.7$ indicating the unusual type of charge transport mechanism [238]. To our knowledge, this value of critical exponent of $x \sim 0.66$ was observed for $MoTe_2$ for the first time [40]. Due to the immeasurably small Hall component R_H, the transverse resistivity tensor element could not be resolved.

To examine environmental stability of $MoTe_2$ layers, the capped and uncapped samples

were exposed to different conditions. In a dedicated desiccator the atmosphere was periodically changed from vacuum, through nitrogen to air. The desiccator was equipped with the electric wires to set the electric current and to measure the longitudinal resistances of the two separate samples at the same time and at the same experimental conditions. For almost two weeks both samples were kept in the desiccator where every 24 hours the gas environment was changed from vacuum (p~1 mbar), through nitrogen to ambient with a controlled humidity and temperature in the vicinity of the samples. The measurements were performed at room temperature (T=24^{o}C). Figure 6.25(a) shows variation of the resistivity as a function of time and gas environment for the uncapped (black) and capped (blue) samples. The vacuum, nitrogen and air are indicated by blue, orange dashes and white background patterns, respectively.

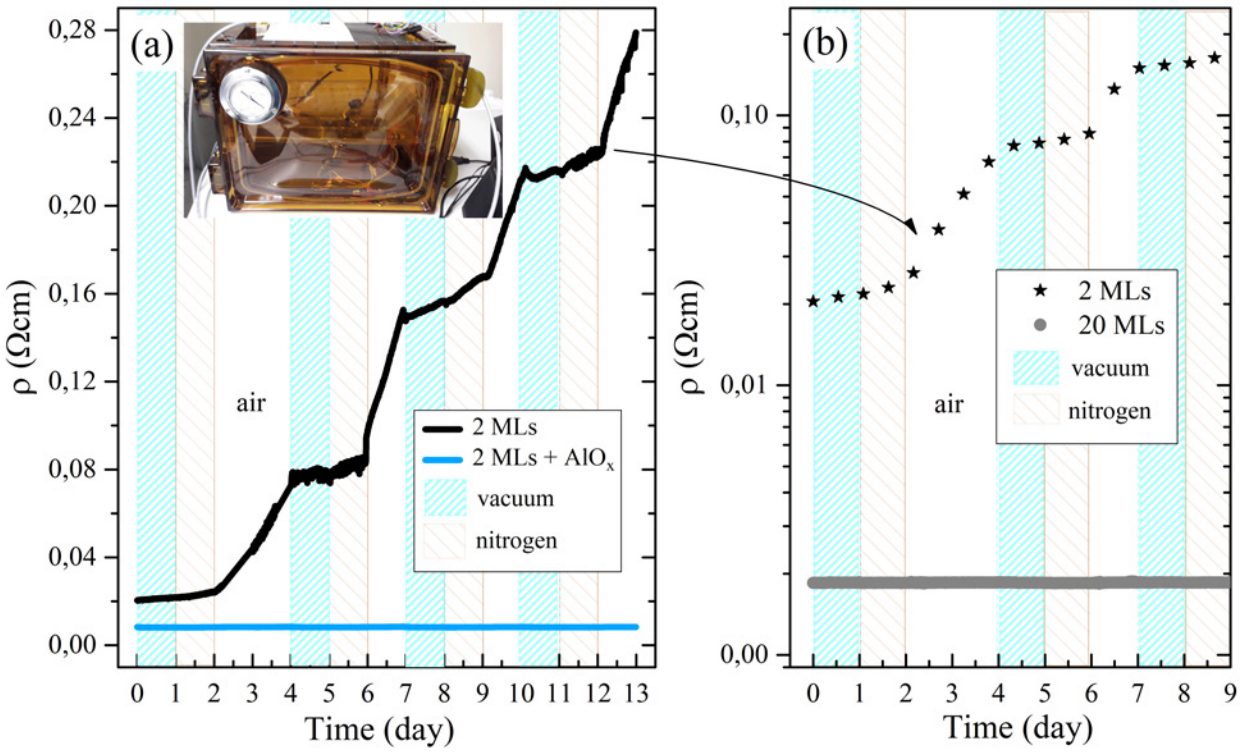

Figure 6.25: Electrical characterization of $MoTe_2$ layers. (a) Resistivity of the uncapped (black curve) and capped (blue curve) 2 MLs of $MoTe_2$, as a function of time in different environments. Inset: the photo of the desiccator [40]. (b) Resistivity (in log scale) of the uncapped 2 MLs (black asterisks) and uncapped 20 MLs (gray curve) as a function of time in different environments. The vacuum, nitrogen and air environments are indicated by blue, orange dashes and white background pattern, respectively. The 2 MLs and 20 MLs were grown on GaAs (111)B and on a sapphire substrates, respectively.

The initial resistivity of the sample without the capping layer is slightly higher than that of the sample capped with AlO_x. It is most probably related to the air exposure during sample preparation, which was also observed in dependence of resistivity on temperature (Figure 6.23). A strong increase of the resistivity over time is observed for the uncapped sample, in contrast to the resistivity of the capped one, whose resistivity remains constant. A small

rise of the resistivity of the uncapped sample under low vacuum conditions is observed. It is faster in the nitrogen atmosphere and much faster in the air. The results demonstrate that applying in-situ AlO_x capping shields the samples from degradation upon air exposure. In order to verify if the thicker layers are more resilient to air degradation, uncapped 20 MLs-thick was also measured. Figure 6.25(b) shows the resistivity dependence of the thick uncapped sample as a function of time and gas environment (gray curve), compared with thin, uncapped 2 MLs (black asterisks, note that the black curve from Figure 6.25(a) are the same data, just in different scales). The resistivity of the 20 MLs remains almost constant. Sample remained unchanged for several years so far.

During the measurements, the average humidity of air slightly changed, affecting the resistance change rate. Figure 6.26 shows the relative change of the resistivity ($\Delta\rho$) of the uncapped sample as a function of time in air, of two average humidity (AH) values. The data showed that for higher average humidity, the relative change of the resistivity was higher.

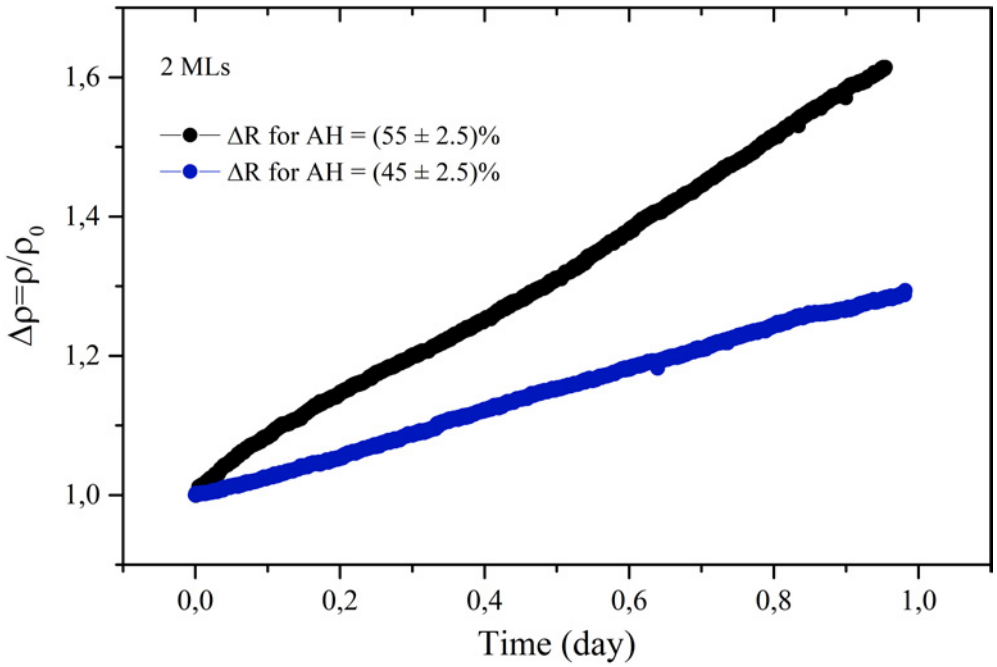

Figure 6.26: Electrical characterization of $MoTe_2$ layers. The room-temperature relative change of the resistivity of the uncapped 2 MLs as a function of time in air, under two average humidity (AH) values.

The above findings demonstrate that ultra-thin uncapped $MoTe_2$ layers degrade fast. The sample resistivity rises both in vacuum and in nitrogen and in air. The rise of the resistivity can be minimized for the thick samples, where probably the oxidation of the top layers protects the bulk. In order to protect the ultra-thin layers, the protection cap is necessary and AlO_x capping is shown to prevent samples from degradation.

To verify the electric properties of $MoTe_2$ grown on the sapphire substrate, the 20 MLs of the 2H-$MoTe_2$ were chosen for magnetotransport measurements. The sample was cleaved and the In contacts were deposited on top of the sample. The geometry of the Hall-bar was defined with the scriber. Figure 6.27 shows the dependence of resistivity on temperature ρ(T) for the studied layer. An increase of resistivity is observed when the temperature is decreased, as expected for the semiconducting phase. Studied layers are stable and do not degrade as their resistivity dependence is practically the same as measured one year later.

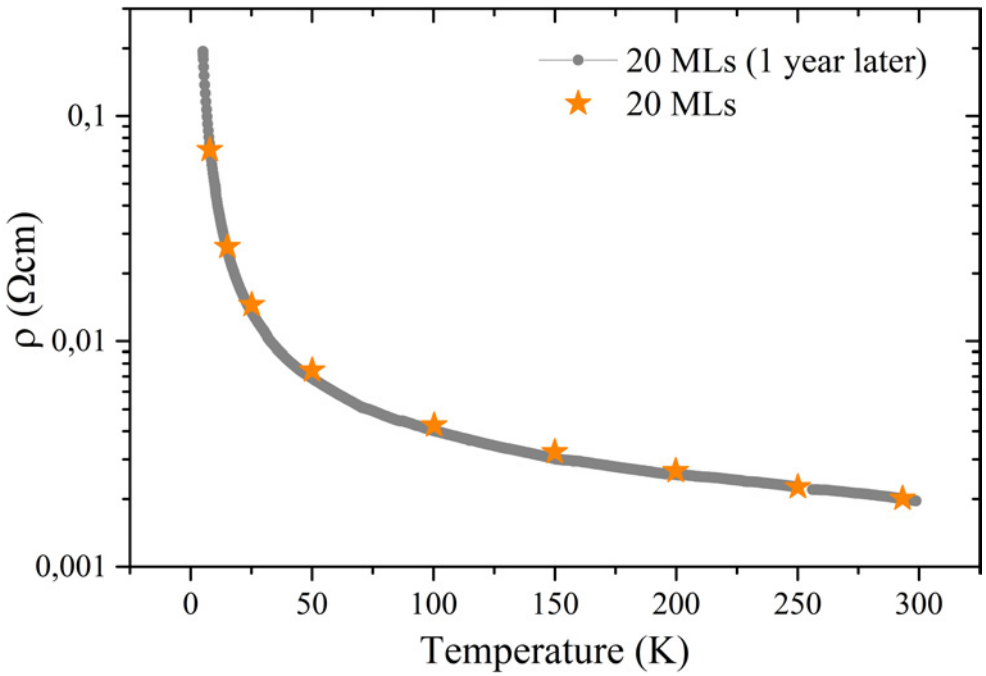

Figure 6.27: Electrical studies of $MoTe_2$ layers. The resistivity dependence on temperature for uncapped 20 MLs.

Figure 6.28(a) presents the Arrhenius plot: resistivity of the sample as a function of the inverse temperature. The data are displayed in this way to verify whether a linear fit is indicative of band transport. The results show that temperature dependence of resistivity does not follow the typical, semiconducting character with activation in the whole temperature range.

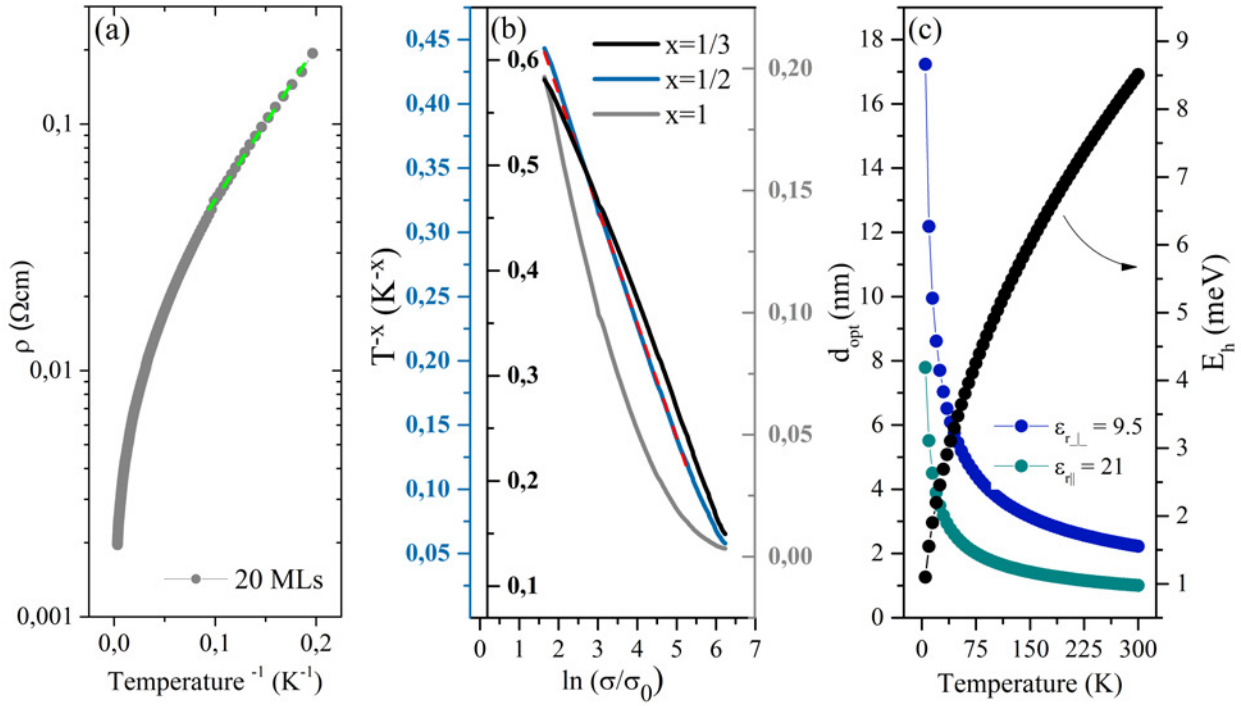

Figure 6.28: Electrical characterization of $MoTe_2$ layers. (a) Resistivity as a function of inverse temperature. The green, dashed line presents a linear fit for the activation energy calculations. (b) The conductivity models applied for the data. Grey, black and blue curves correspond to the band transport model, Mott and Efros-Shklovskii VRH, respectively. Dotted, red line shows fit, providing the optimal hopping distance and the optimal hopping energy, presented in (c) as a function of temperature. ε_r defines relative permittivity ($\varepsilon_{r\perp}$=9.5, $\varepsilon_{r\parallel}$=21 for 2 MLs of 2H-$MoTe_2$ [239]).

Although the band transport model does not fit in the whole temperature range, it can be applied to some parts of data (see green, dashed line). The activation energy E_A below T=10 K is $E_A = (0.53 \pm 0.01)$ meV. It is considerably lower than the energy gap of 2H-$MoTe_2$ ($E_g \sim 1$ eV) but it reasonably corresponds to the energies of shallow impurities in 2H-$MoTe_2$ layers, grown by MBE technique, and being equal to 18 meV [240] or 120 meV [190]. Hopping models were also taken into account as a fisrt description. The data were plotted in transformed coordinates such that a linear behavior suggests consistency with a particular charge transport model. Figure 6.28(b) presents the dependence of the inverse temperature on the power of x, as a function of the natural logarithm of the conductivity $\sigma(T)$. The Mott VRH and band transport models are presented by black and gray curves, respectively. Both curves exhibit nonlinear dependence, meaning that the data do not correspond well to the models. The best $\sigma(T)$ description is obtained for Efros-Shklowvkii model, described by $x = \frac{1}{2}$ as shown by the blue curve and red, dashed line. The wide-temperature linear behavior of $\ln(\sigma(T^{-1/2})/\sigma_0)$, consistent with the Efros–Shklovskii model, suggests a certain degree of disorder in the sample. STEM analysis revealed the presence of grains boundaries (see Figure 8.2(a)), supporting this interpretation. In the frame of this model, charge transport is described by a hopping energy difference (E_h) and an optimal hopping distance (d_{opt}). From linear fit (see red, dashed line) one can obtain the T_0 parameter, defined as $ln(\sigma(T)/\sigma_0) \cdot T^{-x}$

slope. Typical values of T_0 are of order of one thousand kelvins or higher [190]. From T_0 parameter ($T_0 \sim 104$ K), α, d_{opt} and E_h were calculated (see equations 3.5, 3.6 and 3.7). Figure 6.28(c) shows values of d_{opt} and E_h as a function of temperature. The optimal hopping distance decreases as a function of temperature and it is of order of single nanometers which corresponds to the size of the grain boundaries captured in the STEM images. The optimal hopping energies are of order of a few meV. Their values increase with temperature. Low-temperature E_h matches effective activation energy obtained from Arrhenius plot.

Figure 6.29 presents the magnetoresistance dependence on magnetic field for different values of temperatures for the same 20 MLs of $MoTe_2$ on sapphire. The resistivity tensor measurements in a wide temperature range showed that the longitudinal resistivity (ρ_{xx}) component is strongly magnetic field- and temperature-dependent.

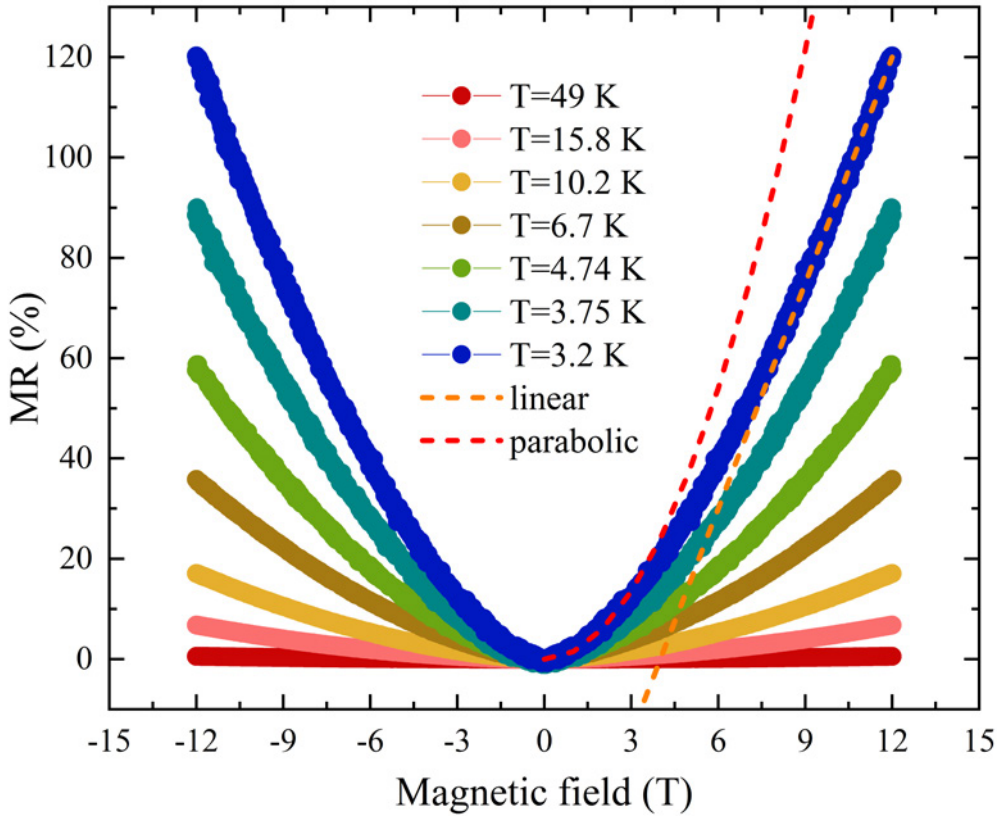

Figure 6.29: Electrical characterization of $MoTe_2$ layers. The magnetoresistance dependence on magnetic field for different values of temperatures. The weak- and strong-magnetic field contributions to the magnetoresostance were marked by the dashed red parabola and orange line, respectively.

At T=3.2 K and at B=12 T, the MR reaches more than 120%. In the systems with a band transport, large magnetoresistance is governed by the high mobility of the carriers. In this case, a charge transport is dominated by hopping and carriers with high mobilities are not expected. For disordered systems one may refer to the wave-function shrinkage model [241, 242]. The wave-function shrinkage model describes the way the magnetic field affects s-shaped wave-functions. This leads to decrease in their overlap and thus to reduction of the hopping probability between two sites. It causes an increase of the resistivity with increasing magnetic

field and thus MR occurs. The parabolic MR dependence is present in a weak magnetic field range (marked by the red, dashed line) but becomes linear at strong one (marked by the orange dashed line) which may reflect the presence of disorder [243].

No variation of the transverse resistivity (ρ_{yx}) component was resolved. The unmeasurable Hall resistivity may indicate a high concentration of the carriers.

6.2.3.3 The role of layer thickness

To verify whether the charge transport depends on the thickness of the $MoTe_2$ layers, magnetotransport studies were performed on samples with various numbers of monolayers (1 ML, 3 MLs, 6 MLs, 12 MLs, and 30 MLs) grown on SI GaAs (111)B substrates. The substrate temperature was set to T_S = 270 ^{o}C, to obtain 2H semiconducting phase. All the samples were annealed after the growth for 10 minutes at T_S = 450 ^{o}C and then capped with AlO_x. Figure 6.30(a) presents the temperature dependence of the resistivity $\rho(T)$ of layers with different thicknesses, starting from the 30 MLs, down to 1 ML.

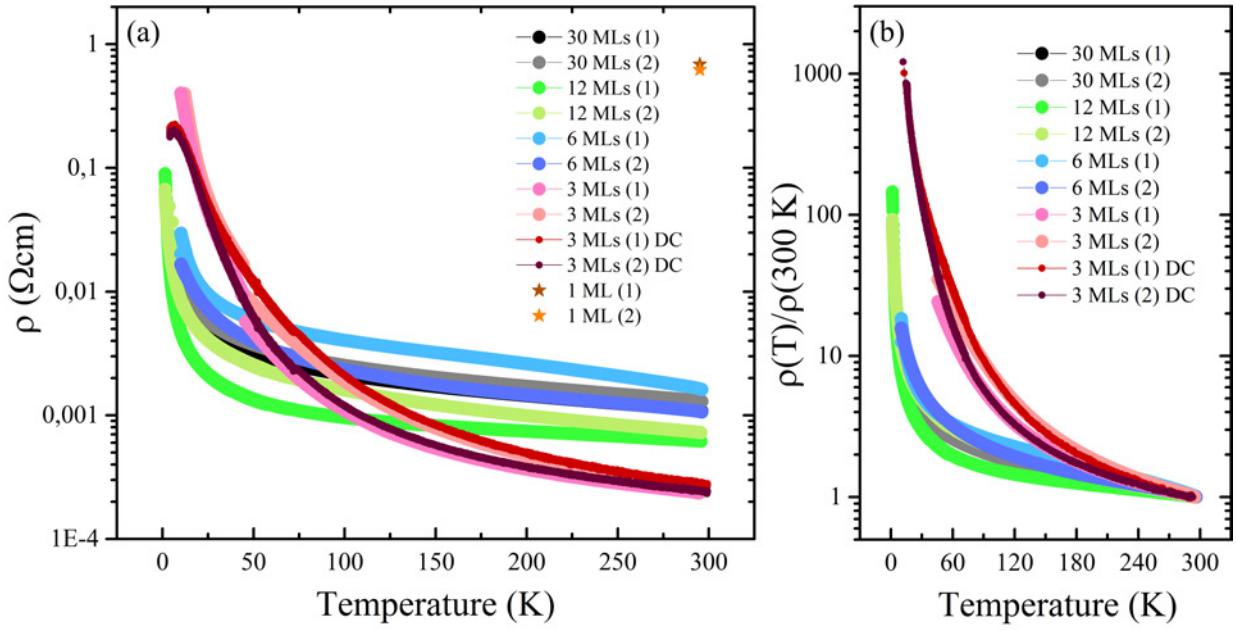

Figure 6.30: Electrical characterization of $MoTe_2$ layers. (a) Resistivity of $MoTe_2$ as a function of temperature for various $MoTe_2$ thicknesses. (b) The temperature resistivity dependence, normalized to the room temperature, for samples of various thicknesses.

The numbers (1) and (2) in the legend refer to two different pairs of contacts. The room temperature resistivity values present a large variation of about one order of magnitude. The resistivities of the two nominally identical longitudinal signals were observed to vary by 50%. As the geometry of the samples is well defined, the resistivity discrepancy has to reflect sample inhomogeneity. All the $MoTe_2$ samples have a similar (but not identical) character of $\rho(T)$ dependence with a rise of resistance at low temperature. Qualitatively, this kind of

dependence is indeed expected for the 2H-semiconducting phase as already discussed in the previous chapters. A correlation between thickness and room temperature resistivity was not observed. Although the rise of the $\rho(T)$ at low temperatures is observed for all the samples, the character of the relative change of the $\rho(T)$ is different, as presented in Figure 6.30(b). One can observe that the characteristics for all the samples group in two classes: those of the thickness equal or higher than 6 MLs and those of 3 MLs. The resistivity of the 1 ML is significantly higher than for other samples, as presented by the orange asterisks in Figure 6.30(a), differing almost by four orders of magnitude at room temperature. The temperature dependence of the resistance of 1 ML is presented in Figure 6.31(a). To experimentally reach the teraohm resistances, the measurements were conducted in a special setup with voltage followers. The room-temperature resistance of the semiconducting 1 ML exceeds R = 150 MΩ (~ 1 Ω· cm). With decreasing temperature, the resistance of the sample increases exponentially reaching R=225 $T\Omega$ (2.5 MΩ · cm) at T=60 K. The room-temperature resistance of the SI GaAs (111)B substrates, guaranteed by AXT Company, which supplies epitaxial substrates, is greater than R = 12 GΩ (200 MΩ · cm), confirming that the observed room-temperature signal originates purely from $MoTe_2$ layer. At 60 K, the resistance of the 1 ML sample is so high that it is unclear whether it originates from the layer itself or from the substrate. To mark the different character of the temperature dependence of the resistivity between the 1 ML and 3 MLs, two $\rho(T)$ curves were presented in Figure 6.31(b).

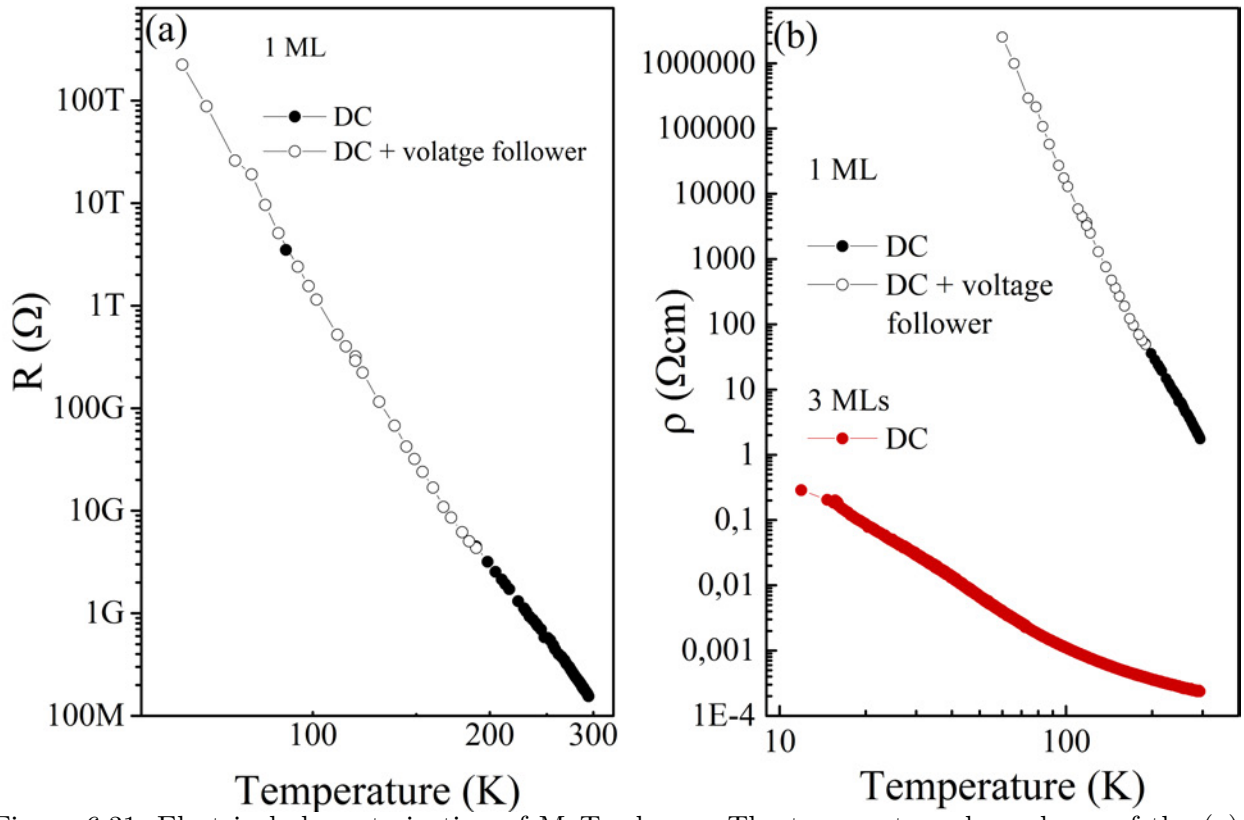

Figure 6.31: Electrical characterization of $MoTe_2$ layers. The temperature dependence of the (a) resistance of 1 ML and (b) resistivity of 1 ML and 3 MLs of $MoTe_2$.

In order to explain the observed character of $\rho(T)$ dependence of all samples, two models of conductivity were taken into account: band transport and hopping, as previously described. As before, instead of fitting the data to a specific model, the data were presented in such a way that a most linear dependence would indicate the applicability of a given charge transport mechanism. Figures 6.32(a)-(b) show the dependencies of the inverse temperature on the power of x, as a function of the natural logarithm of conductivity for 1 ML.

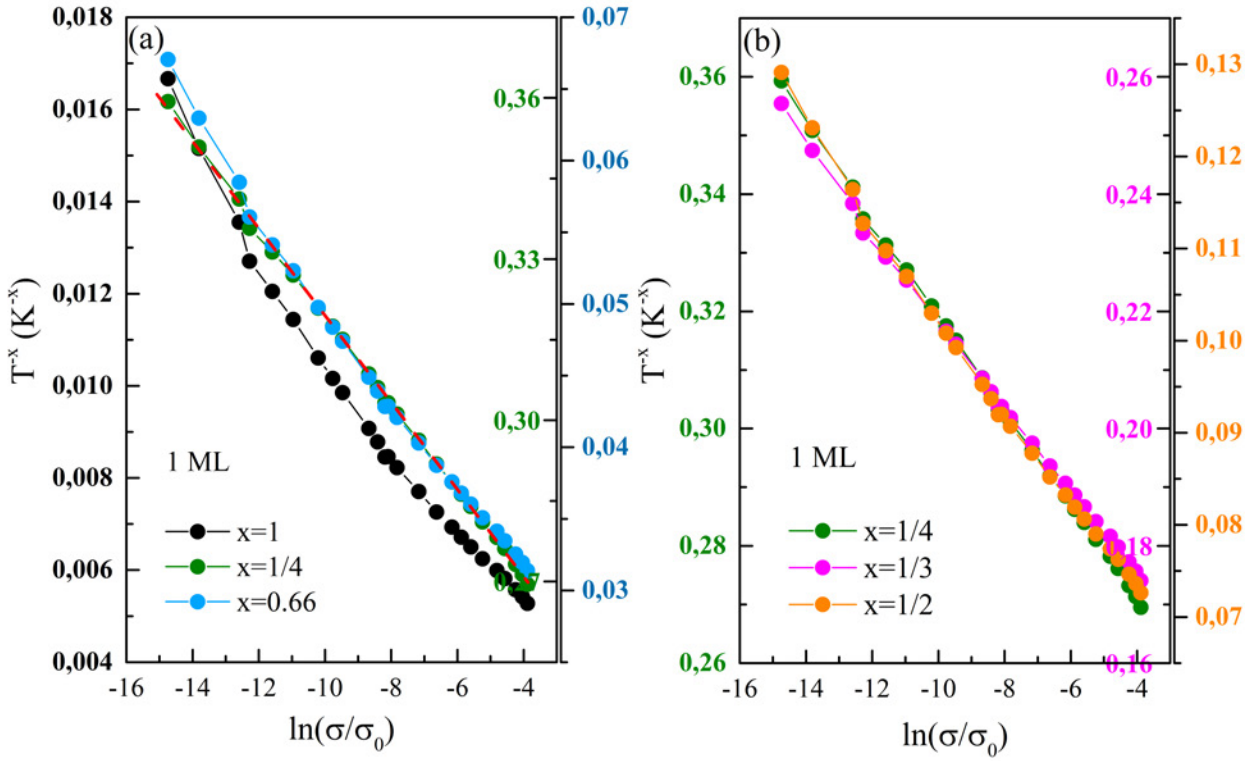

Figure 6.32: Electrical characterization of $MoTe_2$ layers. (a)-(b) The conductivity models for 1 ML. Black and green curves correspond to the band transport and Mott VRH models, respectively. The blue curve corresponds to an anomalous exponent of x=0.66, previously observed in 2 MLs of 2H-$MoTe_2$ [40]. The pink and orange curves correspond to the 2D Mott and the Efros–Shklovskii VRH models.

The band transport and the 3D Mott VRH models are presented by black and green curves, respectively. The blue curve corresponds to an anomalous exponent of x=0.66, previously observed in 2 MLs of 2H-$MoTe_2$ [40]. The linear behavior, shown by the red, dashed line, is observed for x=1/4, suggesting that the charge transport is realized by hopping. Figure 6.32(b) presents the hopping conductivity models including also Efros-Shklovskii and 2D Mott VRH regimes. The similar linear trends are observed in all models. Thus it is not possible to conclude about the model basing on these results.

Figures 6.33(a)-(d) present the conductivity models for 3 MLs and 30 MLs, respectively.

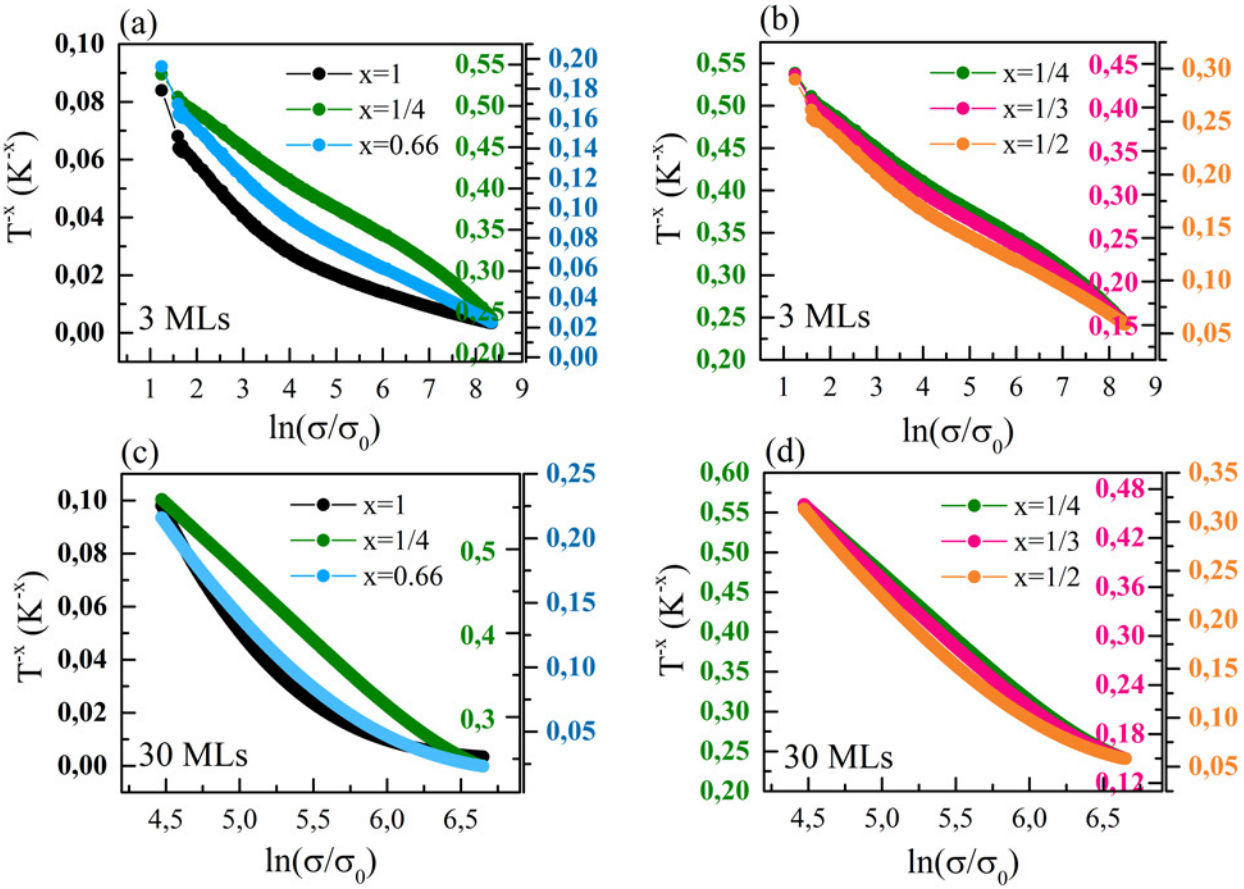

Figure 6.33: Electrical characterization of $MoTe_2$ layers. The conductivity models for (a)-(b) 3 MLs and (c)-(d) 30 MLs. Black and green curves correspond to the band transport model and Mott VRH, respectively. The blue curve corresponds to an anomalous exponent of x=0.66, previously observed in 2 MLs of 2H-$MoTe_2$ [40]. The pink and orange curves correspond to the 2D Mott and the Efros–Shklovskii VRH models, respectively.

The band transport and the 3D Mott VRH models are presented by black and green curves, respectively. The blue curve corresponds to an anomalous exponent of x=0.66. The pink and orange curves correspond to the 2D Mott and the Efros–Shklovskii VRH models. None of the exponent gives linear dependence in $ln(\sigma)$ versus T^{-x} coordinates. The best agreement is obtained for x=1/3 i.e. 2D Mott VHR.

Resistivity tensor measurements was measured as a function of magnetic field up to 12 T for various temperatures. It revealed no expected features in the longitudinal magnetoresistance. Figure 6.34 presents typical dependence of magnetoresistance for 30 MLs, measured at T=1.5 K.

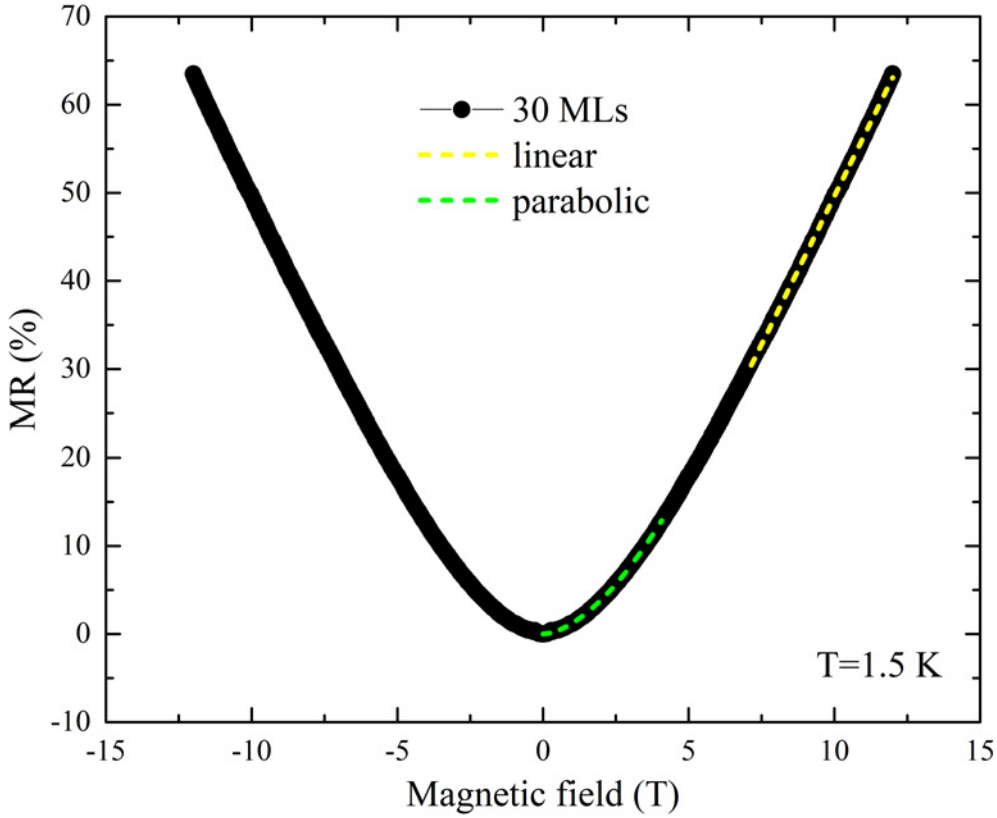

Figure 6.34: Electrical characterization of $MoTe_2$ layers. The MR of the 30 MLs measured at T=1.5 K. The green and yellow curves show the parabolic and linear fits, respectively.

The MR does not exceed 65% at low temperature at 12 T. The parabolic contribution is observed at weak magnetic fields (marked by the green, dashed curve), while at strong magnetic fields, a linear, non-saturating MR is observed, marked by the yellow, dashed line. The linear component may originate from disorder [243], which is presumably present in the system. Due to the high carrier concentrations and substantial inhomogeneity of the layers the transverse component of the resistivity tensor was not measurable.

Supplementary preliminary results of $MoTe_2$ layers grown on InAs (111) substrate are included in Appendix C in section C.3.2.

Chapter 7

TaAs

7.1 State of knowledge

7.1.1 Crystal structure

Tantalum arsenide (TaAs) is a transition metal pnictide, belonging to the family of the binary compounds, also including TaP, NbAs and NbP. tetragonal TaAs (t-TaAs) crystallizes in a body-centered-tetragonal NbAs-type structure with a non centrosymmetric space group $I4_1md$ (#109, C_{4v}) and the lattice parameters of a=b=3.4338 $\AA$ and c=11.641 $\AA$ [244]. The scheme of the crystal structure of the TaAs in the tetragonal phase is presented in Figure 7.1(a).

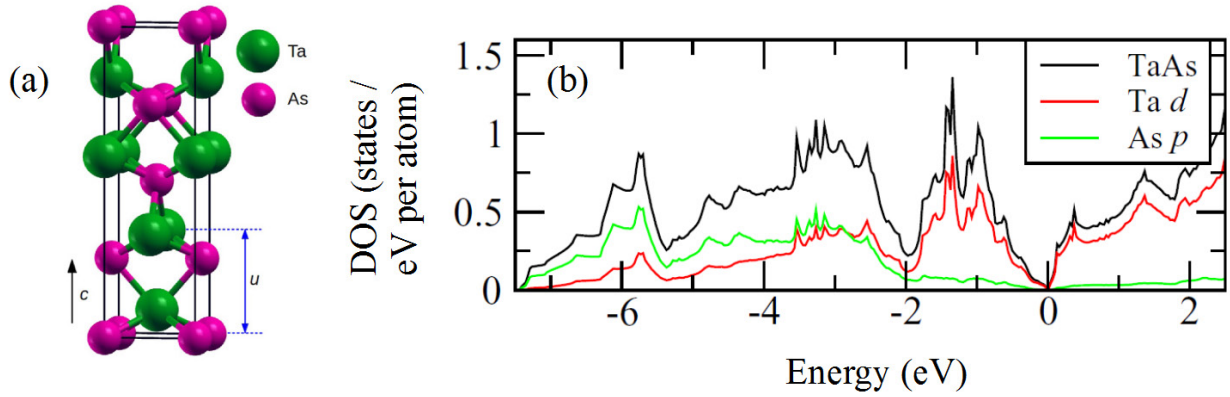

Figure 7.1: (a) The body-centered crystal structure of tetragonal t-TaAs. The green and violet balls represent the Ta and As atoms, respectively. (b) DOS and Ta-d and As-p orbital contributions for the bulk TaAs, marked by the black, red and green curves, respectively [245].

The crystal structure of TaAs consists of the two interpenetrating Ta and As sublattices, shifted relative to each other by $(\frac{a}{2}, \frac{a}{2}, \frac{c}{12})$ vector [246]. Ab-initio studies of TaAs bonding properties showed that in addition to ionic and covalent bondings, TaAs has also some metallic bondings as well [247]. Symmetry operations of t-TaAs include the fourfold screw (C_{4v}) rotation along the z axis and two mirror reflections with respect to the x and y axes. Due

to the lack of the horizontal mirror plane, TaAs has no inversion symmetry [245]. Inversion symmetry breaking leads to the emergence of the Weyl state, with Weyl nodes of opposite chiralities. Electron configurations of Ta and As atoms are $[Xe]6s^2 4f^{14} 5d^3$ and $[Ar]4s^2 3d^{10} 4p^3$, respectively. Covalent bonds are formed by electrons from Ta-5d orbital and electrons from As-4p orbital, as shown in Figure 7.1b, where the projection of the total DOS and Ta-d and As-p orbital contributions are presented. The zero energy (E=0 eV) defines the E_F position.

7.1.2 Bulk and surface Weyl fermions

Figure 7.2(a) shows the bulk Brillouin zone and its (001) surface projection of TaAs with the corresponding high-symmetry points, marked by the green and red dots, respectively [248].

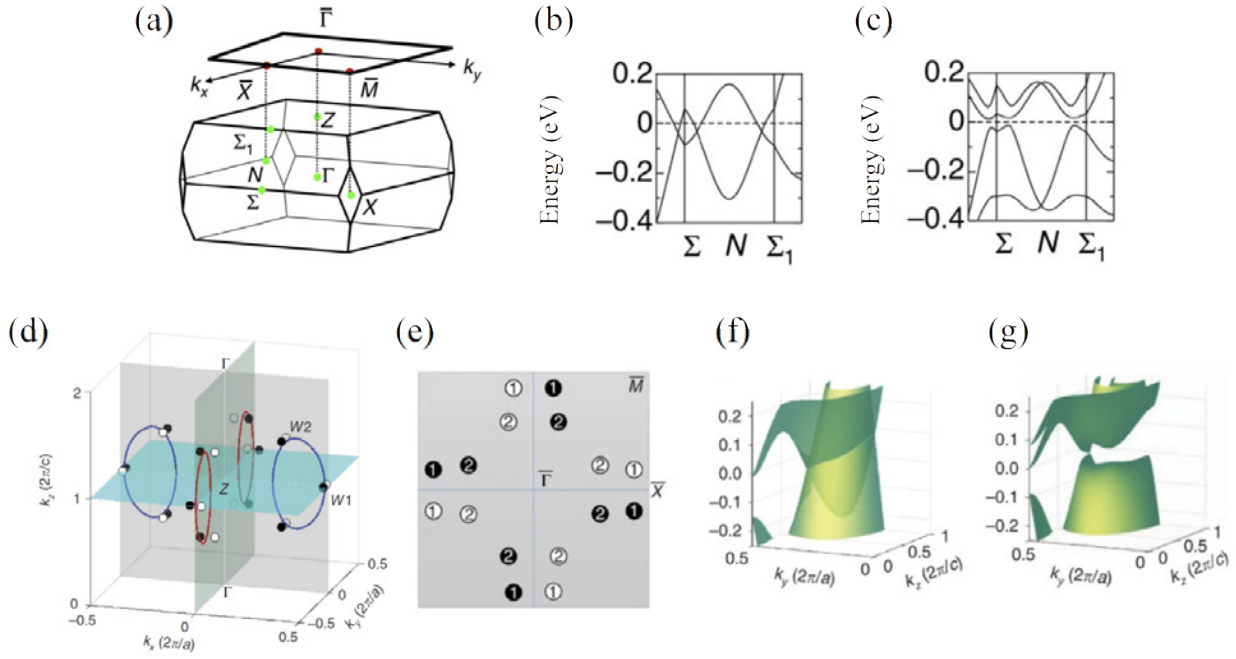

Figure 7.2: (a) The bulk and (001) surface high symmetry points in the TaAs BZ, marked by the green and red dots, respectively. TaAs bulk band diagram (b) without and (c) with the SOC. The zero-energy defines the position of the E_F. (d) The scheme of the nodal lines and the Weyl points in the reciprocal (k_x, k_y, k_z) lattice. (e) The scheme of the projected Weyl points on to (001) surface BZ. The TaAs bulk band diagram around one red nodal line (f) in the absence or (g) in the presence of the SOC [248].

As shown in Figure 7.2(b), in the bulk structure of TaAs without the SOC, conduction and valence bands cross along $\Sigma - N - \Sigma_1$ direction, giving rise to the nodal line semimetal (see Figure 1.1(a)). However, if the SOC is taken into account, the nodal line transforms into 6 Weyl points, as presented in Figure 7.2(c). There are 24 Weyl nodes in total. Figure 7.2(d)

shows the position of the nodal lines (in the presence of SOC) and Weyl points (without SOC). 8 Weyl points are on the k_z plane, called W1, and 16 other Weyl points, called W2, are slightly shifted from the k_z mirror plane. The projection of the Weyl points into the (001) plane is shown in Figure 7.2(e). Figures 7.2(f)-(g) present the energy dispersions near one of the W1 Weyl nodes (f) without the SOC, around one of the red nodal line and (g) in the presence of the SOC, where the touching point appear, forming a Weyl point. The W_1 and W_2 Weyl nodes are separated by $\Delta E \sim 13$ meV offset, as schematically presented in Figure 7.3(a) [68].

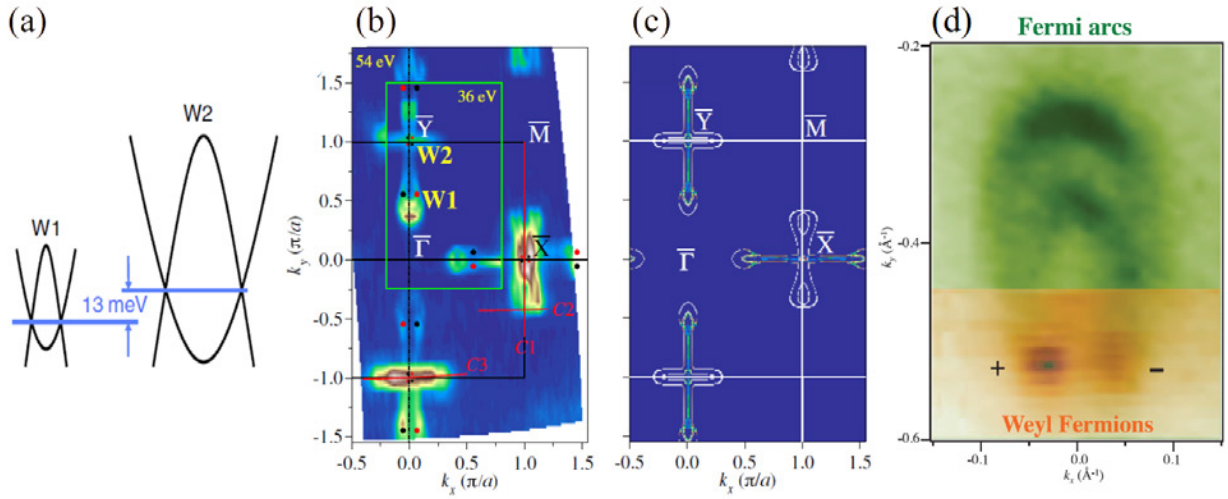

Figure 7.3: (a) The schematic illustration of the energy dispersions of the W_1 and W_2 Weyl cones [68]. The (b) ARPES measurements and (c) the theoretical calculations of the TaAs (001) surface states [249]. (d) The high-resolution ARPES maps of Fermi arcs and the bulk Weyl fermion nodes [246].

Lv et al., and Xu et al., have investigated the electronic structure of the TaAs with the use of the photoemission studies. Figures 7.3(b)-(c) show the surface ARPES measurements on TaAs sample, grown by CVT method, and the corresponding DFT calculations. The spectrum, taken at E=36 eV shows the position of the W_1 and W_2 Weyl points along $\Gamma \rightarrow L$ and $\Gamma \rightarrow X$ directions, marked by the smaller and larger black and red dots, corresponding to opposite chiralities [249]. Figure 7.3(d) shows the surface-bulk high resolution ARPES map of the Fermi arcs and the Weyl fermion nodes [246].

7.1.3 Structure of tetragonal TaAs samples

At the time this project was initiated, the structural and magnetotransport properties of TaAs layers had not yet been fully investigated, and no samples had been grown using the MBE method. Achieving large-scale, monocrystalline growth of TaAs remained a significant challenge. The idea was to grow this material by MBE and to study its physical properties. The MBE was used for the first time for the growth of this material, however, Yanez et al. [100] have also published their MBE-grown TaAs results in 2022. The growth procedure

of the first TaAs samples can be found in the paper by Sadowski et al. [250]. In this PhD dissertation an extension of the observations is presented, both with wide analysis, leading to discovery of new Weyl semimetal TaAs phase. In the following two sections experimental results of bulk tetragonal t-TaAs are presented, supplemented with the structural results for MBE-TaAs, to show the typical defects.

A large-scale and high quality selective growth of TaAs still remains a challenge due to its frequent non-stoichiometric composition and a large amount of planar defects such as stacking faults, commonly reported in literature [245, 251, 252, 253, 250, 254]. Stacking faults disorder has already beed observed in 1954 [255] and 1984 [256] in other three semimetals: NbP, TaP, NbAs. Figure 7.4(a) shows the scheme of the TaAs cross-section with the proper arrangement of the Ta and As atoms without the stacking faults. The cell of four Ta and two As atoms is marked by the blue box and pink and green balls, respectively, are shifted along [001] axis.

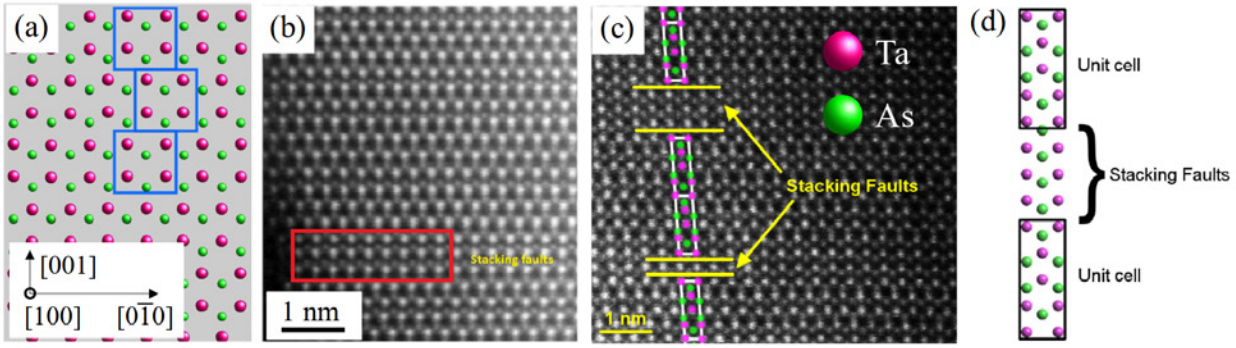

Figure 7.4: (a) The scheme of the proper arrangement of the tetragonal t-TaAs atoms without the stacking faults [250]. (b)-(c) The TEM cross-section image of the single crystal TaAs, grown by CVT method, with the indicated stacking faults disorder [253]. (d) The scheme of the stacking fault between the stoichiometric TaAs unit cells. The pink and green balls represent Ta and As atoms, respectively [251].

If that shift is disturbed, the planar defects appear in the form of the stacking faults as presented in Figures 7.4(b)-(c). The scheme of the stacking fault defect between the stoichiometric t-TaAs unit cells is presented in Figure 7.4(d).

A microscopic picture of the TaAs morphology can be obtained from the high angle annular dark-field scanning transmission electron microscopy images, presented in Figures 7.5(a)-(b).

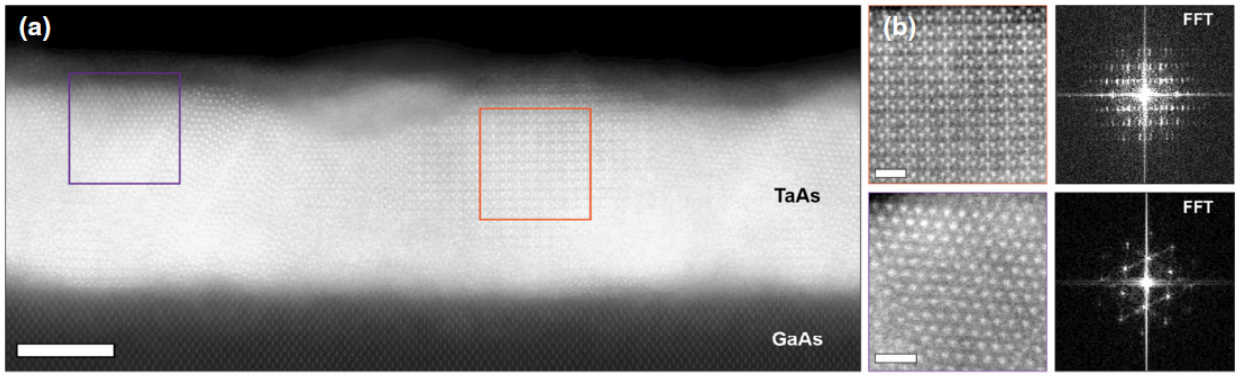

Figure 7.5: (a) The TEM cross-section image of the TaAs grown on GaAs substrate. The violet and orange boxes show the TaAs areas with different crystal orientations. (b) The zoomed area of the (a) of two individual TaAs crystal orientations. (c) The FFT images of the corresponding TEM areas. The white bar depicts a 5 nm scale [100].

Figure 7.5(a) shows STEM image of the MBE-grown TaAs [253] with two crystalline regions of different TaAs orientations, marked by the violet and orange boxes. The crystallographic structure can be also analyzed by the Fourier transform of smaller sections of the film which also show the individual crystal orientations, as shown in four panels of Figure 7.5(b). It shows the polycrystalline nature of the TaAs film and the grain-boundary regions. The lack of single crystal growth of TaAs is possibly resulting from the large lattice mismatch between TaAs film and GaAs substrate, being 17.5% in the [100] direction and 16.5% in the [110] direction. For the same reason, the clean and sharp interface between the layer and the substrate is not observed. Weyl semimetals are robust against any weak perturbations that preserve translational symmetry. For instance, a slight lattice distortion would shift only the position of the Weyl points [257]. However, if the translational symmetry is broken or the surface termination is disturbed by the dangling bonds, the surface band structure of the studied material significantly changes. Figures 7.6(a)-(b) show the surface projected Fermi surfaces of the P- or Ta-terminated TaP.

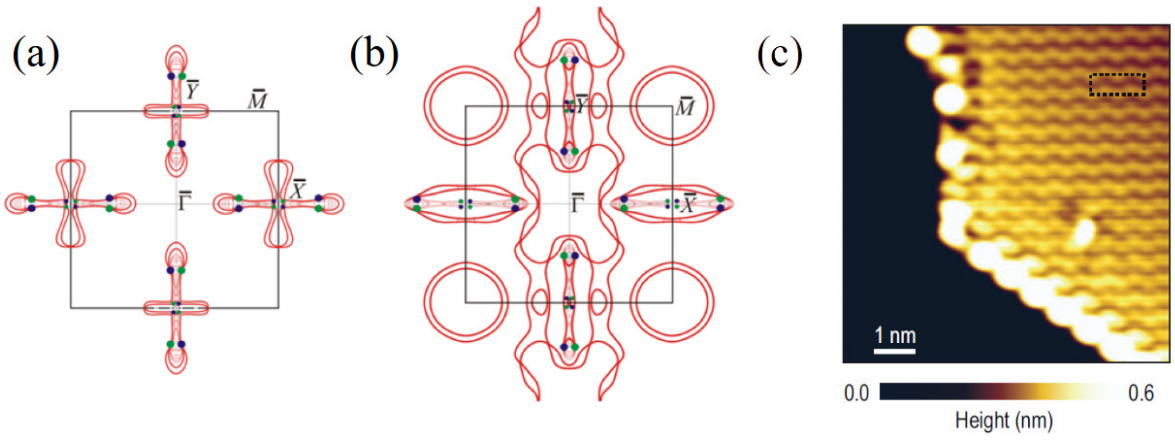

Figure 7.6: The Fermi surfaces of the (a) P-terminated and (b) Ta-terminated TaP [257]. (c) The HR STM topographic image of the cleaved (112) TaAs surface. The black rectangle depicts the TaAs inverse lattice unit cell [258].

It is visible that depending on the anion or the cation terminations, both the Fermi surface symmetry and the projections of the Weyl points significantly differ. Moreover, the grain-boundary regions also induce the presence of the higher-symmetry surfaces on the edges of the sample such as (112) or (114) planes. Figure 7.6(c) shows the HR STM topographic image of the cleaved (112) TaAs surface. Zheng et al. [258] have shown that some planes like (001) are the arc allowed surfaces (AAS) and on some, like (100) or (110), topological Fermi arcs are not expected to exist [259], forming the arc-forbidden surfaces (AFS).

7.1.4 Electrical properties

Figure 7.7 shows the normalized resistivity as a function of the temperature for TaAs samples, grown by CVT method.

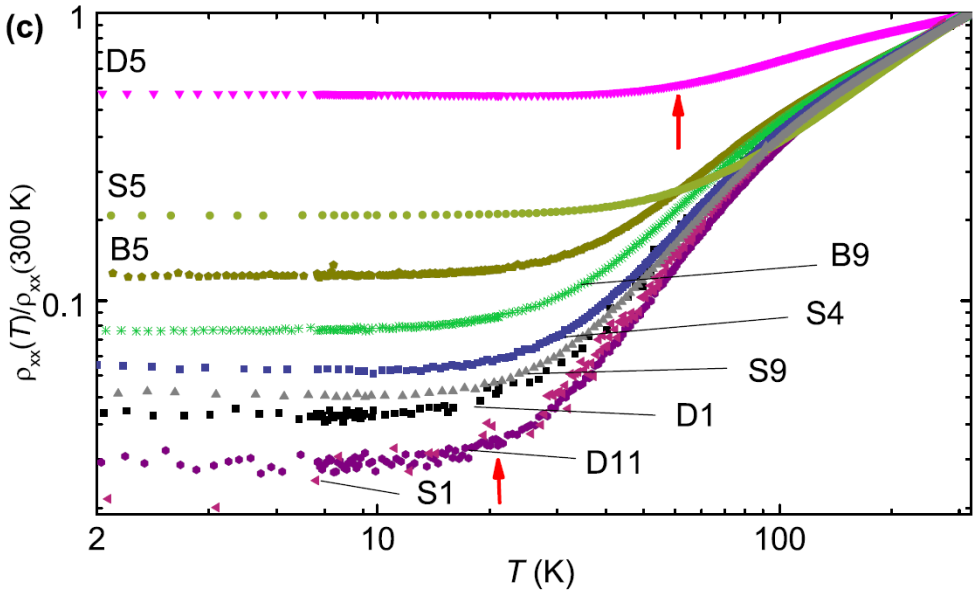

Figure 7.7: The double-logarithmic plot of the normalized resistivity as a function of the temperature for CVT TaAs sample [260].

The resistivity dependence on temperature shows a metallic profile. It is characterized by relatively low RRR, not exceeding 49. One can see that the growth parameters can significantly change the quality of the layers by shifting the crossover to plateaus, marked by the red arrows, and thus decreasing the low temperature residual resistivity. The samples with lower RRR were shown to have much more stacking disorder, most probably induced by the pnictide deficiency [261]. Xiang et al. [262] have demonstrated that TaAs shows a distinct anisotropy in the electrical transport. Figure 7.8(a) presents the TaAs temperature resistivity dependence, measured for two current directions, along a or c crystal axes.

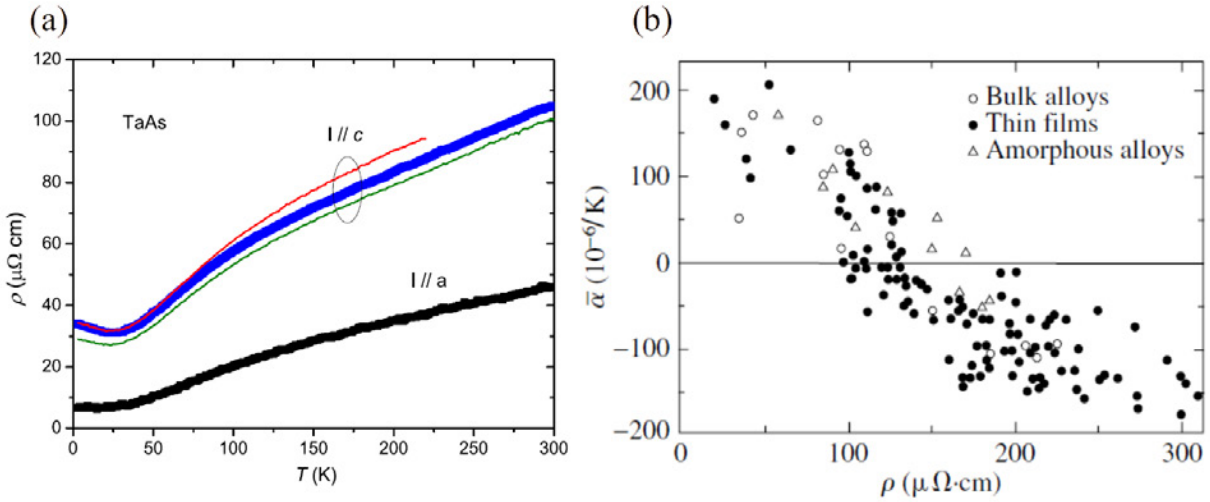

Figure 7.8: (a) The TaAs temperature resistivity dependence, measured for two current directions along a or c crystal structure axes [262]. (b) The correlation between the resistivity of the various transition metal alloys and their temperature coefficient α [263].

The resistivity dependence on temperature measured along a axis is lower than measured along c axis. The room-temperature resistivity along the c axis is almost three times larger than that along the a axis. The electrical anisotropy of the TaAs is related to the W2 Fermi surface which shows a high anisotropy compared to the W1 FS which is isotropic [264, 262]. Consequently, the projection of the W2 FSs onto the (001) plane is much smaller than onto the (100) plane. The calculations also confirm higher resistivity observed for c axis, due to W2 FS pockets playing major role in the TaAs electrical transport.

In 1973 an interesting rule was proposed by J. H. Mooij [263], who showed that there is a correlation between the resistivity of the disordered metal alloys and their temperature resistance coefficient α, described by formula 7.1:

$$\alpha = \frac{1}{R} \cdot \frac{dR}{dT} \tag{7.1}$$

Figure 7.8(b) shows a trend between the resistivity of the different transition metal alloys and their temperature coefficient α. Whether the sample resistivity is higher or lower than $\rho \sim 100$ $\mu\Omega$cm, the material resistance derivative is either positive or negative, leading to metallic-like or semiconducting-like behavior. In 1965 Campbell et al. [265] proposed an explanation for the case of thin films which is based on the assumption that they are composed of a mixture of both metallic and oxidized phases. In a consequence, the positive α of the metal is compensated by the negative α of the semiconducting oxide. One can notice that the TaAs resistivity, measured for the current $I \parallel c$ is close to the $\rho \sim 100$ $\mu\Omega$cm, being at the metal to semiconducting oxide compensation boundary.

Magnetotransport investigations were performed by C. L. Zhang et al. [266], who investigated the MR of TaAs samples in different current configurations. Magnetic field was parallel to the current, which was along either a or c axes. Figures 7.9(a)-(d) present the relative

change of the resistivity with respect to the zero magnetic field for samples measured with current along (a)-(b) a or (c)-(d) c axes.

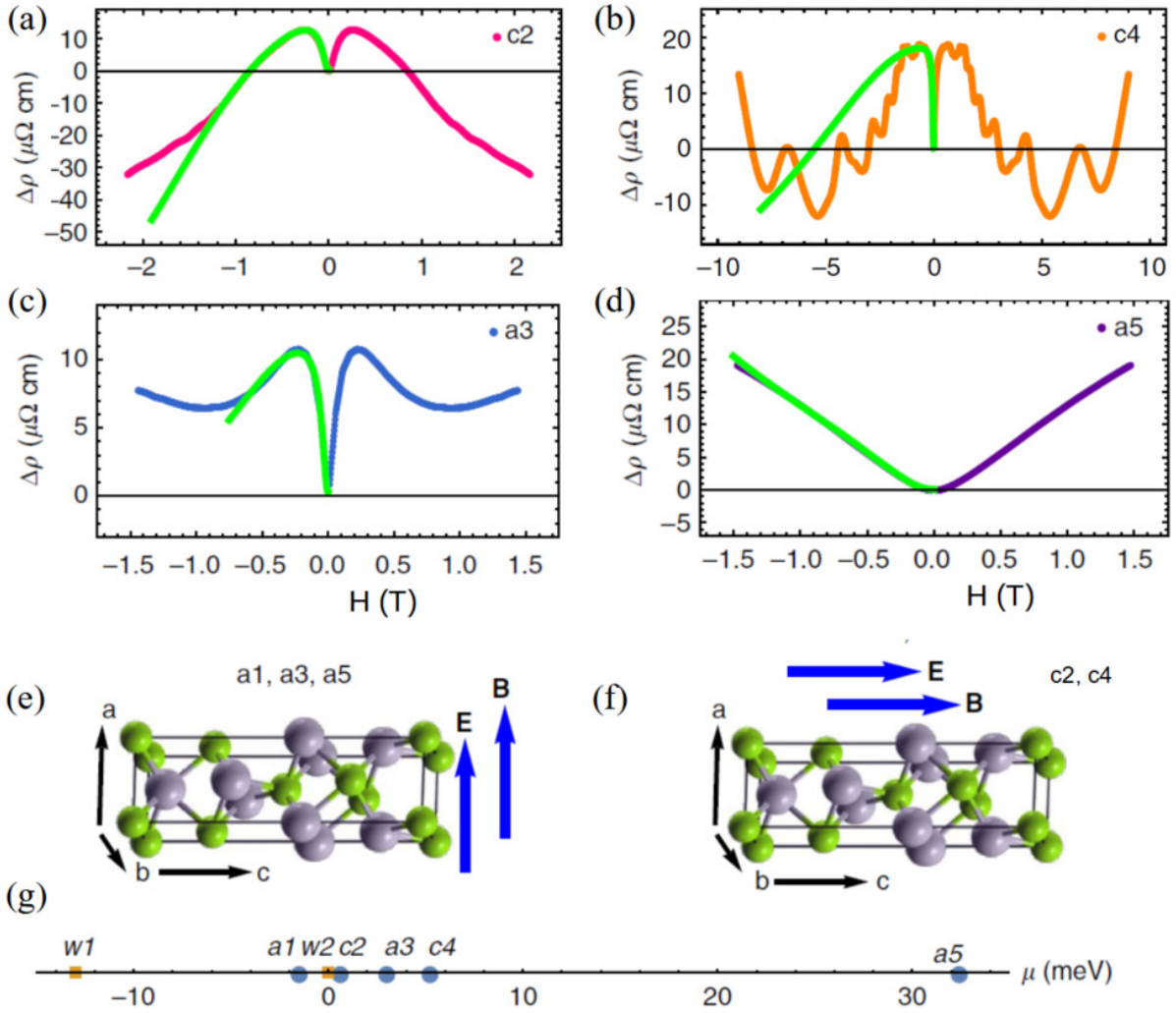

Figure 7.9: The magnetoresistance dependencies (a)-(d) for samples with different chemical potentials at two measurement geometries. The green curves present the fits in the semiclassical regime. Scheme of the TaAs measurement geometry with electric and magnetic fields (e) perpendicular or (f) parallel to the c axis with the corresponding samples' numbers. (g) The values of the samples' chemical potential with respect to the energy of the Weyl nodes, W1 and W2 [266].

The scheme of the TaAs measurement geometry with electric and magnetic fields (e) perpendicular or (f) parallel to the c axis is presented in Figures 7.9(e)-(f). The obtained results (a)-(d) reveal different contributions: negative MR, quantum oscillations and positive MR. Sample chemical potential was in different positions with respect to the Weyl points. As the topological properties arise from the Weyl fermions, its contribution to the overall transport may be limited if the E_F is far from the Weyl cones. Figure 7.9(g) shows the values of the chemical potential (blue dots) with respect to the energy of the Weyl (W1 and W2) nodes (orange dots). If the chemical potential is far from the Weyl points, as for the a5 sample, the NMR and the SdH oscillations vanish, leaving only small, positive and trivial MR.

7.2 Experimental results

The samples of the following numbers have been investigated experimentally: V195, V204, V222 V248, V250 and V272.

7.2.1 Substrate selection for the MBE-growth

As TaAs unit cell is square in the base, a 3D substrate of GaAs (001) (see Figure 7.10(a)) has been used for the TaAs growth [250]. To avoid any parallel conduction, all the samples were grown on semi-insulating (SI) substrate.

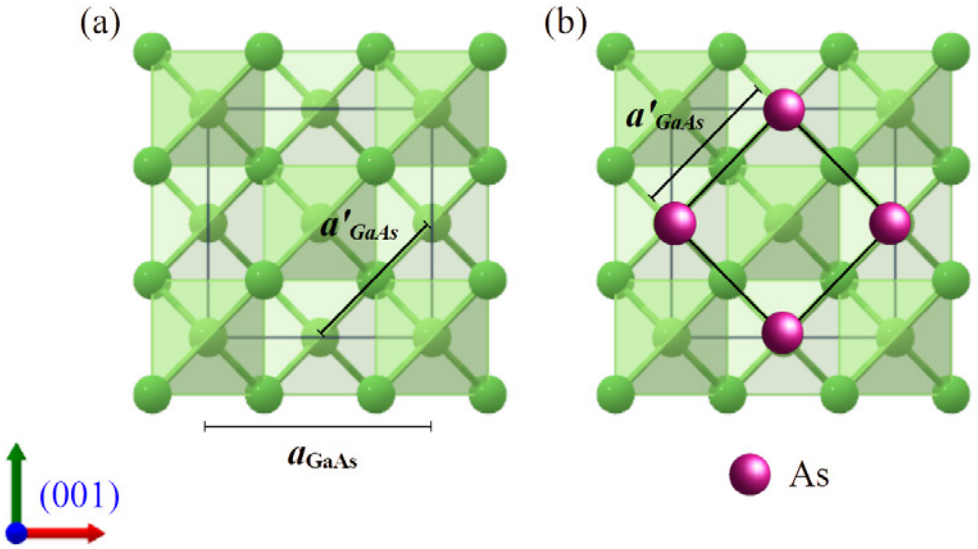

Figure 7.10: (a) The scheme of the top view of the GaAs (001), used as a substrate for the TaAs MBE growth [150]. (b) Orientation of the TaAs bottom unit cell during the MBE growth. The violet atoms correspond to the As atoms.

The in-plane lattice parameter of GaAs (001) is $a = 5.65$ Å [152] giving a substantial lattice mismatch (about 16.34%) between the GaAs (001) substrate and TaAs epilayer. The linear thermal expansion coefficient for the GaAs substrate is $\alpha_T = 5.73 \cdot 10^{-6}$ K^{-1}[152], much smaller than the linear thermal expansion coefficient of TaAs which is $\alpha_T = 1.741 \cdot 10^{-5}$ K^{-1} [247]. We found out that to minimize the lattice mismatch between the TaAs layer and GaAs substrate, the TaAs film naturally prefers to grow rotated by 45 degrees [250] as presented in Figure 7.10(b), where the bottom of the TaAs unit cell, schematically marked by the four violet As atoms, was layered onto the GaAs structure. An epitaxial relation to the substrate and the 45 degrees rotation of the corresponding [110] directions of the TaAs layer and the GaAs substrate was shown by XRD patterns in $2\Theta/\omega$ scans, as presented by Sadowski et al. [250]. Taking into account the temperature evolution of both materials, the high and low temperature values of strain are 16% and 20%, respectively, indicating that during the cooling process the layer gets additionally strained. This is a possible reason of resistivity instabilities observed during the cool-down processes (see Figure 7.25).

7.2.2 Growth parameters and sample characterization

After thermal oxide desorption upon heating to 600 ^{o}C in the As_2 flux, the 150 nm-thick GaAs buffer was grown at standard conditions: substrate temperature of T_S = 590 ^{o}C and As_2/Ga flux ratio of about 10. The TaAs growth was performed at the same temperature as used for GaAs buffer and with the same As_2 flux intensity. From the very beginning of TaAs deposition and throughout the whole growth, the streaky 2D surface diffraction RHEED patterns have been observed [250]. On the other hand, some differences in intensities of RHEED images, observed along [110] and $[\bar{1}10]$ azimuths of the GaAs (001) substrate, have been observed. The RHEED pattern along $[\bar{1}10]$ was slightly less intense and more blurred than along [110], suggesting some directional surface morphology.

7.2.2.1 AFM analysis

In order to clarify the origin of the observed differences in the RHEED patterns, the atomic force microscopy (AFM) analysis was performed. Images of the TaAs confirmed its surface anisotropy and have revealed a stripe-like surface morphology, consisting of the nanocolumns (NCs), always oriented along [110] direction. Figures 7.11(a)-(d) show the AFM images of the TaAs samples with different thicknesses: (a) ~ 8 nm, (b) 8 nm, (c) 16 nm, (d) 18.1 nm and (d) 220 nm. The red bar depicts the 200-nm scale bar. The widths and the lengths of the nanocolumns are of order of tens and hundreds of nm, respectively. One can notice that with increasing thickness of the TaAs layers, the size of the nanocolumns systematically increased. Similar rectangular grains with a size of up to 100 nm × 50 nm were also observed in the MBE-grown TaAs [100, 254] as well as in other epitaxial Weyl semimetal thin films such as NbP and TaP grown by MBE [267]. An open question remains as to whether the nanocolumnar structure is intrinsic to those materials or a consequence of MBE growth.

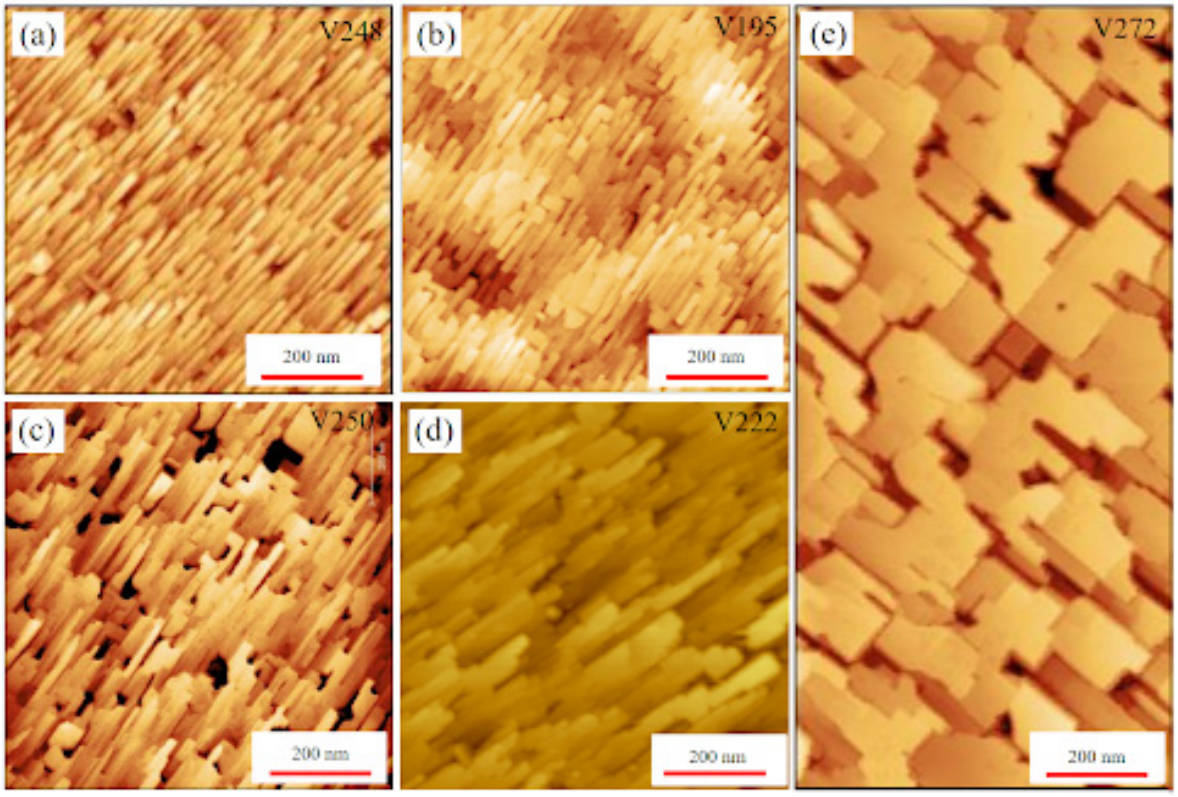

Figure 7.11: The atomic force microscopy image of TaAs of thickness of (a) ~ 8 nm (V248), (b) 8 nm (V195) (c) 16 nm (V250), (d) 18 nm (V222) and (e) 220 nm (V272). The thicknesses of the layers were obtained from XRD measurements, TEM cross-sections or AFM edge imaging. [The images were taken by Dr. R. Bożek and Dr. M. Borysiewicz, Faculty of Physics, UW. The data analysis and Figure preparation: Z. Ogorzałek-Sory.]

Figures 7.12(a)-(b) show analysis of nanocolumns dimensions: the histograms of their lengths and widths, for chosen samples of various thicknesses from 3 nm to 18 nm.

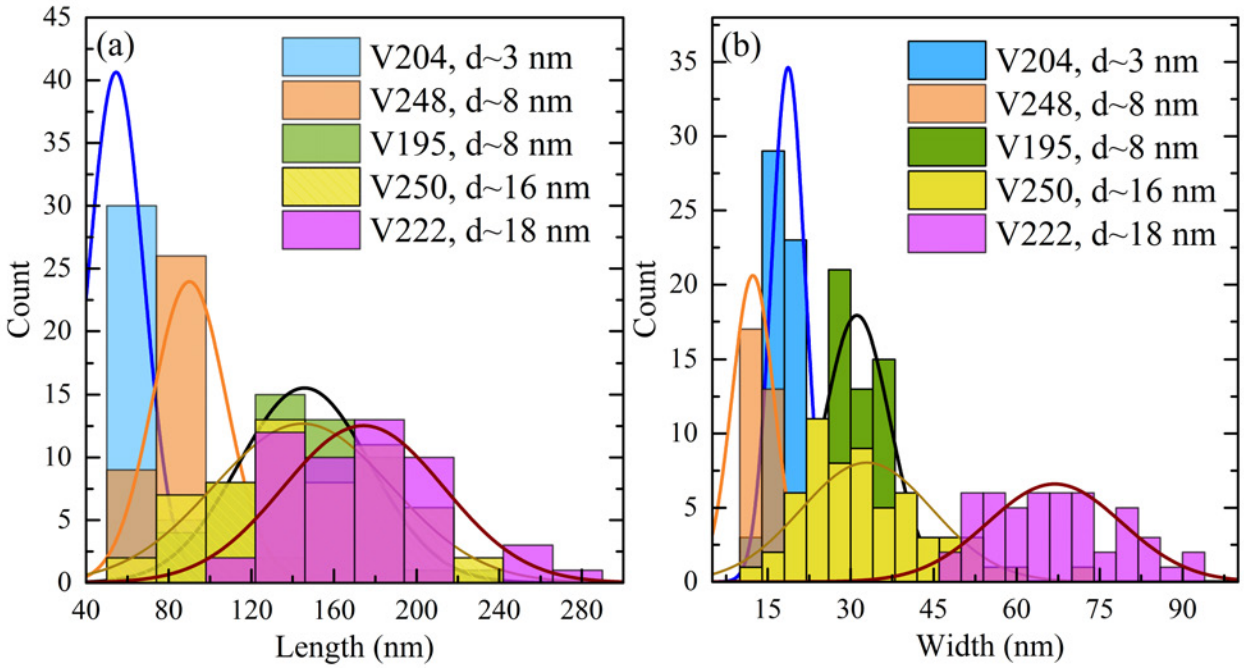

Figure 7.12: The (a) length and (b) width histograms of the TaAs nanocolumns for different TaAs samples of various thicknesses. The solid lines of corresponding colors show the fitted normal distributions.

Although with limited data, in both histograms a correlation is visible: with increasing thickness, both W and L increase as well. Indeed, for a thick sample different morphology was observed (see Figure 7.11(e)), with grains more rectangular, of order of 200 nm to 200 nm, without a distinguished long axis, similarly to the results of Nelson et al. [254]. This AFM image analysis shows that further increase of the thickness of the TaAs layers may lead to an increase of nanocolumns dimensions, and eventually to their merging.

7.2.2.2 TEM analysis

To obtain insight at atomic scale, TaAs samples were analyzed by TEM studies. Figures 7.13(a)-(c) present the high-resolution STEM cross-section of TaAs samples revealing (from the bottom to the top) (a) SI GaAs (001) buffer on top of the SI GaAs (001) substrate and the TaAs layers of 15 nm and (b)-(c) the zoom of the HR-STEM images of the TaAs layers of thickness of 18.1 nm.

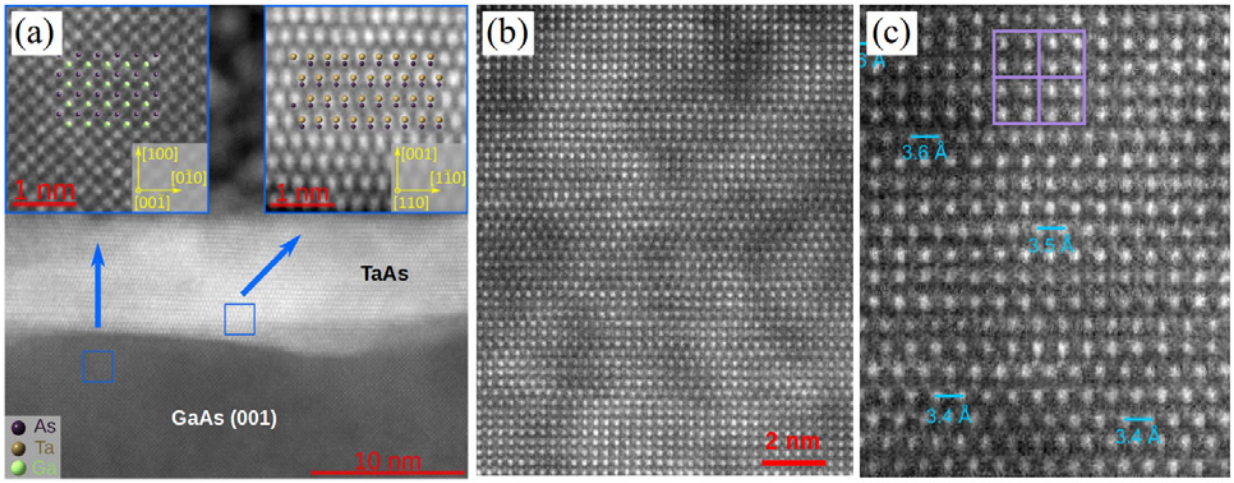

Figure 7.13: HR STEM image cross-sections of TaAs grown on SI GaAs (100) buffer of thickness of (a) 8 nm (V195) [250] and (b)-(c) 18.1 nm (V222). The As, Ta, and Ga atoms are marked by the violet, dark-green and light-green balls, respectively. [The images were taken by Dr. S. Kret and MSc W. Zajkowska-Pietrzak, Institute of Physics, PAS.]

The left and right insets in Figure 7.13(a) show the zoomed regions of the SI GaAs (111)B buffer and TaAs layers. The TEM analysis proves the perfect arrangement of the Ta and As atoms. Moreover, the azimuthal orientations of the TaAs layer with respect to the GaAs (001) substrate are identified as follows: $\mathrm{TaAs}_{[1\bar{1}0]} \parallel \mathrm{TaAs}_{[0\bar{1}0]}$. On the other hand, the TEM analysis showed a large amount of planar defects i.e. stacking faults disorder, commonly observed in literature (see Figure 7.4). In Figures 7.13(b)-(c) there are regions in which the atomic plane order shifts are disturbed. In fact, the TEM analysis has shown that the contribution of the new elemental arrangement reaches 75%. Potentially, such a huge number of the stacking faults may significantly change the crystal structure of the studied material. The careful study revealed a presence of a new kind of elementary cell arrangement, presented by the violet boxes in Figure 7.13(c). Such an extensive amount of new atomic arrangements may suggest that the physical properties of the studied TaAs layers may significantly differ from the regular tetragonal TaAs.

7.2.2.3 XRD analysis

To address and identify new elementary cell, selected samples of different thicknesses were examined by XRD studies. Figure 7.14(a) shows a wide-range $2\theta/\theta$ scans of 3 samples with different thicknesses, revealing a sequence of reflexes for GaAs and TaAs, as shown by black and red arrows, respectively.

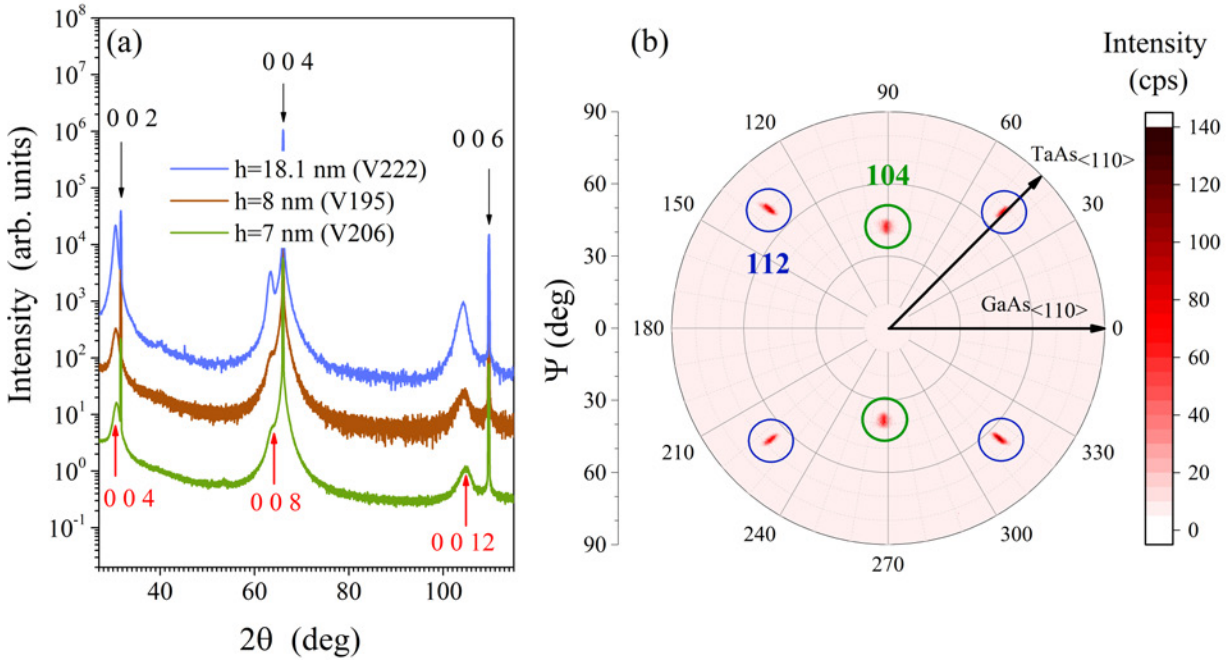

Figure 7.14: (a) Wide-range $2\theta/\theta$ scans for 3 TaAs samples of different thicknesses. (b) Polar plot with 112 and 104 reflections with the corresponding Ψ angles [268]. [The XRD data were measured by Dr. J. Domagala, Institute of Physics, PAS. The data analysis and Figure preparation: Z. Ogorzałek-Sory.]

The (001) planes of TaAs are parallel to the GaAs (001) ones, as both are presented in these scans. However, apart from symmetrical reflexes, some asymmetrical one, not allowed for the tetragonal structure have also been observed. Asymmetric reflexes were detected in the so-called skew configuration, with substantial tilt angles Ψ (angle of inclination from the sample surface), to bring the plane to the Bragg condition. Figure 7.14(b) shows a map of family of 112 and 104 reflexes. Such a 2D map is a compilation of scans with Ψ ranging from 0^0 to 90^0, plotting the intensity against azimuthal angle φ for a specific angle Ψ. Sample rotation scheme for pole figure measurement can be found in Supporting Information in paper by Z. Ogorzałek et al. [268]. The 112 reflection, which is symmetry-allowed in the tetragonal phase, exhibits pronounced intensity compared to other reflections. However, an additional 104 peak was also observed. According to the symmetry rules presented in the International Tables for Crystallography [269], reflections of the type $h0l$ are forbidden in the tetragonal lattice if the sum of h and l is odd, making 104 systematically absent. The identification of TaAs was initially based on the conventional tetragonal structure with space group No.109, as the obtained reflections closely matched those reported for bulk TaAs crystals[244]. Simulated XRD patterns, however, reveal a clear distinction between the tetragonal and new phases: the 104 peak is uniquely predicted for the orthorhombic structure. The presence of this reflection therefore provides unambiguous experimental evidence for a new orthorhombic phase of TaAs (o-TaAs), characterized by a space group symmetry distinct from the conventional tetragonal form.

7.2.2.4 Electrical characterization

In order to electrically characterize the TaAs layers and to address the sample anisotropic morphology, two sets of samples (in the Hall-bar and in the van der Pauw configurations) were prepared, with current paths aligned predominantly along ($I \parallel NC$) or across ($I \perp NC$) the nanocolumns. The photo and the scheme of the sample configuration with the defined Hall-bar geometry are presented in the Figures 7.15(a)-(c).

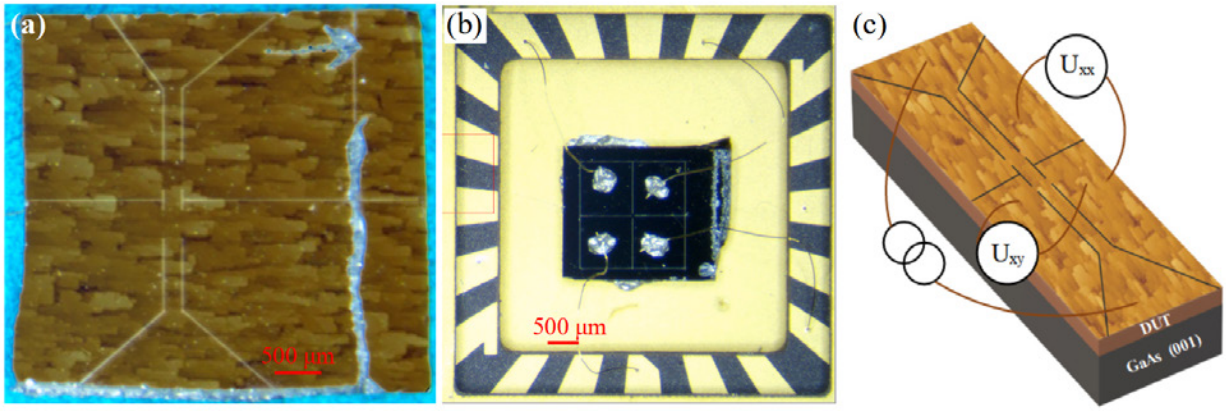

Figure 7.15: The optical images of TaAs samples in (a) the Hall-bar and (b) the van der Pauw configurations. The arrow indicates the direction of the nanocolumns relative to the easy cleavage direction of the SI GaAs (001) wafer. The AFM image on the Hall-bar structures is only illustrative and does not correspond to the real dimensions of the sample. (c) The scheme of the sample measurement configuration with the Hall-bar with the current along the nanocolumns. An AFM image of TaAs nanocolumns is illustrative and serves only to demonstrate the position of the nanocolumns. The scale bars correspond to the sample size, not the AFM image.

The typical sizes of the Hall-bars were a few hundreds of μm, for instance the current path of 2 mm in length and 200 μm in width. Several samples with various configurations have been studied by means of the resistivity tensor measurements. Figure 7.16(a) presents the typical temperature resistivity dependence for TaAs layers, here an 8 nm-thick sample (V195) for two current directions.

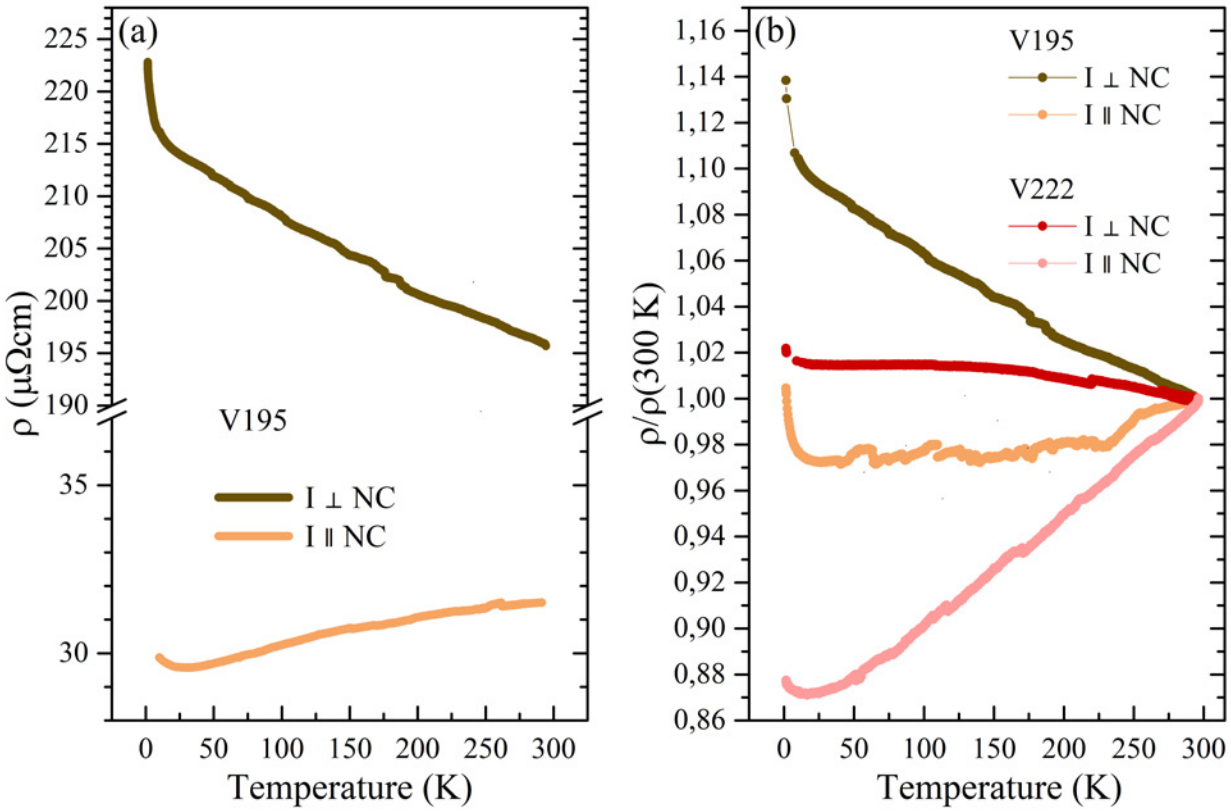

Figure 7.16: Electrical characterization of TaAs. (a) Resistivity dependence on temperature measured for two current directions along and across nanocolumns for 8-nm TaAs sample (V195). (b) Temperature resistivity dependencies, normalized to the room temperature, for two samples with various thicknesses, 8 nm- (V195) and 18.1 nm-thick (V222), and for two current directions. Dark brown and red curves correspond to current aligned predominantly across (⊥) NCs. Light brown and red curves correspond to current aligned predominantly along (∥) NCs [268].

One can see that already at room temperature there is a distinct in-plane resistivity anisotropy reaching 5. It indicates the crucial role of the grain boundaries scattering in the electron drift, with the lower value of resistivity for the current aligned along NCs. Consequently, the resistivity of the system is composed of the resistivity of the TaAs and the resistivity of the NCs boundaries. With decreasing temperature, the resistivity of the sample drops for the current aligned predominantly along the NCs, while it rises for the current aligned predominantly across the NCs. Surprisingly, this peculiar behavior is in a good agreement with the Mooij rule [263] (see Figure 7.8(b)) observed for the disordered alloys. Sometimes, a metallic-like drop in resistivity may also serve as a fingerprint of topological states, which are indeed expected for Weyl semimetals. Unfortunately, the RRR of the metallic-like dependencies stay relatively low, of order of 1. Figure 7.16(b) presents the normalized to the room temperature, temperature resistivity dependencies for two samples of different thicknesses (8 nm and 18.1 nm), measured for two current directions. Compared to the sample of 8-nm thickness, the thicker sample becomes more metallic and has higher RRR for the current aligned predominantly along NCs. In the same way, the resistivity for the current aligned predominantly across the NCs, is almost temperature independent, behaving as metal-alloys.

Due to the high degree of disorder and nonhomogeneous current paths, the $\rho(T)$ dependencies were not smooth, and subsequent measurements revealed slight fluctuations and jumps in the signal (see Figure 7.25). In addition, below T=25 K, in all samples and measurement configurations a resistivity upturn emerges. Identical tendency was observed before in topological insulators [270, 271], where the following mechanisms were considered: disorder [272, 273], WL [101] or electron-electron (e-e) interactions [155]. We have demonstrated, based on mobility values, that the resistivity upturn at low temperature does not originate from disorder [268]. The mobility threshold below which the system becomes insulating is given by $\mu_{IR} = e/\left[(3\pi^2(p_{2D}/d))^{2/3}\hbar\right]$ [271], where d is the layer thickness. For our o-TaAs samples, the calculated μ_{IR} is below 1 $cm^2/(V \cdot s)$, allowing us to rule out disorder-driven mechanisms as the origin of the resistivity upturn. Alternative effects that should be considered include electron–electron interactions and the Kondo effect [274]. The coexistence of these mechanisms calls for a more detailed investigation to disentangle their individual contributions.

To correlate the value of the TaAs resistivity with the size of the NCs, the in-plane resistivities of the three samples with different NCs dimensions were compared. Figures 7.17(a)-(c) show the resistivities as a function of temperature for three samples, measured for two current orientations.

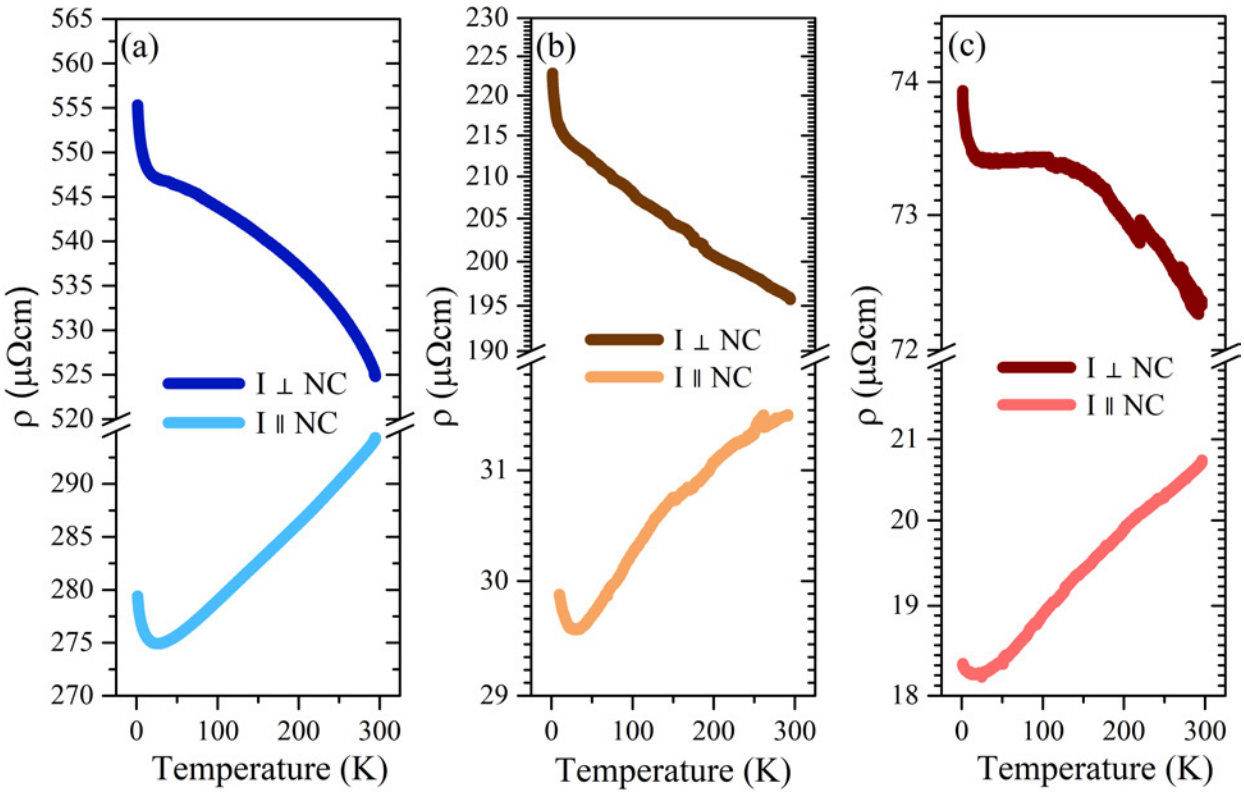

Figure 7.17: Electrical characterization of TaAs. The resistivity as a function of temperature for TaAs layers, measured for two current orientations for sample with (a) small (V248), (b) larger (V195) and (c) large (V222) NCs. [The V248 sample was measured by Dr. M. Borysiewicz, Faculty of Physics, UW. The data analysis and Figure preparation: Z. Ogorzałek-Sory.]

All the samples reveal in-plane anisotropic resistivity dependencies with the semiconducting- or metallic-like temperature behavior depending on the current versus NCs orientation. Comparing AFM images of the V248, V195 and V222 samples (see Figures 7.11(a)-(b) and (d)) one can see that with increasing NCs dimensions, the in-plane resistivity values decrease. Although the in-plane resistivity anisotropy shows resemblance to the Mooij rule, not all samples follow this behavior (see Figure 7.17(a)), suggesting that additional contributions may be involved, possibly related only to the nanocolumnar morphology or other yet unidentified mechanisms. Because of the pronounced disorder and irregular current distribution, the $\rho(T)$ curves lacked smoothness, and repeated measurements showed minor random fluctuations in the signal (see also Figure 7.25).

To investigate the in-plane anisotropic resistivity dependence on magnetic field, several samples of various thicknesses were measured in a magnetic field up to 12 T. Figure 7.18 shows the transverse Hall resistivity dependencies as a function of the magnetic field for 8 nm-thick TaAs sample (V195), measured for two current configurations at low- and at room-temperature.

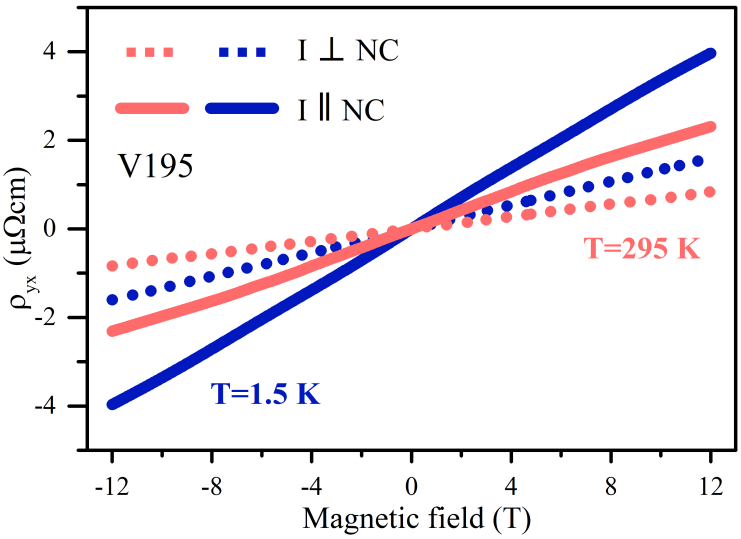

Figure 7.18: Electrical characterization of TaAs. The low- (marked by the blue curves) and room-temperature (marked by the red curves) transverse Hall resistivity dependencies for current along (solid curves) or across (dotted curves) NCs [268].

The Hall resistivities for all TaAs samples, for various current versus NCs orientations are linear, revealing most probably one type of carrier with the p-type conductivity and hole concentration of the order of $p \sim 10^{21}$ cm^{-3}. The Hall concentration practically does not depend on the temperature, as it has been shown in Figure 7.18 by the blue and red curves. In fact, a nearly temperature-independent carrier concentration is considered to be a fingerprint of Dirac or Weyl semimetals [270]. The carrier concentration is almost the same, equal for the two current configuration, as it has been shown by dotted and solid curves. The low and room-temperature Hall carrier concentration are summarized in Table 7.1.

Table 7.1: The low and room-temperature Hall concentrations and Hall mobilities for three samples (7.9 nm-thick V248, 8 nm-thick V195 and 18.1 nm-thick V222), measured for two current configurations.

Sample and configuration:		T=1.5 K		T=300 K	
		n_H^{2D} (cm^{-2})	n_H^{3D} (cm^{-3})	n_H^{2D} (cm^{-2})	n_H^{3D} (cm^{-3})
V248	I ∥ NC	$1.5 \cdot 10^{15}$	$2.3 \cdot 10^{21}$	$1.7 \cdot 10^{15}$	$2.15 \cdot 10^{21}$
	I ⊥ NC	$1.4 \cdot 10^{15}$	$1.7 \cdot 10^{21}$	$1.9 \cdot 10^{15}$	$2.4 \cdot 10^{21}$
V195	I ∥ NC	$(1.49 \pm 0.07) \cdot 10^{15}$	$(1.86 \pm 0.01) \cdot 10^{21}$	$(2.56 \pm 0.01) \cdot 10^{15}$	$(3.20 \pm 0.02) \cdot 10^{21}$
	I ⊥ NC	$(3.74 - 5.37) \cdot 10^{15}$	$(4.68 - 6.72) \cdot 10^{21}$	$(4.70 - 7.19) \cdot 10^{15}$	$(5.88 - 8.98) \cdot 10^{21}$
V222	I ∥ NC	$(4.06 \pm 0.01) \cdot 10^{15}$	$(2.24 \pm 0.01) \cdot 10^{21}$	$(4.69 \pm 0.01) \cdot 10^{15}$	$(2.59 \pm 0.01) \cdot 10^{21}$
	I ⊥ NC	$4.7 \cdot 10^{15}$	$2.6 \cdot 10^{21}$	$5.7 \cdot 10^{15}$	$3.1 \cdot 10^{21}$

The obtained values are in a good agreement with the concentrations of the MBE-grown TaAs samples, studied by Nelson et al. [254] and Yanez et al. [100]. Yet, they are much higher than for samples grown by other techniques [253, 35, 260, 275].

As the resistivity of the NCs is anisotropic (see Figure 7.16(a)) and the carrier concentrations are almost independent of the current orientation, the TaAs anisotropic conductivity is most probably governed by the carrier mobilities. To address sample magnetotransport properties, the resistivity tensor was measured in various configurations. Figure 7.19 presents the low temperature MR dependencies on magnetic field for 8 nm (V195) and 18.1 nm-thick (V222) TaAs samples, measured for current aligned either along or across NCs.

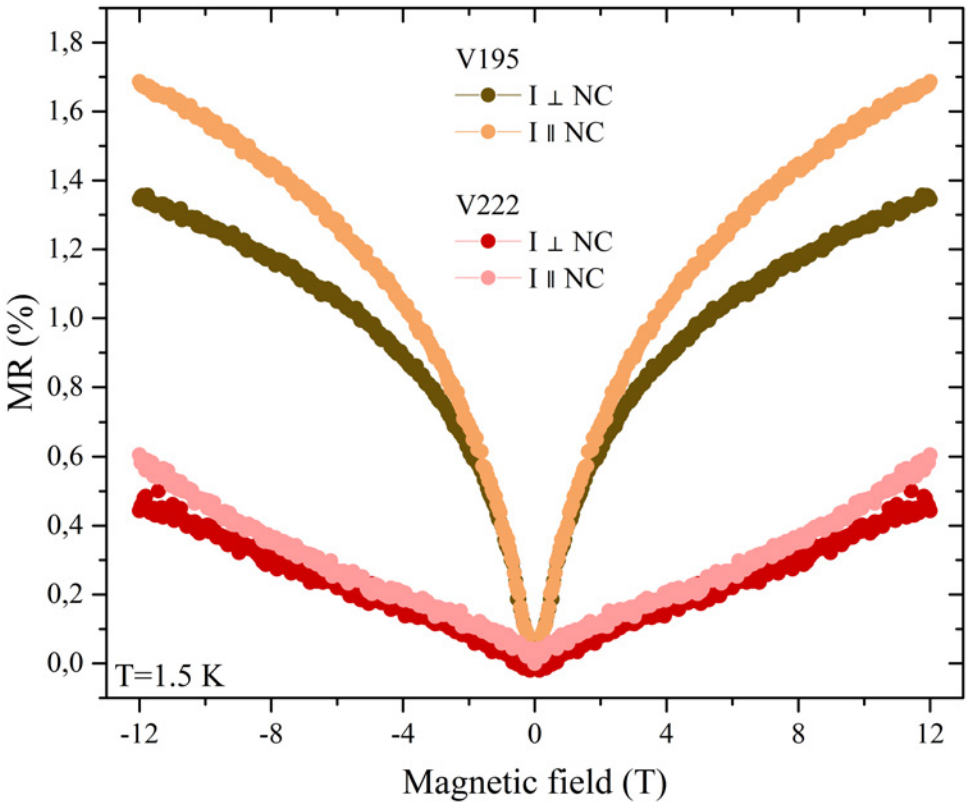

Figure 7.19: Electrical characterization of TaAs. MR of TaAs, measured for two samples (V195 and V222) and current orientations. Dark (brown / red) and light (orange / pink) curves correspond to current aligned across or along NCs, respectively.

Resistivity tensor measurements revealed a small, positive, MR not exceeding 2% for all configurations. In the whole magnetic field range, a large resistivity drop was observed for both samples. The resistivity drop appears in all configuration. The Hall mobilities substantially differ depending on the current configuration. Low and room-temperature Hall mobilities for TaAs samples with different thicknesses d and for two current orientations, obtained from the Hall measurements, are presented in Table 7.2.

Table 7.2: The low and room-temperature Hall mobilities for TaAs samples with different thicknesses d for two current orientations.

Sample:	d, the measurement configuration:	$\mu_H^{1.4\ K}$ ($cm^2/V \cdot s$)	$\mu_H^{300\ K}$ ($cm^2/V \cdot s$)
V248	7.9 nm, I ∥ NC	15	12
	7.9 nm, I ⊥ NC	8	6
V195	8 nm, I ∥ NC	115	65
	8 nm, I ⊥ NC	6	2.3-5.4
V222	18.1 nm, I ∥ NC	150	114
	18.1 nm, I ⊥ NC	30	25

The carrier mobilities stay relatively low, not exceeding $\mu_H \sim 150\ cm^2/V \cdot s$, and show weak temperature dependence. A constant carrier mobility is expected for the topologically protected states where the back-scattering should be reduced which can be indicative of topological carriers contribution. Interestingly, the Hall mobility depends on the current orientation and it is always 2 to 5 times larger for the current aligned predominantly along NCs.

In order to clarify the origin of the resistivity drop in the longitudinal component of the resistivity tensor, its temperature dependence has been measured. Figures 7.20(a)-(b) show the temperature dependence of the calculated magneto-conductivity in the units of electrical conductance for a 8 nm-thick TaAs sample (V195) for two current configurations.

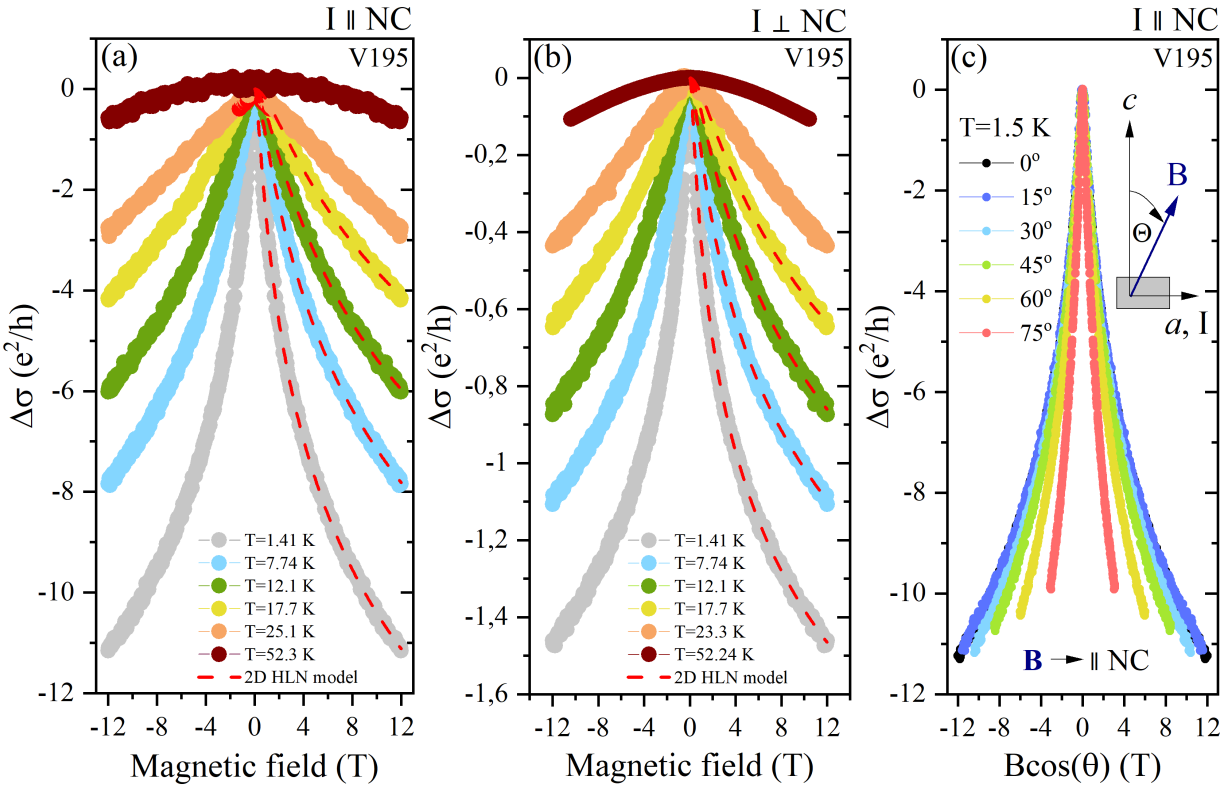

Figure 7.20: Electrical characterization of TaAs. Magneto-conductivity dependence for two current directions with current aligned predominantly (a) along or (b) across NCs at different temperatures. Dashed red lines show a fitted 2D HLN model. (c) The magneto-conductivity as a function of the perpendicular component of the magnetic field $B_{\perp} = B \cdot cos(\theta)$ for current aligned predominantly along NCs. Inset: the scheme of the magnetic field B tilt versus electric current and TaAs crystallographic a and c axes [268].

There is a clear temperature evolution observed with $\sigma_{xx}(B)$, up to ~ 50 K, where $\sigma_{xx}(B)$ shows a parabolic character. The evident temperature behavior suggests the presence of the interference effects, here the weak antilocalization [90, 93]. To confirm this hypothesis, the 2D Hikami-Larkin-Nagaoka (HLN) model [101] has been applied to data. The fitted curves, presented by the dashed, red lines in Figures 7.20(a)-(b), fit nicely to all data. Although the sample seemed to be 2D, the dimensionality of the studied layers was checked by the angle-resolved measurements. Sample was put in the rotator system, which allowed to rotate the sample versus magnetic field direction (see section 2.7.1) to verify if the perpendicular component of the magnetic field influences the WAL effect. The low-temperature angle-resolved WAL measurements are presented in Figure 7.20(c). The magnetic field was tilted from the out-of-plane (0^o) to in-plane (90^o) configuration. In the in-plane configuration, the magnetic field was parallel to the direction of the current and to the NCs. The obtained results show that curves do not collapse into a one curve thus do not depend on the perpendicular component of the magnetic field. It means that the observed effect does not originate from the 2D surface channels. Different configurations of the magnetic field to electric current and to

NCs were investigated. The results will be shown further in Table 7.3 and in Figure 7.22(b).

To investigate the studied layers dimensionality, both 2D and 3D HLN models were applied to the data, showing a good agreement and suggesting quasi 2D character of the layers. Temperature dependencies of the phase coherence length (l_ϕ), obtained from 2D (squares) and 3D HLN (asterisks) models for two current orientations, are presented in Figure 7.21(a).

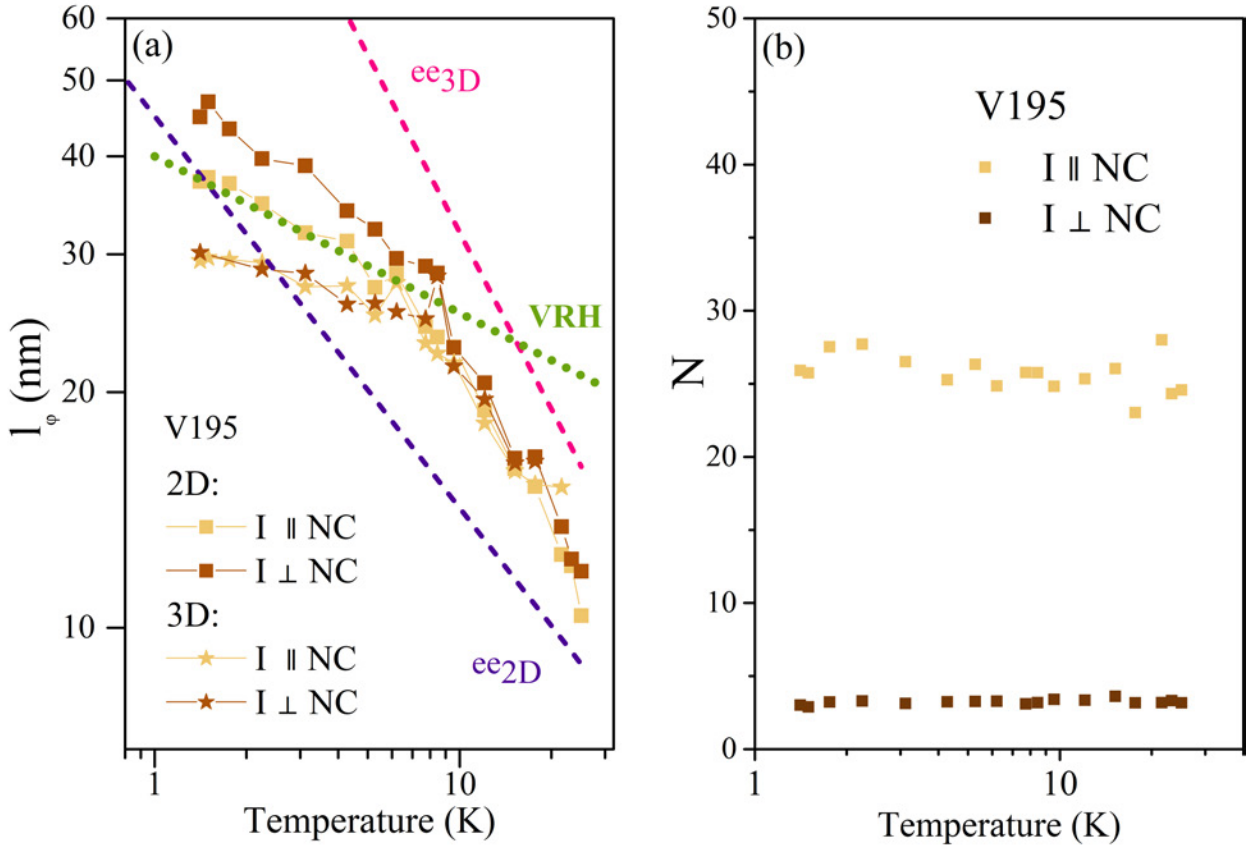

Figure 7.21: Electrical characterization of TaAs. Temperature dependence of (a) l_ϕ obtained from 2D (squers) and 3D HLN (asterisks) models for two current orientations. The pink and blue dashed lines represents the 3D and 2D dephasing mechanism, respectively [276]. The green, dotted line shows a trend predicted for variable-range hopping (VRH) [277]. (b) The number of the conducting channels N for two current directions, obtained from a fitted 2D HLN model. Light and dark brown points correspond to the current aligned predominantly along or across the nanocolumns, respectively [268].

The two models applied showed that l_ϕ reaches 40 nm at the lowest temperature. The l_ϕ value is independent of nanocolumn orientation. The temperature dependence of l_ϕ is quite weak and vanishes above T=25 K. The pink and blue dashed lines show the expected temperature l_ϕ dependence for 3D and 2D systems, respectively in the presence of the e-e interactions [276]. The high temperature data fall between the two model lines. The e-e interactions are possibly responsible for the temperature resistivity upturn below T=25 K. The green, dotted line shows a trend predicted for variable-range hopping (VRH) as argued by Ref. [277]. This model seems to work below 10 K. Figure 7.21(b) shows the temperature dependence of the

number of the conducting channels (N). Depending on the nanocolumns orientation, the number of the conducting channels in the system switches from 3 to 26.

To observe a chiral anomaly effect, the magnetic field was aligned along the current path. In this configuration, in the systems with the Weyl fermions, one should expect a negative magnetoresistance (positive magneto-conductivity). To verify if the chiral carriers are present in the system, the temperature in-plane magneto-conductivity measurements were performed. Figure 7.22 shows the temperature dependence of the in-plane magneto-conductivity ($\Theta = 90^o$) for 8 nm-thick sample (V195), measured for two current orientations with the current aligned predominantly along or across NCs, marked by the light or dark colored dots, respectively.

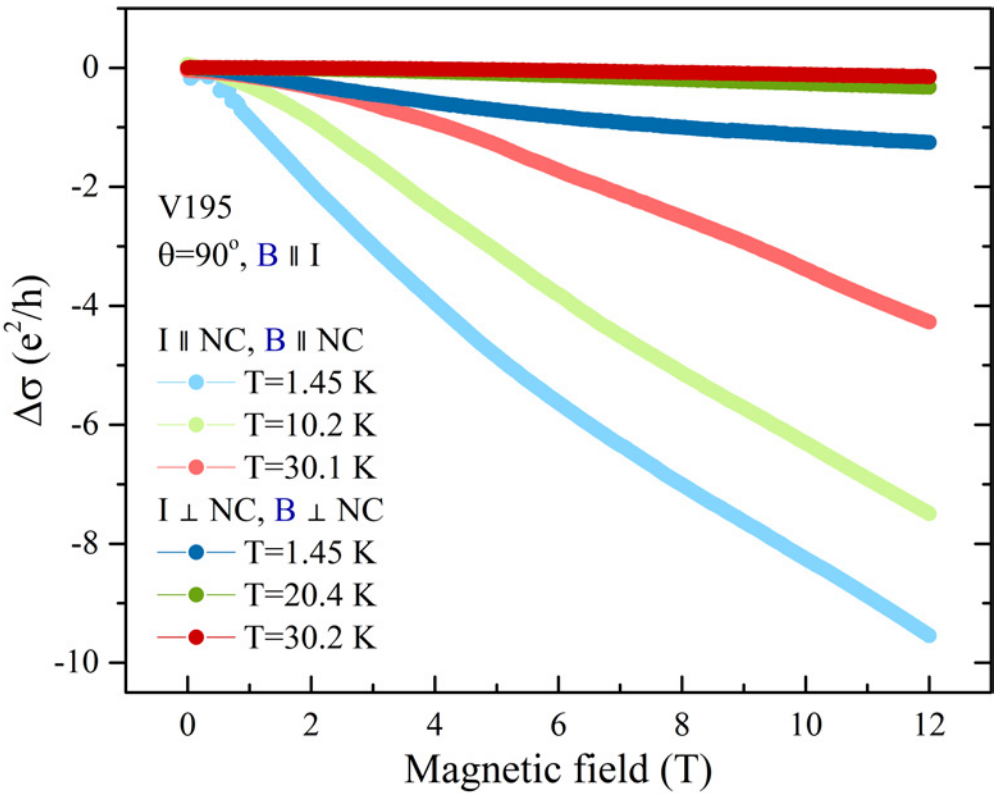

Figure 7.22: Electrical characterization of TaAs. (a) Temperature dependence of the in-plane magneto-conductivity ($\Theta = 90^o$) for 8 nm-thick sample (V195), measured for two current orientations with the current aligned either along or across NCs.

Independently from the current orientation, the positive magneto-conductivity was not observed. Moreover, increasing the temperature did not suppress the weak antilocalization background, which could otherwise have revealed a chiral anomaly contribution. Due to high, unintentional p-type doping and 3D character of the bulk conductivity, the possible contribution of the chiral Weyl fermions to the overall transport is probably much limited.

Figure 7.23 shows the comparison of the WAL effect for the out-of-plane and the in-plane configurations. It shows that the in-plane WAL effect is strong and visible in the wide magnetic field range. WAL is present for magnetic field aligned both across or along NCs.

However, the in-plane WAL amplitude is smaller than for the out-of-plane configuration. Similar observations have been made in topological insulators such as $Bi_2Te_xSe_{3-x}$ thin films, where the high-magnetic field chiral anomaly effect was present [270].

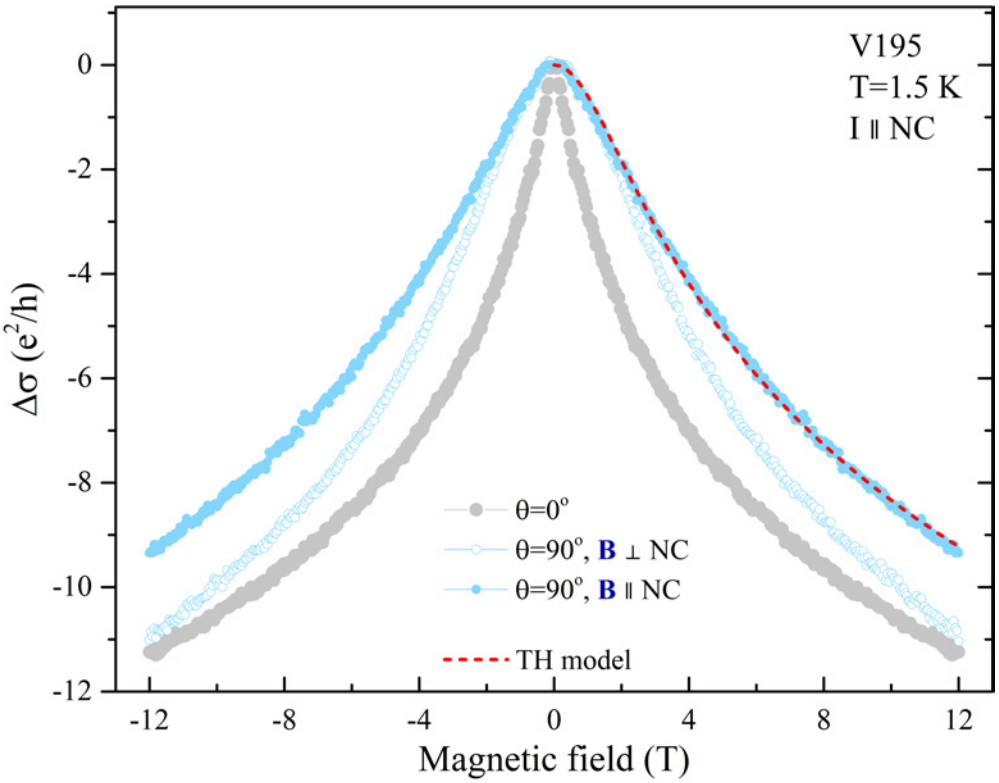

Figure 7.23: Electrical characterization of TaAs. (a) Low-temperature in-plane ($\Theta = 0^o$) and out-of-plane ($\Theta = 0^o$) magneto-conductivity for the current aligned predominantly along NCs. (b) The in-plane magneto-conductivity dependence for the current and magnetic field aligned along NCs for 8 nm-thick sample (V195). The red line shows a fitted Tkachov-Hankiewicz model.

To address the origin of the in-plane WAL effect, the Tkachov-Hankiewicz model [102] was applied to the low-temperature in-plane ($\Theta = 90^o$) data. Red dashed line in Figure 7.23 shows a fit of the Tkachov-Hankiewicz model to the low-temperature in-plane WAL, measured for both current and magnetic field aligned along NCs. The fit describes data very well. The number of the conducting channels (N), the phase coherence length (l_ϕ) and the decay length into the bulk (λ) for 8 nm-thick sample (V195), obtained from Tkachov-Hankiewicz model, were collected in Table 7.3.

Table 7.3: Parameters of the TH model: number of the conducting channels (N), phase coherence length (l_ϕ) and the decay length into the bulk (λ) for 8 nm-thick sample (V195) for data at T=1.5 K with various magnetic filed and current configurations.

Sample:	Configuration:	λ (nm)	l_ϕ (nm)	N
V195	I ∥ NC, B ∥ NC	8.28	29.25	15.71
	I ∥ NC, B ⊥ NC	6.20	45.77	17.17
	I ⊥ NC, B ∥ NC	8.24	31.04	1.95
	I ⊥ NC, B ⊥ NC	7.16	42.33	2.04

Four types of experimental configurations were investigated with the current and the mag-

netic field in the (001) plane, set either across or along NCs. The decay length stays between 6 nm to 8 nm independently on the current configuration, meaning that the in-plane WAL effect is purely 3D. Similarly, as it has been shown using the HLN model, the phase coherence length does not depend on the configuration of current. Interestingly, the phase coherence length depends on the magnetic field versus NCs configurations. It reaches 30 nm and 45 nm for the magnetic field set parallel or perpendicular to NCs, respectively.

The resistivity tensor measurements were performed on samples with the defined two types of geometry configurations: the van der Pauw and the Hall-bar. To compare both geometries, few representative measurements were made on both types of sample. The results show a good agreement between two configurations, however the results of the critical magnetic field (B_c) and thus the phase coherence length (l_ϕ) differ by 10%. To understand the differences between the obtained results, some of the experiments were repeated several times with the use of the samples in both configurations. Figure 7.24 shows the MR of the 8 nm-thick TaAs sample (V195), measured at T=1.5 K and T=10 K in the van der Pauw (vdP) and the Hall-bar configurations, for the current aligned predominantly across NCs.

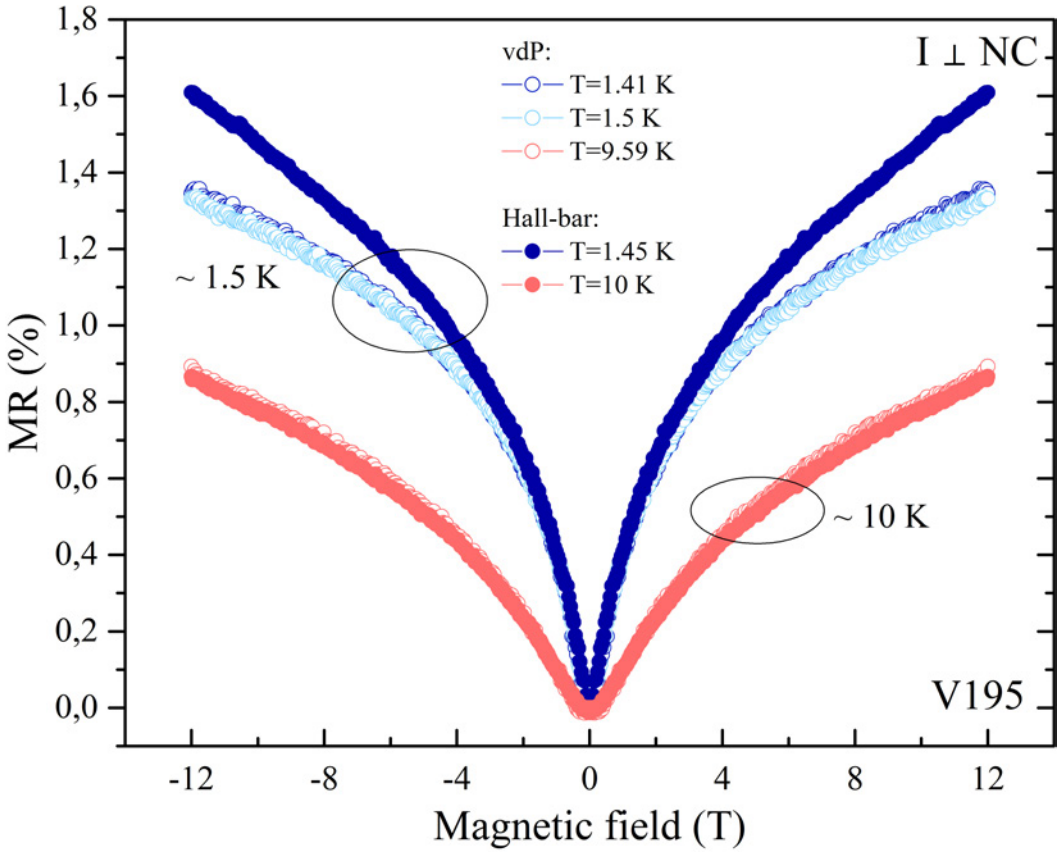

Figure 7.24: Electrical characterization of TaAs. MR of the 8 nm-thick TaAs sample (V195), measured at T=1.5 K and T=10 K in the van der Pauw and the Hall-bar configurations, for the current aligned across NCs.

One can see that the results obtained in T=10 K, marked by the open and solid pink dots, show good agreement between the two geometries. On the other hand, a distinct difference

between those two configurations is observed at the lowest temperature, as presented by the open and solid blue curves. The results of the low-temperature critical magnetic field (B_c), phase coherence length (l_ϕ), α parameter and number of the conducting channels (N) for 8 nm-thick sample (V195), obtained from the 2D HLN model for the current aligned across NCs for two samples with different geometries are presented in Table 7.4.

Table 7.4: Low-temperature critical magnetic field (B_c), phase coherence length (l_ϕ), α parameter and number of the conducting channels (N) for 8 nm-thick sample (V195), obtained from the 2D HLN model for the current aligned predominantly across NCs. l_ϕ is directly calculated from the B_c.

Geometry of the sample:	B_c (T)	l_ϕ (nm)	α	N
the van der Pauw	0.08	44.91	-1.50	3.01
the Hall-bar	0.12	37.09	-1.66	3.32

The variations in the data may originate from the inhomogeneity of the studied layers. Figure 7.25 shows a series of R(T) measurements ((1)–(4)) measured for 8-nm-thick sample (V195), with the current predominantly aligned along NCs.

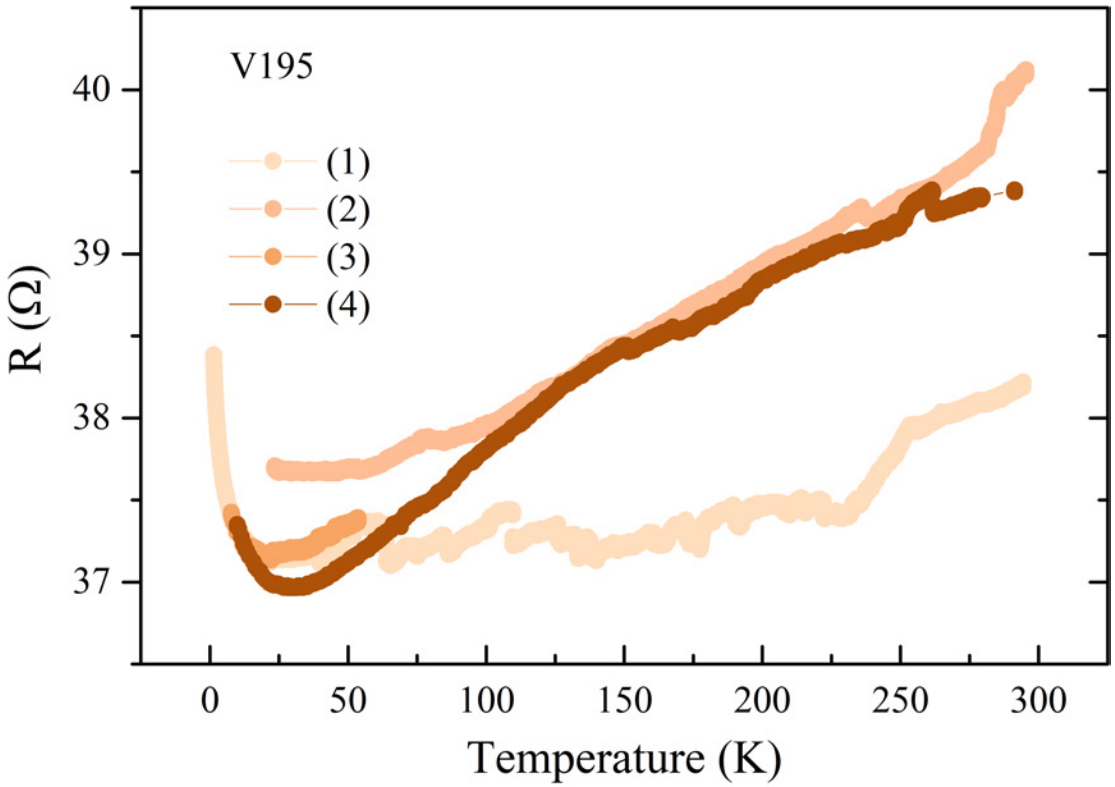

Figure 7.25: Electrical characterization of TaAs. The subsequent temperature resistance dependencies ((1)-(4)), measured for 8-nm TaAs sample (V195) for the current aligned along NCs.

This results evidences some instabilities of the thin samples. In some cases, they were observed on two pairs of longitudinal contacts, evidencing current paths instability. These differences in the $R(T)$ curves affect the extracted fit parameters; however, within a given configuration, a clear correlation can still be observed.

7.2.2.5 Theoretical description of the orthorhombic o-TaAs

To address the stacking faults contribution to the TaAs band structure and its topological and electrical properties we have invited to collaboration Prof. Hsin Lin (Institute of Physics, Academia Sinica, Taiwan), Prof. Chi-Cheng Lee (Department of Physics, Tamkang University, Taiwan) and MSc Bao-Huei Huang (Institute of Physics, Academia Sinica, Taiwan) who performed DFT calculations. The theoretical results showed that stacking faults form a new phase of TaAs. The stacking sequence, presented in Figure 7.26(a) (compare with the regular, body-centered-tetragonal TaAs in Figure 7.1(a)) requires only additional formation energy of 2.0 meV/atom compared to that of the tetragonal TaAs.

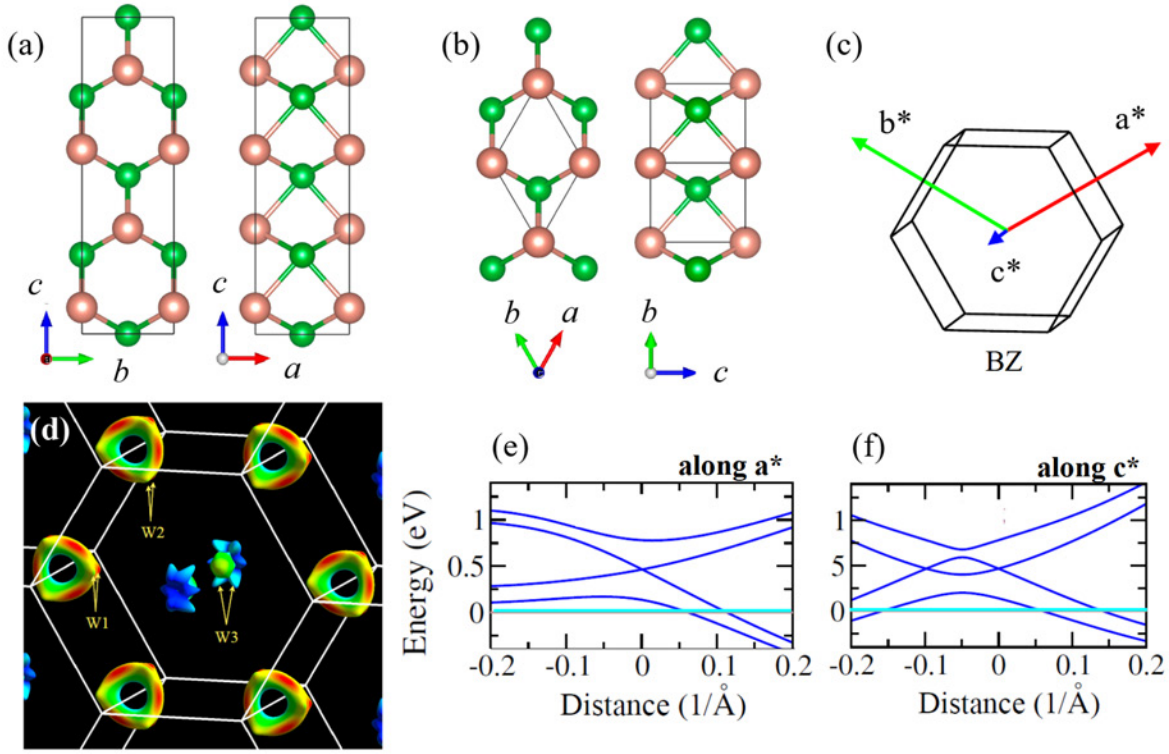

Figure 7.26: The scheme of the (a) crystal structure, (b) the primitive cell of the new orthorhombic TaAs. (c) The Brillouin zone of the orthorhombic TaAs. (d) The Fermi surface of the orthorhombic TaAs Weyl semimetal at $E_F = 0\ eV$ with marked W1, W2 and W3 Weyl points. Band dispersion around W1 Weyl point for carrier concentration $p = 2 \cdot 10^{21}$ cm^{-3} along (e) a^* and (f) c^* crystallographic directions [268]. [Schemes and DFT calculations were made by Prof. C.-C. Lee, Department of Physics, Tamkang University.]

The new phase of TaAs, identified in TEM and XRD measurements, has an orthorhombic structure (o-TaAs) with the $\Lambda mm2$ space group. The primitive cell and the first BZ of the o-TaAs are presented in Figures 7.26(b)-(c). Note the huge difference in symmetry between the BZ of the regular and the orthorhombic TaAs structures. The new phase of o-TaAs

maintains its topological features yet with different Weyl nodes number, location and energy dispersion. The o-TaAs has 20 Weyl points in total: 4 W1, 8 W2 and 8 W3. The Fermi surface of the o-TaAs Weyl semimetal at $E_F = 0\ eV$ with marked W1, W2 and W3 Weyl points is presented in Figure 7.26(d). Figures 7.26(e)-(f) present the dispersions around W1 Weyl point for the experimental carrier concentration of $p = 2 \cdot 10^{21}$ cm^{-3}, calculated along a^* and c^* crystallographic directions, respectively. Fermi energy is relatively deep, marked by the light blue lines, in respect to the Weyl points. As one can see, before these bands get down to the Fermi level, they would coalesce (undergoing Lifshitz transition). Therefore their character at E_f might be trivial and no signatures of the chiral properties have been evidenced in magnetotransport studies. Additional computational details and Weyl points identification can be found in paper by Ogorzałek-Sory et al. [268].

Chapter 8

Comment on the MBE growth of transition metal compounds

The growth of the 2D epilayer on the 3D substrate significantly differs from the growth of the 2D epilayer (which does not have any dangling bonds in perpendicular direction) on the 2D substrate. The differences are presented in Figures 8.1(a)-(c) where the schemes [278] and the TEM image examples of the (a) conventional, (b) van der Waals and (c) quasi-van der Waals epitaxy are presented [278].

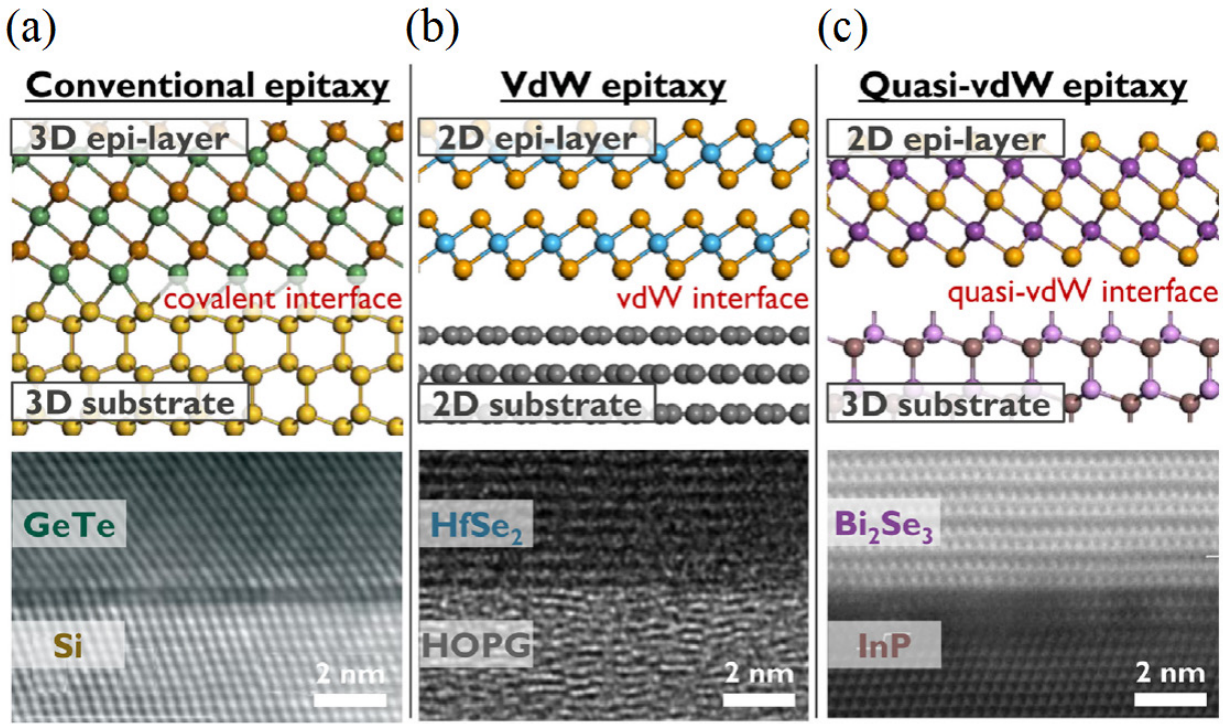

Figure 8.1: The schemes [278] and the TEM image examples of the (a) conventional [279], (b) van der Waals [280] and (c) quasi-van der Waals epitaxy [281].

Compared to the conventional epitaxy, where the covalent bondings arise between the layer and the substrate, in the van der Waals epitaxy, van der Waals forces create interfaces

between the subsequent layers and the substrate. In the case of the quasi-van der Waals epitaxy that interface is distorted and incomplete. That phenomenon was described for the first time already in 1999 by A. Koma [282]. In the case of the quasi-vdW heteroepitaxy the interface between the substrate and the layers has a quasi-vdW nature. Due to dangling bonds the interactions are neither of van der Waals type nor fully covalent, ionic, metallic. Usually, the proper substrate passivation or the buffer layer growth helps to better control the growth process, however in the quasi-van der Waals epitaxy the multidirectional in-plane registries, stacking faults and strain are more favored to occur. The consequences of quasi-van der Waals epitaxy may influence the growth of both $MoTe_2$ and $NiTe_2$ layers. It was evidenced by STEM by the presence of some clearings between the trilayers and at the interface between the substrate and the layers in both materials, suggesting the presence of additional electron densities (see Figure 5.2.3(b)). Figures 8.2(a)-(f) show the transmission electron microscope images of cross-sections of various transition metal compounds grown either on sapphire or SI GaAs substrates revealing different types of defects.

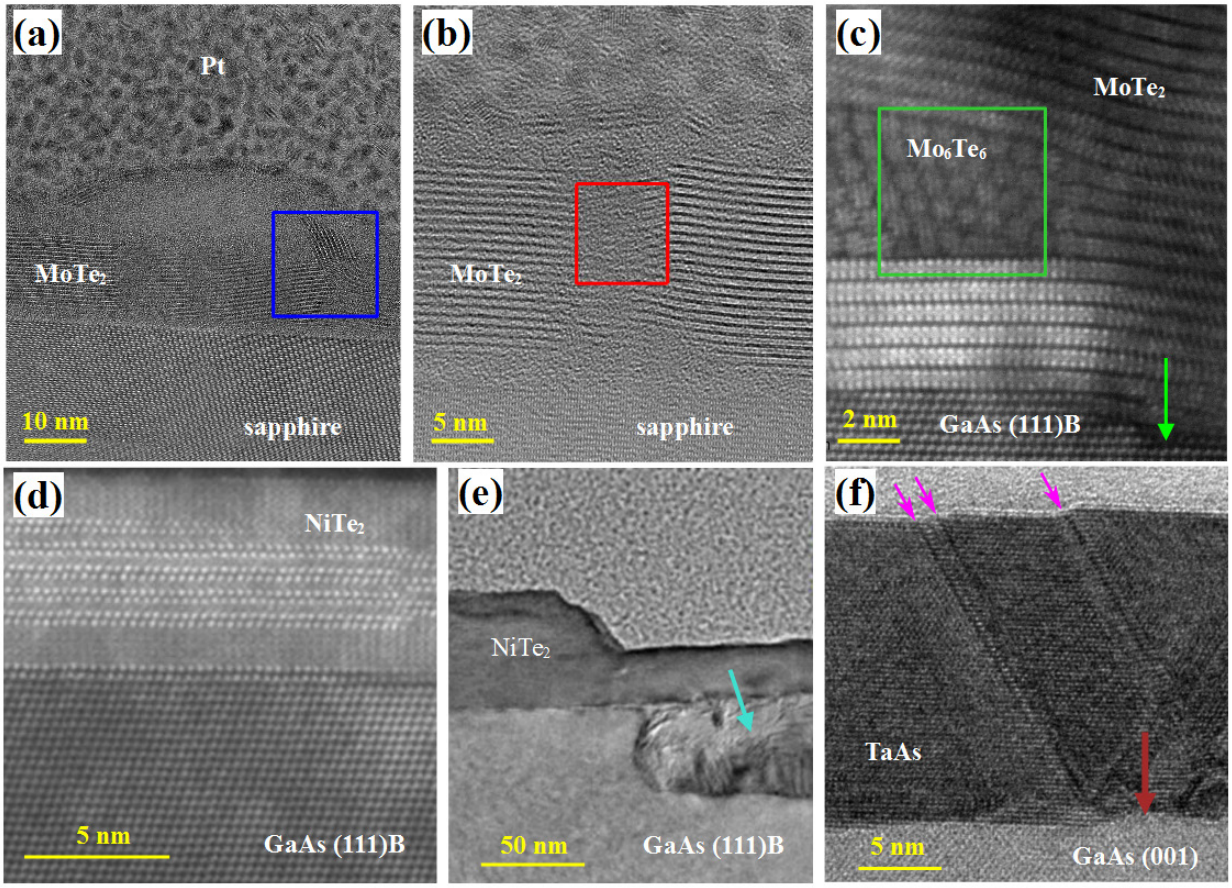

Figure 8.2: The transmission electron microscope images of cross-sections of various transition metal compounds grown either on sapphire or SI GaAs substrates. The different types of defects in (a)-(c) $MoTe_2$, (d)-(e) $NiTe_2$ and (f) TaAs layers. [TEM images were taken by Dr. S. Kret, Dr. A. Kaleta and MSc W. Zajkowska-Pietrzak, Institute of Physics, PAS. The data analysis and Figure preparation: Z. Ogorzałek-Sory.].

Figures 8.2(a)-(c) present (a) a low angle tilt grain boundary, (b) amorphous grain bound-

ary and (c) NWs, marked by the blue, red and green boxes, respectively. Following, Figures 8.2(d)-(f) show (d) line defects in $NiTe_2$ layers such as edge dislocations, (e) GaAs (111)B substrate groove defects, marked by the blue arrow and (f) an incoherent phase boundary in TaAs layers, marked by the pink arrows.

The MBE growth of layered transition metal compounds such as $MoTe_2$, $NiTe_2$, and TaAs is highly sensitive to substrate preparation, source stability and interface quality, with quasi-van der Waals epitaxy introducing additional challenges like interfacial disorder and structural defects. The observed variations in microstructure and defect types, illustrated by STEM highlight the necessity of precise, consistent growth conditions to achieve reproducible electronic properties.

Chapter 9

Summary

This thesis focuses on the physical properties of three transition metal compounds: $NiTe_2$, $MoTe_2$, and TaAs, and presents their broad experimental characterization, supported by theoretical calculations. The properties of these thin-film materials differ significantly from those of their bulk counterparts (e.g., graphene versus graphite), as the reduced dimensionality, confinement effects, and modified inter-layer interactions lead to novel structural, electronic, optical and mechanical characteristics. The results include a wide range of magnetotransport measurements conducted across a broad temperature range and in magnetic fields up to 12 T. The magnetotransport data are complemented by structural and optical studies, including scanning transmission electron microscopy (STEM), atomic force microscopy (AFM), X-ray diffraction (XRD), Raman spectroscopy and angle-resolved photoemission spectroscopy (ARPES). To better understand the observed phenomena, several theoretical models were applied to interpret the transport data and address the peculiar transport mechanisms present in these materials. For some compounds ($NiTe_2$ and TaAs) advanced density functional theory (DFT) calculations were performed by pioneering researchers, providing valuable insights into electronic structures.

$NiTe_2$: the semi-insulating GaAs (111)B was selected as substrate due to its minimal lattice mismatch with $NiTe_2$, which allowed for high-quality epitaxial growth. Structural characterization using high-resolution TEM and XRD confirmed the formation of high-quality, $NiTe_2$ layers with smooth morphology, sharp interfaces, and well-ordered atomic arrangements. Lattice parameter analysis revealed significant tensile strain, in both in-plane and out-of-plane directions. XRD studies further confirmed that substrate temperature and thickness of the layer influence the lattice strain. This strain results from possible inter-layer defects or intercalated atoms, as evidenced by bright features in the STEM images. The substrate-related local strain was evidenced, as well. Electronic structure measurements using ARPES identified several topological surface states (TSS), including TSS1 and TSS2, in a good agreement with the previous theoretical and experimental reports. Transport studies revealed different electric properties depending on the growth conditions. Films grown

at low substrate temperatures (less than T_S = 180 ^{o}C) exhibited metallic temperature dependence, while samples grown at high temperatures (T_S = 430 ^{o}C and higher) showed semiconducting behavior. It was shown that they were tellurium deficient. The quality of the layers was assessed using the residual resistivity ratio (RRR). As T_S decreased, the RRR increased, however, even for the best samples it did not exceed 10, in stark contrast to the bulk samples, where it reached 374. The highest-quality samples displayed non-trivial transport effects: at low temperature, weak antilocalization was observed for the sample grown at T_S = 230 ^oC. WAL effects were modeled using the Hikami–Larkin–Nagaoka and Tkachov–Hankiewicz models and shown to be three-dimensional in nature, involving both bulk and surface states. Hall measurements indicated that carrier concentration increased with T_S temperature. Interestingly, for samples grown at T_S = 180 ^{o}C, 2-carrier band transport with both electrons and holes was observed. The Hall resistivity changed sign with temperature, suggesting a possible temperature-driven Lifshitz transition. These findings were supported by mobility spectrum analysis and 2-carrier model fits, which showed that both types of carriers had similar concentrations ($\sim 10^{21} \cdot \mathrm{cm}^{-3}$) and mobilities up to 280 cm^2/Vs at low temperatures. DFT calculations showed strained samples were still Dirac semimetals, however the energies of the type-II bulk Dirac points slightly differed for the two samples studied.

$MoTe_2$: the morphology can be changed from 2D one to the net of nanowires by changing the substrate temperature T_s or tellurium source temperature T_{Te}. At low substrate temperature (T_s = 270 ^{o}C) a semiconducting 2H phase was observed, while at higher temperatures (T_s = 350 ^{o}C), the growth of nanowires occurs. Moreover, a higher tellurium source temperature ($T_{Te} > 385$ ^{o}C) favors 2H semiconducting $MoTe_2$ phase, while lower one ($T_{Te} < 360$ ^{o}C) results in a nanowire morphology, showing that it is Te deficiency promoting nanowire formation. Interestingly, there is no impact of substrate on the phases of the $MoTe_2$ layers. The wide substrate selection such as GaAs (111)B, sapphire or InAs (111) did not provide different phases. Only one sample contained topological 1T′$MoTe_2$ phase. Unfortunately, the phase was sandwiched between two conducting materials making meaningful characterization by electronic transport measurements impossible. Contrarily to literature results, InAs (111) did not promote the growth of the $1T'-$phase in our case. The findings indicate that in our case phase evolution is independent of the substrate and can be controlled only by growth parameters, specifically adjusted to individual substrates. It might be related to the van der Waals character of the $MoTe_2$ bonds, much different than for standard epitaxy, where substrate symmetry and lattice matching plays a key role for the quality of the crystal. High atmosphere sensitivity of thin 2H-$MoTe_2$ layer was observed. In-situ deposited AlO_x capping layer was proposed and shown to be essential for $MoTe_2$ protection from environment degradation. The use of a thin AlO_x capping layer ensures both effective protection and reliable ohmic contact formation. However, too thin or too thick aluminum layer results in incomplete

surface coverage or not fully oxidized layers, respectively, the latter leading to additional parallel conducting channel. All $MoTe_2$ layers have similar R(T) dependencies, dominated by hopping charge transport. Some of the layers are characterized by an anomalous hopping exponent of $x \sim 0.66$, to our knowledge observed for TMDs for the first time.

TaAs: was grown on GaAs (001) substrates despite a substantial lattice mismatch (16%). TEM and XRD analysis revealed a predominant presence of stacking faults, known for the tetragonal TaAs, leading to the discovery of a new orthorhombic topological phase (o-TaAs). The AFM images showed that the surface morphology of the layers is composed of nanocolumns (NCs) aligned along the [110] direction. The dimensions of NCs, typically of 40 nm in width and 150 nm in length, increase with layer thickness. This structural anisotropy was mirrored in the anisotropic in-plane electrical resistivity, with significantly lower resistivity and higher carrier mobility for the current aligned along NCs. Low-temperature transport studies revealed weak antilocalization effect. It was shown to be 3D in nature, confirmed by angular dependence and fits to the Tkachov-Hankiewicz model. No clear signs of chiral anomaly were detected, likely due to the high hole concentration ($\sim 10^{21}$ cm^{-3}), which positions the Fermi level deep into the valence bands. The new phase was confirmed by density functional theory calculations and it was shown to maintain topological Weyl features, albeit with modified Brillouin zone symmetry and 20 Weyl points with a changed distribution in respect to the tetragonal phase. The results show that MBE-grown TaAs hosts new crystalline arrangements, potentially offering new platforms for exploring the topological phenomena.

The work demonstrates the potential of $NiTe_2$, $MoTe_2$ and TaAs transition metal compounds for future applications in topological Dirac and Weyl electronics. Along with their topological properties, they offer an excellent platform for fundamental research, as their structural and electronic characteristics can be tuned by growth parameters such as substrate temperature and film thickness. The growth of 2D layers on 3D substrates frequently leads to quasi-van der Waals epitaxy, characterized by interfacial interactions that are neither purely van der Waals nor covalent, resulting in strain, defects, and stacking faults. These findings underscore the need for further experimental and theoretical investigations into strain effects, defect formation and the underlying mechanisms of van der Waals epitaxy with particular emphasis on understanding how these factors influence charge transport mechanisms in layered materials.

Chapter 10

Summary of scientific activity

Author's publications

1. Ogorzałek-Sory, Z., Lee, C.-C., Domagała, J. Z., Zajkowska-Pietrzak, W., Kret, S., Bożek, R., Pacuski, W., Lutsyk, I., Ryś, W., Kowalczyk, P. J., Tokarczyk, M., Polakowski, M., Wąsik, D., Sadowski, J., Huang, B.-H., Lin, H., and Gryglas-Borysiewicz, M. (2025). Orthorhombic TaAs – a new topological phase of the archetypical Weyl semimetal. ACS Applied Materials & Interfaces.
   https://doi.org/10.1021/acsami.5c04474

2. Piskorski, M., Lutsyk, I., Ryś, W., Le Ster, M., Ogorzałek-Sory, Z., Binder, J., Toczek, K., Nadolska, A., Dunal, R., Przybysz, P., Rogala, M., Dąbrowski, P., Pacuski, W., Sadowski, J., Gryglas-Borysiewicz, M., Wysmołek, A., Kowalczyk, P. J., Kozłowski, W., and Krukowski, P. (2025). The integration of Raman spectrometer with glove box for high-purity investigation in an inert gas condition. Measurement, 251, Article 117190.
   https://doi.org/10.1016/j.measurement.2025.117190

3. Sadowski, J., Domagała, J. Z., Zajkowska, W., Kret, S., Seredyński, B., Gryglas-Borysiewicz, M., Ogorzałek-Sory, Z., Bożek, R., and Pacuski, W. (2022). Structural properties of TaAs Weyl semimetal thin films grown by molecular beam epitaxy on GaAs(001) substrates. Crystal Growth & Design, 22 (10), 6039–6045.
   https://doi.org/10.1021/acs.cgd.2c00669

4. Seredyński, B., Ogorzałek-Sory, Z., Zajkowska, W., Bożek, R., Tokarczyk, M., Suffczyński, J., Kret, S., Sadowski, J., Gryglas-Borysiewicz, M., and Pacuski, W. (2021).

Molecular beam epitaxy of a 2D material nearly lattice matched to a 3D substrate: $NiTe_2$ on GaAs. Crystal Growth & Design, 21(10), 5773–5779. https://doi.org/10.1021/acs.cgd.1c00673

5. Kumanek, B., Stando, G., Stando, P., Matuszek, K., Milowska, K. Z., Krzywiecki, M., Gryglas-Borysiewicz, M., Ogorzałek-Sory, Z., Payne, M. C., MacFarlane, D., and Janas, D. (2021). Enhancing thermoelectric properties of single-walled carbon nanotubes using halide compounds at room temperature and above. Scientific Reports, 11(1), 8649. https://doi.org/10.1038/s41598Ś021Ś88079Św

6. Ogorzałek-Sory, Z., Seredyński, B., Kret, S., Kwiatkowski, A., Korona, K. P., Grzeszczyk, M., Mierzejewski, J., Wasik, D., Pacuski, W., Sadowski, J., and Gryglas-Borysiewicz, M. (2020). Charge transport in MBE-grown 2H-$MoTe_2$ bilayers with enhanced stability provided by an AlO_x capping layer. Nanoscale, 12(5), 16535–16542. https://doi.org/10.1039/D0NR03148H

7. Gryglas-Borysiewicz, M., Kwiatkowski, A., Juszyński, P., Ogorzałek-Sory, Z., Puźniak, K., Tokarczyk, M., Kowalski, G., Baj, M., Wasik, D., Szwacki, N. G., Przybytek, J., Sadowski, J. Z., Sawicki, M., Dziawa, P., and Domagała, J. Z. (2020). Hydrostatic pressure influence on T_C in (Ga,Mn)As. Physical Review B, 101(5), 054413. https://doi.org/10.1103/PhysRevB.101.054413

8. Borysiewicz, M. A., Ekielski, M., Ogorzałek-Sory, Z., Wzorek, M., Kaczmarski, J., and Wojciechowski, T. (2017). Highly transparent supercapacitors based on ZnO/MnO_2 nanostructures. Nanoscale, 9(22), 7577–7587. https://doi.org/10.1039/C7NR01320E

Manuscripts intended for future publication:

- Ogorzałek-Sory, Z., Ferreira, P. P., Tokarczyk, M., Dziawa, P., Manesco, A. L. R., Heil, C., Kret, S., Zajkowska, W., Baj, M., Pacuski, W., Seredyński, B., Elano, T. F. L., Sadowski, J., and Gryglas-Borysiewicz, M. Strain-induced Dirac cone shifts in the MBE-grown anisotropic tensile-strained type-II Dirac semimetal $NiTe_2$. (in preparation).

- Ogorzałek-Sory, Z., Tokarczyk, M., Kret, S., Kwiatkowski, A., Seredyński, B., Korona, K., Wąsik, D., Pacuski, W., Sadowski, J., and Gryglas-Borysiewicz, M. Thin films of transition metal dichalcogenides grown by MBE method. The influence of substrate on $MoTe_2$ structure, morphology and magnetotransport properties. (in preparation).

Author's conference speeches and poster presentations:

1. 2022 MRS Fall Meeting & Exhibit, Boston, Massachusetts, USA, Nov 27 – Dec 2, 2022
   Oral presentation: "Magnetotransport properties of MBE-grown $NiTe_2$"

2. JEMS 2022, Warsaw, Poland, Jul 24–29, 2022
   Oral presentation: "Magnetotransport properties of TaAs layers grown by MBE"

3. 2022 European Physical Society Forum, Paris, France, Jun 1–4, 2022
   Poster presentation: "Magnetotransport properties of TaAs layers grown by MBE"

4. "Jaszowiec" International School & Conference on the Physics of Semiconductors, Sep 1–10, 2021
   Poster presentation: "Magnetotransport properties of MBE-grown $NiTe_2$ - a new candidate for Dirac fermion studies"

5. 2020 MRS Fall Meeting & Exhibit, Boston, Massachusetts, USA, Nov 27 – Dec 4, 2020
   Oral presentation: "Charge transport in MBE-grown 2H-$MoTe_2$ bilayer with enhanced stability provided by the AlO_x capping layer"

6. 2020 Young Scientists Symposium, Warsaw, Poland, Aug 24, 2020
   Oral presentation: "Charge transport in MBE-grown 2H-$MoTe_2$ bilayer with enhanced stability provided by the AlO_x capping layer"

7. 2019 MRS Fall Meeting & Exhibit, Boston, Massachusetts, USA, Dec 1–6, 2019
   Poster presentation: "Towards large scale $MoTe_2$ layers grown by MBE"

8. European Magnetic Field Laboratory User Meeting 2019, Warsaw, Poland, Jun 25, 2019
   Poster presentation: "Magnetotransport properties of the $MoTe_2$ layers grown by molecular beam epitaxy"

9. "Jaszowiec" International School and Conference on the Physics of Semiconductors, Szczyrk, Poland, Jun 8–14, 2019
   Poster presentation: "Magnetotransport properties of the $MoTe_2$ layers grown by molecular beam epitaxy"

10. 2018 MRS Fall Meeting & Exhibit, Boston, Massachusetts, USA, Nov 25–30, 2018
    Poster presentation: "Magnetotransport properties of the $MoTe_2$ layers grown by molecular beam epitaxy"

11. International School and Conference on the Physics of Semiconductors (ICPS 2018), Montpellier, France, Jul 29 – Aug 3, 2018
    Poster presentation: "Magnetocurrent anisotropy induced by rotation of the magnetization vector in ferromagnetic, paramagnetic and superparamagnetic (Ga,Mn)As/GaAs Esaki diodes"

12. "Jaszowiec" International School and Conference on the Physics of Semiconductors, Szczyrk, Poland, Jun 16–22, 2018
    Poster presentation: "Preliminary transport studies of the $MoTe_2$ layers grown by molecular beam epitaxy"

13. "Jaszowiec" International School and Conference on the Physics of Semiconductors, Szczyrk, Poland, Jun 17–23, 2017
    Poster presentation: "Magnetocurrent anisotropy of (Ga,Mn)As/GaAs Esaki diodes"

14. "Jaszowiec" International School and Conference on the Physics of Semiconductors, Szczyrk, Poland, Jun 18–24, 2016
    Poster presentation: "Capacitance studies of (Ga,Mn)As/GaAs Esaki diodes"

The author has participated in the following research grants:

1. Narodowe Centrum Nauki
   PRELUDIUM 20, 2021/41/N/ST5/04206
   Title: Cienkie warstwy dichalkogenków metali przejściowych. Wpływ podłoża na strukturę, morfologię i własności magnetotransportowe $MoTe_2$
   Project leader: Zuzanna Ogorzałek-Sory
   https://projekty.ncn.gov.pl/index.php?projekt˙id=521513

2. Narodowe Centrum Nauki
   OPUS 14, 2017/27/B/ST5/02284
   Title: Wzrost metodą epitaksji z wiązek molekularnych i badanie heterostruktur topologicznych półmetali z ferromagnetykami i antyferromagnetykami
   Project leader: dr hab. Janusz Sadowski
   https://projekty.ncn.gov.pl/index.php?projekt˙id=395431

Appendix A

Experimental methods

A.1 Keysight (Agilent) E4980A

The Keysight (Agilent) E4980A is a precise general-purpose LCR meter for evaluating LCR components, materials and semiconductor devices over a wide range of frequencies from f=20 Hz to f=2 MHz. Typically, it was used for capacitance studies to test the quality of the ohmic contacts or to measure the impedance of the studied layers with the capacitor-like behavior.

A.2 Bonding

Figures A.1(a)-(b) present the wire bonder machines: (a) a reference schematic image with labelled parts, and (b) a photograph of the actual system used in the experiments.

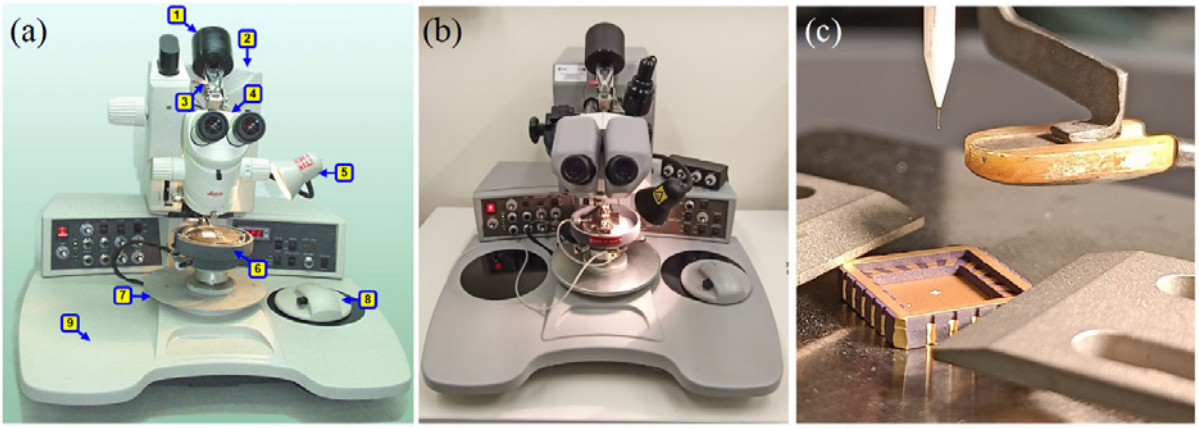

Figure A.1: The photos of the (a) wire bonder machine [283], (b) wire bonder machine at the Faculty of Physics of the University of Warsaw and (c) the zoom of the wire bonder machine sample holder with the needle threaded with a 20 μm-thick golden thread and sample chip carrier.

The chip carrier is mounted on the workholder (6), (see Figure A.1(c)), which position can be adjusted with the rotary table (7) or multi mouse (8). The main head of the wire bonder

machine (2) is composed of the spool feed system (1), the microscope (4) and the area light (5). The left control panel allows to choose the appropriate bonding parameters such as a power of the ultrasounds, the applied force and the time, implying the quality of the bonds. Furthermore, the loop knob allows to change the length of the golden wires outgoing the chip carrier. A ball diameter setting option is also available in the right panel. Although all the parameters could be adjusted well, the direct bonding to the indium contacts of the studied layers was impossible. It is followed by the layered structure of the TMDs and their easy exfoliation process. Even a small force of the bond, applied to the sample, caused wire detaching. Obviously, that point did not refer to the TMPs, including TaAs which bonding is ionic and covalent.

A.3 Buehler Isomet low speed saw

Figures A.2(a)-(e) present Buehler Isomet low speed saw, used for sample cutting, and optical images of the diamond saw cut and the length between the manually attached golden wires to the indium pads.

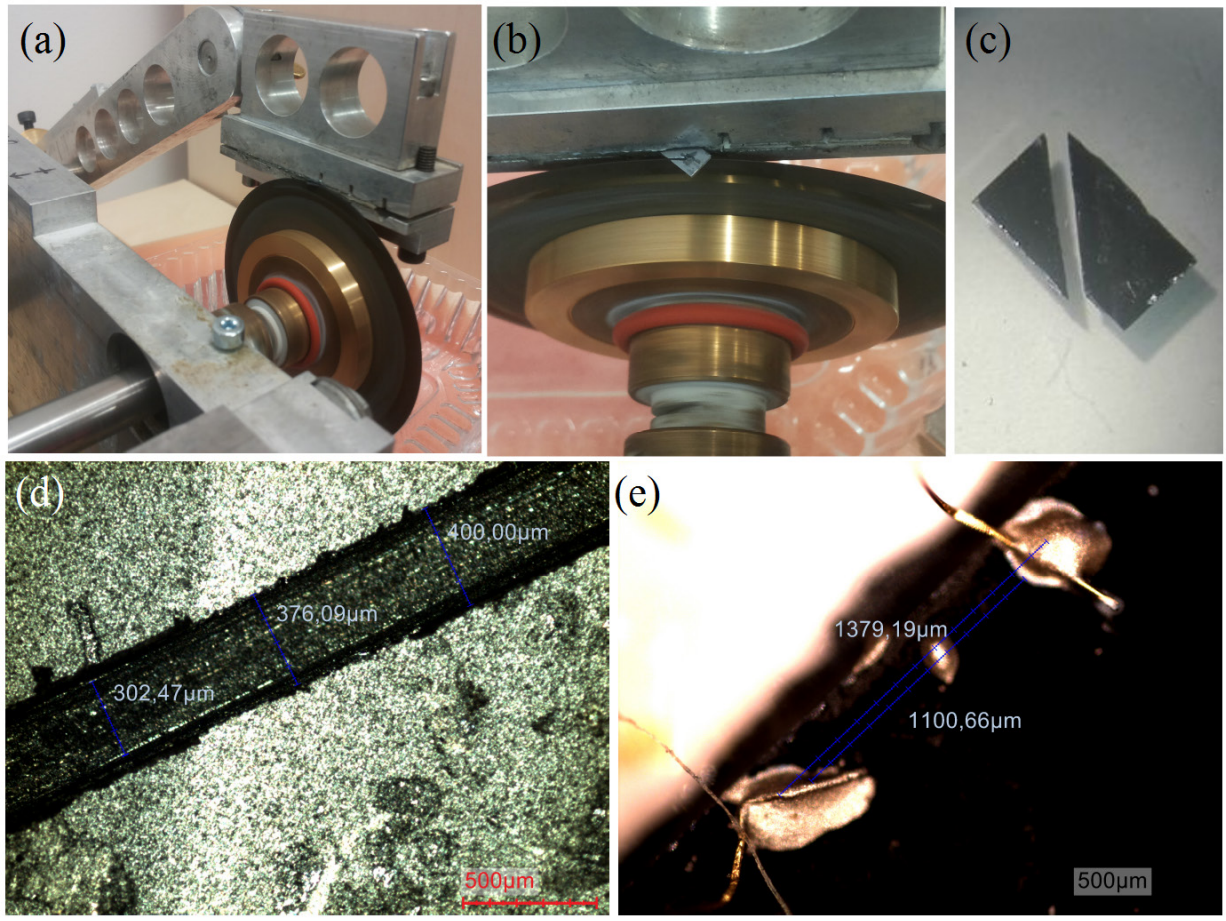

Figure A.2: The photos of the (a)-(b) diamond saw and (c) the cut GaAs (100) substrate. The dimensions of sample in (c) are of order few mm. The optical images of (d) the width of the diamond saw cut and (e) the length between the manually attached golden wires to the indium pads.

The electric saw allowed the samples to be cut by the diamond blades. The wafers were placed into a sample holder, positioned with the micrometer screw to the axis of the saw. Then, the arm of the saw had to be balanced with the adequate weights to allow its uniform linear motion. The whole process was not efficient and the cut widths were of order of 300 μm to 400 μm making this procedure not accurate enough (see Figures A.2(c)-(d)). To avoid diamond blade heating, dust rising and to have a clean cut, the blades had to be partially immersed into a distilled water during the cut. Obviously, that method was also introducing many chemical impurities which might have been contaminating the sample surface. Indeed, J. Choi et al. has shown that the intrinsic properties of the TMDs can dramatically modify in various fabrication processes due to electron transfer from or to the TMD, thus changing the chemical potential of the TMDs [284]. Undoubtedly, another, better method of wafer cutting had to be found. Furthermore, the cutting did not solve the problem of the uniformity of the current flow. The contacts, made manually with a silver paste, were not identical. Even a small amount of the paste, going outside the indium area, caused electric field inhomogeneity and impeded setting of the real width to length (W/L)

ratio (see Figure A.2(e)).

Appendix B

$NiTe_2$

B.1 Additional information

Additional optical characterization results such as Raman spectroscopy, atomic force microscopy images or the photoluminescence spectra of the selected $NiTe_2$ samples, which were not the subject of this dissertation, can be found in the paper of Seredyński et al. [42].

During the growth of $NiTe_2$, an alternative process was applied to the (001) GaAs substrate, which has a square lattice and a lattice parameter of a = 5.653 $\mathring{A}$ [152]. The preliminary 2- and 4-probe current-voltage characteristics of the two sample types differed substantially. For samples grown on GaAs (001), the IV curves were nonlinear, whereas for those grown on GaAs (111)B, the characteristics were linear. Although other factors may have contributed to the nonlinearity (e.g., non-ohmic contacts or improper measurement conditions), the substrate itself was considered the primary cause in the first approximation.

B.2 Band structure: theory and experiment

Figure B.1 presents ARPES spectrum of $NiTe_2$ along $H' \leftarrow A \rightarrow H$ showing layered bulk states and corresponding DFT calculations [134].

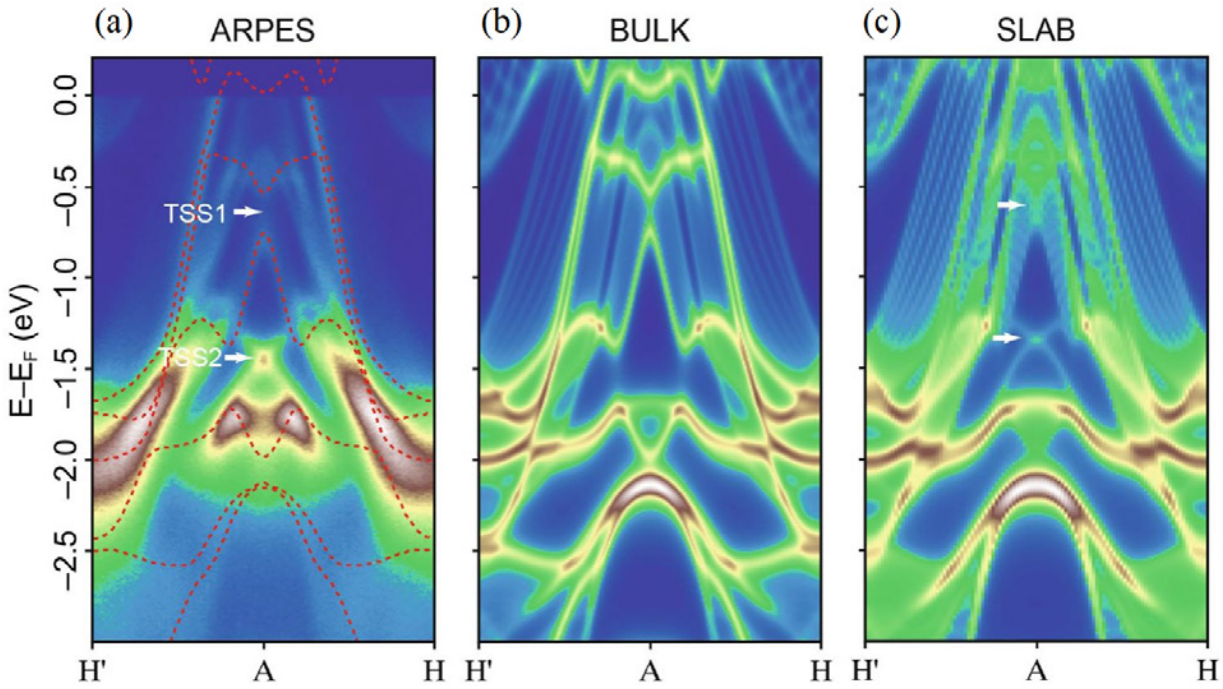

Figure B.1: (a) The ARPES $NiTe_2$ spectrum taken along $H' \leftarrow A \rightarrow H$ directions with the layered bulk states, marked by the red dashed lines. The corresponding DFT calculations of the band structure for (b) the bulk system and (c) the slab surface [134].

B.3 Fingerprints of relativistic and trivial Dirac fermions

Figures B.2(a)-(b) present ARPES measurements along with DFT calculations on the MBE-grown $NiTe_2$ samples while changing their thickness from one tri-layer to five tri-layers.

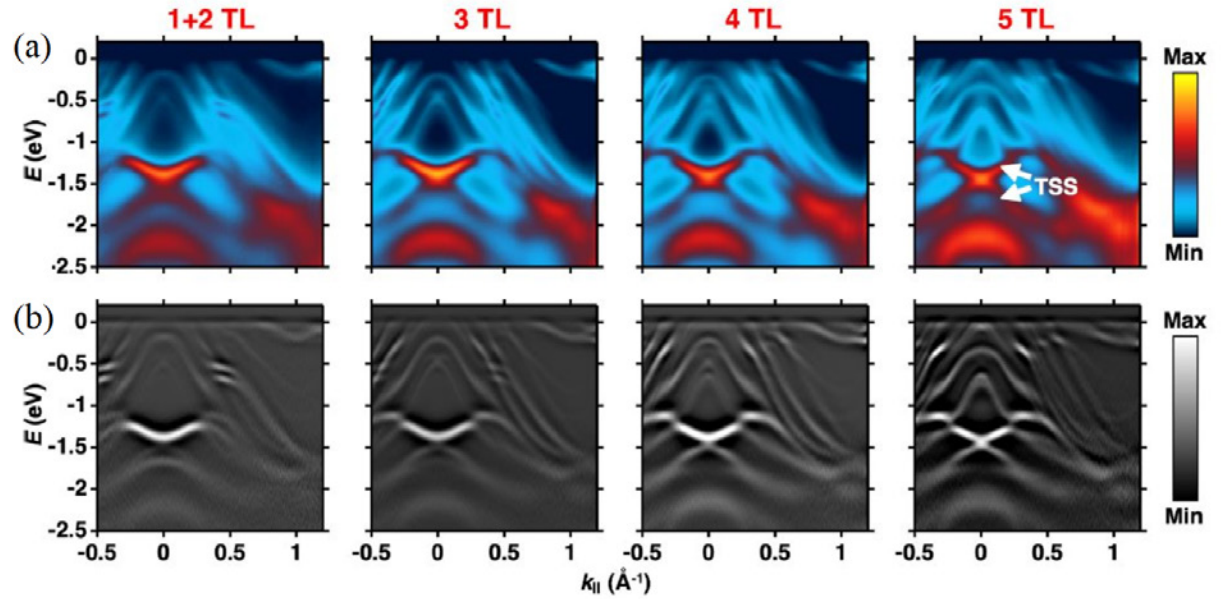

Figure B.2: (a) The thickness-dependent (1+2 TL corresponds to a mixture of 1 and 2 TLs) ARPES maps along $\Gamma \rightarrow K$ direction and (b) the corresponding second-derivative maps for the MBE-grown $NiTe_2$ [30].

B.4 XRD analysis

Two HR STEM cross-section images of the samples grown at T_S = 180 ^{o}C and T_S = 230 ^{o}C were investigated to analyze the distances between tellurium atoms (d_{Te-Te}) within one TL and the distances between tellurium atoms between the subsequent TLs (d_{Te-Te} vdW gap), as schematically shown in Figure B.3(a).

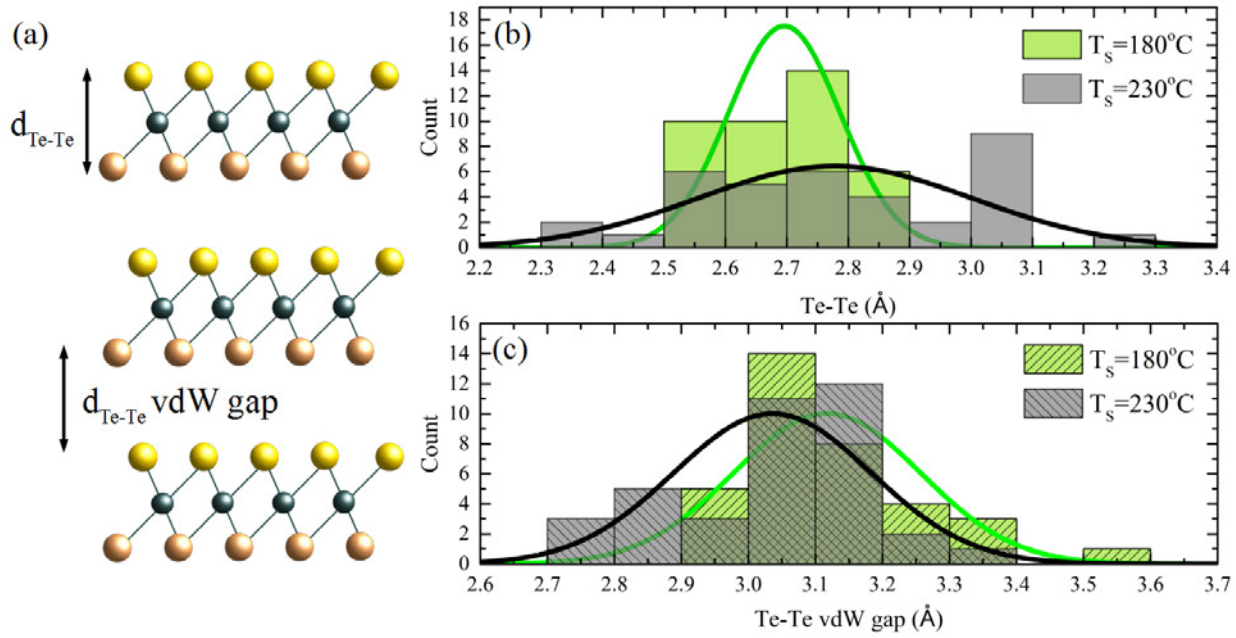

Figure B.3: (a) Scheme of the $NiTe_2$ TLs with the defined distances between the Te-Te atoms. The values were obtained from the zoomed HR-STEM cross-section images, marked in the red frames in Figures 5.11(a)-(b) for two samples grown at T_S = 180 ^{o}C (UW1723) and T_S = 230 ^{o}C (UW1651). The distances between the Te-Te atoms (b) within TL and between the Te-Te atoms (b) between the subsequent TLs.

Figures B.3(b)-(c) show the histograms of d_{Te-Te} and d_{Te-Te} vdW gap distances for two samples with the highest tensile strain values. Although the data statistics is limited, the normal distribution curves applied to the data, marked by the green and black lines, reveal a weak trend. For the sample with a larger strain (grown at T_S = 230 ^{o}C), the interlayer distance is slightly smaller, and TL thickness is slightly larger. However, a larger statistics would be necessary to verify this hypothesis.

B.5 Theoretical description

To verify the crystal stability, the phonon band structure, the isotropic Eliashberg spectral function $\alpha^2F(\hbar\omega)$ and the electron-phonon coupling strength $\lambda(\omega)$ were calculated. The calculations were performed within the scalar-relativistic approximation an without spin–orbit coupling. The phonon band structures for the samples grown at T_S = 230°C and T_S = 180°C are presented in Figures B.4(a)-(b), respectively.

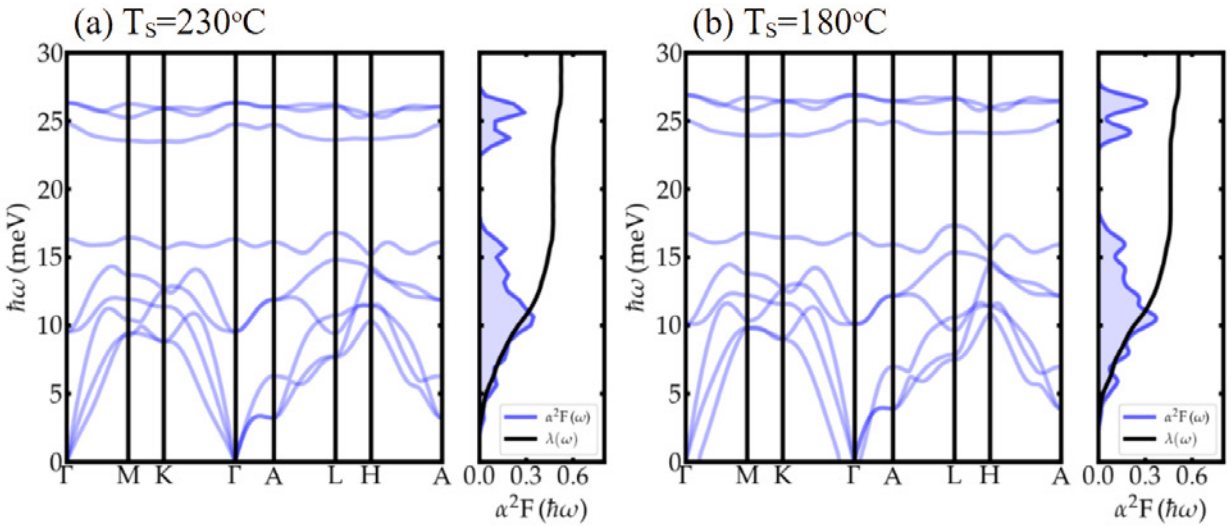

Figure B.4: The phonon band structure, isotropic Eliashberg spectral function, $\alpha^2 \cdot F(\hbar \cdot \omega)$, and the electron-phonon coupling strength, $\lambda(\omega)$, within the scalar-relativistic approximation and without the SOC for the samples grown (a) at T_S = 230 ^{o}C and (b) at T_S = 180 ^{o}C [161].

For both samples, the phonon frequencies are close to $\hbar \cdot \omega = 27\ meV$, proving that tensile-strained $NiTe_2$ is dynamically stable at the experimental conditions.

Appendix C

$MoTe_2$

C.1 Bulk and surface Weyl fermions in 1T′ and T_d phases

Figure C.1(a) presents the 3D scheme of the type-II Weyl semimetal with W1 and W2 points forming hole and electron pockets. Weyl fermions emerge at the boundary between electron and hole pockets. Multiple Fermi arcs arise from topological surface states, marked by the red lines [176].

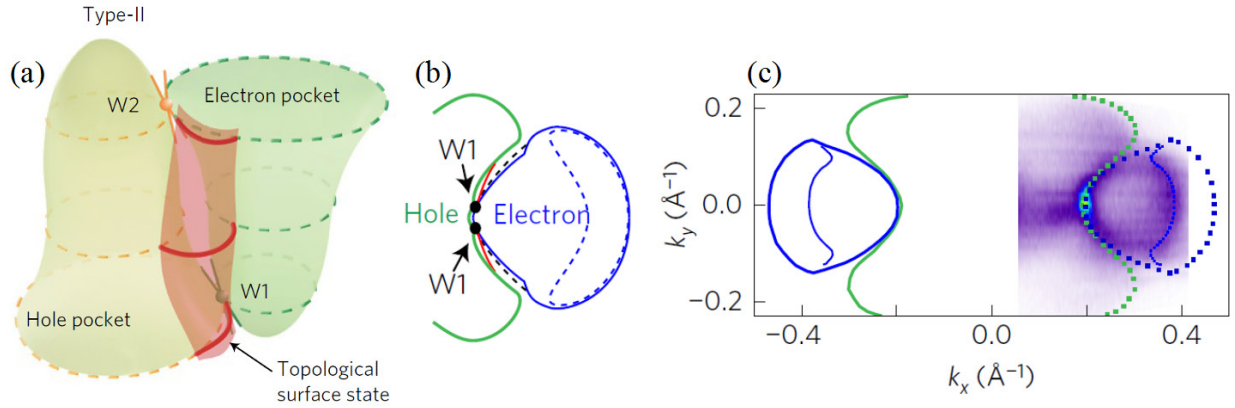

Figure C.1: (a) The scheme of the type-II Weyl semimetal with W1 and W2 points forming hole and electron pockets. The red lines show the topological surface states connecting W1 and W2 points of different chiralities. (b) The scheme of the electron band structure of $T_d - MoTe_2$ around W1 points at the proximity of the E_F. The green and blue line depict the hole and electron pockets, respectively. (c) The electron band structure of $T_d - MoTe_2$ measured at E=E_F by ARPES [176].

Figure C.1(b) shows the 2D scheme of the electron band structure of the $T_d - MoTe_2$ around W1 points at the proximity of the E_F. The red lines depict the Fermi arcs approaching W2 points. In 2016 Deng et al. have experimentally shown the electron band structure of the $T_d - MoTe_2$ measured by ARPES. Figure C.1(c) shows the first experimental electron band structure of $T_d - MoTe_2$ measured at E=E_F. Data were in very good agreement with theoretical calculations, proving topological properties of the $MoTe_2$ layers [176].

C.2 SEM

Figures C.2(a)-(d) show the SEM images of the various $MoTe_x$-type structures grown at different T_S and various annealing processes. The results show different surface morphologies including nanodendrites, "reaction diffusion pattern" [285], dots and other complex precipitations. Inhomogeneous surfaces usually lead to the much more resistive properties of the layers. In this case, the room-temperature 2-probe resistances of the layers were reaching $R = 1000\ M\Omega$.

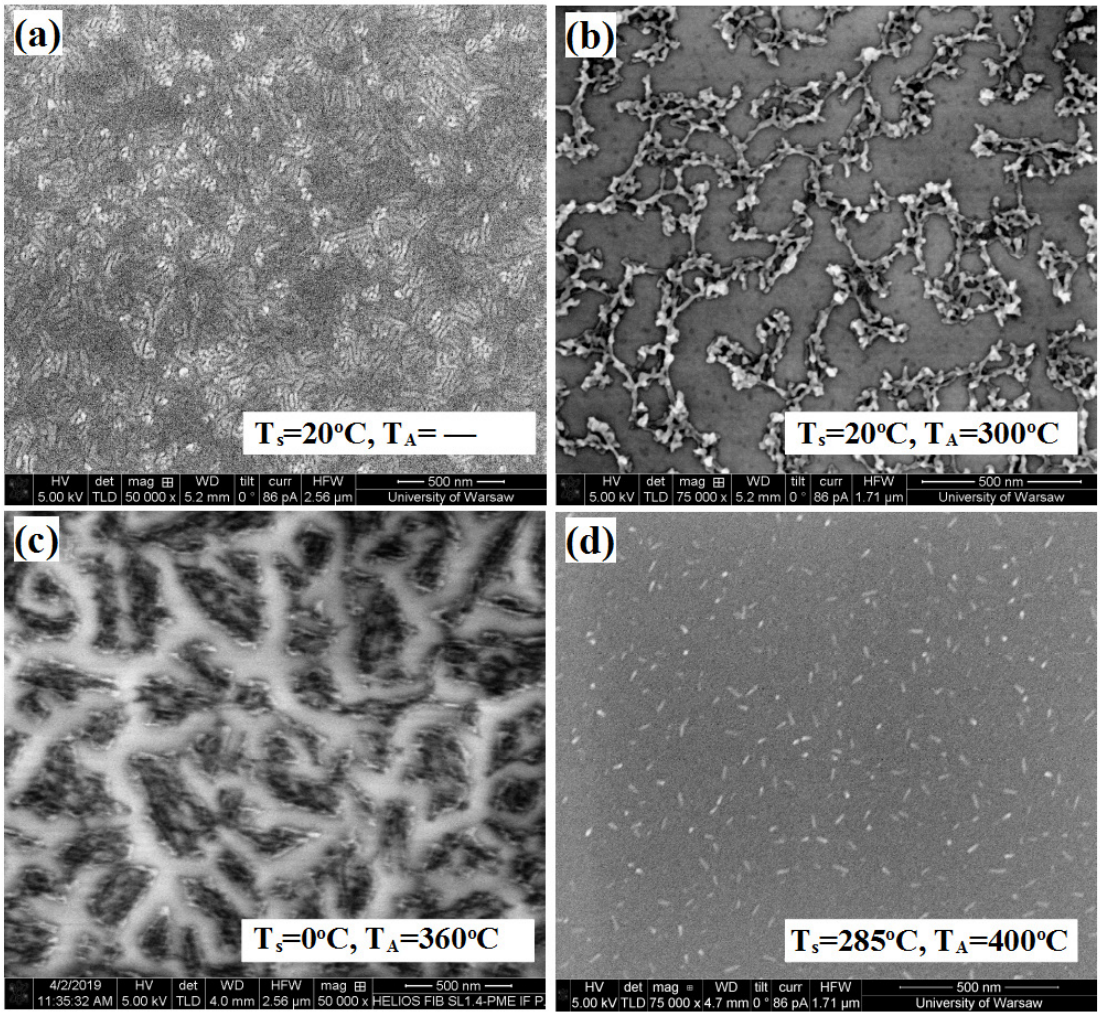

Figure C.2: Structural characterization of $MoTe_x$ layers. The scanning electron microscopy images (a)-(d) of various samples of $MoTe_x$, grown with different parameters. [SEM images were made under supervision of Dr. J. Binder, Faculty of Physics, UW. Figure preparation and analysis: Z. Ogorzałek-Sory]

C.3 Electrical characterization of the $MoTe_x$ layers

C.3.1 Peculiar resistivity features

Figures C.3(a)-(b) show the longitudinal resistance of NWs as a function of magnetic field, where a temperature- and angle-dependent deeps were observed.

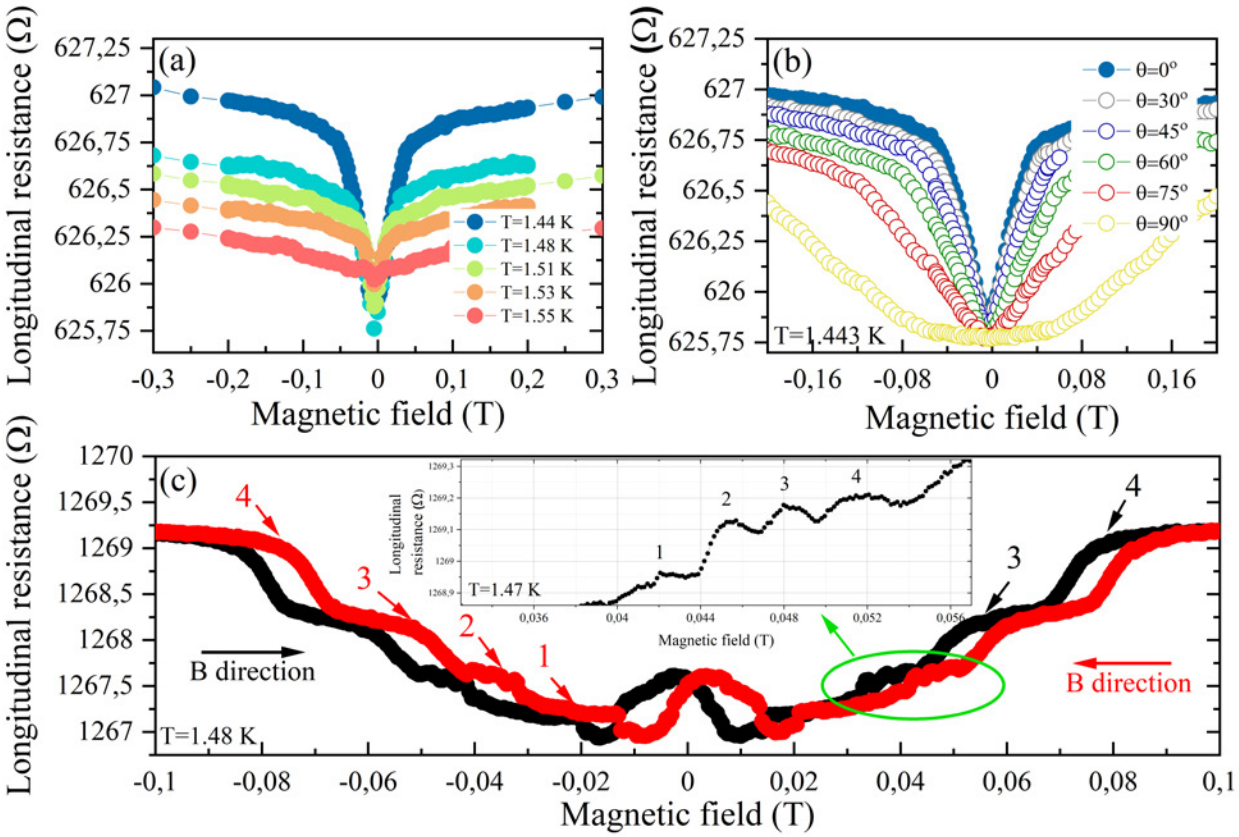

Figure C.3: Electrical characterization of $MoTe_x$ layers. The temperature- (a) and the angle-dependent (b) longitudinal resistance as a function of magnetic field, measured for NWs (UW1004). (c) The longitudinal resistance as a function of the magnetic field, measured for the $MoTe_x$ layers (UW1087). Inset: the periodicity of the longitudinal resistance oscillations.

In this case, the deeps vanishes extremely fast (see Figure C.3(a)), suggesting non topological origin. Moreover, for another $MoTe_x$ layer some peculiar resistivity features were also observed. Figure C.3(c) presents unidentified repetitive structures of the longitudinal resistance as a function of magnetic field. Apart maximum at low magnetic field, additional features e.g. resistance oscillations (see the zoomed region, marked by the green circle, in the inset of Figure C.3(c)) and resistance plateaux emerge. Their origin is currently unknown. It is worth to note that the above effects were observed even at magnetic fields stronger than the critical field for In.

C.3.2 The MBE growth, XRD spectra, TEM images and magnetotransport properties of $MoTe_2$ grown on InAs (111)

The possibility of harnessing the polymorphic nature of $MoTe_2$ and the ability of the selective large-scale growth of each phase would be a huge scientific achievement. Although many growth techniques had been applied to achieve a high quality $MoTe_2$ in each politype, a successful growth of the large-scale Weyl semimetalic phase with thickness control and high crystallinity still remains a challenge. Based on Tsipas's work [172], where 1T′-phase was obtained, the MBE growth of the $MoTe_2$ layers on InAs (111) substrate has been performed. All the samples have been grown on the MBE-grown InAs (111) buffer layer, which was grown on the SI GaAs (111)B substrate. To address the influence of the $MoTe_2$ thickness on its properties, two samples of 1 ML and 3 MLs have been grown. The substrate temperature for the growth of InAs (111) was T_S = 450 ^{o}C, then all wafers were in-situ transferred to the II-VI MBE chamber where $MoTe_2$ layers at T_S = 270 ^{o}C have been grown. To examine the annealing procedure impact on $MoTe_2$ properties, another 3 MLs sample has been grown and in-situ annealed after the growth for 10 minutes at T_A = 450 ^{o}C. To extract the properties of the $MoTe_2$ layers, the reference sample of InAs (111), without the $MoTe_2$ layers, has been grown. All the samples were capped with AlO_x. The experiment included the following samples:

1. V168: The reference sample of InAs (111) of nominal thickness of 18 nm, capped with AlO_x
2. UW1802: 1 ML, T_S = 270 ^{o}C, not annealed after the growth and capped with AlO_x
3. UW1801: 3 MLs, T_S = 270 ^{o}C, not annealed after the growth and capped with AlO_x
4. UW1800: 3 MLs, T_S = 270 ^{o}C, in-situ annealed after the growth for about 10 minutes at temperature T_A = 450 ^{o}C and capped with AlO_x

All the samples were characterized by the wide-temperature angle-resolved resistivity tensor measurements in a magnetic field up to B=12 T. The magnetotransport measurements included among others:

1. Resistivity dependence as a function of temperature
2. Out-of-plane and in-plane MR dependencies for different temperatures
3. The Hall concentration and the Hall mobility determination
4. Angle-resolved WAL measurements combined with the theoretical description using HLN model

5. The Shubnikov de-Haas oscillations dependence as a function of temperature

Figure C.4 presents an example of the longitudinal component of the conductivity tensor, measured at T=1.5 K, attributed to InAs layer.

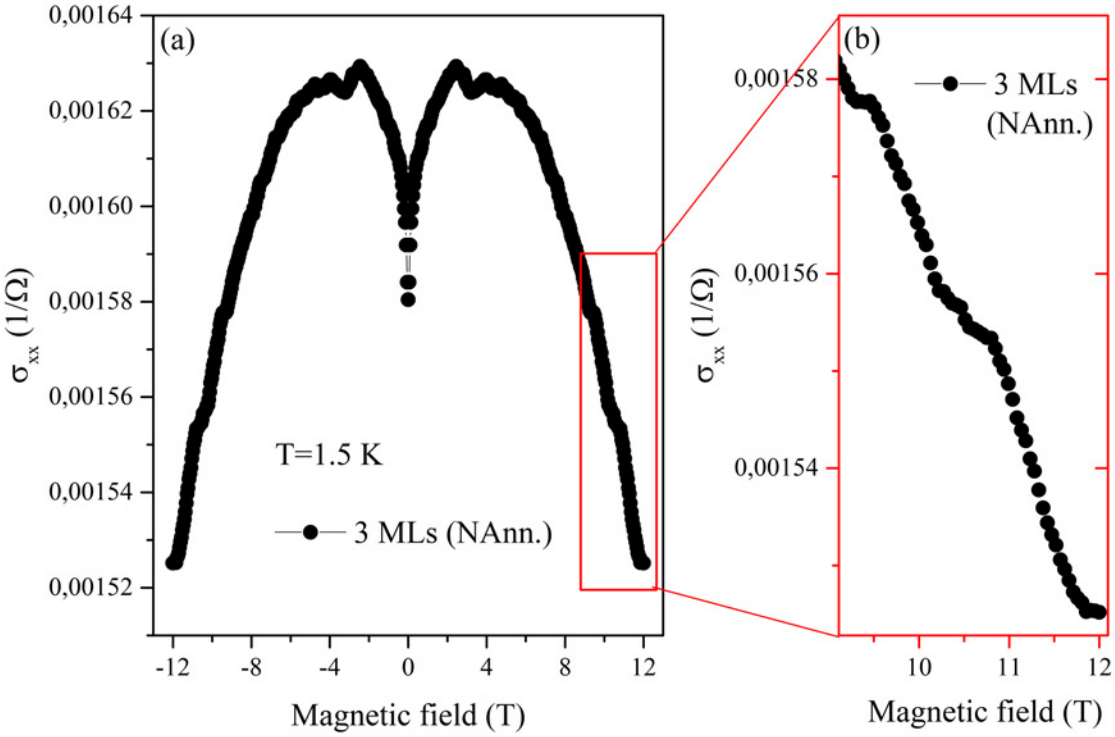

Figure C.4: Electrical studies of $MoTe_2$ layers. The longitudinal conductivity of the as-grown 3 MLs on InAs (111) substrate at T=1.5 K. Visible oscillations are attributed to the InAs layer.

Unfortunately, all the obtained results were inconsistent and not conclusive in terms of $MoTe_2$ phase identification. After the analysis of the magnetotransport data we came to the conclusions that all the interesting features (e.g. WAL or Shubnikov de Haas oscillations) are due to InAs only. An example of the longitudinal component of the conductivity tensor, attributed to InAs is presented in Figure C.4 in Appendix C. In order to verify the structural properties of $MoTe_2$ grown on InAs (111), additional XRD and TEM studies were performed.

Figure C.5 presents the intensity of the $2\Theta/\omega$ scans for the four samples studied.

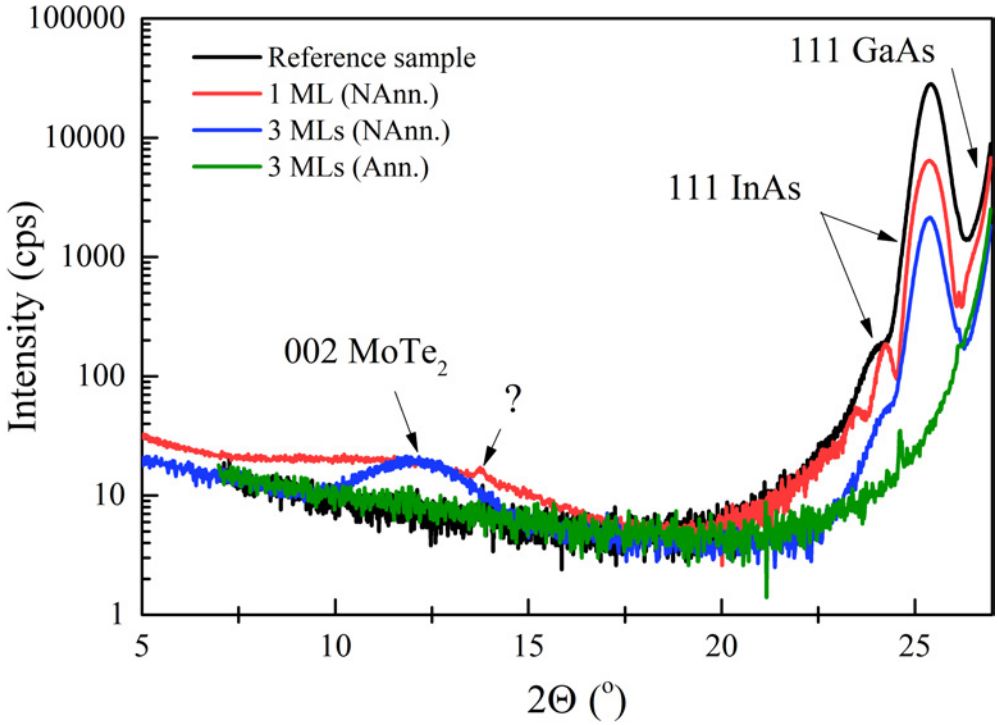

Figure C.5: Structural characterization of $MoTe_2$ layers. The $2\theta/\omega$ scans for four samples studied. [The XRD measurements were performed by J. Domagala, Institute of Physics, PAS. The data analysis and Figure preparation: Z. Ogorzałek-Sory.]

The spectrum for the reference sample, shown by the black curve, reveals both 111 InAs and 111 GaAs reflections, as expected. The spectra for not annealed (NAnn.) 1 ML and 3 MLs, shown by the red and blue curves, respectively, reveal 002, related to the $MoTe_2$. The 002 reflection for the thicker sample is narrower. The peak, observed for $2\Theta = 13.8^o$ is of unknown origin. Since the 002 peak is observed for the 1 ML, it means that occasionally there are more than one ML in the sample. Unfortunately, due to a large width of the peak, it is not possible to distinguish the $MoTe_2$ phase. To do so, the ratio of the higher reflections are required and those are covered by the 111 InAs peak. Surprisingly only 111 GaAs reflection was registered for the in-situ annealed, after the growth, 3 MLs, suggesting that annealing process might have led to the vaporization of both InAs and $MoTe_2$ layers. To understand better the obtained XRD results, all samples were prepared for TEM studies. Figures C.6(a)-(d) show the TEM cross-section images of the InAs (111) reference sample and $MoTe_2$ layers grown on InAs (111).

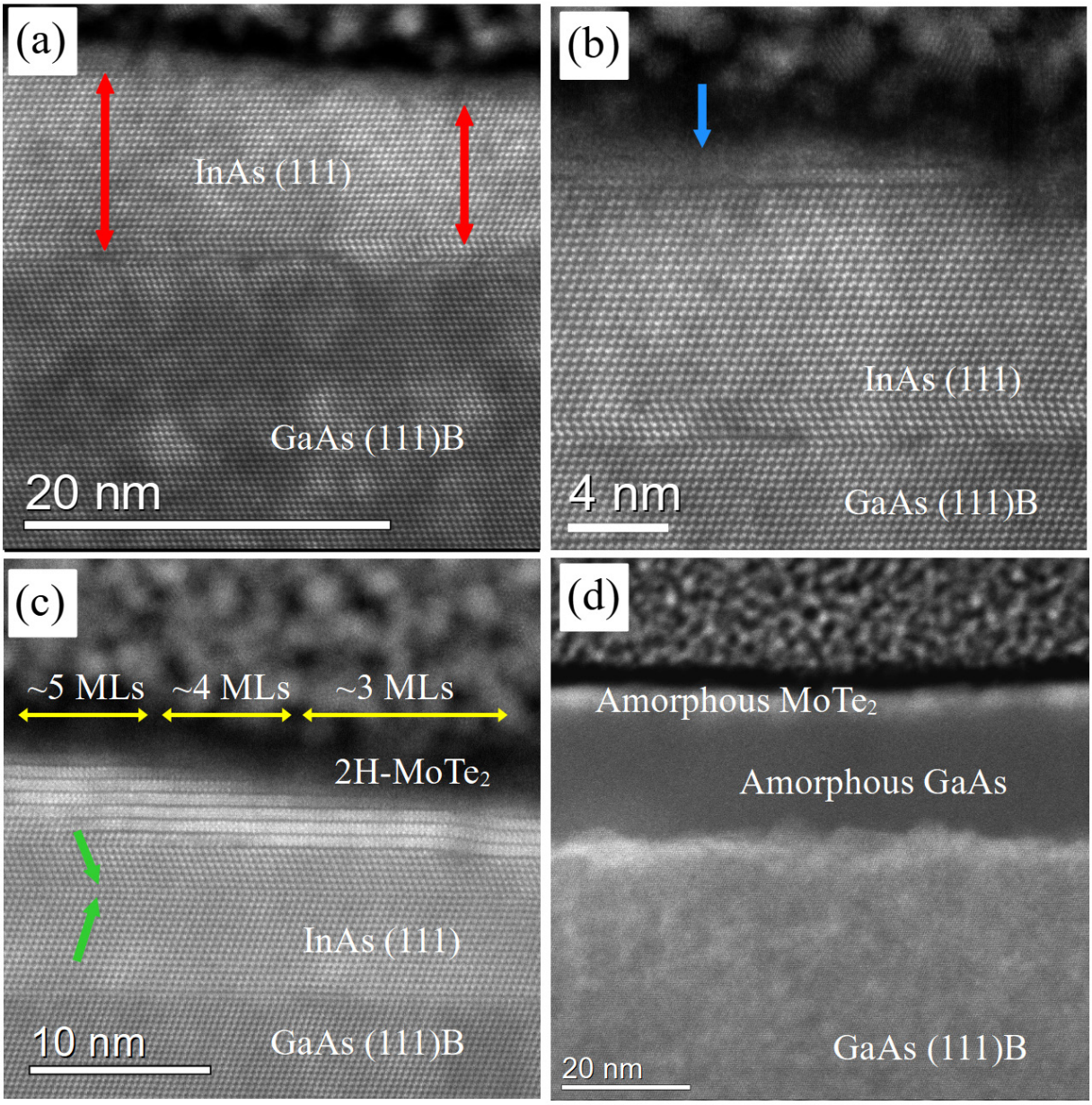

Figure C.6: Structural characterization of $MoTe_2$ layers. TEM cross-section images of the $MoTe_2$ layers grown on InAs (111). (a) The reference sample of InAs (111) of the nominal 18 nm thickness. The red lines show the differences in the InAs (111) thickness. (b) The as-grown 1 ML (NAnn.). The blue arrow marks the inhomogeneity of the layer and the lack of the AlO_x capping layer. (c) The As-grown 3 MLs (NAnn.). The yellow double arrows show the $MoTe_2$ thickness inhomogeneity. The green arrows indicates the InAs (111) crystal's inhomogeneity and difference in the crystal orientations. (d) 3 MLs in-situ annealed (Ann.) revealing the amorphization of the SI GaAs (111)B wafer, InAs (111) substrate and $MoTe_2$ layers. [TEM images were taken by Dr. S. Kret, Dr. A. Kaleta and MSc W. Zajkowska-Pietrzak, Institute of Physics, PAS. The data analysis and Figure preparation: Z. Ogorzałek-Sory.]

The careful TEM analysis revealed that the InAs (111) substrate does not promote the growth of the $1T' - \boldsymbol{MoTe_2}$ and all $MoTe_2$ layers are in the semiconducting 2H-phase. Moreover, several factors contributed to the extremely difficult analysis of the magnetotransport studies. To begin with, the thickness of the InAs (111) layer changes, which is presented

by red double arrows in Figure C.6(a). Statistically, the thickness of the InAs (111) layer changes by even 50% which impedes the determination of the resistivity of the InAs (111) layer. Then, $MoTe_2$ does not form continuous layers as marked by the blue arrow in Figure C.6(b). Moreover, Al film was too thin and not continuous thus did not prevent samples from air degradation. Similarly, due to the poor thickness control the thickness of the 3 MLs is within the range from 3 MLs to even 5 MLs, as marked by the yellow double arrows in Figure C.6(c). Moreover, the InAs (111) layer also changes its crystal orientation as presented by the green arrows in Figure C.6(c). In this case, each crystal orientation may have different electric properties. Surprisingly, the annealing process does not only destroy $MoTe_2$ but also InAs (111), leading to the evaporation of In atoms, leaving only the amorphous $MoTe_2$ and GaAs layers (see Figure C.6(d)). In fact, it is not surprising as the growth temperatures of both materials were much lower than annealing temperature. To conclude, the InAs (111) substrate did not promote in our case the growth of $1T' - MoTe_2$.

After careful magnetotransport, XRD and TEM analysis, showing that the obtained $MoTe_2$ phase is semiconducting, the InAs (111) layer is inhomogeneous and the capping AlO_x layer is not continuous, the project has been finally closed. In future, several growth steps have to be corrected which eventually may potentially help to obtain metallic $MoTe_2$ phase. It is also worth to acknowledge, that $MoTe_2$ samples of different thicknesses, grown on SI GaAs (111)B substrate and whose results have been presented in subsection 6.2.3.2, were grown in the same growing process as samples grown on InAs. As a consequence the same procedure of the Al capping was applied. We assume that the same insufficient amount of Al was deposited onto the studied layers, which caused their inevitable and irreversible degradation in time and thus observed resistivity inhomogeneity.

Appendix D

TaAs

Additional results of Raman, XPS, XRD and STM studies together with computational details of 20 Weyl points identification including their momentum coordinates in units of reciprocal lattice vectors, energy offsets with respect to the Fermi level, chirality and surface states with Fermi arcs can be found in manuscript [268].

Appendix E

Additional compounds

The author during the PhD thesis tested also thin films of crystal tellurium, $MoTe_2$ capped with Co, MnTe layers grown on CdTe and MnAs layers. Due to the preliminary and unpromising results, the data have not been presented in this dissertation.

Bibliography

[1] C. Shekhar, A. K. Nayak, Y. Sun, M. Schmidt, M. Nicklas, I. Leermakers, U. Zeitler, Y. Skourski, J. Wosnitza, Z. Liu, Y. Chen, W. Schnelle, H. Borrmann, Y. Grin, C. Felser, and B. Yan, "Extremely large magnetoresistance and ultrahigh mobility in the topological Weyl semimetal candidate NbP," Nature Physics, vol. 11, pp. 645–649, Aug 2015. [Online]. Available: https://doi.org/10.1038/nphys3372

[2] Y. Li, Z. Wang, P. Li, X. Yang, Z. Shen, F. Sheng, X. Li, Y. Lu, Y. Zheng, and Z.-A. Xu, "Negative magnetoresistance in Weyl semimetals NbAs and NbP: Intrinsic chiral anomaly and extrinsic effects," Frontiers of Physics, vol. 12, Jun 2017. [Online]. Available: https://doi.org/10.1007/s11467-016-0636-8

[3] M. Wu, G. Zheng, W. Chu, Y. Liu, W. Gao, H. Zhang, Y. Lu, J.and Han, J. Zhou, W. Ning, and M. Tian, "Probing the chiral anomaly by planar Hall effect in Dirac semimetal Cd_3As_2 nanoplates," Phys. Rev. B, vol. 98, p. 161110, Oct 2018. [Online]. Available: https://link.aps.org/doi/10.1103/PhysRevB.98.161110

[4] F. C. Chen, X. Luo, J. Yan, Y. Sun, H. Y. Lv, W. J. Lu, C. Y. Xi, P. Tong, Z. G. Sheng, X. B. Zhu, W. H. Song, and Y. P. Sun, "Planar Hall effect in the type-II Weyl semimetal T_d - $MoTe_2$," Phys. Rev. B, vol. 98, p. 041114, Jul 2018. [Online]. Available: https://link.aps.org/doi/10.1103/PhysRevB.98.041114

[5] H. Wang, H. Wang, H. Liu, H. Lu, W. Yang, S. Jia, X.-J. Liu, X. C. Xie, J. Wei, and J. Wang, "Observation of superconductivity induced by a point contact on 3D Dirac semimetal Cd_3As_2 crystals," Nature Materials, vol. 15, pp. 38–42, Jan 2016. [Online]. Available: https://doi.org/10.1038/nmat4456

[6] Y. Zhou, J. Wu, W. Ning, N. Li, Y. Du, X. Chen, R. Zhang, Z. Chi, X. Wang, X. Zhu, P. Lu, C. Ji, X. Wan, Z. Yang, J. Sun, W. Yang, M. Tian, Y. Zhang, and H. Mao, "Pressure-induced superconductivity in a three-dimensional topological material zrte¡sub¿5¡/sub¿," Proceedings of the National Academy of Sciences, vol. 113, no. 11, pp. 2904–2909, 2016. [Online]. Available: https://www.pnas.org/doi/abs/10.1073/pnas.1601262113

[7] Y. Qi, P. G. Naumov, M. N. Ali, C. R. Rajamathi, W. Schnelle, O. Barkalov, M. Hanfland, S.-C. Wu, C. Shekhar, Y. Sun, V. Sü ß, M. Schmidt, U. Schwarz, E. Pippel, P. Werner, R. Hillebrand, T. Förster, E. Kampert, S. Parkin, R. J. Cava, C. Felser, B. Yan, and S. A. Medvedev, "Superconductivity in Weyl semimetal candidate $MoTe_2$," Nature Communications, vol. 7, p. 11038, Mar 2016. [Online]. Available: https://doi.org/10.1038/ncomms11038

[8] K. S. Novoselov, D. Jiang, F. Schedin, T. J. Booth, V. V. Khotkevich, S. V. Morozov, and A. K. Geim, "Two-dimensional atomic crystals," Proceedings of the National Academy of Sciences, vol. 102, no. 30, pp. 10 451–10 453, 2005. [Online]. Available: https://www.pnas.org/doi/abs/10.1073/pnas.0502848102

[9] S. V. Morozov, K. S. Novoselov, M. I. Katsnelson, F. Schedin, D. C. Elias, J. A. Jaszczak, and A. K. Geim, "Giant intrinsic carrier mobilities in graphene and its bilayer," Phys. Rev. Lett., vol. 100, p. 016602, Jan 2008. [Online]. Available: https://link.aps.org/doi/10.1103/PhysRevLett.100.016602

[10] A. A. Balandin, "Thermal properties of graphene and nanostructured carbon materials," Nature materials, vol. 10, Jul 2011. [Online]. Available: https://pubmed.ncbi.nlm.nih.gov/21778997/

[11] A. H. Castro Neto, F. Guinea, N. M. R. Peres, K. S. Novoselov, and A. K. Geim, "The electronic properties of graphene," Rev. Mod. Phys., vol. 81, pp. 109–162, Jan 2009. [Online]. Available: https://link.aps.org/doi/10.1103/RevModPhys.81.109

[12] A. K. Geim and K. S. Novoselov, "The rise of graphene," Nature Materials, vol. 6, no. 3, pp. 183–91, Mar 2007, prawa autorskie - Copyright Nature Publishing Group Mar 2007. [Online]. Available: https://www.proquest.com/scholarly-journals/rise-graphene/docview/222758504/se-2

[13] K. I. Bolotin, K. J. Sikes, J. Hone, H. L. Stormer, and P. Kim, "Temperature-dependent transport in suspended graphene," Phys. Rev. Lett., vol. 101, p. 096802, Aug 2008. [Online]. Available: https://link.aps.org/doi/10.1103/PhysRevLett.101.096802

[14] C. Lee, X. Wei, J. W. Kysar, and J. Hone, "Measurement of the elastic properties and intrinsic strength of monolayer graphene," Science, vol. 321, no. 5887, pp. 385–388, 2008. [Online]. Available: https://www.science.org/doi/abs/10.1126/science.1157996

[15] W. J. Hyun, O. O. Park, and B. D. Chin, "Foldable graphene electronic circuits based on paper substrates," Advanced Materials, vol. 25, no. 34, pp. 4729–4734, 2013. [Online]. Available: https://onlinelibrary.wiley.com/doi/abs/10.1002/adma.201302063

[16] X. Zhao, C. M. Hayner, M. C. Kung, and H. H. Kung, "In-plane vacancy-enabled high-power si–graphene composite electrode for lithium-ion batteries," Advanced Energy Materials, vol. 1, no. 6, pp. 1079–1084, 2011. [Online]. Available: https://onlinelibrary.wiley.com/doi/abs/10.1002/aenm.201100426

[17] Y. Li, G. Kuang, Z. Jiao, L. Yao, and R. Duan, "Recent progress on the mechanical exfoliation of 2D transition metal dichalcogenides," Materials Research Express, vol. 9, Dec 2022. [Online]. Available: https://iopscience.iop.org/article/10.1088/2053-1591/aca6c6

[18] L. A. Ponomarenko, A. K. Geim, A. A. Zhukov, R. Jalil, R. Jalil, S. V. Morozov, K. S. Novoselov, I. V. Grigorieva, E. H. Hill, V. V. Cheianov, V. I. Fal'ko, K. Watanabe, T. Taniguchi, and R. V. Gorbachev, "Tunable metalal-insulator transition in double-layer graphene heterostructures," Nature Physics, vol. 7, pp. 958–961, Dec 2011. [Online]. Available: https://doi.org/10.1038/nphys2114

[19] A. K. Geim and I. V. Grigorieva, "Van der Waals heterostructures," Nature, vol. 499, pp. 419–425, Jul 2013. [Online]. Available: https://doi.org/10.1038/nature12385

[20] M. Naguib, V. N. Mochalin, M. W. Barsoum, and Y. Gogotsi, "25th anniversary article: Mxenes: A new family of two-dimensional materials," Advanced Materials, vol. 26, no. 7, pp. 992–1005, 2014. [Online]. Available: https://onlinelibrary.wiley.com/doi/abs/10.1002/adma.201304138

[21] A. P. Côté, A. I. Benin, N. W. Ockwig, M. O'Keeffe, A. J. Matzger, and O. M. Yaghi, "Porous, crystalline, covalent organic frameworks," Science, vol. 310, no. 5751, pp. 1166–1170, 2005. [Online]. Available: https://www.science.org/doi/abs/10.1126/science.1120411

[22] S. Manzeli, D. Ovchinnikov, D. Pasquier, O. V. Yazyev, and A. Kis, "2D transition metal dichalcogenides," Nature Reviews Materials, vol. 2, p. 17033, Jun 2017. [Online]. Available: https://doi.org/10.1038/natrevmats.2017.33

[23] Q. Zhang, L. Mei, X. Cao, Y. Tang, and Z. Zeng, "Intercalation and exfoliation chemistries of transition metal dichalcogenides," J. Mater. Chem. A, vol. 8, pp. 15 417–15 444, 2020. [Online]. Available: http://dx.doi.org/10.1039/D0TA03727C

[24] Z. Hu, Z.-B. Liu, and J.-G. Tian, "Stacking of exfoliated two-dimensional materials: A review," Chinese Journal of Chemistry, vol. 38, no. 9, pp. 981–995, 2020. [Online]. Available: https://onlinelibrary.wiley.com/doi/abs/10.1002/cjoc.202000092

[25] M. Heyl, D. Burmeister, T. Schultz, S. Pallasch, G. Ligorio, N. Koch, and E. J. W. List-Kratochvil, "Thermally activated gold-mediated transition metal dichalcogenide exfoliation and a unique gold-mediated transfer," physica status solidi (RRL) – Rapid Research Letters, vol. 14, no. 11, p. 2000408, 2020. [Online]. Available: https://onlinelibrary.wiley.com/doi/abs/10.1002/pssr.202000408

[26] S. Sahu, G. Haider, A. Rodriguez, J. Plšek, M. Mergl, M. Kalbáč, O. Frank, and M. Velický, "Large-area mechanically-exfoliated two-dimensional materials on arbitrary substrates," Advanced Materials Technologies, vol. 8, no. 12, p. 2201993, 2023. [Online]. Available: https://onlinelibrary.wiley.com/doi/abs/10.1002/admt.202201993

[27] Y. Yoo, Z. P. DeGregorio, Y. Su, S. J. Koester, and J. E. Johns, "In-plane 2H-1T $MoTe_2$ homojunctions synthesized by flux-controlled phase engineering," Advanced Materials, vol. 29, no. 16, p. 1605461, 2017. [Online]. Available: https://onlinelibrary.wiley.com/doi/abs/10.1002/adma.201605461

[28] D. D. Liang, Y. J. Wang, W. L. Zhen, J. Yang, S. R. Weng, X. Yan, Y. Y. Han, W. Tong, W. K. Zhu, L. Pi, and C. J. Zhang, "Origin of planar Hall effect in type-II Weyl semimetal $MoTe_2$," AIP Advances, vol. 9, no. 5, p. 055015, May 2019. [Online]. Available: https://doi.org/10.1063/1.5094231

[29] S. Dissanayake, C. Duan, J. Yang, M. Matsuda, C. Yue, J. A. Schneeloch, J. C. Y. Teo, and D. Louca, "Electronic band tuning under pressure in $MoTe_2$ topological semimetal," npj Quantum Materials, vol. 4, p. 45, Aug 2019. [Online]. Available: https://doi.org/10.1038/s41535-019-0187-7

[30] J. A. Hlevyack, L.-Y. Feng, M.-K. Lin, R. A. B. Villaos, R.-Y. Liu, P. Chen, Y. Li, S.-K. Mo, F.-C. Chuang, and T.-C. Chiang, "Dimensional crossover and band topology evolution in ultrathin semimetallic $NiTe_2$ films," npj 2D Materials and Applications, vol. 5, p. 40, Apr 2021. [Online]. Available: https://doi.org/10.1038/s41699-021-00218-z

[31] Y. Je, E. Kim, N. V. Binh, H. Kim, S. Cho, D. Lee, M. J. Kwon, M. Choi, J. H. Lee, W. H. Nam, Y. Lee, J. Y. Cho, and J. H. Park, "Analysis of physical and electrical properties of $NiTe_2$ single crystal grown via molten salt flux method," Electronic Materials Letters, vol. 19, pp. 452–461, Sep 2023. [Online]. Available: https://doi.org/10.1007/s13391-023-00419-2

[32] T. J. S. Anand, M. Zaidan, M. A. Azam, and Z. Buang, "Structural studies of $NiTe_2$ thin films with the influence of amino additives," International Journal of

Mechanical and Materials Engineering, vol. 9, p. 18, Sep 2014. [Online]. Available: https://doi.org/10.1186/s40712-014-0018-3

[33] K. TaeWan, J. DaeHwa, and P. Jonghoo, "Electrical metal contacts to atomically thin 2h-phase $MoTe_2$ grown by metal–organic chemical vapor deposition," Current Applied Physics, vol. 18, no. 7, pp. 843–846, 2018. [Online]. Available: https://www.sciencedirect.com/science/article/pii/S1567173918300877

[34] A. Rani, K. DiCamillo, M. A. H. Khan, M. Paranjape, and M. E. Zaghloul, "Tuning the polarity of $MoTe_2$ FETs by varying the channel thickness for gas-sensing applications," Sensors, vol. 19, no. 11, 2019. [Online]. Available: https://www.mdpi.com/1424-8220/19/11/2551

[35] Q. R. Zhang, B. Zeng, Y. C. Chiu, R. Schönemann, S. Memaran, W. Zheng, D. Rhodes, K.-W. Chen, T. Besara, R. Sankar, F. Chou, G. T. McCandless, J. Y. Chan, N. Alidoust, S.-Y. Xu, I. Belopolski, M. Z. Hasan, F. F. Balakirev, and L. Balicas, "Possible manifestations of the chiral anomaly and evidence for a magnetic field induced topological phase transition in the type-I Weyl semimetal TaAs," Phys. Rev. B, vol. 100, p. 115138, Sep 2019. [Online]. Available: https://link.aps.org/doi/10.1103/PhysRevB.100.115138

[36] T. A. Empante, Y. Zhou, V. Klee, A. E. Nguyen, I.-H. Lu, M. D. Valentin, S. A. Naghibi Alvillar, E. Preciado, A. J. Berges, C. S. Merida, M. Gomez, S. Bobek, M. Isarraraz, E. J. Reed, and L. Bartels, "Chemical vapor deposition growth of few-layer $MoTe_2$ in the 2H, 1T, and 1T phases: Tunable properties of $MoTe_2$ films," ACS Nano, vol. 11, no. 1, pp. 900–905, 2017, pMID: 27992719. [Online]. Available: https://doi.org/10.1021/acsnano.6b07499

[37] B. Zhao, W. Dang, Y. Liu, B. Li, J. Li, J. Luo, Z. Zhang, R. Wu, H. Ma, G. Sun, Y. Huang, X. Duan, and X. Duan, "Synthetic control of two-dimensional $NiTe_2$ single crystals with highly uniform thickness distributions," Journal of the American Chemical Society, vol. 140, no. 43, pp. 14 217–14 223, 2018. [Online]. Available: https://doi.org/10.1021/jacs.8b08124

[38] J. Wang, T. Li, Q. Wang, W. Wang, R. Shi, N. Wang, A. Amini, and C. Cheng, "Controlled growth of atomically thin transition metal dichalcogenides via chemical vapor deposition method," Materials Today Advances, vol. 8, p. 100098, 2020. [Online]. Available: https://www.sciencedirect.com/science/article/pii/S259004982030045X

[39] D. J. Hynek, R. M. Singhania, S. Xu, B. Davis, L. Wang, M. Yarali, J. V. Pondick, J. M. Woods, N. C. Strandwitz, and J. J. Cha, "cm2-scale synthesis of $MoTe_2$ thin

films with large grains and layer control," ACS Nano, vol. 15, no. 1, pp. 410–418, 2021, pMID: 33211473. [Online]. Available: https://doi.org/10.1021/acsnano.0c08069

[40] Z. Ogorzałek, B. Seredyński, S. Kret, A. Kwiatkowski, K. P. Korona, M. Grzeszczyk, J. Mierzejewski, D. Wasik, W. Pacuski, J. Sadowski, and M. Gryglas-Borysiewicz, "Charge transport in MBE-grown 2H-$MoTe_2$ bilayers with enhanced stability provided by an AlO_x capping layer," Nanoscale, vol. 12, pp. 16 535–16 542, 2020. [Online]. Available: http://dx.doi.org/10.1039/D0NR03148H

[41] W. Pacuski, M. Grzeszczyk, K. Nogajewski, A. Bogucki, K. Oreszczuk, J. Kucharek, K. E. Połczyńska, B. Seredyński, A. Rodek, R. Bożek, T. Taniguchi, K. Watanabe, S. Kret, J. Sadowski, T. Kazimierczuk, M. Potemski, and P. Kossacki, "Narrow excitonic lines and large-scale homogeneity of transition-metal dichalcogenide monolayers grown by molecular beam epitaxy on hexagonal boron nitride," Nano Letters, vol. 20, no. 5, pp. 3058–3066, 2020, pMID: 32105481. [Online]. Available: https://doi.org/10.1021/acs.nanolett.9b04998

[42] B. Seredyński, Z. Ogorzałek, W. Zajkowska, R. Bożek, M. Tokarczyk, J. Suffczyński, S. Kret, J. Sadowski, M. Gryglas-Borysiewicz, and W. Pacuski, "Molecular beam epitaxy of a 2D material nearly lattice matched to a 3D substrate: $NiTe_2$ on GaAs," Crystal Growth & Design, vol. 21, no. 10, pp. 5773–5779, 2021. [Online]. Available: https://doi.org/10.1021/acs.cgd.1c00673

[43] C.-H. Yeh, Z.-Y. Liang, Y.-C. Lin, H.-C. Chen, T. Fan, C.-H. Ma, Y.-H. Chu, K. Suenaga, and P.-W. Chiu, "Graphene–transition metal dichalcogenide heterojunctions for scalable and low-power complementary integrated circuits," ACS Nano, vol. 14, no. 1, pp. 985–992, 2020, pMID: 31904930. [Online]. Available: https://doi.org/10.1021/acsnano.9b08288

[44] Y. Liu, Y. Gao, S. Zhang, J. He, J. Yu, and Z. Liu, "Valleytronics in transition metal dichalcogenides materials," Nano Research, vol. 12, pp. 2695–2711, Nov 2019. [Online]. Available: https://doi.org/10.1007/s12274-019-2497-2

[45] B. A. Volkov and O. A. Pankratov, "Two-dimensional massless electrons in an inverted contact," JETP Letters, vol. 42, p. 145, Jun 1985. [Online]. Available: http://jetpletters.ru/ps/1420/article˙21570.shtml

[46] B. A. Bernevig, T. L. Hughes, and S.-C. Zhang, "Quantum spin Hall effect and topological phase transition in HgTe quantum wells," Science, vol. 314, no. 5806, pp. 1757–1761, 2006. [Online]. Available: https://www.science.org/doi/abs/10.1126/science.1133734

[47] T. Shirokura, K. Yao, Y. Ueda, and P. N. Hai, "Origin of the giant spin Hall effect in BiSb topological insulator," arXiv:1810.10840, Oct 2018. [Online]. Available: https://doi.org/10.48550/arXiv.1810.10840

[48] Y. Wang, P. Deorani, K. Banerjee, N. Koirala, M. Brahlek, S. Oh, and H. Yang, "Topological surface states originated spin-orbit torques in Bi_2Se_3," Phys. Rev. Lett., vol. 114, p. 257202, Jun 2015. [Online]. Available: https://link.aps.org/doi/10.1103/PhysRevLett.114.257202

[49] M. Z. Hasan and C. L. Kane, "Colloquium: Topological insulators," Rev. Mod. Phys., vol. 82, pp. 3045–3067, Nov 2010. [Online]. Available: https://link.aps.org/doi/10.1103/RevModPhys.82.3045

[50] H. Wang and J. Wang, "Electron transport in Dirac and Weyl semimetals," Chinese Physics B, vol. 27, no. 10, p. 107402, oct 2018. [Online]. Available: https://dx.doi.org/10.1088/1674-1056/27/10/107402

[51] ——, "Electron transport in Dirac and Weyl semimetals," Chinese Physics B, vol. 27, no. 10, p. 107402, 2018.

[52] C. Fang, H. Weng, X. Dai, and Z. Fang, "Topological nodal line semimetals*," Chinese Physics B, vol. 25, no. 11, p. 117106, nov 2016. [Online]. Available: https://dx.doi.org/10.1088/1674-1056/25/11/117106

[53] H. Wang and J. Wang, "Electron transport in Dirac and Weyl semimetals," Chinese Physics B, vol. 27, no. 10, p. 107402, oct 2018. [Online]. Available: https://dx.doi.org/10.1088/1674-1056/27/10/107402

[54] B. Xie, H. Liu, H. Cheng, Z. Liu, J. Tian, and S. Chen, "Dirac points and the transition towards Weyl points in three-dimensional sonic crystals," Light: Science & Applications, vol. 9, no. 1, p. 201, 2020. [Online]. Available: https://doi.org/10.1038/s41377-020-00416-2

[55] M. V. Berry, "Quantal phase factors accompanying adiabatic changes," Proceedings of the Royal Society of London. A. Mathematical and Physical Sciences, vol. 392, no. 1802, pp. 45–57, 1984. [Online]. Available: https://royalsocietypublishing.org/doi/abs/10.1098/rspa.1984.0023

[56] D. Xiao, M.-C. Chang, and Q. Niu, "Berry phase effects on electronic properties," Rev. Mod. Phys., vol. 82, pp. 1959–2007, Jul 2010. [Online]. Available: https://link.aps.org/doi/10.1103/RevModPhys.82.1959

[57] B. Yan and C. Felser, "Topological materials: Weyl semimetals," Annual Review of Condensed Matter Physics, vol. 8, no. 1, pp. 337–354, 2017. [Online]. Available: https://doi.org/10.1146/annurev-conmatphys-031016-025458

[58] H. Li, H. He, H.-Z. Lu, H. Zhang, H. Liu, R. Ma, Z. Fan, S.-Q. Shen, and J. Wang, "Negative magnetoresistance in dirac semimetal cd_3as_2," Nature Communications, vol. 7, no. 1, p. 10301, 2016. [Online]. Available: https://doi.org/10.1038/ncomms10301

[59] S.-M. Huang, S.-Y. Xu, I. Belopolski, C.-C. Lee, G. Chang, B. Wang, N. Alidoust, G. Bian, M. Neupane, C. Zhang, S. Jia, A. Bansil, H. Lin, and M.-Z. Hasan, "A Weyl Fermion semimetal with surface Fermi arcs in the transition metal monopnictide TaAs class," Nat. Commun., vol. 6, Jun 2015. [Online]. Available: https://www.nature.com/articles/ncomms8373

[60] A. A. Soluyanov, D. Gresch, Z. Wang, Q.-S. Wu, M. Troyer, X. Dai, and B. A. Bernevig, "Type-II Weyl semimetals," Nature, vol. 527, no. 7579, p. 495–498, Nov. 2015. [Online]. Available: http://dx.doi.org/10.1038/nature15768

[61] Y. Noda, S. Ono, and K. Ohno, "Metallic three-coordinated carbon networks with eight-membered rings showing high density of states at the fermi level," Phys. Chem. Chem. Phys., vol. 16, pp. 7102–7107, 2014. [Online]. Available: http://dx.doi.org/10.1039/C4CP00159A

[62] M. Yan, H. Huang, K. Zhang, E. Wang, W. Yao, K. Deng, G. Wan, H. Zhang, M. Arita, H. Yang, Z. Sun, H. Yao, Y. Wu, S. Fan, W. Duan, and S. Zhou, "Lorentz-violating type-II Dirac fermions in transition metal dichalcogenide $ptte_2$," Nature Communications, vol. 8, Aug 2017. [Online]. Available: https://doi.org/10.1038/s41467-017-00280-6

[63] P. P. Ferreira, A. L. R. Manesco, T. T. Dorini, L. E. Correa, G. Weber, A. J. S. Machado, and L. T. F. Eleno, "Strain engineering the topological type-II Dirac semimetal $NiTe_2$," Phys. Rev. B, vol. 103, p. 125134, Mar 2021. [Online]. Available: https://link.aps.org/doi/10.1103/PhysRevB.103.125134

[64] H. Chi, C. Zhang, G. Gu, D. E. Kharzeev, X. Dai, and Q. Li, "Lifshitz transition mediated electronic transport anomaly in bulk zrte5," New Journal of Physics, vol. 19, no. 1, p. 015005, Jan 2017. [Online]. Available: https://dx.doi.org/10.1088/1367-2630/aa55a3

[65] I. M. Lifshitz, "Anomalies of electron characteristics of a metal in the high pressure region," Sov. Phys. JEPT, vol. 11, p. 1569, Nov 1960. [Online]. Available: http://www.jetp.ras.ru/cgi-bin/dn/e˙011˙05˙1130.pdf

[66] J. Xiong, S. K. Kushwaha, T. Liang, J. W. Krizan, M. Hirschberger, W. Wang, R. J. Cava, and N. P. Ong, "Evidence for the chiral anomaly in the Dirac semimetal Na_3Bi," Science, vol. 350, no. 6259, pp. 413–416, 2015. [Online]. Available: https://www.science.org/doi/abs/10.1126/science.aac6089

[67] T. Liang, Q. Gibson, M. N. Ali, M. Liu, R. J. Cava, and N. P. Ong, "Ultrahigh mobility and giant magnetoresistance in the dirac semimetal cd_3as_2," Nature Materials, vol. 14, pp. 280–284, Mar 2015. [Online]. Available: https://doi.org/10.1038/nmat4143

[68] C.-L. Zhang, S.-Y. Xu, I. Belopolski, Z. Yuan, Z. Lin, B. Tong, G. Bian, N. Alidoust, C.-C. Lee, S.-M. Huang, T.-R. Chang, G. Chang, C.-H. Hsu, H.-T. Jeng, M. Neupane, D. S. Sanchez, H. Zheng, J. Wang, H. Lin, C. Zhang, H.-Z. Lu, S.-Q. Shen, T. Neupert, M. Zahid Hasan, and S. Jia, "Signatures of the Adler–Bell–Jackiw chiral anomaly in a Wey fermion semimetal," Nature Communications, vol. 7, pp. 2041–1723, 2016. [Online]. Available: https://doi.org/10.1038/ncomms10735

[69] C. V. Raman, "A new radiation," Current Science, vol. 74, no. 4, pp. 382–386, 1998. [Online]. Available: http://www.jstor.org/stable/24101519

[70] W. H. Bragg and W. L. Bragg, X-rays and crystal structure. G. Bell and Sons, Ltd. London, 1915. [Online]. Available: http://books.google.com/books?id=K5Y3AAAAMAAJ

[71] G. Binnig, C. F. Quate, and C. Gerber, "Atomic force microscope," Phys. Rev. Lett., vol. 56, pp. 930–933, Mar 1986. [Online]. Available: https://link.aps.org/doi/10.1103/PhysRevLett.56.930

[72] H. Ardebili, J. Zhang, M. Pecht, and J. Licari, Encapsulation Technologies for Electronic Applications, ser. Materials and Processes for Electronic Applications. Elsevier Science, 2018. [Online]. Available: https://books.google.pl/books?id=qEFyDwAAQBAJ

[73] Nanotech. Laboratoria nanotechnologii i struktur półprzewodnikowych (lansp). [Online]. Available: https://nanotech.fuw.edu.pl/?page˙id=229

[74] K. Birdi, Scanning Probe Microscopes: Applications in Science and Technology. CRC Press, 2003. [Online]. Available: https://books.google.pl/books?id=YdKSc˙5yOtAC

[75] T. P. S. U. O. R. P. Jeanne Kagle. Bsc 3271: Microbiology for the health sciences. [Online]. Available: https://bio.libretexts.org/Courses/Mansfield˙University˙of˙Pennsylvania/BSC˙3271%3A˙Microbiology˙for˙Health˙Sciences˙Sp21˙(Kagle)/01%3A˙Introduction/1.03%3A˙How˙We˙See˙the˙Invisible˙World/1.3.03%3A˙Instruments˙of˙Microscopy

[76] B. L. L. C. Melissa Bollmeyer. Transmission electron microscopy (tem): Tem versus stem and haadf. [Online]. Available: https://chem.libretexts.org/Courses/Franklin˙and˙Marshall˙College/Introduction˙to˙Materials˙Characterization˙˙CHM˙412˙Collaborative˙Text/Electron˙and˙Probe˙Microscopy/Transmission˙electron˙microscopy˙(TEM)%3A˙TEM˙versus˙STEM˙and˙HAADF

[77] N. S. R. C. S. J. University, "The ultra resolved angular photoelectron spectroscopy beamline (uranos)." [Online]. Available: https://synchrotron.uj.edu.pl/en˙GB/linie-badawcze/uranos

[78] S. Hüfner, Photoelectron Spectroscopy: Principles and Applications, 3rd ed., ser. Advanced Texts in Physics. Springer Berlin, Heidelberg, 2003, originally published as volume 82 in the series: Springer Series in Solid-State Sciences.

[79] E. H. Hall, "On a new action of the magnet on electric currents," American Journal of Mathematics, vol. 2, no. 3, pp. 287–292, 1879. [Online]. Available: http://www.jstor.org/stable/2369245

[80] P. YU and M. Cardona, Fundamentals of Semiconductors: Physics and Materials Properties, ser. Graduate Texts in Physics. Springer Berlin Heidelberg, 2010. [Online]. Available: https://books.google.pl/books?id=5aBuKYBT˙hsC

[81] R. G. Chambers, Electrons in Metals and Semiconductors R.G. Chambers. Chapman and Hall, 1990. [Online]. Available: https://books.google.pl/books?id=TwMPyAEACAAJ

[82] S. Harrison, PhD thesis: Exploring and Exploiting Charge-Carrier Confinement in Semiconductor Nanostructures: Heterodimensionality in Sub-Monolayer InAs in GaAs and Photoelectrolysis Using type-II Heterojunctions. Lancaster University, Nov 2016.

[83] J. P. Toennies, Helium Nanodroplets: Formation, Physical Properties and Superfluidity. Cham: Springer International Publishing, 2022, pp. 1–40. [Online]. Available: https://doi.org/10.1007/978-3-030-94896-2˙1

[84] S. M. Sze, Semiconductor devices: physics and technology, 2nd ed. New York: Wiley, 2002.

[85] S. Kasap and P. Capper, Eds., Springer Handbook of Electronic and Photonic Materials. Boston, MA: Springer, 2007.

[86] S. Kasap, C. Koughia, and P. Capper, Springer Handbook of Electronic and Photonic Materials, ser. Springer Handbook of Electronic and Photonic Materials. Springer US, 2007. [Online]. Available: https://books.google.pl/books?id=rVVW22pnzhoC

[87] N. F. Mott, "Conduction in non-crystalline materials," The Philosophical Magazine: A Journal of Theoretical Experimental and Applied Physics, vol. 19, no. 160, pp. 835–852, 1969. [Online]. Available: https://doi.org/10.1080/14786436908216338

[88] N. F. Mott and E. A. Davis, Electronic Processes in Non-Crystalline Materials, 2nd ed. Oxford: Clarendon Press, 1979.

[89] A. L. Efros and B. I. Shklovskii, Electronic Properties of Doped Semiconductors. Berlin, Heidelberg: Springer, 1984.

[90] G. Bergmann, "Weak localization in thin films: a time-of-flight experiment with conduction electrons," Physics Reports, vol. 107, no. 1, pp. 1–58, 1984. [Online]. Available: https://www.sciencedirect.com/science/article/pii/0370157384901030

[91] ——, "Influence of spin-orbit coupling on weak localization," Phys. Rev. Lett., vol. 48, pp. 1046–1049, Apr 1982. [Online]. Available: https://link.aps.org/doi/10.1103/PhysRevLett.48.1046

[92] H.-Z. Lu and S.-Q. Shen, "Weak localization and weak anti-localization in topological insulators," Chinese Physics B, vol. 25, no. 11, p. 117202, 2016.

[93] J. H. Garcia, M. Vila, A. W. Cummings, and S. Roche, "Spin transport in graphene/transition metal dichalcogenide heterostructures," Chem. Soc. Rev., vol. 47, pp. 3359–3379, 2018. [Online]. Available: http://dx.doi.org/10.1039/C7CS00864C

[94] M. Dayah. Periodic table - ptable. ptable. [Online]. Available: https://ptable.com

[95] R. Gracia-Abad, S. Sangiao, C. Bigi, S. Kumar Chaluvadi, P. Orgiani, and J. M. De Teresa, "Omnipresence of weak antilocalization (wal) in bi(2)se(3) thin films: A review on its origin," Nanomaterials, vol. 11, May 2021. [Online]. Available: https://www.ncbi.nlm.nih.gov/pmc/articles/PMC8143463/

[96] M. M. H. Polash, S. Yalameha, H. Zhou, K. Ahadi, Z. Nourbakhsh, and D. Vashaee, "Topological quantum matter to topological phase conversion: Fundamentals, materials, physical systems for phase conversions, and device applications," Materials Science and Engineering: R: Reports, vol. 145, p. 100620, 2021. [Online]. Available: https://www.sciencedirect.com/science/article/pii/S0927796X21000152

[97] H.-J. Kim, K.-S. Kim, J.-F. Wang, M. Sasaki, N. Satoh, A. Ohnishi, M. Kitaura, M. Yang, and L. Li, "Dirac versus Weyl Fermions in topological insulators: Adler-Bell-Jackiw anomaly in transport phenomena," Phys. Rev. Lett., vol. 111, p. 246603, Dec 2013. [Online]. Available: https://link.aps.org/doi/10.1103/PhysRevLett.111.246603

[98] K.-S. Kim, H.-J. Kim, and M. Sasaki, "Boltzmann equation approach to anomalous transport in a Weyl metal," Phys. Rev. B, vol. 89, p. 195137, May 2014. [Online]. Available: https://link.aps.org/doi/10.1103/PhysRevB.89.195137

[99] Q. Li, D. E. Kharzeev, C. Zhang, Y. Huang, I. Pletikosić, A. V. Fedorov, R. D. Zhong, J. A. Schneeloch, G. D. Gu, and T. Valla, "Chiral magnetic effect in zrte5," Nature Physics, pp. 550–554, Jun 2016. [Online]. Available: https://doi.org/10.1038/nphys3648

[100] W. Yanez, Y. Ou, R. Xiao, S. Ghosh, J. Dwivedi, E. Steinebronn, A. Richardella, K. A. Mkhoyan, and N. Samarth, "Giant dampinglike-torque efficiency in naturally oxidized polycrystalline *taas* thin films," Phys. Rev. Appl., vol. 18, p. 054004, Nov 2022. [Online]. Available: https://link.aps.org/doi/10.1103/PhysRevApplied.18.054004

[101] S. Hikami, A. I. Larkin, and Y. Nagaoka, "Spin-Orbit Interaction and Magnetoresistance in the Two Dimensional Random System," Progress of Theoretical Physics, vol. 63, no. 2, pp. 707–710, 02 1980. [Online]. Available: https://doi.org/10.1143/PTP.63.707

[102] G. Tkachov and E. M. Hankiewicz, "Weak antilocalization in hgte quantum wells and topological surface states: Massive versus massless dirac fermions," Phys. Rev. B, vol. 84, p. 035444, Jul 2011. [Online]. Available: https://link.aps.org/doi/10.1103/PhysRevB.84.035444

[103] H.-Z. Lu and S.-Q. Shen, "Quantum transport in topological semimetals under magnetic fields," Frontiers of Physics, vol. 12, p. 127201, Jun 2017. [Online]. Available: https://doi.org/10.1007/s11467-016-0609-y

[104] W. Shi, J. Ye, Y. Zhang, R. Suzuki, M. Yoshida, J. Miyazaki, N. Inoue, Y. Saito, and Y. Iwasa, "Superconductivity series in transition metal dichalcogenides by ionic gating," Scientific Reports, vol. 5, Aug 2015. [Online]. Available: https://doi.org/10.1038/srep12534

[105] Y. Wang, J. C. Kim, R. J. Wu, J. Martinez, X. Song, J. Yang, F. Zhao, A. Mkhoyan, H. Y. Jeong, and M. Chhowalla, "Van der Waals contacts between three-dimensional metals and two-dimensional semiconductors," Nature, vol. 568, pp. 70–74, Apr 2019. [Online]. Available: https://doi.org/10.1038/s41586-019-1052-3

[106] J. Meyer and A. L. Kahn, "Electronic structure of molybdenum-oxide films and associated charge injection mechanisms in organic devices," Journal of Photonics for Energy, vol. 1, no. 1, p. 011109, 2011. [Online]. Available: https://doi.org/10.1117/1.3555081

[107] J. Hölzl and F. K. Schulte, Work function of metals. Berlin, Heidelberg: Springer Berlin Heidelberg, 1979, pp. 1–150. [Online]. Available: https://doi.org/10.1007/BFb0048919

[108] C.-Z. Chang, J. Zhang, X. Feng, J. Shen, Z. Zhang, M. Guo, K. Li, Y. Ou, P. Wei, L.-L. Wang, Z.-Q. Ji, Y. Feng, S. Ji, X. Chen, J. Jia, X. Dai, Z. Fang, S.-C. Zhang, K. He, Y. Wang, L. Lu, X.-C. Ma, and Q.-K. Xue, "Experimental observation of the quantum anomalous Hall effect in a magnetic topological insulator," Science, vol. 340, no. 6129, pp. 167–170, 2013. [Online]. Available: https://www.science.org/doi/10.1126/science.1234414

[109] L. Tingyan, P. Baojun, Z. Kenan, D. Youqing, Z. Chao, G. Zhiyang, and Z. Lijie, "Electron beam lithography induced doping in multilayer $MoTe_2$," Applied Surface Science, vol. 540, p. 148276, 2021. [Online]. Available: https://www.sciencedirect.com/science/article/pii/S0169433220330336

[110] C. Xu, B. Li, W. Jiao, W. Zhou, B. Qian, R. Sankar, N. D. Zhigadlo, Y. Qi, D. Qian, F.-C. Chou, and X. Xu, "Topological type-ii dirac fermions approaching the fermi level in a transition metal dichalcogenide $NiTe_2$," Chemistry of Materials, vol. 30, no. 14, pp. 4823–4830, 2018. [Online]. Available: https://doi.org/10.1021/acs.chemmater.8b02132

[111] J. F. H. L. Monteiro, M. B. Marciniak, A. R. Jurelo, E. C. Siqueira, F. T. Dias, and J. L. Pimentel Júnior, "Synthesis and microstructure of $NiTe_2$," Journal of Crystal Growth, vol. 478, pp. 129–133, 2017. [Online]. Available: https://www.sciencedirect.com/science/article/pii/S0022024817305237

[112] M. T. James, S. Mandal, N. K. Sebastian, P. Mishra, R. Ganesan, and P. S. A. Kumar, "Probing electron-phonon and phonon-phonon coupling in type-II Dirac semi-metal $NiTe_2$ via temperature-dependent raman spectroscopy," Journal of Physics: Condensed Matter, vol. 35, no. 12, p. 125701, jan 2023. [Online]. Available: https://dx.doi.org/10.1088/1361-648X/acb18a

[113] E. Uchida and H. Kondoh, "Magnetic properties of Nickel Telluride," J. Phys. Soc. Jpn., vol. 11, pp. 21–27, 1956. [Online]. Available: https://doi.org/10.1143/JPSJ.11.21

[114] Q. Mao, Y. Zhang, Q. Chen, R. Li, X. Geng, J. Yang, H. Hao, and M. Fang, "Metallicity and paramagnetism of single-crystalline NiTe and $NiTe_2$," physica status solidi (b), vol. 257, no. 1, p. 1900224, 2020. [Online]. Available: https://onlinelibrary.wiley.com/doi/abs/10.1002/pssb.201900224

[115] W. Zheng, R. Schönemann, S. Mozaffari, Y.-C. Chiu, Z. B. Goraum, N. Aryal, E. Manousakis, T. M. Siegrist, K. Wei, and L. Balicas, "Bulk fermi surfaces of the

Dirac type-II semimetallic candidate $NiTe_2$," Phys. Rev. B, vol. 102, p. 125103, Sep 2020. [Online]. Available: https://link.aps.org/doi/10.1103/PhysRevB.102.125103

[116] M. Ettenberg, K. L. Komarek, and E. Miller, "Thermodynamic properties of nickel-tellurium alloys," Journal of Solid State Chemistry, vol. 1, no. 3, pp. 583–592, 1970. [Online]. Available: https://www.sciencedirect.com/science/article/pii/0022459670901453

[117] K. Klepp and K. Komarek, "Transition metal-chalcogene systems, iii: The system ni-te; [Übergangsmetall-chalkogensysteme, 3. mitt.: Das system nickel-tellur]," Monatshefte für Chemie, vol. 103, no. 4, p. 934 – 946, 1972. [Online]. Available: https://www.scopus.com/inward/record.uri?eid=2-s2.0-0000058246&doi=10.1007%2fBF00905166&partnerID=40&md5=4ef2aad8af4fde286d26ce26048c6078

[118] L. Norén, V. Ting, R. L. Withers, and G. Van Tendeloo, "An electron and x-ray diffraction investigation of ni1+xte2 and ni1+xse2cdi2/nias type solid solution phases," Journal of Solid State Chemistry, vol. 161, no. 2, pp. 266–273, 2001. [Online]. Available: https://www.sciencedirect.com/science/article/pii/S0022459601993090

[119] P. J. Orders, J. Liesegang, R. C. G. Leckey, J. G. Jenkin, and J. D. Riley, "Angle-resolved photoemission from the valence bands of $NiTe_2$, $PdTe_2$ and $PtTe_2$," Journal of Physics F: Metal Physics, vol. 12, no. 11, p. 2737, nov 1982. [Online]. Available: https://dx.doi.org/10.1088/0305-4608/12/11/031

[120] G. Y. Guo and W. Y. Liang, "Study of the electronic structures of ni-group metal ditellurides: $NiTe_2$, $PdTe_2$ and $PtTe_2$ by the self-consistent lmto-asa method," Journal of Physics C: Solid State Physics, vol. 19, no. 27, p. 5365, Sep 1986. [Online]. Available: https://dx.doi.org/10.1088/0022-3719/19/27/011

[121] W. Bensch, W. Heid, M. Muhler, S. Jobic, R. Brec, and J. Rouxel, "Anionic polymeric bonds in nickel ditelluride: Crystal structure, and experimental and theoretical band structure," Journal of Solid State Chemistry, vol. 121, no. 1, pp. 87–94, 1996. [Online]. Available: https://www.sciencedirect.com/science/article/pii/S0022459696900134

[122] T. R. Finlayson, W. Reichardt, and H. G. Smith, "Lattice dynamics of layered-structure compounds: $PdTe_2$," Phys. Rev. B, vol. 33, pp. 2473–2480, Feb 1986. [Online]. Available: https://link.aps.org/doi/10.1103/PhysRevB.33.2473

[123] C. Soulard, P. E. Petit, P. Deniard, M. Evain, S. Jobic, M.-H. Whangbo, and A.-C. Dhaussy, "Why pressure induces an abrupt structural rearrangement in pdte2 but not in ptte2," Journal of Solid State Chemistry, vol. 178, no. 6, pp.

2008–2014, 2005. [Online]. Available: https://www.sciencedirect.com/science/article/pii/S0022459605001623

[124] Y. Liu, J.-Z. Zhao, L. Yu, C.-T. Lin, A.-J. Liang, C. Hu, Y. Ding, Y. Xu, S.-L. He, L. Zhao, G.-D. Liu, X.-L. Dong, J. Zhang, C.-T. Chen, Z.-Y. Xu, H.-M. Weng, X. Dai, Z. Fang, and X.-J. Zhou, "Identification of topological surface state in pdte2 superconductor by angle-resolved photoemission spectroscopy," Chinese Physics Letters, vol. 32, no. 6, p. 067303, jun 2015. [Online]. Available: https://dx.doi.org/10.1088/0256-307X/32/6/067303

[125] H. Huang, S. Zhou, and W. Duan, "Type-II Dirac fermions in the $PtSe_2$ class of transition metal dichalcogenides," Phys. Rev. B, vol. 94, p. 121117, Sep 2016. [Online]. Available: https://link.aps.org/doi/10.1103/PhysRevB.94.121117

[126] Y. Wang, J. Zhang, W. Zhu, Y. Zou, C. Xi, L. Ma, T. Han, J. Yang, J. Wang, J. Xu, L. Zhang, L. Pi, C. Zhang, and Y. Zhang, "De hass-van alphen and magnetoresistance reveal predominantly single-band transport behavior in pdte2," Scientific Reports, vol. 6, p. 31554, Aug 2016. [Online]. Available: https://doi.org/10.1038/srep31554

[127] F. Fei, X. Bo, R. Wang, B. Wu, J. Jiang, D. Fu, M. Gao, H. Zheng, Y. Chen, X. Wang, H. Bu, F. Song, X. Wan, B. Wang, and G. Wang, "Nontrivial berry phase and type-II Dirac transport in the layered material $PdTe_2$," Phys. Rev. B, vol. 96, p. 041201, Jul 2017. [Online]. Available: https://link.aps.org/doi/10.1103/PhysRevB.96.041201

[128] K. Zhang, M. Yan, H. Zhang, H. Huang, M. Arita, Z. Sun, W. Duan, Y. Wu, and S. Zhou, "Experimental evidence for type-II Dirac semimetal in $PtSe_2$," Phys. Rev. B, vol. 96, p. 125102, Sep 2017. [Online]. Available: https://link.aps.org/doi/10.1103/PhysRevB.96.125102

[129] H.-J. Noh, J. Jeong, E.-J. Cho, K. Kim, B. I. Min, and B.-G. Park, "Experimental realization of type-II Dirac fermions in a $PdTe_2$ superconductor," Phys. Rev. Lett., vol. 119, p. 016401, Jul 2017. [Online]. Available: https://link.aps.org/doi/10.1103/PhysRevLett.119.016401

[130] R. C. Xiao, P. L. Gong, Q. S. Wu, W. J. Lu, M. J. Wei, J. Y. Li, H. Y. Lv, X. Luo, P. Tong, X. B. Zhu, and Y. P. Sun, "Manipulation of type-I and type-II Dirac points in $PdTe_2$ superconductor by external pressure," Phys. Rev. B, vol. 96, p. 075101, Aug 2017. [Online]. Available: https://link.aps.org/doi/10.1103/PhysRevB.96.075101

[131] W. Zheng, R. Schönemann, N. Aryal, Q. Zhou, D. Rhodes, Y.-C. Chiu, K.-W. Chen, E. Kampert, T. Förster, T. J. Martin, G. T. McCandless, J. Y. Chan, E. Manousakis, and L. Balicas, "Detailed study of the Fermi surfaces of the type-II Dirac semimetallic

candidates XTe_2 (X=Pd, Pt),” Phys. Rev. B, vol. 97, p. 235154, Jun 2018. [Online]. Available: https://link.aps.org/doi/10.1103/PhysRevB.97.235154

[132] K. Kim, S. Kim, J. S. Kim, H. Kim, J.-H. Park, and B. I. Min, “Importance of the van hove singularity in superconducting $PdTe_2$,” Phys. Rev. B, vol. 97, p. 165102, Apr 2018. [Online]. Available: https://link.aps.org/doi/10.1103/PhysRevB.97.165102

[133] B. Ghosh, D. Mondal, C.-N. Kuo, C. S. Lue, J. Nayak, J. Fujii, I. Vobornik, A. Politano, and A. Agarwal, “Observation of bulk states and spin-polarized topological surface states in transition metal dichalcogenide Dirac semimetal candidate $NiTe_2$,” Phys. Rev. B, vol. 100, p. 195134, Nov 2019. [Online]. Available: https://link.aps.org/doi/10.1103/PhysRevB.100.195134

[134] S. Mukherjee, S. W. Jung, S. F. Weber, C. Xu, D. Qian, X. Xu, P. K. Biswas, T. K. Kim, L. C. Chapon, M. D. Watson, J. B. Neaton, and C. Cacho, “Fermi-crossing type-II Dirac fermions and topological surface states in $NiTe_2$,” Scientific Reports, vol. 10, Jul 2020. [Online]. Available: https://doi.org/10.1038/s41598-020-69926-8

[135] M. Nurmamat, S. V. Eremeev, X. Wang, T. Yoshikawa, T. Kono, M. Kakoki, T. Muro, Q. Jiang, Z. Sun, M. Ye, and A. Kimura, “Bulk Dirac cone and highly anisotropic electronic structure of $NiTe_2$,” Phys. Rev. B, vol. 104, p. 155133, Oct 2021. [Online]. Available: https://link.aps.org/doi/10.1103/PhysRevB.104.155133

[136] N. H. Lam, P. L. Nguyen, B. K. Choi, T. T. Ly, G. Duvjir, T. G. Rhee, Y. J. Jo, T. H. Kim, C. Jozwiak, A. Bostwick, E. Rotenberg, Y. Hwang, Y. J. Chang, J. Lee, and J. Kim, “Controlling spin–orbit coupling to tailor type-II Dirac bands,” ACS Nano, vol. 16, no. 7, pp. 11 227–11 233, 2022, pMID: 35838605. [Online]. Available: https://doi.org/10.1021/acsnano.2c04301

[137] F. Fischer, A. Torche, M. Prada, and G. Bester, “GW effects on the topology of type-II Dirac cones in $NiTe_2$, $PtSe_2$ and $PtTe_2$,” Physical Review B, vol. 110, no. 16, Oct 2024. [Online]. Available: http://dx.doi.org/10.1103/PhysRevB.110.165146

[138] W.-X. Wang, K. Li, X. Dong, H. Xie, J. Qiu, C. Xu, K. Liu, J. Song, Y. Liu, K.-K. Bai, Y.-W. Wei, and X. Xu, “Visualizing the atomic defects by scanning tunneling microscopy in the type-II Dirac semimetal $NiTe_2$,” Physica Scripta, vol. 98, no. 1, p. 015020, Dec 2022. [Online]. Available: https://dx.doi.org/10.1088/1402-4896/acaa0e

[139] M. Qi, C. An, Y. Zhou, H. Wu, B. Zhang, C. Chen, Y. Yuan, S. Wang, Y. Zhou, X. Chen, R. Zhang, and Z. Yang, “Pressure-driven lifshitz transition in type-II Dirac semimetal $NiTe_2$,” Phys. Rev. B, vol. 101, p. 115124, Mar 2020. [Online]. Available: https://link.aps.org/doi/10.1103/PhysRevB.101.115124

[140] L. Cheng, F. C. Fei, H. Hu, Y. M. Dai, F. Q. Song, and J. Qi, "Ultrafast carrier and lattice dynamics in the Dirac semimetal $NiTe_2$," Phys. Rev. B, vol. 106, p. 104308, Sep 2022. [Online]. Available: https://link.aps.org/doi/10.1103/PhysRevB.106.104308

[141] H. Pfau, R. Daou, S. Lausberg, H. R. Naren, M. Brando, S. Friedemann, S. Wirth, T. Westerkamp, U. Stockert, P. Gegenwart, C. Krellner, C. Geibel, G. Zwicknagl, and F. Steglich, "Interplay between Kondo suppression and Lifshitz transitions in $YbRh_2Si_2$ at high magnetic fields," Phys. Rev. Lett., vol. 110, p. 256403, Jun 2013. [Online]. Available: https://link.aps.org/doi/10.1103/PhysRevLett.110.256403

[142] S. Beaulieu, S. Dong, N. Tancogne-Dejean, M. Dendzik, T. Pincelli, J. Maklar, R. P. Xian, M. A. Sentef, M. Wolf, A. Rubio, L. Rettig, and R. Ernstorfer, "Ultrafast dynamical lifshitz transition," Science Advances, vol. 7, no. 17, p. eabd9275, 2021. [Online]. Available: https://www.science.org/doi/abs/10.1126/sciadv.abd9275

[143] F. Zheng, X.-B. Li, P. Tan, Y. Lin, L. Xiong, X. Chen, and J. Feng, "Emergent superconductivity in two-dimensional $NiTe_2$ crystals," Phys. Rev. B, vol. 101, p. 100505, Mar 2020. [Online]. Available: https://link.aps.org/doi/10.1103/PhysRevB.101.100505

[144] B. S. de Lima, R. R. de Cassia, F. Santos, L. E. Correa, T. W. Grant, A. L. R. Manesco, G. W. Martins, L. T. F. Eleno, M. S. Torikachvili, and A. J. S. Machado, "Properties and superconductivity in Ti-doped $NiTe_2$ single crystals," Solid State Communications, vol. 283, pp. 27–31, 2018. [Online]. Available: https://www.sciencedirect.com/science/article/pii/S0038109818306112

[145] E. M. Lifshits and A. M. Kosevich, "Theory of the shubnikov—de haas effect," Journal of Physics and Chemistry of Solids, vol. 4, no. 1, pp. 1–10, 1958. [Online]. Available: https://www.sciencedirect.com/science/article/pii/0022369758901896

[146] D. Shoenberg, Magnetic Oscillations in Metals, ser. Cambridge Monographs on Physics. Cambridge University Press, 1984.

[147] Q. Liu, F. Fei, B. Chen, X. Bo, B. Wei, S. Zhang, M. Zhang, F. Xie, M. Naveed, X. Wan, F. Song, and B. Wang, "Nontopological origin of the planar Hall effect in the type-II Dirac semimetal $NiTe_2$," Phys. Rev. B, vol. 99, p. 155119, Apr 2019. [Online]. Available: https://link.aps.org/doi/10.1103/PhysRevB.99.155119

[148] R. Singha, S. Roy, A. Pariari, B. Satpati, and P. Mandal, "Planar Hall effect in the type-II Dirac semimetal VAl_3," Phys. Rev. B, vol. 98, p. 081103, Aug 2018. [Online]. Available: https://link.aps.org/doi/10.1103/PhysRevB.98.081103

[149] B. Seredyński, "Epitaksja dwuwymiarowych materiałów warstwowych z grupy dichalkogenków metali przejściowych: *mote*$_2$, *mose*$_2$ oraz *nite*$_2$," Nov 2021.

[150] T. M. Project, "Materials data on gaas by materials project," 7 2020. [Online]. Available: https://www.osti.gov/biblio/1200591

[151] J. Ross, M. Rubin, and T. K. Gustafson, "Single crystal wurtzite gan on (111) gaas with aln buffer layers grown by reactive magnetron sputter deposition," Journal of Materials Research, vol. 8, pp. 2613–2616, Oct 1993. [Online]. Available: https://doi.org/10.1557/JMR.1993.2613

[152] I. Institute. https://www.ioffe.ru/en/. [Online]. Available: https://www.ioffe.ru/SVA/NSM/Semicond/GaAs/thermal.html

[153] A. M. Miller, M. Lemon, M. A. Choffel, S. R. Rich, F. Harvel, and D. C. Johnson, "Extracting information from X-ray diffraction patterns containing laue oscillations," Zeitschrift für Naturforschung B, vol. 77, no. 4-5, pp. 313–322, 2022. [Online]. Available: https://doi.org/10.1515/znb-2022-0020

[154] W. J. de Haas, J. de Boer, and G. J. van dën Berg, "The electrical resistance of gold, copper and lead at low temperatures," Physica, vol. 1, no. 7, pp. 1115–1124, 1934. [Online]. Available: https://www.sciencedirect.com/science/article/pii/S0031891434803102

[155] P. A. Lee and T. V. Ramakrishnan, "Disordered electronic systems," Rev. Mod. Phys., vol. 57, pp. 287–337, Apr 1985. [Online]. Available: https://link.aps.org/doi/10.1103/RevModPhys.57.287

[156] Y. Takagaki, A. Giussani, K. Perumal, R. Calarco, and K.-J. Friedland, "Robust topological surface states in sb_2te_3 layers as seen from the weak antilocalization effect," Phys. Rev. B, vol. 86, p. 125137, Sep 2012. [Online]. Available: https://link.aps.org/doi/10.1103/PhysRevB.86.125137

[157] D. Backes, D. Huang, R. Mansell, M. Lanius, J. Kampmeier, D. Ritchie, G. Mussler, G. Gumbs, D. Grutzmacher, and V. Narayan, "Disentangling surface and bulk transport in topological-insulator $p-n$ junctions," Phys. Rev. B, vol. 96, p. 125125, Sep 2017. [Online]. Available: https://link.aps.org/doi/10.1103/PhysRevB.96.125125

[158] B. L. Altshuler, A. G. Aronov, and D. E. Khmelnitsky, "Effects of electron-electron collisions with small energy transfers on quantum localisation," Journal of Physics C: Solid State Physics, vol. 15, no. 36, p. 7367, dec 1982. [Online]. Available: https://dx.doi.org/10.1088/0022-3719/15/36/018

[159] P. Y. Yu and M. Cardona, Fundamentals of semiconductors. Physics and materials properties. Springer Heidelberg Dorderecht London New York, 2010.

[160] K. Kaasbjerg, K. S. Thygesen, and A.-P. Jauho, "Acoustic phonon limited mobility in two-dimensional semiconductors: Deformation potential and piezoelectric scattering in monolayer mos_2 from first principles," Phys. Rev. B, vol. 87, p. 235312, Jun 2013. [Online]. Available: https://link.aps.org/doi/10.1103/PhysRevB.87.235312

[161] Z. Ogorzalek, P. P. Ferreira, T. M., P. Dziawa, A. L. R. Manesco, C. Heil, S. Kret, W. Zajkowska, M. Baj, W. Pacuski, B. Seredyński, T. F. L. Elano, J. Sadowski, and M. Gryglas-Borysiewicz, "In preparation: Strain-induced dirac cone shifts in the mbe-grown anisotropic tensile-strained type-ii dirac semimetal $NiTe_2$," -, vol. -, pp. –, - 2025. [Online]. Available: -

[162] W. Kohn and L. J. Sham, "Self-consistent equations including exchange and correlation effects," Phys. Rev., vol. 140, pp. A1133–A1138, Nov 1965. [Online]. Available: https://link.aps.org/doi/10.1103/PhysRev.140.A1133

[163] P. Hohenberg and W. Kohn, "Inhomogeneous electron gas," Phys. Rev., vol. 136, pp. B864–B871, Nov 1964. [Online]. Available: https://link.aps.org/doi/10.1103/PhysRev.136.B864

[164] Z. Zhao, H. Zhang, H. Yuan, S. Wang, Y. Lin, Q. Zeng, G. Xu, Z. Liu, G. K. Solanki, K. D. Patel, Y. Cui, H. Y. Hwang, and W. L. Mao, "Pressure induced metallization with absence of structural transition in layered molybdenum diselenide," Nature Communications, vol. 6, p. 7312, Jun 2015. [Online]. Available: 10.1038/ncomms8312

[165] A. V. Kolobov, P. Fons, and J. Tominaga, "Electronic excitation-induced semiconductor-to-metal transition in monolayer $MoTe_2$," Phys. Rev. B, vol. 94, p. 094114, Sep 2016. [Online]. Available: https://link.aps.org/doi/10.1103/PhysRevB.94.094114

[166] Y. Cheon, S. Y. Lim, K. Kim, and H. Cheong, "Structural phase transition and interlayer coupling in few-layer 1T and Td $MoTe_2$," ACS Nano, vol. 15, no. 2, pp. 2962–2970, 2021, pMID: 33480685. [Online]. Available: https://doi.org/10.1021/acsnano.0c09162

[167] C. Ruppert, B. Aslan, and T. F. Heinz, "Optical properties and band gap of single- and few-layer $MoTe_2$ crystals," Nano Letters, vol. 14, no. 11, pp. 6231–6236, 2014, pMID: 25302768. [Online]. Available: https://doi.org/10.1021/nl502557g

[168] D. Puotinen and R. E. Newnham, "The crystal structure of $MoTe_2$," Acta Crystallographica, vol. 14, no. 6, pp. 691–692, Jun 1961. [Online]. Available: https://doi.org/10.1107/S0365110X61002084

[169] R. He, S. Zhong, H. H. Kim, G. Ye, Z. Ye, L. Winford, D. McHaffie, I. Rilak, F. Chen, X. Luo, Y. Sun, and A. W. Tsen, "Dimensionality-driven orthorhombic $MoTe_2$ at room temperature," Phys. Rev. B, vol. 97, p. 041410, Jan 2018. [Online]. Available: https://link.aps.org/doi/10.1103/PhysRevB.97.041410

[170] J. Guo and K. Liu, "Recent progress in two-dimensional $MoTe_2$ hetero-phase homojunctions," Nanomaterials, vol. 12, no. 1, p. 110, Dec 2021. [Online]. Available: http://dx.doi.org/10.3390/nano12010110

[171] D. H. Keum, S. Cho, J. H. Kim, D.-H. Choe, H.-J. Sung, M. Kan, H. Kang, J.-Y. Hwang, S. W. Kim, H. Yang, K. J. Chang, and Y. H. Lee, "Bandgap opening in few-layered monoclinic $MoTe_2$," Nature Physics, vol. 11, pp. 482–486, Jun 2015. [Online]. Available: https://doi.org/10.1038/nphys3314

[172] P. Tsipas, S. Fragkos, D. Tsoutsou, C. Alvarez, R. Sant, G. Renaud, H. Okuno, and A. Dimoulas, "Direct observation at room temperature of the orthorhombic Weyl semimetal phase in thin epitaxial $MoTe_2$," Advanced Functional Materials, vol. 28, no. 33, p. 1802084, 2018. [Online]. Available: https://onlinelibrary.wiley.com/doi/abs/10.1002/adfm.201802084

[173] Y. Sun, S.-C. Wu, M. N. Ali, C. Felser, and B. Yan, "Prediction of Weyl semimetal in orthorhombic $MoTe_2$," Phys. Rev. B, vol. 92, p. 161107, Oct 2015. [Online]. Available: https://link.aps.org/doi/10.1103/PhysRevB.92.161107

[174] Z. Wang, D. Gresch, A. A. Soluyanov, W. Xie, S. Kushwaha, X. Dai, M. Troyer, R. J. Cava, and B. A. Bernevig, "$MoTe_2$: A type-II Weyl topological metal," Phys. Rev. Lett., vol. 117, p. 056805, Jul 2016. [Online]. Available: https://link.aps.org/doi/10.1103/PhysRevLett.117.056805

[175] S. Kourtis, J. Li, Z. Wang, A. Yazdani, and B. A. Bernevig, "Universal signatures of Fermi arcs in quasiparticle interference on the surface of Weyl semimetals," Phys. Rev. B, vol. 93, p. 041109, Jan 2016. [Online]. Available: https://link.aps.org/doi/10.1103/PhysRevB.93.041109

[176] K. Deng, G. Wan, P. Deng, K. Zhang, S. Ding, E. Wang, M. Yan, H. Huang, H. Zhang, Z. Xu, J. Denlinger, A. Fedorov, H. Yang, W. Duan, H. Yao, Y. Wu, S. Fan, H. Zhang, X. Chen, and S. Zhou, "Experimental observation of topological

fermi arcs in type-II Weyl semimetal $MoTe_2$," Nature Physics, vol. 12, pp. 1105–110, Dec 2016. [Online]. Available: https://doi.org/10.1038/nphys3871

[177] F. C. Chen, H. Y. Lv, X. Luo, W. J. Lu, Q. L. Pei, G. T. Lin, Y. Y. Han, X. B. Zhu, W. H. Song, and Y. P. Sun, "Extremely large magnetoresistance in the type-II Weyl semimetal $MoTe_2$," Phys. Rev. B, vol. 94, p. 235154, Dec 2016. [Online]. Available: https://link.aps.org/doi/10.1103/PhysRevB.94.235154

[178] S. Thirupathaiah, R. Jha, B. Pal, J. S. Matias, P. K. Das, P. K. Sivakumar, I. Vobornik, N. C. Plumb, M. Shi, R. A. Ribeiro, and D. D. Sarma, "$MoTe_2$: An uncompensated semimetal with extremely large magnetoresistance," Phys. Rev. B, vol. 95, p. 241105, Jun 2017. [Online]. Available: https://link.aps.org/doi/10.1103/PhysRevB.95.241105

[179] D. D. Liang, Y. J. Wang, W. L. Zhen, J. Yang, S. R. Weng, X. Yan, Y. Y. Han, W. Tong, W. K. Zhu, L. Pi, and C. J. Zhang, "Origin of planar Hall effect in type-II Weyl semimetal $MoTe_2$," AIP Advances, vol. 9, no. 5, p. 055015, May 2019. [Online]. Available: https://doi.org/10.1063/1.5094231

[180] S. Nandy, G. Sharma, A. Taraphder, and S. Tewari, "Chiral anomaly as the origin of the planar Hall effect in Weyl semimetals," Phys. Rev. Lett., vol. 119, p. 176804, Oct 2017. [Online]. Available: https://link.aps.org/doi/10.1103/PhysRevLett.119.176804

[181] G. Xu, H. Weng, Z. Wang, X. Dai, and Z. Fang, "Chern semimetal and the quantized anomalous Hall effect in $HgCr_2Se_4$," Phys. Rev. Lett., vol. 107, p. 186806, Oct 2011. [Online]. Available: https://link.aps.org/doi/10.1103/PhysRevLett.107.186806

[182] D. T. Son and B. Z. Spivak, "Chiral anomaly and classical negative magnetoresistance of Weyl metals," Phys. Rev. B, vol. 88, p. 104412, Sep 2013. [Online]. Available: https://link.aps.org/doi/10.1103/PhysRevB.88.104412

[183] S. Liang, S. Shi, C.-H. Hsu, K. Cai, Y. Wang, P. He, Y. Wu, V. M. Pereira, and H. Yang, "Spin-orbit torque magnetization switching in $MoTe_2$/permalloy heterostructures," Advanced Materials, vol. 32, no. 37, p. 2002799, 2020. [Online]. Available: https://onlinelibrary.wiley.com/doi/abs/10.1002/adma.202002799

[184] B. Radisavljevic, A. Radenovic, J. Brivio, V. Giacometti, and A. Kis, "Single-layer mos2 transistors," Nature Nanotechnology, vol. 6, p. 147, Mar 2011. [Online]. Available: https://doi.org/10.1038/nnano.2010.279

[185] N. Zibouche, A. Kuc, J. Musfeldt, and T. Heine, "Transition-metal dichalcogenides for spintronic applications," Annalen der Physik, vol. 526, no. 9-10, pp. 395–401, 2014. [Online]. Available: https://onlinelibrary.wiley.com/doi/abs/10.1002/andp.201400137

[186] Z. Yin, H. Li, H. Li, L. Jiang, Y. Shi, Y. Sun, G. Lu, Q. Zhang, X. Chen, and H. Zhang, "Single-layer mos2 phototransistors," ACS Nano, vol. 6, no. 1, pp. 74–80, 2012, pMID: 22165908. [Online]. Available: https://doi.org/10.1021/nn2024557

[187] H. S. Lee, S.-W. Min, Y.-G. Chang, M. K. Park, T. Nam, H. Kim, J. H. Kim, S. Ryu, and S. Im, "Mos2 nanosheet phototransistors with thickness-modulated optical energy gap," Nano Letters, vol. 12, no. 7, pp. 3695–3700, 2012, pMID: 22681413. [Online]. Available: https://doi.org/10.1021/nl301485q

[188] L. Gao, "Flexible device applications of 2D semiconductors," Small, vol. 13, no. 35, p. 1603994, 2017. [Online]. Available: https://onlinelibrary.wiley.com/doi/abs/10.1002/smll.201603994

[189] K.-A. N. Duerloo, Y. Li, and E. J. Reed, "Structural phase transitions in two-dimensional Mo- and W-dichalcogenide monolayers," Nature Communications, vol. 5, no. 1, p. 4214, 2014. [Online]. Available: https://doi.org/10.1038/ncomms5214

[190] Q. He, P. Li, Z. Wu, B. Yuan, Z. Luo, W. Yang, J. Liu, G. Cao, W. Zhang, Y. Shen, P. Zhang, S. Liu, G. Shao, and Z. Yao, "Molecular beam epitaxy scalable growth of wafer-scale continuous semiconducting monolayer $MoTe_2$ on inert amorphous dielectrics," Advanced Materials, vol. 31, no. 32, p. 1901578, 2019. [Online]. Available: https://onlinelibrary.wiley.com/doi/abs/10.1002/adma.201901578

[191] R. Oliva, T. Wozniak, P. E. J. Faria, F. Dybala, J. Kopaczek, J. Fabian, P. Scharoch, and R. Kudrawiec, "Strong substrate strain effects in multilayered ws_2 revealed by high-pressure optical measurements," ACS Applied Materials & Interfaces, vol. 14, no. 17, pp. 19 857–19 868, 2022, pMID: 35442641. [Online]. Available: https://doi.org/10.1021/acsami.2c01726

[192] J. Tu, X. B. Chen, X. Z. Ruan, Y. F. Zhao, H. F. Xu, Z. D. Chen, X. Q. Zhang, X. W. Zhang, J. Wu, L. He, Y. Zhang, R. Zhang, and Y. B. Xu, "Direct observation of hidden spin polarization in 2H- $MoTe_2$," Phys. Rev. B, vol. 101, p. 035102, Jan 2020. [Online]. Available: https://link.aps.org/doi/10.1103/PhysRevB.101.035102

[193] B. T. Zhou, C.-P. Zhang, and K. Law, "Highly tunable nonlinear Hall effects induced by spin-orbit couplings in strained polar transition-metal dichalcogenides," Phys. Rev. Appl., vol. 13, p. 024053, Feb 2020. [Online]. Available: https://link.aps.org/doi/10.1103/PhysRevApplied.13.024053

[194] X. Xu, S. Chen, S. Liu, X. Cheng, W. Xu, P. Li, Y. Wan, S. Yang, W. Gong, K. Yuan, P. Gao, Y. Ye, and L. Dai, "Millimeter-scale single-crystalline semiconducting $MoTe_2$ via solid-to-solid phase transformation," Journal of the American Chemical

Society, vol. 141, no. 5, pp. 2128–2134, 2019, pMID: 30633514. [Online]. Available: https://doi.org/10.1021/jacs.8b12230

[195] Y. Tao, J. A. Schneeloch, C. Duan, M. Matsuda, S. E. Dissanayake, A. A. Aczel, J. A. Fernandez-Baca, F. Ye, and D. Louca, "Appearance of a T_d^* phase across the $T_d - 1T'$ phase boundary in the Weyl semimetal $MoTe_2$," Phys. Rev. B, vol. 100, p. 100101, Sep 2019. [Online]. Available: https://link.aps.org/doi/10.1103/PhysRevB.100.100101

[196] C. Heikes, I.-L. Liu, T. Metz, C. Eckberg, P. Neves, Y. Wu, L. Hung, P. Piccoli, H. Cao, J. Leao, J. Paglione, T. Yildirim, N. P. Butch, and W. Ratcliff, "Mechanical control of crystal symmetry and superconductivity in Weyl semimetal $MoTe_2$," Phys. Rev. Mater., vol. 2, p. 074202, Jul 2018. [Online]. Available: https://link.aps.org/doi/10.1103/PhysRevMaterials.2.074202

[197] M. B. Vellinga, R. de Jonge, and C. Haas, "Semiconductor to metal transition in $MoTe_2$," Journal of Solid State Chemistry, vol. 2, no. 2, pp. 299–302, 1970. [Online]. Available: https://www.sciencedirect.com/science/article/pii/002245967090085X

[198] R. Clarke, E. Marseglia, and H. P. Hughes, "A low-temperature structural phase transition in $\beta - MoTe_2$," Philosophical Magazine B, vol. 38, no. 2, pp. 121–126, 1978. [Online]. Available: https://doi.org/10.1080/13642817808245670

[199] H. P. Hughes and R. H. Friend, "Electrical resistivity anomaly in beta-$MoTe_2$," 1978. [Online]. Available: https://api.semanticscholar.org/CorpusID:99133474

[200] Y. Wang, J. Xiao, H. Zhu, Y. Li, Y. Alsaid, K. Y. Fong, Y. Zhou, S. Wang, W. Shi, Y. Wang, A. Zettl, E. J. Reed, and X. Zhang, "Structural phase transition in monolayer $MoTe_2$ driven by electrostatic doping," Nature, vol. 550, pp. 487–491, Oct 2017. [Online]. Available: https://doi.org/10.1038/nature24043

[201] S. Song, D. H. Keum, S. Cho, D. Perello, Y. Kim, and Y. H. Lee, "Room temperature semiconductor–metal transition of $MoTe_2$ thin films engineered by strain," Nano Letters, vol. 16, no. 1, pp. 188–193, 2016, pMID: 26713902. [Online]. Available: https://doi.org/10.1021/acs.nanolett.5b03481

[202] V. O. Khaustov, D. Convertino, J. Köster, A. A. Zakharov, M. J. Mohn, Z. M. Gebeyehu, L. Martini, S. Pace, G. Marini, M. Calandra, U. Kaiser, S. Forti, and C. Coletti, "Heterocontact-triggered 1H to 1T phase transition in cvd-grown monolayer $MoTe_2$: Implications for low contact resistance electronic devices," ACS Applied Nano Materials, vol. 0, no. 0, p. null, 2023. [Online]. Available: https://doi.org/10.1021/acsanm.3c01314

[203] J. Li, H. Gao, G. Zhou, Y. Li, Y. Chai, and G. Hao, "Controllable growth of large-area 1T, 2H ultrathin $MoTe_2$ films, and 1T–2H in-plane homojunction," Journal of Applied Physics, vol. 131, no. 18, p. 185302, May 2022. [Online]. Available: https://doi.org/10.1063/5.0087432

[204] Y. Tan, F. Luo, M. Zhu, X. Xu, Y. Ye, B. Li, G. Wang, W. Luo, X. Zheng, N. Wu, Y. Yu, S. Qin, and X.-A. Zhang, "Controllable 2H-to-1T phase transition in few-layer $MoTe_2$," Nanoscale, vol. 10, pp. 19 964–19 971, 2018. [Online]. Available: http://dx.doi.org/10.1039/C8NR06115G

[205] F. Herling, C. Morrison, C. S. Knox, S. Zhang, O. Newell, M. Myronov, E. H. Linfield, and C. H. Marrows, "Spin-orbit interaction in InAs/GaSb heterostructures quantified by weak antilocalization," Phys. Rev. B, vol. 95, p. 155307, Apr 2017. [Online]. Available: https://link.aps.org/doi/10.1103/PhysRevB.95.155307

[206] D. A. Rhodes, A. Jindal, N. F. Q. Yuan, Y. Jung, A. Antony, H. Wang, B. Kim, Y. Chiu, T. Taniguchi, K. Watanabe, K. Barmak, L. Balicas, C. R. Dean, X. Qian, L. Fu, A. N. Pasupathy, and J. Hone, "Enhanced superconductivity in monolayer Td-$MoTe_2$," Nano Letters, vol. 21, no. 6, pp. 2505–2511, 2021, pMID: 33689385. [Online]. Available: https://doi.org/10.1021/acs.nanolett.0c04935

[207] G. Mirabelli, C. McGeough, E. K. Schmidt, M.and McCarthy, S. Monaghan, I. M. Povey, M. McCarthy, F. Gity, R. Nagle, G. Hughes, A. Cafolla, P. K. Hurley, and R. Duffy, "Air sensitivity of MoS_2, $MoSe_2$, $MoTe_2$, HfS_2, and $HfSe_2$," Journal of Applied Physics, vol. 120, no. 12, p. 125102, Sep 2016. [Online]. Available: https://doi.org/10.1063/1.4963290

[208] D. Rhodes, S. H. Chae, R. Ribeiro-Palau, and J. Hone, "Disorder in van der Waals heterostructures of 2D materials," Nature materials, vol. 18, pp. 541–549, Jun 2019. [Online]. Available: https://www.nature.com/articles/s41563-019-0366-8

[209] W. Park, J. Park, J. Jang, H. Lee, H. Jeong, K. Cho, S. Hong, and T. Lee, "Oxygen environmental and passivation effects on molybdenum disulfide field effect transistors," Nanotechnology, vol. 24, no. 9, p. 095202, Feb 2013. [Online]. Available: https://dx.doi.org/10.1088/0957-4484/24/9/095202

[210] H. C. Diaz, R. Chaghi, Y. Ma, and M. Batzill, "Molecular beam epitaxy of the van der Waals heterostructure $MoTe_2$ on MoS_2: phase, thermal, and chemical stability," 2D Materials, vol. 2, no. 4, p. 044010, Nov 2015. [Online]. Available: https://dx.doi.org/10.1088/2053-1583/2/4/044010

[211] A. Rani, K. DiCamillo, M. A. H. Khan, M. Paranjape, and M. E. Zaghloul, "Tuning the polarity of $MoTe_2$ FETs by varying the channel thickness for gas-sensing applications," Sensors, vol. 19, no. 11, 2019. [Online]. Available: https://www.mdpi.com/1424-8220/19/11/2551

[212] I. Shackery, A. Pezeshki, J. Y. Park, U. Palanivel, H. J. Kwon, H. S. Yoon, S. Im, J. S. Cho, and S. C. Jun, "Few-layered $\alpha - MoTe_2$ Schottky junction for a high sensitivity chemical-vapour sensor," J. Mater. Chem. C, vol. 6, pp. 10 714–10 722, 2018. [Online]. Available: http://dx.doi.org/10.1039/C8TC02635A

[213] S.-H. Yang, C.-Y. Lin, Y.-M. Chang, M. Li, K.-C. Lee, C.-F. Chen, F.-S. Yang, C.-H. Lien, K. Ueno, K. Watanabe, T. Taniguchi, K. Tsukagoshi, and Y.-F. Lin, "Oxygen-sensitive layered $MoTe_2$ channels for environmental detection," ACS Applied Materials & Interfaces, vol. 11, no. 50, pp. 47 047–47 053, 2019, pMID: 31746187. [Online]. Available: https://doi.org/10.1021/acsami.9b15036

[214] G. Stan, C. V. Ciobanu, S. R. J. Likith, A. Rani, S. Zhang, C. A. Hacker, S. Krylyuk, and A. V. Davydov, "Doping of $MoTe_2$ via surface charge transfer in air," ACS Applied Materials & Interfaces, vol. 12, no. 15, pp. 18 182–18 193, 2020, pMID: 32192325. [Online]. Available: https://doi.org/10.1021/acsami.0c04339

[215] L. Yang, H. Wu, W. Zhang, Z. Chen, J. Li, X. Lou, Z. Xie, R. Zhu, and H. Chang, "Anomalous oxidation and its effect on electrical transport originating from surface chemical instability in large-area, few-layer 1T-$MoTe_2$ films," Nanoscale, vol. 10, pp. 19 906–19 915, 2018. [Online]. Available: http://dx.doi.org/10.1039/C8NR05699D

[216] B. Sirota, N. Glavin, S. Krylyuk, A. V. Davydov, and A. A. Voevodin, "Hexagonal $MoTe_2$ with amorphous bn passivation layer for improved oxidation resistance and endurance of 2D field effect transistors," Scientific Reports, vol. 8, p. 8668, Jun 2018. [Online]. Available: https://doi.org/10.1038/s41598-018-26751-4

[217] B. Chen, H. Sahin, A. Suslu, L. Ding, M. I. Bertoni, F. M. Peeters, and S. Tongay, "Environmental changes in $MoTe_2$ excitonic dynamics by defects-activated molecular interaction," ACS Nano, vol. 9, no. 5, pp. 5326–5332, 2015, pMID: 25868985. [Online]. Available: https://doi.org/10.1021/acsnano.5b00985

[218] H. Zhu, Q. Wang, L. Cheng, R. Addou, J. Kim, M. J. Kim, and R. M. Wallace, "Defects and surface structural stability of $MoTe_2$ under vacuum annealing," ACS Nano, vol. 11, no. 11, pp. 11 005–11 014, 2017, pMID: 29116754. [Online]. Available: https://doi.org/10.1021/acsnano.7b04984

[219] D. Qu, X. Liu, M. Huang, C. Lee, F. Ahmed, H. Kim, R. S. Ruoff, J. Hone, and W. J. Yoo, "Carrier-type modulation and mobility improvement of thin $MoTe_2$," Advanced Materials, vol. 29, no. 39, p. 1606433, 2017. [Online]. Available: https://onlinelibrary.wiley.com/doi/abs/10.1002/adma.201606433

[220] M. J. Mleczko, A. C. Yu, C. M. Smyth, V. Chen, Y. C. Shin, S. Chatterjee, Y.-C. Tsai, Y. Nishi, R. M. Wallace, and E. Pop, "Contact engineering high-performance n-type $MoTe_2$ transistors," Nano Letters, vol. 19, no. 9, pp. 6352–6362, 2019, pMID: 31314531. [Online]. Available: https://doi.org/10.1021/acs.nanolett.9b02497

[221] J. P. Fraser, L. Masaityte, J. Zhang, S. Laing, J. C. Moreno-Lopez, A. F. McKenzie, J. C. McGlynn, V. Panchal, D. Graham, O. Kazakova, T. Pichler, D. A. MacLaren, D. A. J. Moran, and A. Y. Ganin, "Selective phase growth and precise-layer control in $MoTe_2$," Communications Materials, vol. 1, p. 45, Jul 2020. [Online]. Available: https://doi.org/10.1038/s43246-020-00048-4

[222] Q. Wang, H. Zhu, C. Zhang, R. Addou, K. Cho, R. M. Wallace, and M. J. Kim, "In situ heating study of 2H-$MoTe_2$ to Mo_6Te_6 nanowire phase transition," Microscopy and Microanalysis, vol. 23, no. S1, p. 1764–1765, Jul 2017.

[223] H. Zhu, Q. Wang, C. Zhang, R. Addou, K. Cho, R. M. Wallace, and M. J. Kim, "New Mo_6Te_6 sub-nanometer-diameter nanowire phase from 2H-$MoTe_2$," Advanced Materials, vol. 29, no. 18, p. 1606264, 2017. [Online]. Available: https://onlinelibrary.wiley.com/doi/abs/10.1002/adma.201606264

[224] Y. Yu, G. Wang, Y. Tan, N. Wu, X.-A. Zhang, and S. Qin, "Phase-controlled growth of one-dimensional mo6te6 nanowires and two-dimensional $MoTe_2$ ultrathin films heterostructures," Nano Letters, vol. 18, no. 2, pp. 675–681, 2018, pMID: 29262252. [Online]. Available: https://doi.org/10.1021/acs.nanolett.7b03058

[225] Y. Yoo, J. S. Jeong, R. Ma, S. J. Koester, and J. E. Johns, "Ultrathin one-dimensional molybdenum telluride quantum wires synthesized by chemical vapor deposition," Chemistry of Materials, vol. 32, no. 22, pp. 9650–9655, 2020. [Online]. Available: https://doi.org/10.1021/acs.chemmater.0c03264

[226] R. S. Lee, D. Kim, S. A. Pawar, T. Kim, J. C. Shin, and S.-W. Kang, "van der Waals epitaxy of high-mobility polymorphic structure of Mo_6Te_6 nanoplates/$MoTe_2$ atomic layers with low schottky barrier height," ACS Nano, vol. 13, no. 1, pp. 642–648, 2019. [Online]. Available: https://doi.org/10.1021/acsnano.8b07720

[227] D. Farson, J. Ready, and T. Feeley, LIA Handbook of Laser Materials Processing. Springer Berlin Heidelberg, 2001. [Online]. Available: https://books.google.pl/books?id=TQwoAAAACAAJ

[228] J. A. Medrano, N. C. A. De Nooijer, F. Gallucci, and M. Van Sint Annaland, "Advancement of an infra-red technique for whole-field concentration measurements in fluidized beds," Sensors, vol. 16, no. 3, 2016. [Online]. Available: https://www.mdpi.com/1424-8220/16/3/300

[229] M. Kan, H. G. Nam, Y. H. Lee, and Q. Sun, "Phase stability and Raman vibration of the molybdenum ditelluride ($MoTe_2$) monolayer," Phys. Chem. Chem. Phys., vol. 17, pp. 14 866–14 871, 2015. [Online]. Available: http://dx.doi.org/10.1039/C5CP01649E

[230] A. Ohtake, X. Yang, and J. Nara, "Structure and morphology of 2H-$MoTe_2$ monolayer on GaAs(111)B grown by molecular-beam epitaxy," npj 2D Materials and Applications, vol. 6, p. 35, May 2022. [Online]. Available: https://doi.org/10.1038/s41699-022-00310-y

[231] J. T. Ross, M. D. Rubin, and T. K. Gustafson, "Single crystal wurtzite gan on (111) gaas with ain buffer layers grown by reactive magnetron sputter deposition," Journal of Materials Research, vol. 8, no. 10, pp. 2613–2616, 10/1993 1991.

[232] D. Puotinen and R. E. Newnham, "The crystal structure of $MoTe_2$," Acta Crystallographica, vol. 14, no. 6, pp. 691–692, 1961. [Online]. Available: https://onlinelibrary.wiley.com/doi/abs/10.1107/S0365110X61002084

[233] B. Hen, X. Zhang, V. Shelukhin, A. Kapitulnik, and A. Palevski, "Superconductor–insulator transition in two-dimensional indium–indium-oxide composite," Proceedings of the National Academy of Sciences, vol. 118, no. 2, p. e2015970118, 2021. [Online]. Available: https://www.pnas.org/doi/abs/10.1073/pnas.2015970118

[234] R. W. Shaw, D. E. Mapother, and D. C. Hopkins, "Critical fields of superconducting tin, indium, and tantalum," Phys. Rev., vol. 120, pp. 88–91, Oct 1960. [Online]. Available: https://link.aps.org/doi/10.1103/PhysRev.120.88

[235] P. Dumas, J. P. Dubarry-Barbe, D. Rivière, Y. Levy, and J. Corset, "Growth of thin alumina film on aluminium at room temperature: a kinetic and spectroscopic study by surface plasmon excitation," J. Phys. Colloques, vol. 44, no. C10, pp. C10–205–C10–208, 1983. [Online]. Available: https://doi.org/10.1051/jphyscol:19831042

[236] N. Markovic, C. Christiansen, D. E. Grupp, A. M. Mack, G. Martinez-Arizala, and A. M. Goldman, "Anomalous hopping exponents of ultrathin metal

films," Phys. Rev. B, vol. 62, pp. 2195–2200, Jul 2000. [Online]. Available: https://link.aps.org/doi/10.1103/PhysRevB.62.2195

[237] J. C. Phillips, "Anomalous hopping exponents of ultrathin metal films," Phys. Rev. B, vol. 64, p. 035411, Jun 2001. [Online]. Available: https://link.aps.org/doi/10.1103/PhysRevB.64.035411

[238] C. J. Adkins and E. G. Astrakharchik, "Screened hopping conduction in ultrathin metal films," Journal of Physics: Condensed Matter, vol. 10, no. 30, pp. 6651–6657, aug 1998.

[239] A. Laturia, M. L. Van de Put, and W. G. Vandenberghe, "Dielectric properties of hexagonal boron nitride and transition metal dichalcogenides: from monolayer to bulk," npj 2D Materials and Applications, vol. 2, p. 6, Mar 2018. [Online]. Available: https://doi.org/10.1038/s41699-018-0050-x

[240] A. Roy, H. C. P. Movva, B. Satpati, K. Kim, R. Dey, A. Rai, T. Pramanik, S. Guchhait, E. Tutuc, and S. K. Banerjee, "Structural and electrical properties of $MoTe_2$ and $MoSe_2$ grown by molecular beam epitaxy," ACS Applied Materials & Interfaces, vol. 8, no. 11, pp. 7396–7402, 2016, pMID: 26939890. [Online]. Available: https://doi.org/10.1021/acsami.6b00961

[241] V. range hopping conduction in doped germanium at very low temperatures and high magnetic fields, "Schoepe, w." Zeitschrift fur Physik B Condensed Matter, vol. 71, pp. 455–463, Dec 1988. [Online]. Available: https://doi.org/10.1007/BF01313932

[242] H. Gu, J. Guo, X. Zhang, Q. He, Y. Huang, H. A. Colorado, N. Haldolaarachchige, H. Xin, D. P. Young, S. Wei, and Z. Guo, "Giant magnetoresistive phosphoric acid doped polyaniline–silica nanocomposites," The Journal of Physical Chemistry C, vol. 117, no. 12, pp. 6426–6436, 2013. [Online]. Available: https://doi.org/10.1021/jp311471f

[243] M. M. Parish and P. B. Littlewood, "Non-saturating magnetoresistance in heavily disordered semiconductors," Nature, vol. 426, pp. 162–165, Nov 2003. [Online]. Available: https://doi.org/10.1038/nature02073

[244] S. Furuseth, K. Selte, and A. Kjekshus, "On the arsenides and antimonides of tantalum," Acta Chemica Scandinavica, Ser. A and Ser. B, vol. 19, 1 1965. [Online]. Available: https://www.osti.gov/biblio/4610754

[245] C.-C. Lee, S.-Y. Xu, S.-M. Huang, D. S. Sanchez, I. Belopolski, G. Chang, G. Bian, N. Alidoust, H. Zheng, M. Neupane, B. Wang, A. Bansil, M. Z. Hasan, and H. Lin,

"Fermi surface interconnectivity and topology in Weyl fermion semimetals TaAs, TaP, NbAs, and NbP," Phys. Rev. B, vol. 92, p. 235104, Dec 2015. [Online]. Available: https://link.aps.org/doi/10.1103/PhysRevB.92.235104

[246] S.-Y. Xu, I. Belopolski, N. Alidoust, M. Neupane, G. Bian, C. Zhang, R. Sankar, G. Chang, Z. Yuan, C.-C. Lee, S.-M. Huang, H. Zheng, J. Ma, D. S. Sanchez, B. Wang, A. Bansil, F. Chou, P. P. Shibayev, H. Lin, S. Jia, and M. Z. Hasan, "Discovery of a Weyl fermion semimetal and topological Fermi arcs," Science, vol. 349, no. 6248, pp. 613–617, 2015. [Online]. Available: https://www.science.org/doi/abs/10.1126/science.aaa9297

[247] M. I. Naher and S. H. Naqib, "An ab-initio study on structural, elastic, electronic, bonding, thermal, and optical properties of topological Weyl semimetal TaX (X= P, As)," Scientific Reports, vol. 11, p. 5592, Mar 2021. [Online]. Available: https://doi.org/10.1038/s41598-021-85074-z

[248] S.-M. Huang, S.-Y. Xu, I. Belopolski, C.-C. Lee, G. Chang, B. Wang, N. Alidoust, G. Bian, M. Neupane, C. Zhang, S. Jia, A. Bansil, H. Lin, and M. Z. Hasan, "A Weyl fermion semimetal with surface Fermi arcs in the transition metal monopnictide TaAs class," Nature Communications, vol. 6, p. 7373, Jun 2015. [Online]. Available: https://doi.org/10.1038/ncomms8373

[249] B. Q. Lv, H. M. Weng, B. B. Fu, X. P. Wang, H. Miao, J. Ma, P. Richard, X. C. Huang, L. X. Zhao, G. F. Chen, Z. Fang, X. Dai, T. Qian, and H. Ding, "Experimental discovery of Weyl semimetal TaAs," Phys. Rev. X, vol. 5, p. 031013, Jul 2015. [Online]. Available: https://link.aps.org/doi/10.1103/PhysRevX.5.031013

[250] J. Sadowski, J. Z. Domagala, W. Zajkowska, S. Kret, B. Seredynski, M. Gryglas-Borysiewicz, Z. Ogorzalek, R. Bozek, and W. Pacuski, "Structural properties of TaAs Weyl semimetal thin films grown by molecular beam epitaxy on GaAs(001) substrates," Crystal Growth and Design, vol. 22, pp. 6039–6045, 2022. [Online]. Available: https://doi.org/10.1021/acs.cgd.2c00669

[251] T. Besara, D. A. Rhodes, K.-W. Chen, S. Das, Q. R. Zhang, J. Sun, B. Zeng, Y. Xin, L. Balicas, R. E. Baumbach, E. Manousakis, D. J. Singh, and T. Siegrist, "Coexistence of Weyl physics and planar defects in the semimetals TaP and TaAs," Physical Review B, vol. 93, no. 24, Jun 2016. [Online]. Available: https://doi.org/10.1103%2Fphysrevb.93.245152

[252] J. Buckeridge, D. Jevdokimovs, C. R. A. Catlow, and A. A. Sokol, "Nonstoichiometry and Weyl fermionic behavior in TaAs," Phys. Rev. B, vol. 94, p. 180101, Nov 2016. [Online]. Available: https://link.aps.org/doi/10.1103/PhysRevB.94.180101

[253] R. Sankar, G. Peramaiyan, I. P. Muthuselvam, S. Xu, M. Z. Hasan, and F. C. Chou, "Crystal growth and transport properties of Weyl semimetal TaAs," J. Phys.: Condens. Matter, vol. 30, Nov 2017. [Online]. Available: https://iopscience.iop.org/article/10.1088/1361-648X/aa9a75#Acknowledgments

[254] J. N. Nelson, A. D. Rice, R. Kurleto, A. Shackelford, Z. Sierzega, C.-S. Jiang, A. G. Norman, M. E. Holtz, J. S. Mangum, I. A. Leahy, K. N. Heinselman, H. Ness, M. Van Schilfgaarde, D. S. Dessau, and K. Alberi, "Thin film TaAs: developing a platform for Weyl semimetal devices," arXiv:2303.05469v1, 2023. [Online]. Available: https://doi.org/10.48550/arXiv.2303.05469

[255] N. Schönberg, "An x-ray investigation of transition metal phosphides," Acta Chemica Scandinavica, vol. 8, pp. 226–239, 1954. [Online]. Available: http://actachemscand.org/doi/10.3891/acta.chem.scand.08-0226

[256] J.-O. Willerström, "Stacking disorder in nbp, tap, nbas and taas," Journal of the Less Common Metals, vol. 99, no. 2, pp. 273–283, 1984. [Online]. Available: https://www.sciencedirect.com/science/article/pii/002250888490225X

[257] Y. Sun, S.-C. Wu, and B. Yan, "Topological surface states and Fermi arcs of the noncentrosymmetric Weyl semimetals TaAs, TaP, NbAs, and NbP," Phys. Rev. B, vol. 92, p. 115428, Sep 2015. [Online]. Available: https://link.aps.org/doi/10.1103/PhysRevB.92.115428

[258] X. Zheng, Q. Gu, Y. Liu, B. Tong, J.-F. Zhang, C. Zhang, S. Jia, J. Feng, and R.-R. Du, "Observation of 1D Fermi arc states in Weyl semimetal TaAs," National Science Review, vol. 9, no. 8, p. nwab191, Oct 2021. [Online]. Available: https://doi.org/10.1093/nsr/nwab191

[259] H. Weng, C. Fang, Z. Fang, B. A. Bernevig, and X. Dai, "Weyl semimetal phase in noncentrosymmetric transition-metal monophosphides," Phys. Rev. X, vol. 5, p. 011029, Mar 2015. [Online]. Available: https://link.aps.org/doi/10.1103/PhysRevX.5.011029

[260] C.-L. Zhang, Z. Yuan, Q.-D. Jiang, B. Tong, C. Zhang, X. C. Xie, and S. Jia, "Electron scattering in tantalum monoarsenide," Phys. Rev. B, vol. 95, p. 085202, Feb 2017. [Online]. Available: https://link.aps.org/doi/10.1103/PhysRevB.95.085202

[261] H. Boller and E. Parthé, "The transposition structure of NbAs and of similar monophosphides and arsenides of niobium and tantalum," Acta Crystallographica, vol. 16, no. 11, pp. 1095–1101, Nov 1963. [Online]. Available: https://doi.org/10.1107/S0365110X63002930

[262] J. Xiang, S. Hu, M. Lv, J. Zhang, H. Zhao, G. Chen, W. Li, Z. Chen, and P. Sun, "Anisotropic thermal and electrical transport of Weyl semimetal TaAs," Journal of Physics: Condensed Matter, vol. 29, no. 48, p. 485501, nov 2017. [Online]. Available: https://dx.doi.org/10.1088/1361-648X/aa964b

[263] J. H. Mooij, "Electrical conduction in concentrated disordered transition metal alloys," Physica Status Solidi (A), vol. 17, no. 2, pp. 521–530, 1973. [Online]. Available: https://onlinelibrary.wiley.com/doi/abs/10.1002/pssa.2210170217

[264] X. Huang, L. Zhao, Y. Long, P. Wang, D. Chen, Z. Yang, H. Liang, M. Xue, H. Weng, Z. Fang, X. Dai, and G. Chen, "Observation of the chiral-anomaly-induced negative magnetoresistance in 3D Weyl semimetal TaAs," Phys. Rev. X, vol. 5, p. 031023, Aug 2015. [Online]. Available: https://link.aps.org/doi/10.1103/PhysRevX.5.031023

[265] D. S. Campbell and B. Hendry, "The effect of composition on the temperature coefficient of resistance of nicr films," British Journal of Applied Physics, vol. 16, no. 11, p. 1719, Nov 1965. [Online]. Available: https://dx.doi.org/10.1088/0508-3443/16/11/315

[266] C.-L. Zhang, S.-Y. Xu, I. Belopolski, Z. Yuan, Z. Lin, B. Tong, G. Bian, N. Alidoust, C.-C. Lee, S.-M. Huang, T.-R. Chang, G. Chang, C.-H. Hsu, H.-T. Jeng, M. Neupane, D. S. Sanchez, H. Zheng, J. Wang, H. Lin, C. Zhang, H.-Z. Lu, S.-Q. Shen, T. Neupert, M. Zahid Hasan, and S. Jia, "Signatures of the Adler–Bell–Jackiw chiral anomaly in a Weyl fermion semimetal," Nature Communications, vol. 7, pp. 2041–1723, 2016. [Online]. Available: https://doi.org/10.1038/ncomms10735

[267] A. Bedoya-Pinto, A. K. Pandeya, D. Liu, H. Deniz, K. Chang, H. Tan, H. Han, J. Jena, I. Kostanovskiy, and S. S. P. Parkin, "Realization of epitaxial NbP and TaP Weyl semimetal thin films," ACS Nano, vol. 14, no. 4, pp. 4405–4413, 2020, pMID: 32053338. [Online]. Available: https://doi.org/10.1021/acsnano.9b09997

[268] Z. Ogorzałek-Sory, C.-C. Lee, J. Z. Domagala, W. Zajkowska-Pietrzak, S. Kret, R. Bozek, W. Pacuski, I. Lutsyk, W. Rys, P. J. Kowalczyk, M. Tokarczyk, M. Polakowski, D. Wasik, J. Sadowski, B.-H. Huang, H. Lin, and M. Gryglas-Borysiewicz, "Orthorhombic TaAs - a new topological phase of the archetypical Weyl semimetal," ACS Applied Materials Interfaces, 2025.

[269] B. M. S. R. Hall, "International tables for crystallography, volume a: Space-group symmetry," 2005. [Online]. Available: https://doi.org/10.1107/97809553602060000107

[270] G. M. Stephen, O. A. Vail, J. Lu, W. A. Beck, P. J. Taylor, and A. L. Friedman, "Weak antilocalization and anisotropic magnetoresistance as a probe of surface states

in topological $bi_2te_xse_{3-x}$ thin films," Scientific Reports, vol. 10, p. 4845, Mar 2020. [Online]. Available: https://doi.org/10.1038/s41598-020-61672-1

[271] S. Sasmal, J. Mukherjee, D. Suri, and K. V. Raman, "In-depth analysis of anisotropic magnetoconductance in bi_2se_3 thin films with electron–electron interaction corrections," Journal of Physics: Condensed Matter, vol. 33, no. 46, p. 465601, Sep 2021. [Online]. Available: https://dx.doi.org/10.1088/1361-648X/ac1de0

[272] M. Brahlek, N. Koirala, M. Salehi, N. Bansal, and S. Oh, "Emergence of decoupled surface transport channels in bulk insulating Bi_2Se_3 thin films," Phys. Rev. Lett., vol. 113, p. 026801, Jul 2014. [Online]. Available: https://link.aps.org/doi/10.1103/PhysRevLett.113.026801

[273] M. Brahlek, N. Koirala, N. Bansal, and S. Oh, "Transport properties of topological insulators: Band bending, bulk metal-to-insulator transition, and weak anti-localization," Solid State Communications, vol. 215-216, pp. 54–62, 2015. [Online]. Available: https://www.sciencedirect.com/science/article/pii/S0038109814004426

[274] J. Kondo, "Resistance Minimum in Dilute Magnetic Alloys," Progress of Theoretical Physics, vol. 32, no. 1, pp. 37–49, Jul 1964. [Online]. Available: https://doi.org/10.1143/PTP.32.37

[275] N. L. Nair, M.-E. Boulanger, F. Laliberté, S. Griffin, S. Channa, A. Legros, W. Tabis, C. Proust, J. Neaton, L. Taillefer, and J. G. Analytis, "Signatures of possible surface states in taas," Phys. Rev. B, vol. 102, p. 075402, Aug 2020. [Online]. Available: https://link.aps.org/doi/10.1103/PhysRevB.102.075402

[276] S. Singh, R. K. Gopal, J. Sarkar, S. Roy, and C. Mitra, "Evidence of charged puddles and induced dephasing in topological insulator thin films," AIP Conference Proceedings, vol. 1953, no. 1, p. 050040, May 2018. [Online]. Available: https://doi.org/10.1063/1.5032695

[277] J. Liao, Y. Ou, H. Liu, K. He, X. Ma, Q.-K. Xue, and Y. Li, "Enhanced electron dephasing in three-dimensional topological insulators," Nature Communications, vol. 8, no. 1, p. 16071, Jul 2017. [Online]. Available: https://doi.org/10.1038/ncomms16071

[278] W. Mortelmans, S. De Gendt, M. Heyns, and C. Merckling, "Epitaxy of 2D chalcogenides: Aspects and consequences of weak van der Waals coupling," Applied Materials Today, vol. 22, p. 100975, 2021. [Online]. Available: https://www.sciencedirect.com/science/article/pii/S2352940721000408

[279] J. Momand, J. E. Boschker, R. Wang, R. Calarco, and B. J. Kooi, "Tailoring the epitaxy of sb2te3 and gete thin films using surface passivation," CrystEngComm, vol. 20, pp. 340–347, 2018. [Online]. Available: http://dx.doi.org/10.1039/C7CE01825H

[280] R. Yue, A. T. Barton, H. Zhu, A. Azcatl, L. F. Pena, J. Wang, X. Peng, N. Lu, L. Cheng, R. Addou, S. McDonnell, L. Colombo, J. W. P. Hsu, J. Kim, M. J. Kim, R. M. Wallace, and C. L. Hinkle, "$HfSe_2$ thin films: 2D transition metal dichalcogenides grown by molecular beam epitaxy," ACS Nano, vol. 9, no. 1, pp. 474–480, 2015, pMID: 25496648. [Online]. Available: https://doi.org/10.1021/nn5056496

[281] N. V. Tarakina, S. Schreyeck, M. Luysberg, S. Grauer, C. Schumacher, G. Karczewski, K. Brunner, C. Gould, H. Buhmann, R. E. Dunin-Borkowski, and L. W. Molenkamp, "Suppressing twin formation in bi2se3 thin films," Advanced Materials Interfaces, vol. 1, no. 5, p. 1400134, 2014. [Online]. Available: https://onlinelibrary.wiley.com/doi/abs/10.1002/admi.201400134

[282] A. Koma, "Van der Waals epitaxy for highly lattice-mismatched systems," Journal of Crystal Growth, vol. 201-202, pp. 236–241, 1999. [Online]. Available: https://www.sciencedirect.com/science/article/pii/S0022024898013293

[283] K. . S. L. Dicing Systems. K&s 4500 series manual wire bonders. [Online]. Available: https://nano.physics.leidenuniv.nl/dokuwiki/lib/exe/fetch.php?media=kns4500analogwirebond˙-˙manual.pdf

[284] H. Choi, J.and Zhang, H. Du, and J. H. Choi, "Understanding solvent effects on the properties of two-dimensional transition metal dichalcogenides," ACS Applied Materials & Interfaces, vol. 8, no. 14, pp. 8864–8869, 2016, pMID: 27018600. [Online]. Available: https://doi.org/10.1021/acsami.6b01491

[285] A. M. Landge, B. M. Jordan, X. Diego, and P. Müller, "Pattern formation mechanisms of self-organizing reaction-diffusion systems," Developmental Biology, vol. 460, no. 1, pp. 2–11, 2020, systems Biology of Pattern Formation. [Online]. Available: https://www.sciencedirect.com/science/article/pii/S001216061930377X